THE UNIVERSITY *of* EDINBURGH

The crystal chemistry of accessory minerals as a probe of magmatic oxygen fugacity: An experimental study

Thomas Nathanael Stokes

Thesis submitted for the degree of
Doctor of Philosophy

School of GeoSciences
The University of Edinburgh
2018

Author's Declaration

I declare that this thesis was composed by myself, that the work contained herein is my own except where explicitly stated otherwise in the text, and that this work has not been submitted for any other degree or professional qualification except as specified.

Parts of this work has been published in *Stokes, T., Bromiley, G., Gatta, G., Rotiroti, N., Potts, N., & Saunders, K. (2018). Cation distribution and valence in synthetic Al–Mn–O and Fe–Mn–O spinels under varying f_{O_2} conditions. Mineralogical Magazine, 82(4), 975-992.*. This paper has been modified and incorporated in this thesis as Chapter 3. Whilst this is mainly my own work, single crystal X-ray diffraction data and structural refinement was carried out by G. Gatta and N. Rotiroti, and they provided details on the analytical procedure for incorporation into the paper. Minor edits were also suggested by the team of co-authors.

Chapter 4 has been published as: *Stokes, T., Bromiley, G., Potts, N., Saunders, K., Miles, A., and EIMF (2019). The effect of melt composition and oxygen fugacity on manganese partitioning between apatite and silicate melt. Chemical Geology, 506, 162-174.* Again, this is my own work, except for the conception of the project (A. Miles and G. Bromiley) and minor manuscript edits suggested by co-authors and the reviewer James Brenan.

Thomas Stokes

2019

Abstract

It is well established that oxygen fugacity, f_{O_2}, is one of the key parameters that needs to be quantified in order to understand igneous processes, model the geophysical behaviour of the core and mantle, to understand the exchange of C-O-H-S gases between the atmosphere and the interior of the Earth, and to further our understanding of other terrestrial planets. Despite this it remains one of the most poorly constrained geochemical variables, limiting our understanding of terrestrial systems. Recent work has focused on using accessory minerals for determining magmatic f_{O_2}, as a probe to constraining conditions in planetary interiors.

Accessory minerals are already important petrological tools for providing insight into magmatic conditions. These minerals may concentrate a variety of trace elements, and hence are crucial in understanding the elemental budget of magmas. Accessory minerals such as zircon and apatite are also some of the hardier minerals found in igneous rocks and are, therefore, less likely to be altered by processes such as chemical weathering, metasomatism or crustal anatexis. Furthermore, study of detrital accessory minerals in ancient sedimentary rocks could provide much needed insight into the evolution of the oxidation state of the early Earth.

This work aims to assess how the compositions and structures of two accessory minerals, spinel and apatite, respond to variations in magmatic f_{O_2} and to determine whether these minerals could act as probes of f_{O_2} in planetary interiors. Focus has been concentrated on the element manganese, as (1) it is a relatively abundant trace element, (2) it can exist in valence states from Mn^{2+} to Mn^{5+} in nature, and (3) recent work has suggested that Mn may become preferentially concentrated in apatite under reduced conditions. In an initial investigation, large single crystals of Mn-rich spinel were synthesised under a variety of f_{O_2} conditions. X-ray absorption near edge

structure (XANES) spectroscopy and structural refinements of single crystal X-ray diffraction data were used to determine Mn valence state and coordination. Results show that Mn is present in spinel as both Mn^{2+} and Mn^{3+}, distributed over both octahedral and tetrahedral cation sites. However, in contrast to the Fe^{2+}/Fe^{3+} ratio, little variation in Mn valence as a function of f_{O_2} was observed. Results were, however, useful in testing and refining protocols for modelling Mn XANES data in a simple, model system.

In contrast to results from spinel, previous studies have indicated that Mn valence may change significantly in the accessory mineral apatite due to variations in magmatic f_{O_2}. To test this, crystals of apatite in equilibrium with different silicate melt compositions were synthesised at high pressure/temperature. Mn partitioning between apatite and melt was determined by electron probe microanalysis (EPMA), and Mn valence state determined by XANES spectroscopy. Although EPMA data revealed that there is no dependence of Mn partitioning on f_{O_2}, it was noted that partitioning is dependent on melt composition. In more silica-rich melts, a reduction in proportion of non-bridging oxygen reduces the ability of melts to incorporate Mn. As such, apatite crystallising in more evolved melts is expected to be enriched in Mn. These results are confirmed by XANES data, which indicate that Mn is present in coexisting apatite and silicate melt as Mn^{2+}, with no observed variation in Mn valence state with f_{O_2}.

In a final, preliminary investigation, attention was turned to Eu and Ce. Inferred variations in the valence state of these rare earth elements, i.e. Eu^{2+}/Eu^{3+} and Ce^{3+}/Ce^{4+}, are already of use in petrological modelling. Two series of experiments were conducted to synthesise Eu and Ce-bearing silicate glasses (both Fe-bearing and Fe-free) over a range of f_{O_2} conditions, and apatite in equilibrium with various silicate melt compositions at high pressure/temperature, again over a range of f_{O_2} conditions. XANES characterisation of glasses demonstrates systematic variations in Eu^{2+}/Eu^{3+} ratio with f_{O_2}. In contrast, Ce is dominantly present in quenched glasses as Ce^{3+} under all f_{O_2} conditions. In apatite, there is little variation in Eu^{2+}/Eu^{3+}, with Eu dominantly incorporated as Eu^{3+}. Ce in apatite is dominantly incorporated as Ce^{3+}. These results indicate that apatite-melt partitioning of Eu should be dependent on f_{O_2}, potentially

providing a probe of magmatic f_{O_2} once the effects of melt compositions are constrained.

Results presented here highlight the potential use of apatite as a petrological indicator. However, in contrast to previous work, I show that apatite-melt partitioning of Mn is largely independent of f_{O_2}. In fact, observed trends in apatite chemistry previously suggested to indicate variations in magmatic f_{O_2} can instead be fully explained by the observed influence of melt structure/composition on Mn partitioning. In contrast, Eu contents of apatite (for example apatite/whole rock ratios) may provide insight into oxidation state in the deep Earth. However, more work is required to constrain the influence of f_{O_2} on Eu (and other element) partitioning. Importantly, results here highlight the important influence which melt structure has on element partitioning. This control indicates that it is unlikely that f_{O_2} in the early Earth can be inferred from the chemistry of detrital minerals in sedimentary rocks, or inherited minerals in igneous/metamorphic rocks, as the composition of magmas from which these minerals crystallised cannot easily be constrained.

Lay Summary

A rock is a collection of one or more minerals. Minerals are naturally occurring solid substances that are made up of chemicals, and often form crystals with repeating structures. Rocks, and more importantly the minerals inside them, can be used to find out the conditions under which they were formed. This study is interested in igneous rocks that are formed when hot liquid (magma) from the Earth's interior cools and forms rocks. As scientists, we want to know about the temperature, pressure and other variables that can change during a rocks formation. All this information can give us a valuable insight into processes linked to magma inside the Earth. Such processes include why and when volcanoes form, where would be good to look for rocks containing valuable elements (e.g. gold and silver) and understanding how the chemical composition of the atmosphere has changed over very long time scales (millions of years) by the degassing of Earth's interior.

By synthesising rocks in the lab, scientists can control variables, such as pressure, temperature, and redox potential, at which rocks form. By altering variables, scientists can see how the chemical and physical response of rocks and minerals change at different conditions. In this study, I have focused on minerals that only make up a few weight percent of the rock (accessory minerals), as these often become concentrated in a wide variety of elements which are not found in other rock-forming minerals. One such mineral is apatite, which is the same mineral as tooth enamel and bones are made of. I have formed accessory minerals under temperatures and pressures suitable for igneous rocks. The remaining magma from which I have formed these minerals is also quickly cooled to a glass. I am interested in how the concentration of different elements in accessory minerals and the cooled glass vary as a function of my experimental variables. A key variable I have been researching is the redox potential of magmas when they cool

and form minerals. The redox potential describes the tendency of chemical species in the melt to acquire electrons, and become reduced. This variable has been identified in other mineral-melt studies as being important in controlling elemental abundances in minerals and melt.

My research has shown that whilst the redox potential of magmas is important to partitioning of elements in igneous rocks, the actual composition of the melt has a stronger effect on elemental abundances in minerals and their partner melt.

Acknowledgements

Thanks to all the people that have supported this research. I know that those listed below are only a small selection of those who have helped me over my four years as a PhD student. First and foremost, thanks have to go to the Natural Environment Research Council, who supported this PhD via the Edinburgh E^3 doctoral training partnership (Grant NE/L002558/1).

This work would not have been possible without the support of my supervisors, Geoff Bromiley and Kate Saunders. Thank you for all the support, guidance, and advice. Special thanks must go to Geoff, for all those weekend hours spent at Diamond Light Source, and for his assistance in the lab. Thanks to Kate for accompanying me on EPMA trips to Bristol.

Much of this work's success would not be possible without Nicci Potts, who's invaluable help and insight into apatite, the piston cylinder, and help in setting up the Deltech was very much appreciated, and to Andrew Miles who's PhD helped to inspire the project. Additional thanks go to my project advisor, Bryne Ngwenya.

Thanks to the residents of the new attic (and Amelia), for all their support, and patience. A special mention has to go to those who helped me with R (Kirsty) and Python (Ashley, Hannah, Sophie and Rachel), and to the various folk that have inhabited the same booth as me over the years.

Experimental and lab work would not have been possible without Ian Butler, the Workshop staff, and EMMAC, who have all helped fix things when they haven't worked. Thanks to Sally, Jen, Ardith, Holly, Alan, Geoff and Nicci for their support in the lab, from gin on the benches, to live streaming Wimbledon.

Thanks to my family for putting up with me during my PhD, whether that be financially or emotionally. Special thanks to my dad for proof reading. This work would not have been possible without them.

Last but by no means least, thanks has to go to my wonderful fiancée, Kirsten. Your love, support and patience has kept me going throughout the whole process, and this work would not have been possible without you.

Contents

List of Figures

List of Tables

1

Introduction

"If we knew what it was we were doing, it would not be called research, would it?"

– Albert Einstein

1.1 Context of the PhD project

The partitioning of trace elements between minerals and melts is a fundamental mechanism that has to be understood to quantitatively describe various petrological events associated with planetary scale processes (i.e. differentiation of planets, convection of the mantle, generation and destruction of crust, and mantle degassing and atmosphere evolution). Element partitioning is dependent on many factors, including crystal lattice site control, melt composition, temperature, and pressure. Oxygen fugacity (f_{O_2}) is a fundamental parameter which additionally affects redox sensitive element partitioning. As such, evaluation of f_{O_2} is critical for studying planetary processes. Oxygen fugacity not only controls the stability of various sub- and super-solidus phases but also governs electrical conductivity [Dai & Karato, 2014; Duba et al., 1973; Wood & Nell, 1991, etc.], diffusivity [la Tourrette & Wasserburg, 1997; Petry et al., 2004; Ryerson et al., 1989, etc.] and the mechanical behaviour of melts [Frost & McCammon, 2008]. Redox equilibrium has important consequences when considering topics as diverse as condensation in the solar nebula [Grossman et al., 2012], planetary differentiation models [Rubie et al., 2011] and the genesis of magmas [Haggerty, 1990]. Quantifying the effect that the oxidation state of melts has on the partition coefficient of redox sensitive elements should provide us with another invaluable tool for determining the redox state of melts, and the oxidation state of the source mantle region [Canil, 1997; Evans et al., 2012; Lee et al., 2010, etc.].

Oxygen fugacity has a noticeable effect on the crystallisation of minerals, influencing

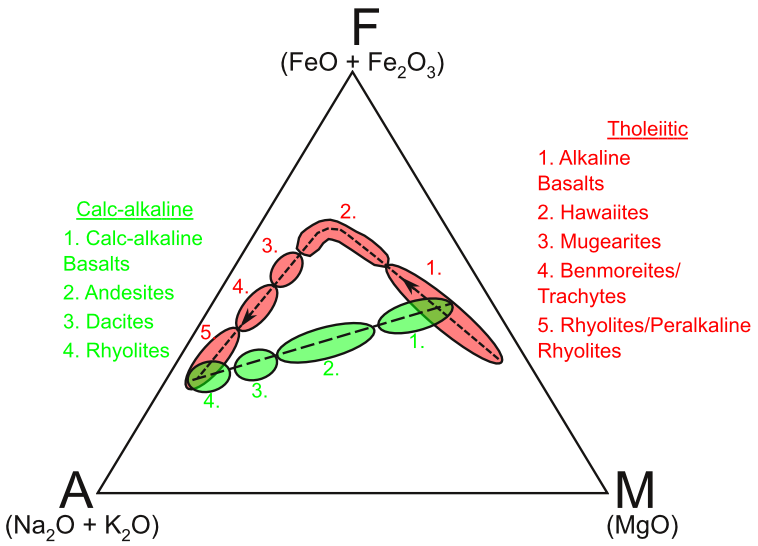

[ht]

Figure 1.1: Difference in the calc-alkaline and tholeiitic sub-alkaline magma trends. The difference between the two trends is linked to the redox state of the magmas (tholeiitic magmas are reduced and calc alkaline magmas are oxidised). The relatively oxidised conditions of the calc-alkaline series allows the precipitation of magnetite, which causes the Fe-Mg ratio to remain relatively constant with crystallisation. By contrast, the tholeiitic series first produces magnesium rich crystals, until the Mg content becomes too low and starts crystallising more Fe-rich phases.

the types of minerals, order, and equilibria assemblage during the evolution of magma, for example, the tholeiitic vs calc-alkaline trend (Figure 1.1). Not only does f_{O_2} dictate which minerals can crystallise during cooling, it also plays a role in the ionic substitutions of elements within minerals, which controls various properties of a mineral including electrical conductivity [Dai & Karato, 2014; Duba et al., 1973], magnetism [Haggerty, 1979] and optical properties [Ihinger & Stolper, 1986]. Oxygen fugacity of geological samples can be determined in 3 main ways: measuring the Fe^{3+}/Fe^{T} ratio in crystal free glasses, the Fe^{3+}/Fe^{T} ratio in coexisting mineral assemblages, or by measuring other redox sensitive elements in minerals where their concentration is dependent on f_{O_2}.

Recent work by Miles et al. [2013a] has suggested that the wt. % of manganese in apatite could be used to determine f_{O_2} in melts. This method would avoid having to measure the oxidation state of redox sensitive elements in minerals, circumvent having to use the ferric to ferrous iron ratio, and would use conventional, easy to access analytical instruments, namely the electron probe micro-analyser (EPMA). Mn-in-apatite would

also provide an invaluable tool in determining magmatic f_{O_2} in Si-rich igneous rocks, which is difficult due to the requisite of having unaltered mineral assemblages or the need for more than one Fe-Ti oxide to apply the magentite-ilmentite oxybarometer [Arató & Audétat, 2017]. Apatite is a common accessory mineral found in a wide range of igneous, metamorphic and sedimentary rocks. Where apatite is detrital in nature, it may still record the f_{O_2} of the protolith from which it has been removed and reworked. On Earth, detrital grains of apatite are often found as inclusions in the mineral zircon. Detrital zircon are the only material which has survived from the early Earth, with some zircon grains surviving for 4.4 billion years of Earth history [Wilde et al., 2001]. Zircon acts as a strong rigid 'shell' which protects the apatite grain from alteration and destruction over the billions of years of Earth's history. Extra-terrestrially, the mineral apatite has been reported in samples from the Moon and Mars [e.g. Boyce et al., 2014; Ewa et al., 2016; Hu et al., 2014; McCubbin et al., 2011]. If a universally applicable oxy-geobarometer based on Mn-in-apatite existed it would also provide knowledge of the redox state in bodies in the inner solar system, and how these have evolved throughout geological time.

The goal of this study is to determine under which conditions a Mn-in-apatite oxy-geobarometer could be used, by examining variation in the oxidation state of Mn in apatite and coexisting silicate melt as a function of f_{O_2}. Currently, one of the most popular, quick, non destructive ways of determining the valence of Mn within minerals is to use X-ray absorption near edge structure (XANES) spectroscopy. However, determining the oxidation state of Mn using XANES is non trivial and requires comparison with standards where Mn is in known coordination and oxidation state. Therefore, work was also carried out to understand the effect Mn in different coordination and oxidation state has on the various characteristics of XANES spectra. Mn spinel have a simpler structure and chemistry than apatite, and the Mn coordination and/or oxidation state can be determined independently. As well as characterising mixed valence mixed coordination standards which could be useful in fingerprinting the oxidation state of Mn in apatite, it also determines whether the spinel structure and particularly Mn in it, is sensitive to f_{O_2}. Finally, follow on work was carried out to investigate the

use of Eu and Ce in further constraining the redox state in apatite and coexisting melts as a function of f_{O_2}.

1.2 Introduction to oxygen fugacity

Equation 1.1 defines oxygen fugacity (f_{O_2}) as equivalent to the partial pressure of oxygen (P_{O_2}) for a given environment, which is corrected for the non-ideal quality of the gas using the fugacity coefficient (γ)

$$f_{O_2} = \gamma * P_{O_2} \tag{1.1}$$

Typically in the magmatic systems for which we model f_{O_2}, there is no 'free' oxygen; instead we refer to f_{O_2}, which denotes a parameter which characterises how reducing or oxidising an environment is. Therefore, in the remainder of this thesis, f_{O_2} is used to describe the potential of redox sensitive elements (Mn, Fe, Ti, Ce, etc.) to occur in their more oxidised or reduced states [Frost, 1991].

Oxygen fugacity (f_{O_2}) is a fundamental parameter in understanding igneous systems due to the large control it has on the course of magmatic differentiation, stability of various mineral assemblies, and the role it plays in the partitioning of elements between minerals, melts and fluid phases [Sato, 1978]. Studies investigating oxygen fugacity are not wholly focused on the effect it has on mineral stabilities [Eugster & Wones, 1962; Hensen, 1986; Nitsan, 1974; Toplis & Carroll, 1995, etc.]. Instead many focus on the importance f_{O_2} has on governing fluids associated with igneous and metamorphic rocks [Gerlach, 1993; Gerlach & Nordlie, 1975; Pawley et al., 1992; Peacock, 1990, etc.]. This is because f_{O_2} not only plays a role in determining the species present in these fluids, but also affects any precipitates formed from these fluids. Oxygen fugacity is, therefore, important in understanding the processes which govern the production of volcanic gases, determining element partitioning, and comprehending phase relations during magmatic melting and crystallisation [Cottrell & Kelley, 2011]. Not only does f_{O_2} dictate the type and geochemistry of melts/solids formed, but also behaves as a critical parameter when examining properties of systems such as the electrical conductivity, diffusivity

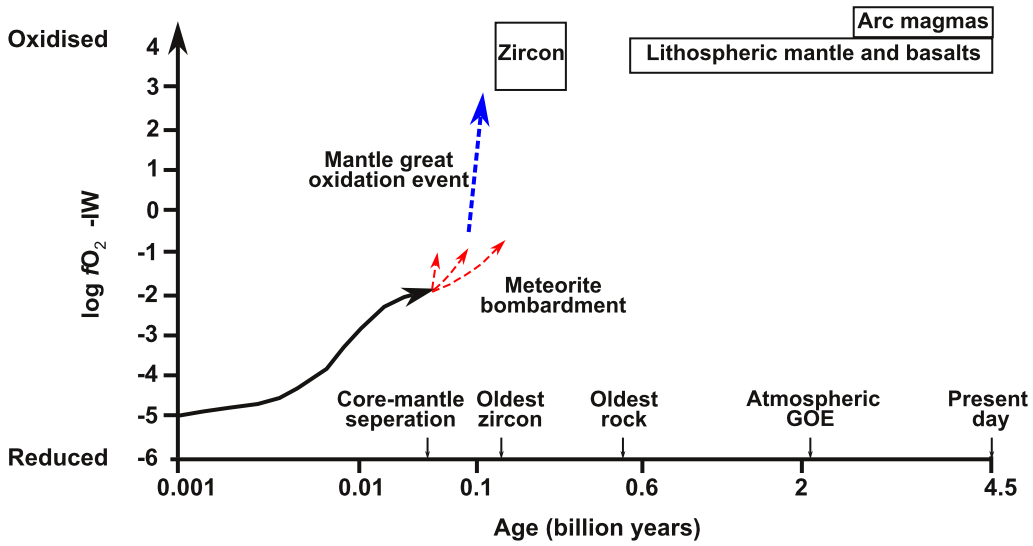

Figure 1.2: Variation of mantle oxygen fugacity through time. The Great Oxidation Event of the mantle is represented by the blue dotted line, which oxidised the mantle to a log f_{O_2} similar to the current value (IW + 2-5.5 [Wood, 1991]). Boxes represent age and f_{O_2} range for measured samples. From Scaillet & Gaillard [2011].

and mechanical behaviour of the mantle [Arculus, 1985; Frost & McCammon, 2008] and when modelling gas inputs into the atmosphere.

The ability to be able to calculate oxygen fugacity from geological samples is fundamental to understanding the secular evolution of the Earth. Determining the oxidation state of the upper mantle through Earth's history has led to hypotheses pertaining to the composition of the atmosphere, hydrosphere and mantle through time [Mattioli et al., 1989]. It is important to understand secular changes of these systems when scrutinising the evolution of the early Earth and the conditions which were prevalent during the rise of life on this planet. Out-gassing of the Earth's interior during early Earth history is likely to have affected the amount of oxygen in Earth's early oceans and atmosphere [Gaillard et al., 2011; Holland, 2002; Trail et al., 2011]. Thus, one of the primary aims for petrologists has been to measure the change in the redox state of magmas through Earth's history to understand the oxidation of the Earth.

The first constraints on the redox state of the early Earth are inferred from the conditions present during the accretion of the Earth from planetesimals [Wood et al., 2006]. During this stage, it is theorised that the proto mantle must have gone through a stage where liquid Fe-rich metal coexisted with liquid silicate (i.e. the magma ocean stage).

This would constrain the redox state of the mantle to approximately 5-8 log units below the iron-wüstite (IW) buffer [Scaillet & Gaillard, 2011] (Figure 1.2, an explanation of the IW buffer can be found in Section 1.4). The first indirect evidence which we are able to use to determine the redox state of the early mantle are remnants from the first solids which formed from melting of early crust: the Jack Hills zircons. These detrital zircon found in metamorphosed sediments of Western Australia are the remains of crustal rocks which were present during the intense period of meteor bombardment in the early Earth's history. Trail et al. [2011] used a 'Ce in zircon' oxy-geobarometer to infer the mantle conditions from which these zircon crystallised. The result of this study suggests that the mantle oxidation state was similar to the present day value (Figure 1.2). If the findings of Trail et al. [2011] are correct, then the mantle would have had to oxidise in 0.1 Gyrs. Self-oxidisation of the mantle during core formation [Frost & McCammon, 2008; Wood et al., 2006] is one possible mechanism by which the mantle may have become oxidised, although the actual oxidation process remains poorly constrained. Therefore, we need more data on mantle f_{O_2} in order to model how the mantle has changed during the early Earth. Unfortunately, determining the redox state of early magmas is often difficult due to the limited applicability of current oxy-geobarometers, and the lack of available material to apply them to.

As well as the Earth, it is also important to understand the redox conditions of the other terrestrial planets and asteroid material to aid in the understanding of planetary formation [Wadhwa, 2008].

Information on mantle redox state of other terrestrial bodies will help in understanding the evolution of volatiles and magmas on these bodies. This in turn, will have far reaching consequences for our understanding of planetary compositions and how surface-mantle and mantle-atmosphere interactions have changed through time.

Current estimates for the prevalent redox conditions in silicate reservoirs of various terrestrial bodies (Mars, Earth, Moon, Venus and Mercury) are shown in Figure 1.3. Earth exhibits a large range in redox conditions compared to other extraterrestrial bodies due to the presence of an oxygen rich atmosphere, liquid water oceans and

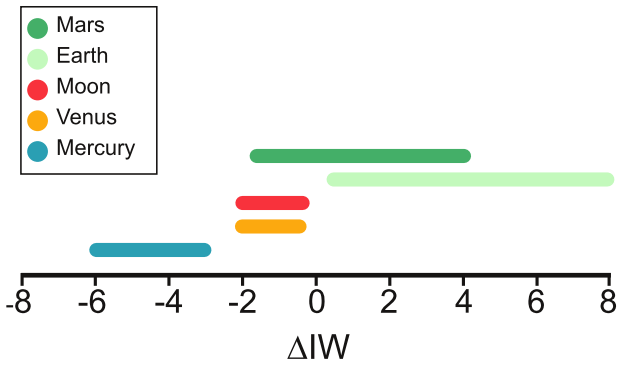

Figure 1.3: Estimated ranges for the redox conditions of the interiors of Mercury, Venus, Moon, Earth and Mars. Adapted from Righter et al. [2016].

a hydrated deep interior [Righter et al., 2016]. Pressure and temperature are other variables which dictate redox conditions of silicate bodies. Both Earth and Mars exhibit IW values greater than +2, which is a result of the dissolution of volatiles at pressure and the subsequent degassing of volatiles in magmas with decompression [Righter et al., 2016]. The Earth has also been subject to large scale geochemical cycling which has also contributed to the modern day value of the oxidation state of the mantle.

1.3 Oxygen fugacity and redox state

Iron is the most abundant redox sensitive element present in the Earth's crust. Iron occurs in three different valences, native iron (Fe^0), which can also be called metallic or pure iron, ferrous iron (Fe^{2+}) and ferric iron (Fe^{3+}). Due to its prevalence in geological systems, the potential state of iron is, therefore, often used to express the comparative f_{O_2} of a system (e.g. planetary interior, magma body, etc.) [Berry et al., 2003; Christie et al., 1986; Cottrell & Kelley, 2011; Fudali, 1965; Kennedy, 1948].

Partitioning of iron between the ferric and ferrous species is commonly used as a proxy for oxygen fugacity in silicate melts, because the redox conditions of silicate reservoirs on Earth are generally too oxidising for the presence of native iron. In unaltered silicate glass, the ferrous-ferric ratio is proportional to oxygen fugacity [Kennedy, 1948]. However, in minerals, the ferrous-ferric ratio is not proportional to oxygen fugacity

because there are constraints imparted from element partitioning into a crystalline structure based on the mineral's preference for certain oxidation states and size of ion [Cottrell & Kelley, 2011] (see section 1.4).

Work into calibrating the relationship between oxygen fugacity and ferrous/ferric iron arose due to the effect f_{O_2} has on paths of igneous crystallisation. It was discovered that when melting and re-crystallising basaltic melts, the minerals present in the starting material only matched those in the finished experimental runs when f_{O_2} was controlled, as this avoided the oxidation or reduction of the initial proportions of FeO and Fe_2O_3 [Eugster, 1957; Kennedy, 1948].

Equation 1.2 describes an empirical equation linking f_{O_2} to the ferrous/ferric ratio, where *a, b, c* and d_i are experimentally determined constants and X_i is the mole fraction of the various oxides present in the liquid [Carmichael & Ghiorso, 1990; Christie et al., 1986].

$$ln[X_{Fe_2O_3}/X_{FeO}] = a.lnf_{O_2} + b/T + c + \sum X_i d_i \tag{1.2}$$

Equation 1.2 can only be used in the absence of crystallisation where there is no crystal chemical control on the partitioning of ferrous and ferric iron [Herd, 2008]. In fact, equation 1.2 may not be true for all glass compositions. Studies have suggested that the ferrous-ferric ratio may be influenced by melt composition and the structural role of cation species [Dickenson & Hess, 1981, 1986; Fudali, 1965; McCanta, 2005]. However, the work by McCanta [2005] suggests that in peraluminous compositions, the compositional variation may only have a minor effect on the ferrous to ferric ratio.

The presence of water in silicate melt also modifies melt structure and may affect the susceptibility of the melt for ferrous or ferric iron. Water reacts with network modifiers and nonbridging oxygen (NBO) in melts to form Si-OH and M(OH) or $M(OH)_2$ complexes, and also polymerises the anhydrous portion of the network [Mysen et al., 1980]. Consensus is growing that dissolved water has an effect on the f_{O_2} of hydrous melts [Baker & Rutherford, 1996; Botcharnikov et al., 2005; Gaillard et al., 2001, 2003]

and, therefore, additional terms may be needed in Equation 1.2 to account for water content of the melt.

Other factors which may affect the applicability of Equation 1.2 to basaltic glass are: 1) it must be assumed that the igneous system of interest is in equilibrium, 2) the processes are reversible [Herd, 2008], and 3) that the ratio of the elements of interest have not been altered post-crystallisation. This is often difficult, as finding a truly unaltered glass is often problematic because oxidation occurs readily in processes such as assimilation, crystallisation and loss of volatiles prior to, syn-eruption, and alteration post eruption [Christie et al., 1986]. Therefore, for most geological samples where crystallisation has taken place a different oxy-barometer is needed.

1.4 Calculating oxygen fugacity from mineral equilibria

There are currently two main alternatives to using the ferric-ferrous ratio in glass to calculate f_{O_2}. These are based on ferrous-ferric mineral equilibria or the characteristics of hetrovalent trace element partitioning in glass or into coexisting minerals [Herd, 2008]. In most rocks, f_{O_2} is monitored via the use of mineral equilibria where the ferric/ferrous ratio is not only dependent on f_{O_2} but is also controlled in part by mineralogical constraints and is strongly affected by the proportion of phases in a rock [Frost, 1991]. Crystallisation complicates determination of f_{O_2} of silicate melts, due to the structural preference of minerals for certain oxidation states. For example, iron in olivine can only be incorporated in one valence state, Fe^{2+}, whereas Fe^{3+} is largely incompatible with the olivine structure, except as point defects.

Crystallisation of minerals such as olivine, which prefer Fe in only one valence state, results in a change in redox state of the remaining melt. The excursion in the oxidation state of the liquid caused by the crystallisation of olivine may be counteracted upon further cooling and crystallisation of other phases which preferentially incorporate Fe^{3+} (i.e. the mineral compositions buffer the oxygen fugacity - Figure 1.4). Therefore, minerals which crystallise close to the magmas solidus temperature may better record redox conditions reflective of the magma prior to the onset of crystallisation (to within

a log unit) [Ghiorso, 1997], as long as the system remained closed in respect to oxygen [Herd, 2008].

An example of some commonly used f_{O_2} mineral assemblages are those used as oxygen buffers in experimental systems. One example of a mineral redox buffer is shown in Equation 1.3, which describes the stability of fayalite forming from magnetite and quartz. Fayalite is an iron-rich olivine whose structure contains ferrous iron. If there is sufficient oxygen in the system, then oxidation of ferrous iron in the olivine structure causes the olivine to break down to a mixture of magnetite (which contains both ferrous and ferric iron) and quartz (Equation 1.3).

$$2Fe_3O_4 + 3SiO_2 \Leftrightarrow 3Fe_2SiO_4 + O_2$$
$$magnetite + quartz = fayalite\ (+\ oxygen) \tag{1.3}$$

It is important to note that Equation 1.3 describes a hypothetical mineral redox buffer, and under most conditions of interest for geologists, f_{O_2} is so low that oxygen tends to be fully combined in mineral phases and so is not present as a gas. In geological systems it is more likely that f_{O_2} is a parameter which is governed by the mineral assemblages in a rock/melt than it is imposed from the environment [Frost, 1991].

Oxygen fugacity for Equation 1.3 can be determined by considering the equilibrium equation for this reaction (Equation 1.4).

$$\frac{a_{O_2} * (a_{Fe_2SiO_4})^3}{(a_{Fe_3O_4})^2 * (a_{SiO_2})^3} = K_{FMQ}(T) \tag{1.4}$$

where a_i is the activity of component i and $K_{FMQ}(T)$ is the reaction coefficient for this reaction at temperature T. The activity of pure substances is unity, therefore equation 1.4 can be simplified to:

$$K_{FMQ} = a_{O_2} = \frac{f_{O_2}}{f^0_{O_2}} \tag{1.5}$$

where f_{O_2} is oxygen fugacity at a given temperature (T) and pressure (P) and $f^0_{O_2}$ is the fugacity of oxygen in its standard state. At 1 bar $f^0_{O_2}$ will be unity and therefore the activity of oxygen can be replaced with f_{O_2} [Frost, 1991] (Equation 1.6).

$$f_{O_2} = K_{FMQ}(T) \tag{1.6}$$

Oxygen fugacity is often expressed in terms of experimental mineral buffers (Figure 1.4). Like the quartz-fayalite-magnetite (FMQ) buffer mentioned above, most of these redox buffers do not occur naturally. However, these buffers are often used to describe natural geological systems because the T - f_{O_2} variation of mineral redox buffers in igneous magmas are usually sub parallel to those of the experimental buffers, and are easily constrained in the lab. Another benefit of expressing oxygen fugacity relative to a solid oxygen buffer is that it makes comparison of the redox state of different magmas easier.

1.4.1 Fe-Ti oxide oxygen barometers

Iron-titanium oxide barometry is a common technique used to determine f_{O_2} using mineral assemblages in igneous rocks. Iron-titanium oxides are present in almost all igneous rocks but are often found only in trace amounts. These 'accessory' minerals are very important for palaeomagnetism and in influencing the fractional crystallisation paths of basaltic melts. Coexisting Fe-Ti oxides such as magnetite, hematite, ulvöspinel and ilmenite can also be used as oxygen barometers and geothermometers [Buddington & Lindsley, 1964; Carmichael & Nicholls, 1967; Ghiorso & Sack, 1991].

Development of this set of mineral oxy-geobarometers/thermometers was generated from observations that the TiO_2 content of magnetite is largely a function of temperature [Buddington et al., 1955; Heier & Buddington, 1956] and that the compositions of Fe-Ti oxides are significantly affected by oxygen fugacity [Verhoogen, 1962]. Ex-

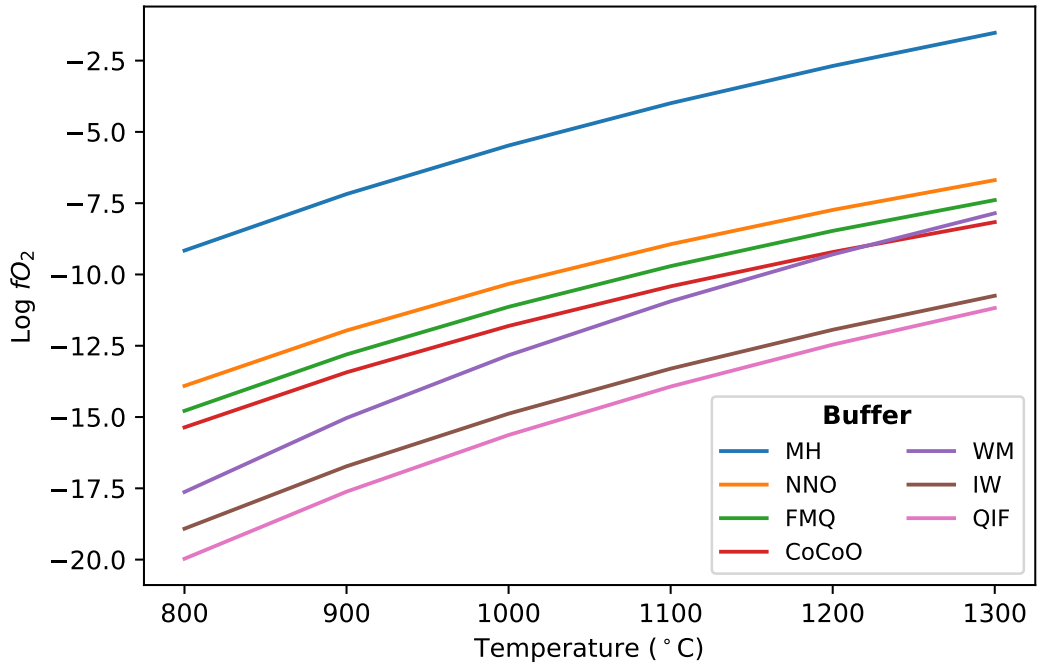

Figure 1.4: Oxygen fugacity for various mineral redox buffers varying with temperature [Eugster & Wones, 1962; Huebner & Sato, 1970]. MH - magnetite-hematite, NNO - nickel-nickel oxide, FMQ - fayalite-magnetite- quartz, CoCoO - cobalt-cobalt oxide, WM - wüstite - magnetite, IW - iron-wüstite, QIF - quartz-iron-fayalite.

perimental data by Buddington & Lindsley [1964] constrained how the composition of Fe-Ti oxides varies as a function of temperature and oxygen fugacity.

Oxy-geobarometers involving Fe-Ti oxides generally explore the relationship between the magnetite-ulvöspinel series and the hematite – ilmenite series (Equation 1.7):

$$Fe_2^{3+}O_3 + Fe_2^{2+}TiO_4 = Fe^{2+}TiO_3 + Fe^{2+}Fe_2^{3+}O_4$$
$$hematite + ulvöspinel = ilmentite + magnetite \tag{1.7}$$

Fe-Ti oxides are one of the last set of minerals to crystallise from silicate magmas, yet may still record the f_{O_2} conditions prevalent in the magma before any crystallisation, when the effect of cooling is taken into account. However, Fe and Ti exchange continues during cooling and so this oxy-geobarometer is prone to resetting. Therefore,

the temperature and oxygen fugacity calculated from Fe-Ti oxides are only representative of the conditions prevalent at the final magmatic temperature, with no signature remaining from earlier in the eruption sequence [Venezky & Rutherford, 1999].

To correctly employ the Fe-Ti oxy-geobarometer, the following criteria should be met [Herd, 2008]:

1. The concentrations of V_2O_3, Al_2O_3, Cr_2O_3, MnO, CaO and ZnO in Fe-Ti oxides should not exceed the concentrations for which the model has been tested.
2. The assemblage must have equilibrated above 600 °C and below 1100 °C.
3. The barometer can only be applied if the oxygen fugacity does not approach the limit of the Fe-Ti oxide stabilities.

Evaluation of oxygen fugacity based on Fe-Ti oxides can be improved when used in conjunction with data from coexisting ferromagnesian silicates (e.g. Equation 1.8 - abbreviated as QUILF). As well as reducing uncertainty in this barometer by accounting for subsolidus re-equilibration, use of coexisting ferromagnesian silicates can also be used as a check to confirm that equilibrium exists between the various phases.

$$\begin{aligned} SiO_2 + 2Fe_2TiO_4 &= 2FeTiO_3 + Fe_2SiO_4 \\ quartz + ulvöpinel &= ilmentite + fayalite \end{aligned} \tag{1.8}$$

To use Fe-Ti oxide in equilibrium with silicates as an oxy-geobarometer the following criteria must be met [Herd, 2008]:

1. Conditions for the assemblages should not exceed oxygen fugacity values above FMQ +2.
2. It cannot be used for cubic oxides which contain significant amounts of Al_2O_3 and Cr_2O_3.

3. Silicate compositions should not contain more than trace amounts of Fe_2O_3 and TiO_2.
4. All minerals must be stoichiometric.

The main weakness of any Fe-Ti oxide geobarometer is that Fe and Ti exchange during cooling, are among the last phases to crystallise, and may be reset by hydrothermal alteration, which can possibly be assessed. This may result in the recorded temperature and f_{O_2} of the mineral pair differing from that of the magma. This technique also requires that a relevant mineral pair is present in the sample [France et al., 2010].

One method of evaluating equilibration for Fe-Ti oxygen barometry is the chemical test outlined by Bacon & Hirschmann [1988]. This test which is useful for a wide range of melt compositions measures the ratios of Mg/Mn in the magnetite and ilmenite phases in igneous rocks. It can be applied to test 1) ilmenite equilibrated with titanomagnetite where multiple populations of one (or both) phase(s) exist, 2) Fe-Ti oxide pairs where one (or more) phase is present as an inclusion in a silicate phenocryst or 3) test the equilibrium in exsolved or oxidised crystals.

1.4.2 Olivine-pyroxene-spinel

The equilibrium between olivine (ol), spinel (sp) and orthopyroxene (opx) governs the ol-opx-sp oxybarometer which was derived for use on mantle xenoliths belonging to the spinel facies (Equation 1.9 and 1.10).

$$6Fe_2SiO_4 + O_2 = 2Fe_3O_4 + 6FeSiO_3$$
$$olivine + oxygen = spinel + orthopyroxene \tag{1.9}$$

$$log f_{O_2} = -6log\, a^{ol}_{Fe_2SiO_4} + 2log\, a^{sp}_{Fe_3O_4} + 6log\, a^{opx}_{FeSiO_3} \tag{1.10}$$

Herd [2008] links the activities (a) of the iron end members (olivine, spinel and pyroxene) with oxygen fugacity, based on the model summarised in Wood & Nell [1991].

Another olivine-pyroxene-spinel geobarometer focuses on the FMQ buffer where the activity of SiO_2 is calculated using the equilibrium between olivine, quartz and orthopyroxene [O'Neill & Wall, 1987].

Equation 1.10 can be used for low pressure basaltic samples for which the Fe end members are co-genetic, in equilibrium, and the pyroxene member has a low Ca content [Herd, 2008]. For oxygen fugacity to be determined, the temperature and pressure of the assemblage crystallising from the melt has to be determined independently. This may be problematic as in some studies the same Fe-Ti oxides are often used to determine temperature of crystallisation. The largest uncertainty in this geobarometer is determining the activity of magnetite in spinel [Herd, 2008].

1.5 Hetrovalent trace element oxy-geobarometers

Partitioning of redox sensitive elements other than iron may be used to determine oxygen fugacity. Elements which exist in a variety of oxidation states associated with planetary redox conditions include some transitional metals such as Ti, V, Mn, Cr and the rare earth elements (REE) Eu and Ce. These elements are often incorporated into common minerals as trace components, and frequently do not affect their phase stability.

To choose an appropriate redox sensitive element to measure oxygen fugacity certain criteria need to be met. The redox element of interest must be stable in multiple oxidation states spanning the log f_{O_2} range of interest (Figure 1.5), there must be a way of linking the ratio of valence states to oxygen fugacity, and finally the element(s) of interest must also be present in the sample. Because Fe^{2+} and Fe^{3+} span the fugacity range of Earth's basalts, there has been substantial prior research into them. Therefore, oxy-geobarometers involving Fe tend to be applied to material from Earth. Vanadium exists in 4 valence states which cover a range of redox conditions from more reduced conditions found in lunar basalts, to more oxidised material from Earth. Therefore, recent work has focused on developing vanadium oxy-geobarometers [Herd, 2008] which can be used on a variety of planetary basalts. Figure 1.5 will be revisited later in the

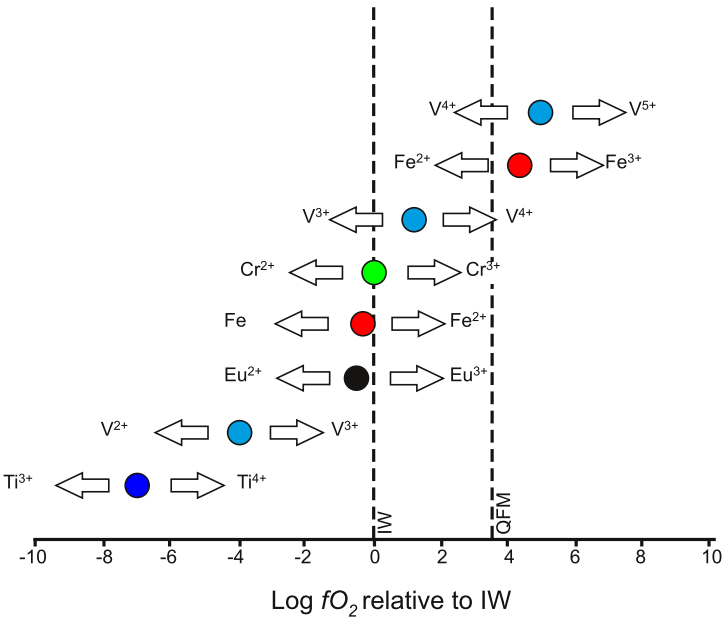

Figure 1.5: Dominant valence states for planetary basalts and their relationship to oxygen fugacity. Circles show the log f_{O_2} position where equal proportions of an element's oxidation states are expected to be present. The arrows infer the suitable range a redox pair can be used to determine f_{O_2} [Herd, 2008].

thesis to add the relative positions of the oxidation states of Mn and Ce which were missed in the original diagrams of Herd [2008] and Papike et al. [2005].

Methods which link how these trace multivalent elements behave in response to oxygen fugacity are often not fully understood, and difficulty arises in finding ways in which to measure the ratio of these valence states in a sample. With the rise in the availability of beam time at synchrotron facilities, much work has focused on using the X-ray absorption near edge structure (XANES) of an element, to determine the various oxidation states which are present in a suite of samples (Figure 2.21 in chapter 2, page 63).

Sutton et al. [2005] developed an oxy-geobarometer for planetary basalts by using micro-XANES analysis of vanadium in basaltic glasses. In this study a series of standard glasses were formed in experiments under known f_{O_2} and temperatures, and were then analysed using synchrotron radiation. Changes in vanadium valence results in an increase/decrease in the energy position of the pre-edge peak or absorption edge (for more information on XANES see section 2.5.5.4.1 in chapter 2, page 65). Sutton et al. [2005] used the pre-edge peak intensity to determine V valence as they resolved it was

more capable of correctly determining valence for the f_{O_2} range of their samples than other XANES analysis techniques.

A problem with the study by Sutton et al. [2005] is that the relationship between the pre-edge intensity of a vanadium XANES spectra and its valence was calibrated for synthetic glasses which contained no iron (Schreiber glasses). Most natural basaltic glass contain Fe. Iron in natural melts interacts with vanadium redox pairs [Schreiber et al., 1987], with the intrinsic f_{O_2} of the system controlled by the ferrous-ferric ratio of iron, and with vanadium acting as a sensor to this [Borisov, 2013]. Further pre-edge problems arise when valence and coordination vary simultaneously. Changes in coordination also affect the shape and particularly the intensity of the 1s→3d transition which manifests itself as the pre-edge peak. Therefore, the relationship between oxidation state and centroid position of the pre-edge peak is non linear with changing coordination.

1.6 An introduction to apatite

The mineral apatite is often misidentified, hence its name, which is derived from απατειν (apatein), the Greek word which means "to deceive". When geologists refer to "apatite" this does not equate to a single mineral; instead it refers to a subgroup of minerals within the apatite group, all of which belong to a supergroup of the same namesake [Hughes, 2015]. "Apatite" in this work, is attributed to three species of calcium phosphate, and their solid solutions, specifically chlor-, fluor- and hydroxy-apatite (ClAp, FAp and OHAp respectively). These three species of apatite have the general formula $Ca_5(PO_4)_3(F,OH,Cl)$, and they typically form as hexagonal crystals.

Apatite is a geologically ubiquitous mineral, found in igneous, metamorphic and sedimentary rocks, and defines 5 on the Mohs mineral hardness scale. Generally it occurs as an accessory phase, but may be a major constituent in sedimentary phosphorites and igneous cumulate deposits. Apatite is also found in extraterrestrial samples, acting as host to water in lunar and martian material [McCubbin et al., 2010]. Apatite chemistry is a powerful tool in geochemistry and petrology due to the ability of the

apatite structure to incorporate and potentially concentrate many different minor and trace elements [Cherniak, 2010]. Apatite is also readily used to determine the thermal history of sediments in basins and orogenic belts using fission track techniques. The mineral apatite can survive many episodes of crustal anatexis, and this, combined with the ability to incorporate a variety of elements, makes it an ideal candidate for investigating petrogenesis at the time of crystallisation [Sha & Chappell, 1999].

Calcium phosphate apatite are not just of interest to geoscientists; their variability in composition has also resulted in applications to fields such as agriculture, biology, dentistry, materials science, and medicine. The interest of apatite to biological sciences is largely due to the fact that most hard tissue (teeth, bones) in the human body is made of hydroxyapatite [Pasteris et al., 2008], and is one of the most common biominerals on Earth. Apatite is also the major source of phosphorous, hence it is critical to the phosphorous cycle and our use of fertilisers.

1.6.1 Structure and composition of apatite

Ideal apatite ($M_{10}(TO_4)_4X_2$) is hexagonal, with the space group $P6_3/m$ and unit cell parameters a = 9.3 - 9.6 and c = 6.7 - 6.9Å [Pasero et al., 2010]. However, pure end member hydroxy- and chlor- apatite both form with a sub symmetric monoclinic form belonging to the space group $P2_1/b$. The structure of fluroapatite belonging to the space group $P6_3/m$ is discussed below.

The $P6_3/m$ space group's vertical symmetry elements are shown in Figure 1.6. There are six-fold screw axes passing through the corners of the unit cell (marked by the light green rhombus on Figure 1.6). This symmetry group also includes two-fold screw axes which are found at the midpoints on the unit cell edges and three-fold rotation axes which are found at $\frac{2}{3}, \frac{1}{3}, 0$ and $\frac{1}{3}, \frac{2}{3}, 0$.

In apatite there are three cation sites (T, M1, M2), as shown in Figure 1.7. There are two crystallographically distinct Ca sites in apatite. Two fifths of the Ca^{2+} ions in the apatite structure are housed on the M1 site (also known as the Ca1 site - green prisms). The M1 site consists of columns of M1 ions with a spacing of $\frac{1}{2}$ c-axes parameter along

the three-fold axes. Each M1 cation shares 3 oxygen atoms (which sit on the mirror plane) with the neighbouring M1 ions above and below. The M1 ions are also connected to an additional three oxygen atoms (O3 ligand) at approximately the same z parameter as the central M1 ion. Therefore the M1 site can be described as a tricapped trigonal prism of nine-fold coordinated CaO_9 [Hughes & Rakovan, 2015], of which there are 4 per unit cell.

Columns of M1 ions are connected by PO_4 tetrahedra (T sites, orange triangles), of which there are 6 per unit cell (dotted area denotes a unit cell on Figure 1.7) [Hughes & Rakovan, 2015]. Three of the oxygen atoms are shared from one column of M1 ions, and another oxygen atom is shared with an adjacent column. The 3D network of T and M1 sites creates 'tunnels' whose axes coincide with the 6_3 screw axis, and denote the corners of the unit cells. It is within these 'tunnels' that the M2 and X sites are present.

The M2 site (Ca2 site, purple spheres) consists of an irregular CaO_6X_1 polyhedron in seven-fold coordination. There are 6 M2 sites per unit cell [Hughes & Rakovan, 2015], and these 6 ions form two triangles which are rotated 60° about the c axis from each

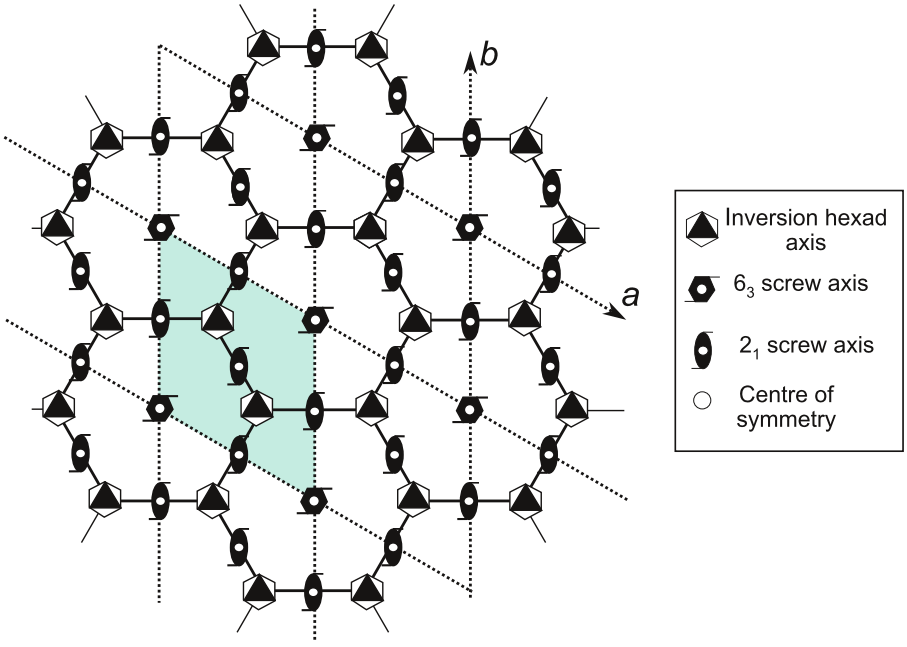

Figure 1.6: Vertical symmetry elements of the $P6_3/m$ space group. The c-axis is out of the plane of the paper and the a and b axes are marked.

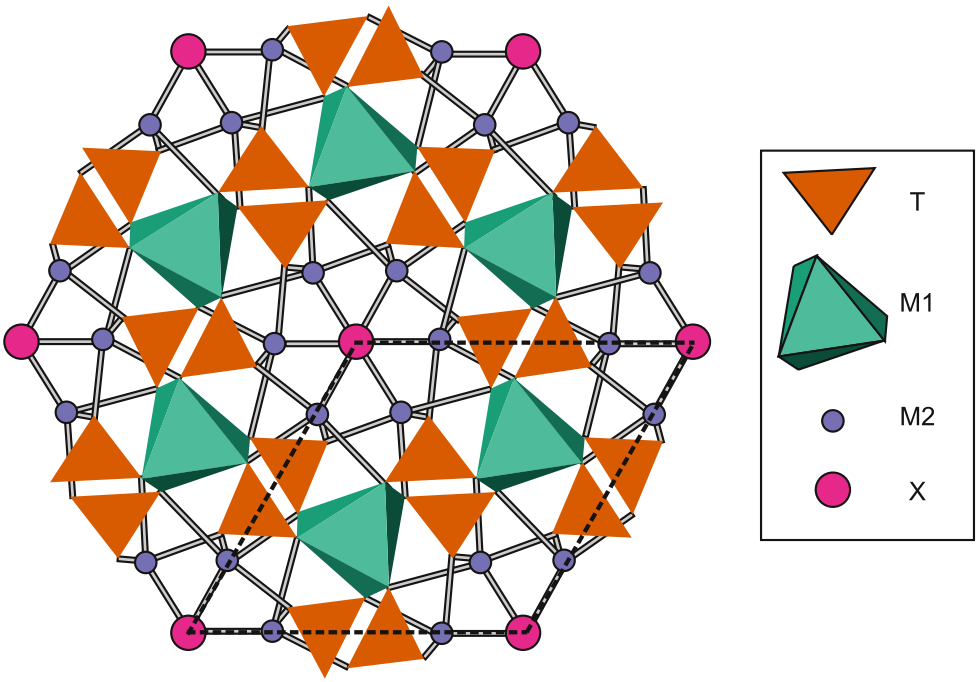

Figure 1.7: Apatite crystal structure as seen down the c axis (Adapted from Pasero et al. [2010]). The bonded O3 ligands are not included in this projection. The dotted area denotes the unit cell.

other, and each sit in each of the mirror planes of the unit cell. Sitting essentially coplanar in the centre of each triangle is an X anion which is in three-fold coordination. The M2 crystallographic site of apatite is of particular importance because, unlike the M1 and T sites, which are largely unaffected by the incorporation of different column anions, the M2 atomic site varies to accommodate them.

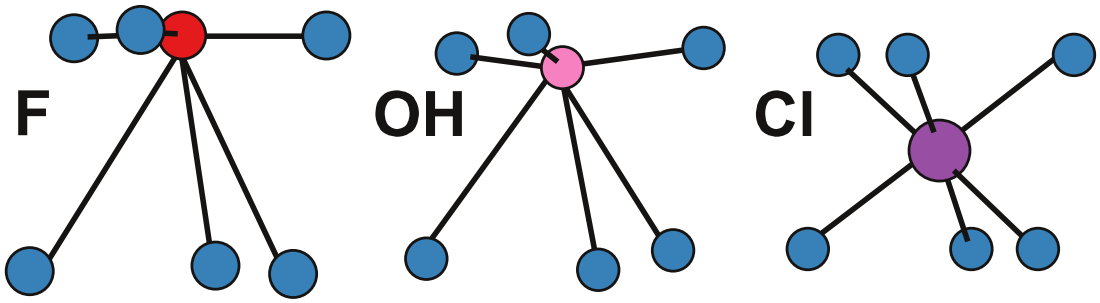

Figure 1.8: Change in M2/anion site geometry for the three most common X anions, after Tait et al. [2015]. Blue - M2 cation, Red - F, Pink - OH, Purple - Cl.

The M2 - X bond lengths for end-member chlor-, hydroxyl- and fluorapatite vary from 2.759 Å to 2.385 Å to 2.311 Å respectively [Hughes et al., 1989] (Figure 1.8). The Cl and OH anions are larger than F and cannot sit coplanar with the M2 cations, and must

be displaced above or below the triangular M2 plane, destroying the $P6_3/m$ symmetry. The structural response to solid solutions between the anions remains largely unknown because the location of the anions are not miscible without a structural change (e.g. reduction of symmetry from hexagonal to monoclinic or the occupancy of new anion positions to maintain the hexagonal symmetry [Vaughn et al., 2018]).

1.6.2 Substitutions in natural apatite

The diversity in apatite composition is largely due to the number of elements that can substitute into this structure. Over half of the elements with long lived isotopes can be incorporated into the apatite structure [Pan & Fleet, 2002; Pasero et al., 2010]. Because of the abundance of substitutions, the crystallisation of apatite in magmas can strongly influence the budget of minor and trace elements. The X anions are dominated by F, OH and Cl. Br and I can be present in trace amounts in natural apatite. Vacancies are common in the X site and neutrality is most likely to be accommodated by the loss of Ca atoms. An extensive number of cations substitute for Ca in the M site. Species found on the M sites include: Ca^{2+}, Ba^{2+}, Bi^{3+}, Ce^{3+}, La^{3+}, Mn^{2+}, Na^{+}, Pb^{2+}, Sr^{2+} and Y^{3+}. Sr is one of the most common cations which substitutes for Ca, almost exclusively substituting onto the M(2) site [Pan & Fleet, 2002]. Mn in apatite is present in nearly all natural apatite. Mn in apatite also has important industrial applications, with Mn doped FAp used extensively in fluorescent lights. Fe also substitutes for Ca, and is generally found in minor to trace amounts in natural samples. Na is a common constituent in natural apatite, and, like other monovalent anions substituting for Ca, preferentially incorporates onto the M(1) site [Pan & Fleet, 2002]. Rare Earth elements (REEs) substituting into the M site prefer to be incorporated into the M(2) site.

Substitution species on the T site can include: P^{5+}, As^{5+}, B^{3+}, S^{6+}, Si^{4+} and V^{5+} [Pasero et al., 2010]. SO_4^{2-} is one of the most important substitutions for PO_4^{3-} in natural apatite, and is commonly found with high silica contents, as a way of charge balancing. CO_3^{2-} is also a common substitution for PO_4^{3-}, and may be charge balanced with the introduction of Ca vacancies [Pasero et al., 2010] (Equation 1.11). Various other CO_3^{2-} substitution methods may include [Pan & Fleet, 2002; Riker et al., 2018]:

$$Ca^{2+} + 2PO_4^{3-} = \square^{Ca} + 2CO_3^{2-} \tag{1.11}$$

$$PO_4^{3-} = CO_3^{2-} + F^- \tag{1.12}$$

$$Ca^{2+} + PO_4^{3-} = Na^+ + CO_3^{2-} \tag{1.13}$$

The other (more dominant) way that CO_3^{2-} can substitute into the apatite structure is incorporation within the X site with the introduction of a OH^- vacancy [Riker et al., 2018]:

$$CO_3^{2-} + \square = 2(OH^-, F^-, Cl^-) \tag{1.14}$$

1.6.3 Apatite in igneous rocks - habit and texture

Apatite is found in almost all igneous rocks from basic to acidic in composition, is dominantly fluorapatite in composition (but incorporates significant amounts of Cl and OH), and generally accounts for 0.1-1% rock volume [White et al., 2005]. Apatite typically forms in igneous rocks as either equant to sub-equant grains or with an acicular form. The growth of equant grains is understood to result from a cooling path which promotes apatite growth in equilibrium with the melt. In contrast, the growth of acicular apatite has been linked to large undercooling [Wyllie et al., 1962], however, not all needles of apatite may be formed due to this process. In the case of most acicular and equant grains, their aspect ratio increases with an increased cooling rate. Acicular apatite commonly contains a hollowed out cavity slightly offset to the centre of the needle which may be filled with glass [Groves & Mourant, 1929; Seghedi et al., 2008; Warner et al., 1998].

Over half the known stable elements can substitute into the apatite structure. Numerous substitutions into apatite makes it an ideal mineral to use for the following purposes: radiometric dating [Terada & Sano, 2012], fission track dating [Fitzgerald et al.,

1995], determining sedimentary provenance [Morton & Yaxley, 2007], volatile inventories [Boyce et al., 2010], metallogenesis [Mao et al., 2016], magma type characterisation, identification of magma hybridisation [Tepper & Kuehner, 1999] and geothermometry [Stormer & Carmichael, 1971].

1.6.4 Apatite as a monitor for oxygen fugacity

Miles et al. [2014] proposed that the redox partition control of manganese into apatite can be used as a proxy for the redox conditions of magma. This work is based on a compilation of measurements for whole rock Mn contents, Mn contents in apatite, and independent values of f_{O_2} for rocks from the Criffel pluton. The Criffel pluton is a post Caledonian granitic pluton in southern Scotland emplaced at ∼410 Ma [Miles et al., 2013a]. The Mn content of apatite from Criffel show a factor of ∼27 increase from the outer to inner zones, whilst the whole rock Mn shows a decrease with increasing SiO_2. Miles et al. [2014] combined the Criffel data with literature data on apatite in intermediate and silicic melts (Figure 1.9) from different volcanic eruptions and identified a linear relationship between Mn content in apatite and f_{O_2}. They suggested that this linear relationship could be used as an oxy-geobarometer. However, the robustness of this potential oxy-geobarometer is yet to be explored.

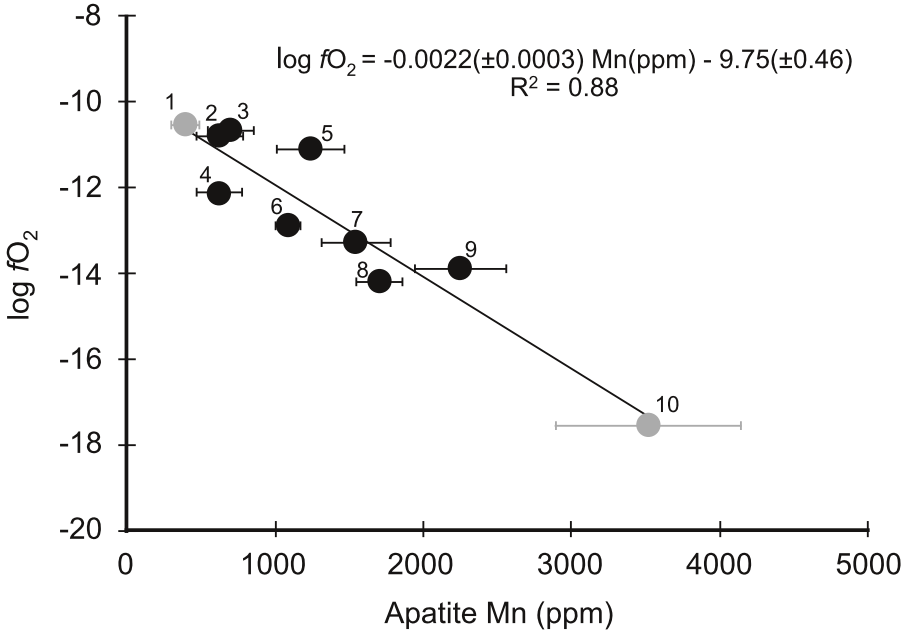

Figure 1.9: Mn concentrations for different volcanic eruptions (Black dots) and Criffel samples (grey dots) against independent estimates of oxygen fugacity [Miles et al., 2014].

The trends identified in Figure 1.9 are believed to occur due to the change in Mn compatibility in the apatite structure with oxidation state. Manganese chiefly substitutes for Ca^{2+} in the apatite structure. It is predicted that Mn becomes more compatible in the crystal lattice with the change from Mn^{3+} to Mn^{2+} with more reducing conditions (lower f_{O_2}) because the ionic radius and charge balance of Mn^{2+} mean the Ca sites of apatite would preferentially incorporate Mn^{2+} over Mn^{3+}. There are two Ca sites in the apatite structure, the Ca(1) site is a nine-fold coordinated site, whilst the Ca(2) site is seven-fold coordinated. It is still contentious which Ca site Mn favours, with many studies indicating a strong preference for the Ca(1) site [Pan & Fleet, 2002] whilst others suggest that there is no preferential ordering of Mn^{2+} across the two sites [Hughes et al., 2004].

It is unlikely that the relationship between Mn content in apatite and f_{O_2} is a simple linear trend due to the strong temperature dependence of f_{O_2} [Marks et al., 2016]. Marks et al. [2016], in comment to Miles et al. [2014], raised the issue that apatite crystallising under reduced conditions is not necessarily Mn rich, and Mn poor apatite does not always indicate oxidised conditions. The pronounced temperature dependence of f_{O_2} dependent mineral reactions (e.g. buffers, Figure 1.4) means that a Mn concentration in apatite may indicate relatively reduced conditions if it crystallised at high temperatures, or oxidised conditions if apatite crystallised at lower temperatures [Marks et al., 2016]. If a Mn-in-apatite oxy-geobarometer was developed, independent temperature measurements would be necessary so f_{O_2} could be expressed relative to a redox buffer. Marks et al. [2016] identified that Mn concentrations in apatite has great potential for constraining f_{O_2} during apatite crystallisation, but expressed that experimental data is needed to constrain how other parameters such as melt composition and crystallisation of other Mn bearing phases will likely influence the Mn content available for apatite.

1.7 Manganese speciation and apatite

Manganese is the third most abundant transition element after Fe and Ti [Chalmin et al., 2009] and is known to exist in up to 4 different oxidation states in natural materials [Manceau et al., 2012; Reiche et al., 2001]. However, the ability to explore

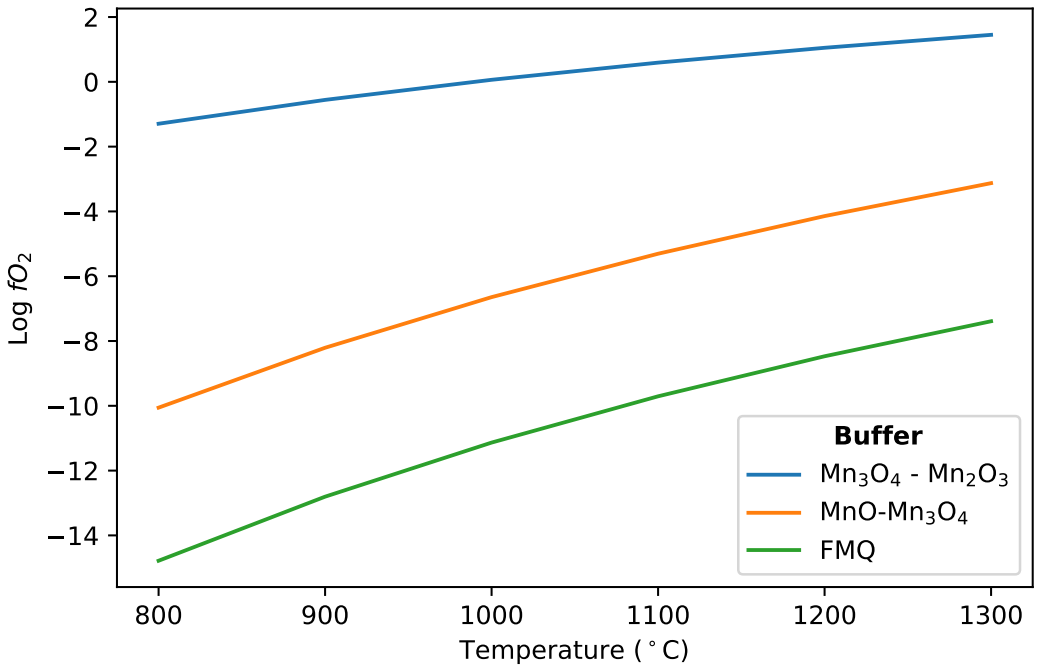

Figure 1.10: Stabilities of manganese oxides with oxygen fugacity relative to the FMQ buffer.

redox conditions in planetary basalts using Mn has largely been ignored.

The 4 naturally occurring oxidation states of manganese found in terrestrial materials are: Mn^{2+}, Mn^{3+}, Mn^{4+} and Mn^{5+}. Only Mn^{2+} is thought to exist in silicate melts, even up to relatively oxidising conditions [Watson, 1977]. However, the speciation of these various valence states in basaltic magmas at various redox conditions still remains largely undocumented. For other multivalent elements such as Fe, V, Ti, Eu and Cr, documentation exists outlining the dominant valence states of these elements as a function of f_{O_2} for planetary basalts [Herd, 2008].

The stabilities of various manganese oxides under reducing and oxidising conditions at various temperatures were explored by Huebner & Sato [1970] (Figure 1.10). Their work shows that if these oxides are used as a proxy for the Mn valence in basaltic melts then Mn^{2+} is persistent up to log f_{O_2} values which are in line with the magnetite-hematite buffer (Figure 1.4). Therefore, because the oxygen fugacity of basalts from Earth generally only reaches +6 log f_{O_2} units above the iron-wüstite buffer, any changes in Mn valence may not be reflective of changes in oxygen fugacity of the melt.

The stability of the various Mn oxidation states in basaltic melts may not be reflective of their stability in various Mn oxide buffers [Huebner & Sato, 1970]. Mutual interactions of redox couples by electron exchange may alter the stabilities of the various Mn valences under different oxygen fugacity conditions [Borisov, 2013; Schreiber et al., 1987] and Mn valence may also be affected by variables such as pressure, crystallisation of minerals from the melt, and by melt structure.

To determine whether the Mn content of apatite can be used as a proxy for oxygen fugacity, further work is required in constraining the controls on Mn partitioning between apatite and melt under various conditions. This involves synthesising apatite and a corresponding melt in the lab and measuring the relative abundance of Mn in each.

Apatite is not the only commonly occurring accessory mineral to contain trace amounts of Mn. Spinel are also common accessory minerals in most magmatic systems which can contain more than one valence state of manganese. Spinel has a basic cubic structure, which usually contains a mixture of divalent and trivalent cations over tetrahedral (T) and octahedral (M) sites. The site preference for Mn in various spinel structures should be easier to determine than apatite, because previous studies (e.g. Eschenfelder, 1958; Hagen & Öestby, 2006; Lenaz & Skogby, 2013) have documented site preferences for the partitioning of Mn cations between the T and M sites. Therefore, studying spinel also provides a useful opportunity to determine the behaviour of the various valence states of Mn in different site symmetries in a crystalline structure. Work in this thesis on spinel will provide invaluable information when determining the site symmetry and valence of Mn in the apatite structure, detailing how features in Mn K-edge spectra vary systematically as a function of valence and coordination of the absorbing atom.

1.8 An introduction to spinel

"Spinel" comes from the latin word *spina* which means spine/thorn, and refers to the spiny form of skeletal quenched crystals in basalts and slags [Haggerty, 2016]. Spinel are a group of oxide minerals with the general formula AB_2O_4 ($A_8B_{16}O_{32}$ per unit cell),

where A, and B can be divalent, trivalent or tetravalent cations [Deer et al., 2013]. The unit cell is face centered cubic and contain 32 oxygens, which form a nearly cubic close packed framework, with cations occupying the interstices within the framework (Figure 1.11) [Sickafus et al., 1999]. The space group symmetry of spinel is $Fd\bar{3}m$. There are two sets of compatible teterahedral (T) and octahedral (M) sites (16d and 8a or 16c and 8b) [Lindsley, 1976]. Cation sites lie at the intersections of the symmetry elements, and are therefore fixed. The position of the oxygen sites must be determined experimentally, and can be described by one parameter, u [Lindsley, 1976]. Normally u is around $\frac{1}{4}$ as this is the value it would take if there was 'true' cubic close packing of the oxygen. Variations in u indicate displacement of oxygen caused by the relative effective radii of cations in the T and M sites. An increase in u from $\frac{1}{4}$ reflects enlargement of the T site relative to the M site and vice versa [Lindsley, 1976]. Smaller and larger cations can also be accommodated by enlargement of the unit cell. It is this flexibility of the oxygen framework and unit cell that permits a large number of elements to occur as cations in oxide spinel.

'Normal' spinel have 8A cations occupying the 8a sites and 16B cations occupying the 16d sites. 'Inverse' spinel have 8 of the 16B cations in the 8a site leading to the formula $B[AB]O_4$. Intermediate distributions may be described by:

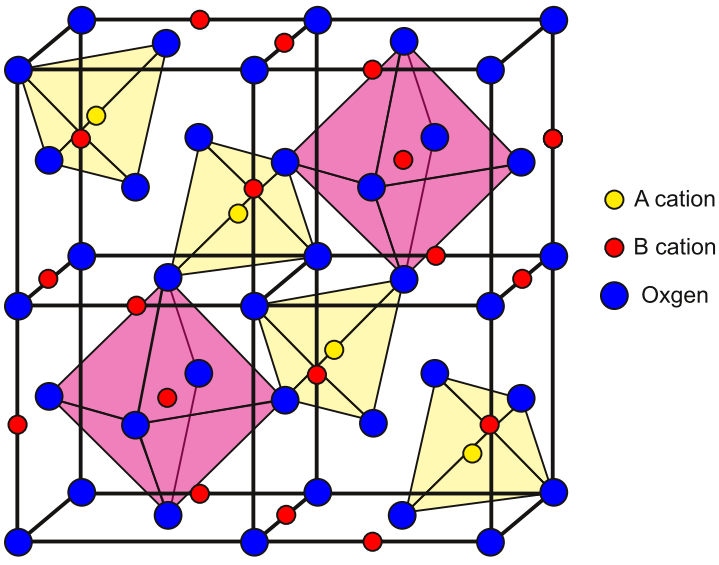

Figure 1.11: Normal spinel structure. Octahedral sites are represented by the pink octahedrons whilst the tetrahedral site is denoted by the pale yellow tetrahedrons.

$$(A_{1-x}B_x)[A_xB_{2-x}]O_4 \tag{1.15}$$

Where x is the degree of inversion, equal to 0 in normal spinel, and 1 in inverse spinel.

Spinel are important peterological minerals, and can be used as geo-thermometers, geo-barometers and geo-speedometers [Biagioni & Pasero, 2014]. Some spinel are ore minerals, and others are considered gemstones. Important in industry for their electric and magnetic properties, spinel are also used in TV and phone screens, and superconducting magnets for MRI and NMR instruments. The spinel structure is also of interest for modelling the Earth's mantle as ringwoodite (γ-Mg_2SiO_4), a high pressure olivine polymorph, is the major phase in the lower part of the mantle transition zone, demarcating the boundary between the upper and lower mantle. The physical and chemical properties of spinel are determined by the type and concentration of cations incorporated in the T and M sites.

1.9 Trace element partitioning

Crucial to the understanding of petrogenetic processes of planetary interiors is having reliable values for distribution coefficients for a suite of rock forming elements. Whilst the ability to measure these elements has increased significantly due to the advancement of analytical instruments, our understanding of partition coefficients in various systems has not kept pace [Blundy & Wood, 2003].

Partition coefficients of trace elements (those present at concentrations < 0.1wt % Blundy & Wood [2003]), due to their low abundance and chemical diversity are often chosen as the best source of data used in the modelling of petrogentic processes. Their low concentration ensures that they generally have negligible impact on the progression of minerals produced by cooling magma, whilst their chemical diversity dictates differences in their compatibility/incompatibility in a wide range of minerals [Blundy & Wood, 2003].

There are various ways to describe the partitioning of trace elements between coexisting

phases. In this thesis I will mainly refer to the Nernst partition coefficient, which describes the partitioning of trace element i between coexisting phases α and β (e.g. mineral-melt):

$$^{\alpha/\beta}D_i = \frac{\text{weight fraction } i \text{ in phase } \alpha}{\text{weight fraction } i \text{ in phase } \beta} \tag{1.16}$$

However, there are other ways to express partition coefficients for trace elements, such as the molar equivalent of Equation 1.16 - Equation 1.17, and the equilibrium constant (Equation 1.18) which takes into account activity-composition relations. Equations 1.19 and 1.20 are partition coefficients which account for the charge and strain of ions entering lattice site M [Blundy & Wood, 2003].

$$^{\alpha/\beta}D_i^* = \frac{\text{molar fraction } i \text{ in phase } \alpha}{\text{molar fraction } i \text{ in phase } \beta} \tag{1.17}$$

$$K_i^{\alpha/\beta} = \frac{\text{activity of } i \text{ in phase } \alpha}{\text{activity of } i \text{ in phase } \beta} \tag{1.18}$$

$$^{\alpha/\beta}D_{0(M)}^{n+} \tag{1.19}$$

$$^{\alpha/\beta}D_{00(M)} \tag{1.20}$$

where 1) $D_{0(M)}^{n+}$ is the strain-compensated partition coefficient for an ion with radius $r_{0(M)}^{n+}$ and charge $n+$ entering lattice site M, and 2) $D_{00(M)}$ is the partition coefficient for a fictive ion that can enter lattice site M without causing elastic strain or electrostatic charging.

An element is said to be incompatible when $D_i \ll 1$ and will, therefore, become concentrated in the liquid during crystallisation. $D_i \geq 1$ indicates an element is compatible within the crystal and will be concentrated in the solid phase. The Nernst partition

coefficient can change as a function of temperature, pressure, composition, and f_{O_2} of the melt [Burnham & Berry, 2012; Mysen & Virgo, 1980; Rubatto & Hermann, 2007; Taura et al., 1998].

If more than one mineral is crystallising from the melt, the behaviour of a trace element can be described using a bulk distribution coefficient $\bar{\mathrm{D}}_i$:

$$\overline{D}_i = \sum_{\phi} X_\phi D_i^\phi \tag{1.21}$$

where X_ϕ is the weight fraction of phase ϕ and D_i^ϕ is the distribution coefficient for component i in phase ϕ.

There is clear evidence that distribution coefficients are strongly composition dependent (e.g. Sr and Ba partitioning between plagioclase and melt depends on anorthite content), which reflects the compositional dependence of the lattice parameters of some crystals, and in these situations, it is often helpful to relate the behaviour of the trace element to the major element it is substituting for. To do this, the trace element distribution coefficient is divided by that of the carrier element. However this requires the measurement of both major and trace elements, and variability in an element's distribution coefficient may also reflect P-T-f_{O_2} conditions. Two dominant factors dictating the substitution of trace elements into the lattice of a particular mineral are its charge and ionic radius. Incompatible elements tend to have ionic radii that are either too large or too small, or their valences are too high or too low.

Classically, mineral-melt partitioning is considered to follow Goldschmidt three rules (1937):

1. Any two ions of the same charge and similar ionic radius have essentially the same crystal-liquid distribution coefficient.
2. If there is a small difference in ionic radius, the smaller ion enters the crystal preferentially.

3. For ions with a similar radius, but different charges, the ion with the higher charge enters the crystal preferentially.

However, whilst these rules are valid in certain circumstances, they are not universally correct or provide any quantitative application. Equilibrium partitioning depends primarily on the energy of elastic strain generated by inserting an ion into a crystal lattice site, and the work done in doing so [Blundy & Wood, 2003].

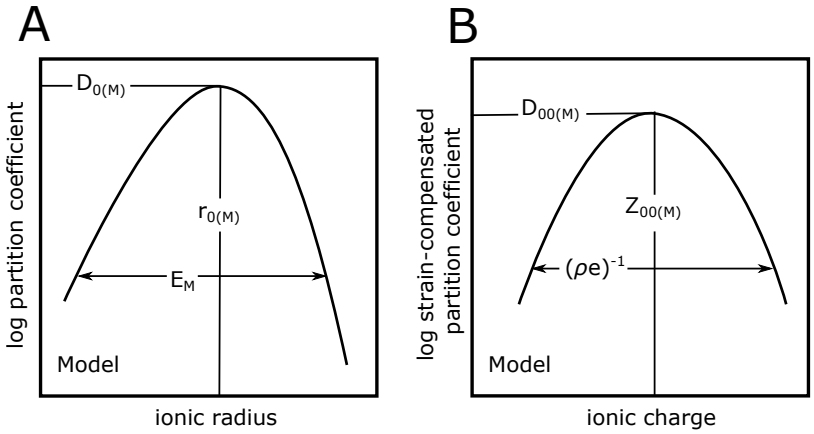

Figure 1.12: A) Illustration of the lattice strain model for a series of isovalent ions of charge n^+ and radius r_i entering a crystal lattice site M. The partition coefficient can be described in terms of three parameters: 1) the radius of that site ($r^{n+}_{0(M)}$), 2) the elastic response of that site (E^{n+}_M - as measured by Young's Modulus) to lattice strain caused by ions that are larger or smaller than $r^{n+}_{0(M)}$ and 3) the strain-compensated partition coefficient ($D^{n+}_{0(M)}$) for a (fictive) ion with radius $r^{+}_{0(M)}$, B) Illustration of the the electrostatic model of trace element partitioning. For ions with the optimum ionic radius partitioning is controlled by the ionic charge (Z_n) relative to the optimum charge at the site of interest, $Z_{0(M)}$. The larger the charge mismatch, the smaller the partition coefficient. (From Blundy & Wood [2003])

Building on Goldschmidt's rules, two new models have been generated to better explain and predict the size of partition coefficients for ions entering a crystallographic lattice. In lattice strain models (Figure 1.12A), trace ions are modelled as point defects in a dielectric elastic continuum [Blundy & Wood, 2003]. To accommodate trace ions in a lattice, disruption of the lattice around the defect is minimised by moving neighbouring ions and distributing excess elastic or electrostatic energy throughout the lattice. Elastic strain energy is inversely correlated with the logarithm of the partition coefficient, and the maximum partition coefficient is found for ions which fit the lattice with the least strain [Blundy & Wood, 2003]. Unlike Goldschmidt's rules where, if there is a

small difference in ionic radius, the smaller ion enters the crystal preferentially, elastic strain energy is roughly symmetrical around an optimum ionic size and therefore so is the partition coefficient (Figure 1.12A) [Blundy & Wood, 2003].

The charge of the ion is also important when modelling partition coefficients, and this is explained in the electrostatic model (Figure 1.12B). Cations with charge X can enter sites with charge Y provided an electrostatic energy penalty is paid. This energy can be quantified assuming it is controlled by the size of the charged region and the dielectric constant of the lattice [Blundy & Wood, 2003]. The electrostatic model and lattice strain model are very useful as they can be used to predict partition coefficients for species of known charge or ionic radius respectively.

The lattice strain model and electrostatic model both fail to consider the effect of melt chemistry on mineral-melt partitioning of trace elements. For most systems, Blundy & Wood [2003] consider the melt phase to be less important than crystal chemistry on trace element partition coefficients.

There are two methods available to directly determine distribution coefficients in geological settings, either by measurements made from suites of natural crystal/whole rock, crystal/glass concentrations or by conducting mineral-melt partitioning experiments.

1.10 Conclusion

Oxygen fugacity is an important variable in geological systems for instance due to the effect it has on the C-O-H-S system of gases and the mantle's interaction with the atmosphere, as well as the effect it has on mineral stability and mantle properties. This parameter is most commonly calculated by examining the ferrous-ferric iron ratio in glasses or Fe-Ti oxides which are in equilibrium. However, both these methods are prone to alteration and the oxygen fugacities they measure can easily be reset.

Log f_{O_2} which are recorded in mechanically strong minerals such as zircon or garnet, or those preserved within them (e.g. apatite), may provide a better way of determining the mantle's redox conditions. However oxygen barometers which involve other redox

sensitive minerals are either in their early stages or still need to be developed. The speciation of manganese into apatite could provide an exciting opportunity to develop an independent oxygen geobarometer.

1.11 Outline of research

This research is concerned with developing and thoroughly testing a Mn in apatite oxy-geobarometer. Miles et al. [2014] proposed that the Mn content of apatite varied as a function of the oxygen fugacity of the melt. This hypothesis was suggested based on numerous measurements of Mn in apatite from granitoids and corresponding estimates of f_{O_2} for the same bodies. This work aims to provide experimental evidence to test Miles et al. [2014] hypothesis.

This experimental work has utilised equipment which can synthesise rocks and melts at high temperature and high pressures to reproduce conditions prevalent in natural systems. The project focuses on determining if there is a direct effect on the oxidation state of Mn in apatite and coexisting melts under various f_{O_2} conditions, and then exploring the partitioning behaviour of Mn into apatite from melt under oxidising and reduced conditions. As a control, first the Mn oxidation state and coordination in spinel was addressed.

1.11.1 Manganese oxidation state in spinel - Outline

X-ray absorption spectroscopy (XAS) is an analytical technique which can be used to determine the oxidation state and coordination of elements in various substances. This technique was used to determine the oxidation state of Mn in apatite. However, determining valence and coordination using XAS relies on the use of standards of known Mn valence and coordination. These have to be similar in structure and valence to the unknown sample. Spinel have a simple cubic structure where Mn can be in one or two different coordination states. Combining X-ray diffraction data and XAS data enables more rigorous estimates of Mn valence and coordination in spinel for use as a standard material for other studies.

1.11.2 Manganese oxidation state in apatite and coexisting melts - Outline

To rigorously test any oxy-geobarometer based on the partitioning of Mn into apatite, the underlying physical changes in the system which cause a change in the Mn's partition coefficient need to be understood. One option is that under more reduced conditions, greater amounts of Mn^{2+} is present in the melt. Mn^{2+} can more easily substitute for Ca^{2+} in the apatite structure compared to Mn^{3+} hence Mn becomes more compatible in the apatite structure under reduced conditions. This chapter aims to understand the physical changes to the oxidation state of Mn in the melt and apatite under different f_{O_2} conditions, and whether this is the main control on the apatite-melt partitioning of Mn.

1.11.3 Ce and Eu oxidation state in apatite and coexisting melts - Outline

Ce and Eu are two rare earth elements (REEs) which can also exist in multiple oxidation states. In a chondorite normalised REE plot for apatite, Ce and/or Eu can display positive or negative anomalies. This is because Ce^{4+}/Eu^{2+}, due to their ionic size, are preferentially excluded from apatite, compared to Ce^{3+} and Eu^{3+} respectively. The intensity and sign of the Eu and Ce anomalies have the potential to be used to determine oxygen fugacity, but currently, very little is known about the direct effect f_{O_2} has on 1) Ce/Eu oxidation state in apatite and coexisting melt, 2) apatite-melt partitioning of Eu and Ce. Chapter 5 is a preliminary investigation, which aims to further understanding of 1 and 2 in simple mono-minerallic systems.

2

Techniques

"Equipped with his five senses, man explores the universe around him and calls the adventure Science."

– Edwin Hubble, *The Exploration of Space*

2.1 Introduction

This chapter details the experimental and instrumental techniques that have been used for sample synthesis and analysis throughout this thesis. Instrumental techniques used for analysis include scanning electron microscope (SEM) imaging, electron probe microanalysis (EPMA), single crystal X-ray diffraction (XRD), secondary ion mass spectrometry (SIMS), and X-ray absorption spectroscopy (XAS).

2.2 Experimental methods

Multiple pieces of specialist equipment have been utilised in this project to synthesise rocks that are analogous to geological materials. High pressures and temperatures were recreated using piston cylinder apparatus, whilst high temperature low pressure experiments were carried out in a vertical tube furnace with gas mixing capabilities.

2.2.1 The piston cylinder apparatus

The piston cylinder apparatus is an instrument that can be used to experimentally simulate conditions of the deep crust to the upper mantle. Piston cylinder instruments are routinely used to achieve temperatures of up to 1600 ℃ and pressures from 0.5 to 4 GPa, which are equivalent to depths ranging from 15 to 120 km below earth's surface. Unlike lower pressure apparatus (cold seal vessels and internally heated gas vessels, where P <1GPa) that generally use gas or fluid to achieve pressure, the piston cylinder apparatus applies hydrostatic pressure to experimental charges housed within a solid assemblage, by compression and deformation of the solid pressure medium. Heating of

the sample is achieved by the use of an internal resistance furnace which is built into the sample cell. Temperature is controlled by the flow of current to the furnace from a fused electrical system, monitored via the use of a thermocouple, and is dissipated from the surrounding apparatus by means of a water cooling system.

This project used two different sized experimental assemblies (1/2" and 3/4") to synthesise samples. The 3/4" assembly has the advantage of either using bigger capsules so that sample volume is larger, or in the case of this project, the volume allows two different capsules to be run in the same assembly.

The main components of the experimental assemblies are shown in Figure 2.1 which shows the typical assemblage parts for a 3/4" and 1/2" assembly. The central part of the assembly is where the metal capsule (Pt or AuPd) containing the sample material is located. The main part of the cell consists of (from the outside to centre): a talc pressure medium, a pyrex sleeve, and graphite furnace. The interior of the assembly contains components designed to make sure the sample sits in the hotspot, and include (from bottom to top): a bottom alumina spacer, the sample in an alumina sheath (to protect and centre the capsule), an alumina disc, and a further alumina top spacer with a hole through the middle for the thermocouple to pass through.

The end loaded piston cylinder press in the School of GeoSciences, University of Edinburgh requires an end load pressure of 150 tonnes to be initially applied to the stacked components of the apparatus (spacers, spacer plate, thermocouple plate, pressure plate and bridge) (Figure 2.2, and Figure 2.3). This is applied via a compressed air pump linked to a hydraulic line. This stabilises the entire stack to allow the second ram to directly pressurise the sample to the required pressure, and is applied using a hand pump connected to a hydraulic line. For each run, a pressure calibration was applied to account for pressure loss associated with internal friction within the assembly.

The sample cell sits within the central part of the stack, the pressure plate. The pressure plate consists of a tungsten carbide (WC) core in which the experimental assembly sits, which is surrounded by a number of press-fit steel rings. The rings minimise lateral extension of the WC core to stabilise the centre of the pressure plate during application

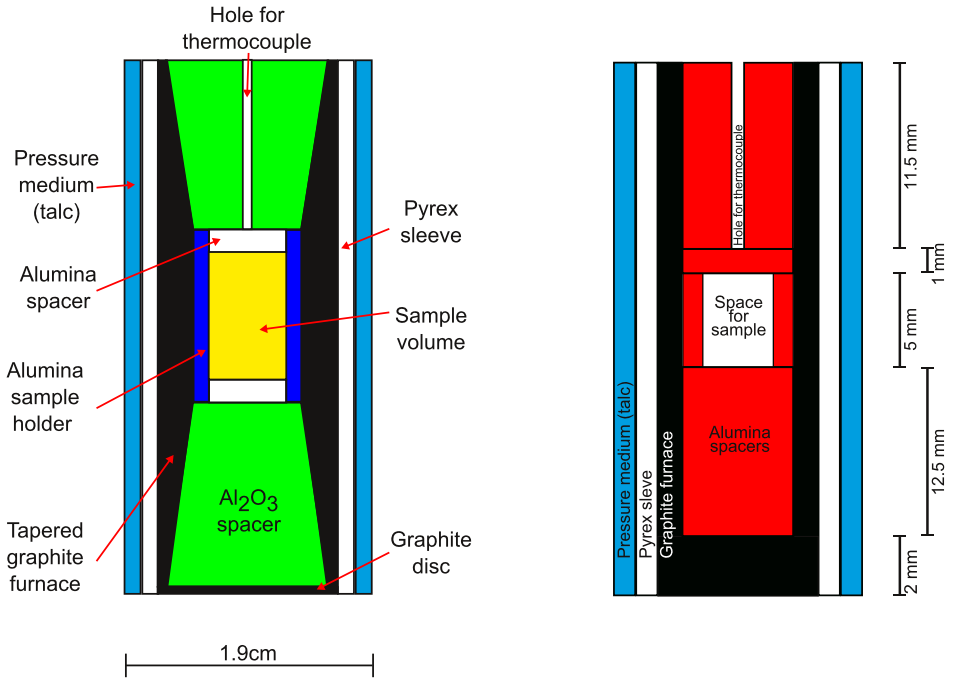

(a) 3/4" sample assembly **(b)** 1/2" sample assembly

Figure 2.1: An example of a 3/4" and 1/2" assembly.

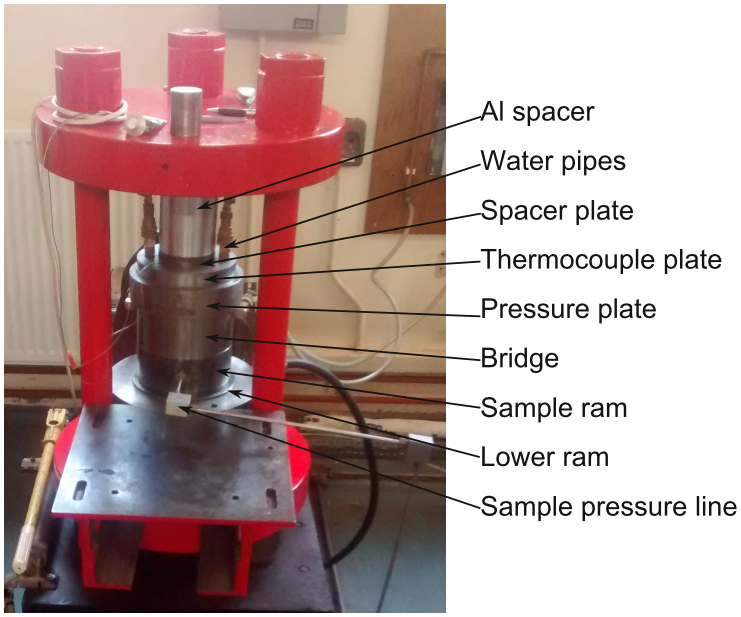

Figure 2.2: An image of the piston cylinder apparatus used in this study. The image shows the apparatus under pressure with the power and cooling systems connected. Barely visible in this image is the lower ram, which is the raised cylindrical support beneath the sample ram which applies pressure to the whole stack. Above the lower ram is the sample ram which applies pressure to the sample assembly.

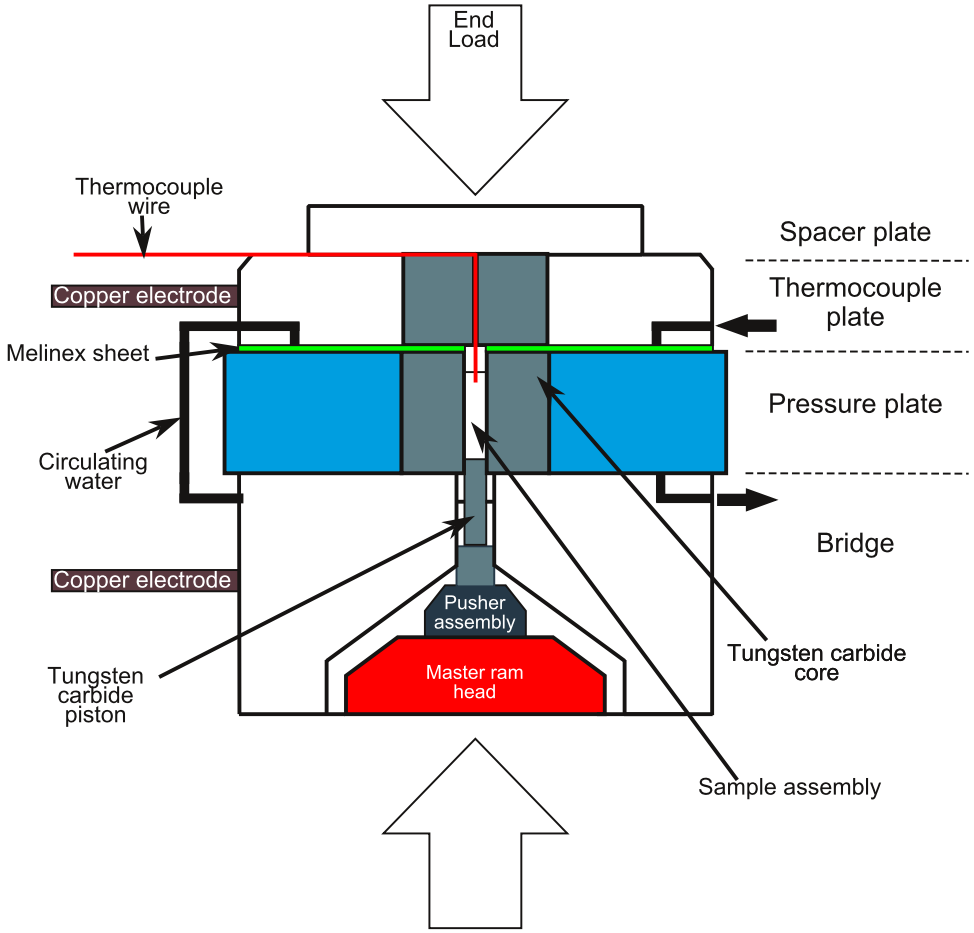

Figure 2.3: Simplified cross section of the piston cylinder apparatus. Labelled are the key components of the apparatus, including: the pressure plate in which the sample assembly sits, the thermocouple plate where half the water cooling pipes and power connections are attached and the bridge where the other water and power connections are attached and in which the load is applied to the piston.

of load. Pressure is applied to the sample by the use of a carbide piston, that is forced into the pressure plate via a small ram housed in the bridge. Temperature is controlled by varying the current sent through the graphite furnace component of the experimental assemblage. Temperature is measured by recording the output voltage difference from a R type thermocouple (Pt_{100}-$Pt_{87}Rh_{13}$) which is positioned within the experimental assembly just above the sample $\approx$ 10 ℃ from the hotspot.

A typical piston cylinder run commences by building up the stack of components (bridge, pressure plate, thermocouple plate, spacer plate and an Al spacer) in the press with the pusher, piston, sample assembly and melinex sheet. Following stacking, a couple of melinex sheets are inserted above the top Al spacer to electrically isolate

the stack from the press. The press is now ready to apply a 150 tonne end load via the compressed air pump. Upon reaching 150 tonne the air pump is switched off and the end load hydraulic lines are then isolated. At this stage the water coolant lines, copper electrodes and thermocouple can then be connected. The sample is then initially pressurised to 0.3 GPa before heating, by moving the carbide piston with a small internal ram housed in the bridge. This is applied using a manual hand pump connected to a hydraulic line. Pressure is then applied simultaneously with increasing temperature at a rate of 100 ℃ per minute, reaching a maximum pressure of 1 GPa for all runs, after ≈ 500 ℃. After reaching super liquidus conditions, a slight over pressurisation is applied to compensate for pressure loss during the first hour.

All piston cylinder experiments were run in Pt capsules due to the high run temperatures (up to 1500 ℃) required to grow apatite. Tubes of Pt (either 2mm or 3mm outer diameter) were cut to the required length, annealed overnight at 1100 ℃ before being triple crimped at one end. The crimp was then welded shut with Ar gas flowing over the capsule using a PUK U4 -TIG impulse micro welder and flattened in a pin press. The Pt bucket was then loaded with the experimental charge before triple-crimping, welding and the remaining end being flattened.

For most solid media experiments used at pressures >0.5 GPa, oxygen fugacity (f_{O_2}) is uncontrolled and is imparted by the components of the experimental assemblage and the initial oxidation state of the sample. However, there are ways to control f_{O_2} via solid redox buffers, or by the choice of the capsule material [Matjuschkin et al., 2015].

Double capsule experiments were used to control f_{O_2} in water bearing experiments (Figure 2.4). In these experiments an outer capsule contains a solid oxygen buffer such as mixtures of Ni + NiO or FeO + Fe_2O_3, with H_2O. If water saturated and as long as all phases remain present, f_{H_2} is set via the f_{O_2} and the water equilibrium constant:

$$K_{eq} = \frac{{f_{O_2}}^{1/2} * f_{H_2}}{f_{H_2O}} \tag{2.1}$$

As H_2 readily diffuses through the inner capsule walls into the experimental charge it

maintains a constant f_{H_2} in both the outer and inner capsules. At equilibrium, both the H_2 and H_2O fugacities are equal in both capsules. From Equation 2.1 it follows that the oxygen fugacity will be the same in both capsules, and imposed by the metal oxide buffer in the outer capsule [Jakobsson et al., 2014].

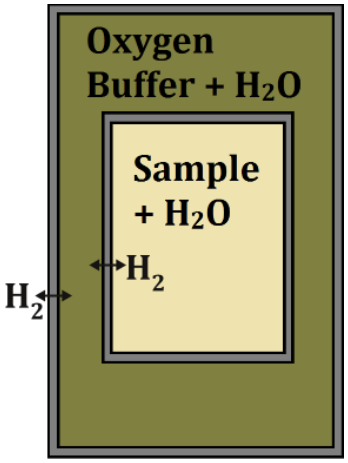

Figure 2.4: Schematic diagram of a double capsule set-up with the solid state oxygen buffer present ($+H_2O$) in the external capsule, and the experimental charge in the inner capsule.

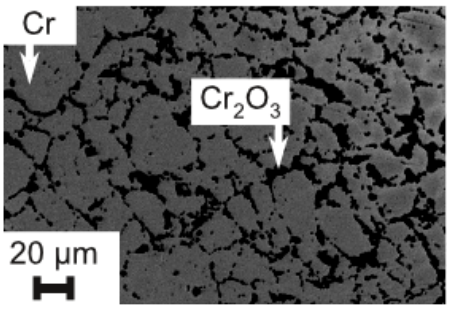

Figure 2.5: A back scattered electron (BSE) image of the Cr-Cr_2O_3 buffer after an experimental run. The Cr oxide appears as the dark black patches whist Cr appears more reflective.

When using the double capsule technique checks have to be made to confirm that following the experimental run, H_2O and both parts of the oxidation-reduction buffer are still present. These checks were made with the use of energy dispersive analysis on the SEM (Figure 2.5) or acquiring X-ray diffraction (XRD) data. If H_2 is lost from the assembly or the activity of H_2O differs between the buffer and the sample, f_{O_2} will deviate from the intended value. In water undersaturated samples ($aH_2O < 1$) there will be a lower f_{O_2} than the coexisting hydrated buffer.

Upon completion of the experimental run, the sample is quenched and retrieved. The sample is isobarically quenched by either removing the heating circuit fuse or by rapidly decreasing power on the eurotherm controller to zero. Whilst the temperature is falling, the sample pressure is kept at constant P by applying hydrostatic pressure with the use of a hand pump. Run temperature drops to < 50 ℃ in a few seconds.

At the end of each experimental run the pressure plate is retrieved from the piston cylinder stack and placed into a small hydraulic press. A rod is used to force the

assembly and piston out of the pressure plate. The press is limited to 4 tonnes of force, but often less is needed to push out the assemblage and piston. Following the separation from the pressure plate, the assembly is delicately crushed with pliers to break away the layers of talc, pyrex, graphite, and alumina which surround the capsule, resulting in the removal of the capsule(s).

2.2.2 Vertical tube gas mixing furnaces.

For high temperature, low pressure experiments (1 atm pressure, < 1600 °C) in which oxygen fugacity was to be accurately controlled, vertical tube furnaces fitted with gas mixing apparatus were used. Three different furnaces were used in this project; a platinum wound furnace for spinel synthesis work, a Lenton furnace with silicon carbide elements for glass and apatite synthesis at temperatures exceeding 1100 ℃, and a Deltech furnace used to synthesise Eu and Ce bearing glasses.

A mixture of CO_2 and H_2 gases were used to buffer the atmosphere inside the furnace at selected f_{O_2} values. The proportion of CO_2/H_2 needed for the various f_{O_2} conditions were obtained from JANAF tables produced by Deines et al. [1974]. Gas mixing was controlled by Bronkhorst mass flow controllers. An Australian Oxytrol System oxygen probe consisting of a solid zirconia electrolyte (SIRO2) oxygen sensor and internal thermocouple was used to calibrate the tabulated f_{O_2} values with the probe readings in the platinum wound furnace, however, this option was not available for other furnace types due to the probe's length. Oxygen fugacity was measured by calculating the oxygen concentration from the temperature and voltage readings of the oxygen probe at a known reference concentration using the Nernst equation.

$$E = 0.0496T * log(\frac{pO_2}{0.209}) \tag{2.2}$$

Where E = sensor electromotive force (mV), T = temperature (K) and p = partial pressure.

Oxygen fugacity in the other furnaces was checked using mineral redox buffers (NNO,

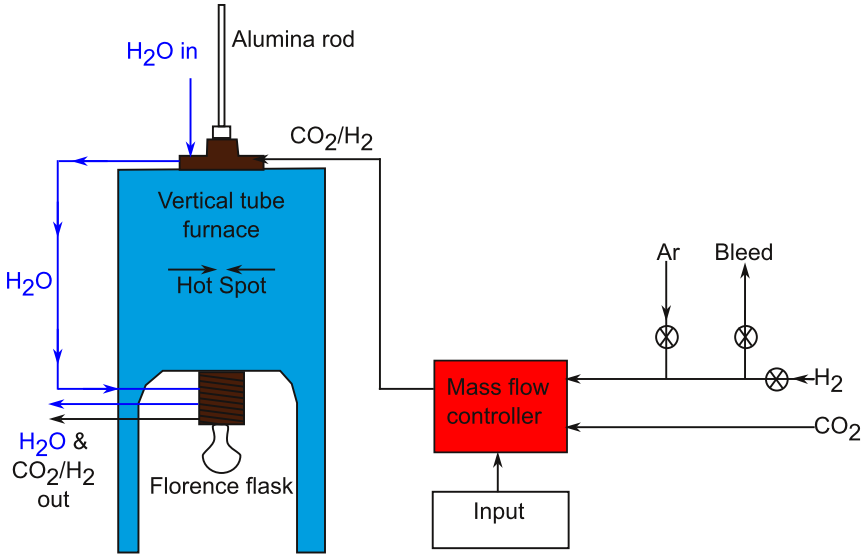

Figure 2.6: Diagram of the gas mixing set-up for the platinum wound furnace. A controlled mixture of CO_2 and H_2 is pumped into the furnace to control the oxygen fugacity of the atmosphere inside the furnace. Also present on the hydrogen lines are a series of valves that can be used to flow argon through the systems to purge the line/furnace of oxygen. A water cooling system (blue arrows) is used to cool the endcaps where the gas enters and exits the furnace.

FMQ, MH) run at the same temperature as experimental runs but under CO_2/H_2 gas mixes [Deines et al., 1974] which would ensure both buffer phases were present. As such, potential errors on absolute f_{O_2} values in these furnaces are larger.

2.3 Preparing starting materials

Starting materials for piston cylinder and gas mixing furnace experiments were prepared from a series of oxide and carbonate powders. Fired powders were kept in a 110 ℃ oven to drive off water before measuring. Powders were measured in the correct proportions to achieve the target starting composition, and were homogenised in agate mortar and pestle under acetone for 30 minutes. Following homogenisation the starting material was loaded into a Pt crucible, placed in a programmable furnace at 600 ℃ and ramped to 1000 ℃ over 6 hours. Following removal from the furnace the starting material was reground in the mortar and pestle for a further 30 minutes. Most starting materials were then glassed. This was carried out by placing the starting material in a clean Pt crucible, placing the crucible in a furnace held above the starting material's liquidus temperature, leaving for half an hour, and then quenching by lowering the bottom of

the crucible into a vat of water. This procedure may result in a slight loss of Fe to the Pt crucible. Starting materials were stored as glass chips in a 110 ℃ oven until needed.

2.4 Sample preparation

On completion of an experimental run, samples were carefully prepared for analysis. Gas mixing glasses were mounted straight into 1" epoxy blocks by pouring the appropriate proportions of epoxy resin and hardener over the samples in a 1" mould. Care was taken to avoid trapping bubbles in the set epoxy blocks. Most piston cylinder experiments were mounted into crystalbond, where samples could be ground and polished, before being easily removed using appropriate solvents and mounted into indium.

Samples in set epoxy/crystalbond were ground with various grades of silicon carbide abrasives, progressively getting finer, until the relevant part of the sample was on the surface, and the samples were flat. Mounts were then thoroughly cleaned in Decon90 and dried, prior to polishing.

Three grades of diamond slurry were used to polish the samples. Mounts were first polished using 6 micron paste for $\approx$ 3 minutes before being ultrasonically cleaned in Deacon90, and then water, before being left to dry. This process was repeated with a 3 micron and 1 micron diamond slurry respectively. 3 minutes at each stage was found sufficient to produce a well polished surface at the end of the 1 micron stage, but avoided rounding grains. At this stage, samples in crystalbond were dissolved out, cleaned, and then cold-pressed into indium for analysis by SIMS or EPMA. Epoxy has a habit of degassing C, H and S during hardening, and this can degrade the SIMS vacuum, causing much higher backgrounds for these elements. It is much easier to achieve a good vacuum for SIMS using indium, which gives markedly lower background counts. Prior to EPMA or SIMS, indium (and/or epoxy) blocks were thoroughly cleaned, and sputter coated using C and Au respectively.

2.5 Analytical techniques

To analyse the experimental charges a range of analytical techniques were implemented. The scanning electron microscope (SEM) and electron probe microanalyser (EPMA) bombard the sample with electrons and observe the electron - sample interactions that take place. Secondary ion mass spectrometry (SIMS) sputters a sample with ions to release secondary ions to analyse. In contrast X-ray - sample interaction is used to probe matter in the following techniques: single crystal X-ray diffraction (SC-XRD) and X-ray absorption spectroscopy (XAS).

2.5.1 The Scanning Electron Microscope (SEM)

Scanning electron microscopy (SEM) is a technique capable of imaging samples down to a resolution of 1nm at 15kV [Griffin & Michael, 2006]. It can also be used to provide semi-quantitative compositional analysis and microstructral characterisation.

The Carl Zeiss SIGMA HD VP Field Emission SEM (Figure 2.7) with Oxford AZtec electron dispersive X-ray spectroscopy (EDS) analysis at the University of Edinburgh was used in the project for:

1. Phase identification within recovered piston cylinder samples, particularly of material that would be further investigated using electron probe microanalysis. This included semi-quantitative analyses using EDX analysis.
2. Producing maps of samples for navigation during subsequent analyses.
3. Confirming all components of the buffer remained.
4. Checking the integrity of capsules.

The Carl Zeiss SIGMA HD VP Field Emission SEM uses a field emission gun (FEG) to produce electrons which can be accelerated and focused on the sample. Accelerated electrons produce a variety of signals following their collision with the solid sample (electron-sample interactions). These include the production of secondary electrons

(SE), backscattered electrons (BSE), diffracted backscattered electrons (EBSD), characteristic X-rays, visible light and heat.

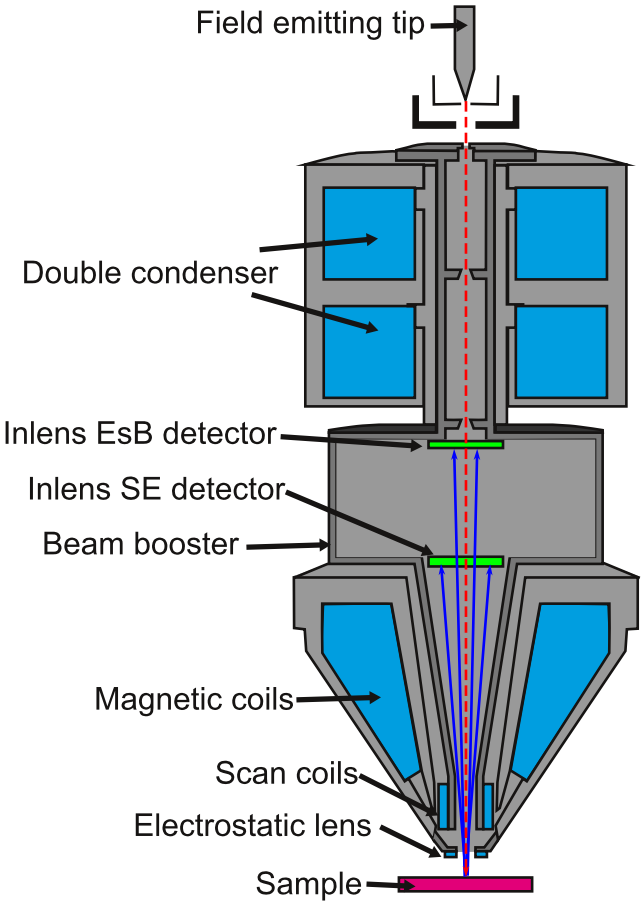

Figure 2.7: Carl Zeiss SIGMA HD VP Field Emission SEM (From Carl Zeiss Microscopy GmbH 2017). The field emission gun (FEG) produces an electron beam at the top of the column which is then focused onto the sample using a variety of lenses and apertures. Electron-sample interactions produce a variety of signals including both secondary and backscattered electrons which are detected at the corresponding in-lens SE detector and in-lens EsB detector respectively.

Whilst SE images are more sensitive to topographic features in a sample and have a higher resolution, BSE images were primarily used in this project, as backscattered electrons are sensitive to the atomic mass (Z) of the element they scatter from. This results in heavier elements scattering more electrons and appearing brighter compared to lighter elements (Figure 2.8). Therefore in silicate rocks, phases such as quartz and feldspars will appear dark whilst Fe-Ti oxides or REE containing minerals will be brighter.

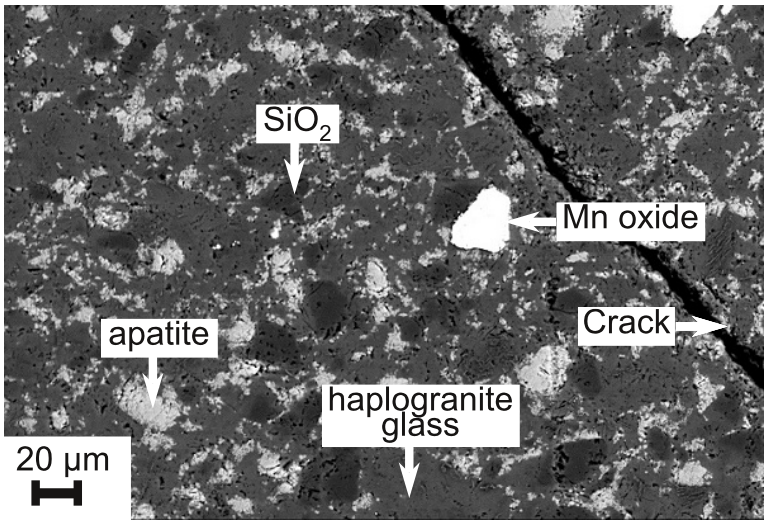

Figure 2.8: NNO-1000 run which shows the variation in greyscale with atomic number. The most reflective phase is blebs of Mn oxide as Mn is the heaviest element (Z=25) in these samples. The darkest patches in this image, which appear darker than the surrounding glass are blebs of SiO_2. The other phases with increasing brightness is the haplogranite glass and apatite crystals.

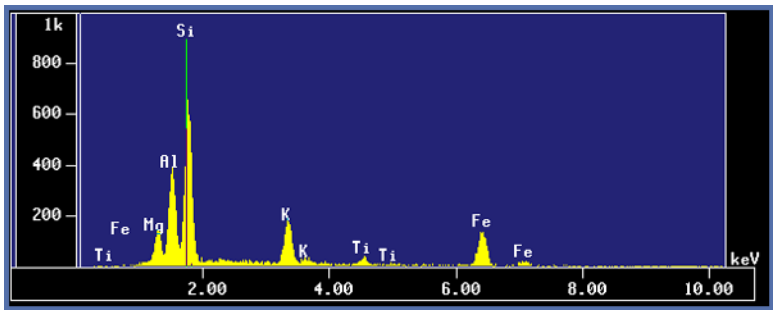

Figure 2.9: EDS spectrum of biotite containing Si, Al, K, Mg, Fe and Ti. Multiple peaks per element correspond to X-rays emitted from different electron transitions (image from https://serc.carleton.edu/research_education/geochemsheets/eds.html).

As well as imaging, the SEM was used for elemental analysis. The attached EDS detector provided a semi-quantitative method to quickly indicate the compositional data from a sample, which was used to identify apatite for subsequent analysis. It is possible to calibrate the instruments' column conditions and working distance to provide quantitative results, but this was not necessary for the purpose of this project. An EDS detector contains a solid state crystal detector that absorbs element characteristic X-rays from the sample and measures them based on the electrical voltages produced. An EDS spectrum is generally displayed as a plot of X-ray counts vs. energy.

Characteristic X-ray peaks are recorded for each element present, but many elements may yield multiple peaks corresponding to X-rays emitted from different energy shells.

EDS analysis is often viewed as semi-quantitative, because wavelength dispersive spectroscopy (WDS) is more precise, capable of measuring lower elemental abundances, and often there are peak overlaps present that are too difficult to resolve by energy dispersive analysis. However, improvements in detector resolution is challenging this view.

2.5.2 Electron Probe Micro Analysis (EPMA)

An electron probe microanalyser (EPMA) is similar in design to a SEM, but where a SEM is primarily set up for imaging, an EPMA is predominantly designed for quantitative analysis (Figure 2.12, page 50). EPMA analysis chiefly uses wavelength dispersive spectrometry (WDS) detectors to measure the characteristic X-rays emitted by elements generated through the interaction of the electron beam with the sample. Each element is sequentially measured allowing for high spectral resolution and low detection limits when compared to EDS. Typical ED detector resolution is 70 - 130 eV whereas WD peak widths are 2 - 20 eV [Oxford Instruments Analytical, 2002]. This enables the EPMA to measure most elements from the periodic table at the ppm level, with the exception of some lighter elements (notably H, He, Li and Be).

The EPMA configuration is similar to the SEM set-up, the main difference being that it is optimised to get precise and accurate quantitative chemical analyses with the addition of 3-5 wavelength dispersive spectrometers. Inside a WD spectrometer, analysing crystals with specific lattice spacing are chosen to diffract characteristic X-rays from the sample to the detector. The wavelength of the X-rays diffracted depends on the position of the analysing crystal with respect to the sample. The position of the sample, crystal, and detector must all lie on the Rowland circle to satisfy Bragg's law and measure the X-rays efficiently. As the position of the samples and incoming X-rays is fixed, the analytical crystal and X-ray counter must both be able to move to optimise data collection. A diffracted beam will only pass to the detector when Bragg's law is met:

$$n\lambda = 2dsin\theta \tag{2.3}$$

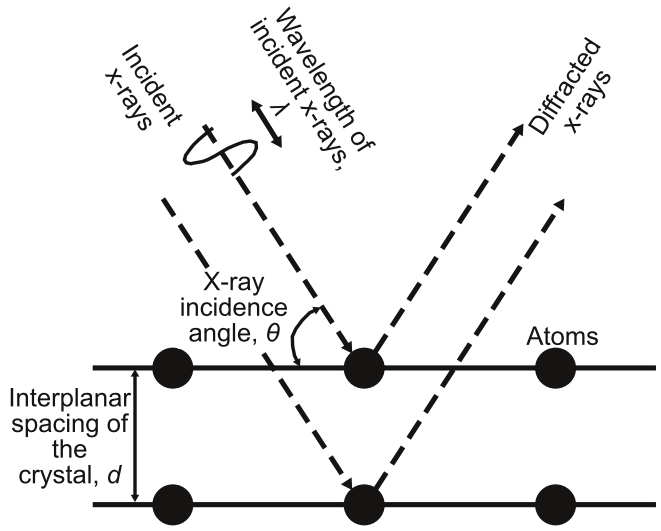

Figure 2.10: A graphical example of X-rays diffracting from crystal planes, where d = inter-planar spacing of the crystal, λ = wavelength of the incident X-rays and θ = angle of incidence.

where λ (nm) is the wavelength, d (nm) is the inter-planar spacing of the sample and θ is the angle of X-ray incidence on the sample, and n is an integer (Figure 2.10).

To satisfy Bragg's law, the crystal position is changed, but this means that only one element at a time can be measured on each spectrometer, until the position of the crystal is adjusted for another element. The geometry of a WD spectrometer can be one of two types. The Johann geometry has the diffracting crystal bent to a radius of 2R, whereas the Johansson geometry (Figure 2.11) has the crystal bent to radius 2R and ground so that the crystal is always in contact with the Rowland circle. This focuses all the X-rays originating from a point source at the same point on the detector, maximising collection efficiency [Oxford Instruments Analytical, 2002].

Several different diffracting crystals with different crystal lattice spacing are required in WDS to cover a range of wavelengths to measure a wide range of elements. Therefore it is typical to have 4-5 spectrometers mounted in a sequence around the sample chamber of the column. Where more than one crystal can be used to measure the same element, the crystal with optimum performance for the wavelength of interest is chosen. Some commonly used crystals are listed in Table 2.1.

The X-ray detector on an electron microprobe usually consists of a gas proportional counter type. In this type of detector, the X-rays enter the detector via a collimator

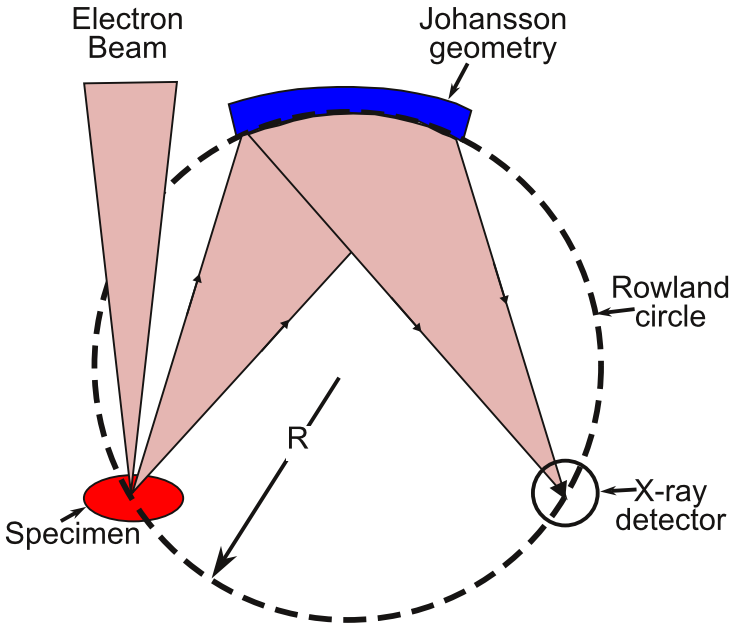

Figure 2.11: Example of the Johansson crystal geometry found within WDS detectors. The diffracting crystal is bent to a radius of 2R, where R is the radius of the Rowland circle, and ground to radius R. This focuses all the refracted X-rays to the same point on the detector. After Oxford Instruments Analytical [2002].

and are absorbed by the counter gas. Absorption of the X-rays causes the emission of photoelectrons, these are then accelerated to a wire where additional ionisation leads to the generation of electrical pulses, which have an amplitude proportional to the energy of the original X-rays absorbed by the gas. Once the counts of X-rays have been measured, these have to be compared to a series of standards containing known proportions of the elements of interest. These standards are used to apply a matrix correction, typically by applying a ZAF correction (atomic number, Z, absorption A,

Table 2.1: Common diffraction crystals used in WD detectors. Also listed is the 2d spacing and elemental range these crystals cover.

Crystal name	**Type**	**2d spacing (Å)**	**Element range for Kα X-rays**
LIF(220)	Lithium Fluoride	2.847	V to Y
LIF(200)	Lithium Fluoride	4.028	Ca to Ge
PET	Pantaerythritol	8.742	Si to Ti
TAP	Thallium acid phthalate	25.745	O to Si
LSM-060/PC1	W-Si	~61	C to F
LSM-080/PC2	Ni-C	~78	B to O
LSM-200	Mo-B_4C	~204	Be and B

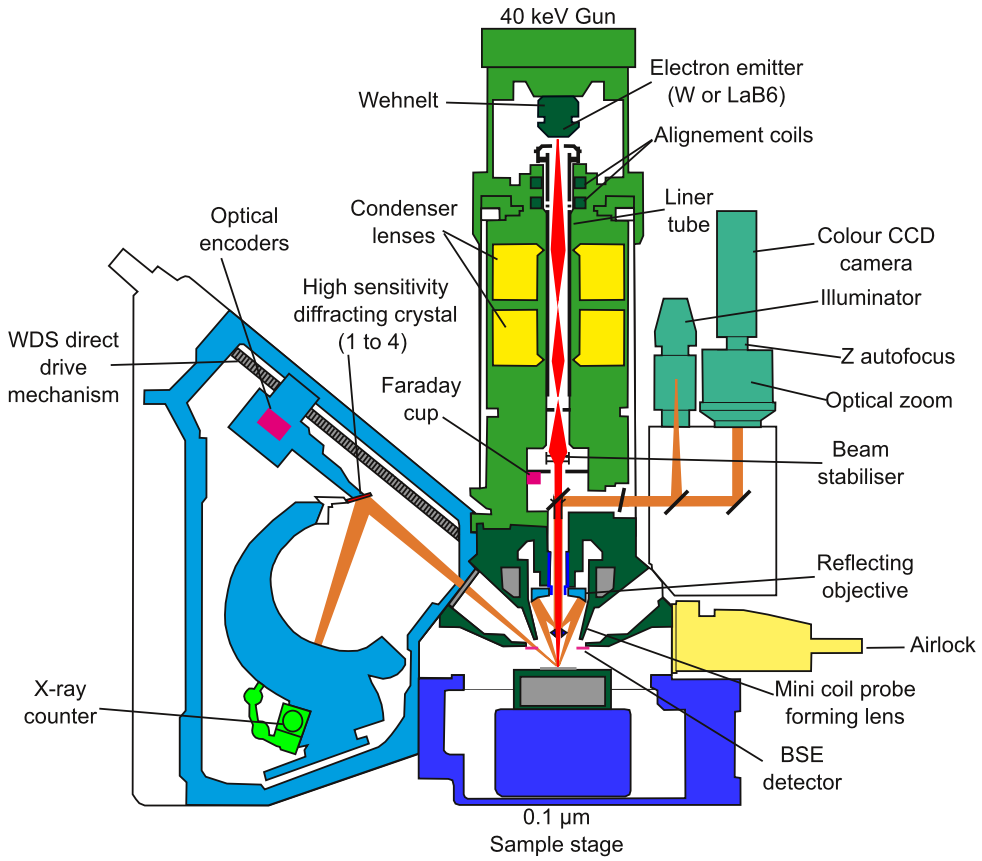

Figure 2.12: Schematic diagram of the CAMECA SX-100 Electron Microprobe Analyser Cameca [2013].

fluorescence, F).

2.5.3 Secondary Ion Mass Spectrometry (SIMS)

Secondary ion mass spectrometry (SIMS) is an analytical technique designed to collect quantitative analyses at very high resolution. SIMS can measure the concentrations of elements (H to U) with a ppm to ppb detection limit (element dependent), with a relatively small spot size (1-25μm), and can also be used to measure isotopic ratios to a precision of 0.5 to 0.05 %.

SIMS works on the premise that when heavy particles (usually O_2^+, O^-, Cs^+, Ar^+, Ga^+ or neutrals) bombard a sample at high energy, it results in the ionisation and ejection of charged particles known as secondary ions. To reduce background noise during data collection, the technique relies on the use of an ultra high vacuum (UHV); hence, both

the sample and mounting medium must be stable under these conditions. A UHV of 5 x 10^{-10} Torr minimises noise in the data as it reduces the chance of a secondary ion hitting a gas molecule (effectively a zero % probability). As well as being mounted in a UHV compatible medium, SIMS samples should also be polished flat and coated in a conductive medium (usually gold) to obtain a constant ion beam. Samples in this project were measured using a Cameca-4f ion microprobe (Figure 2.13) to collect data on the volatile and trace element contents of apatite and glass.

Primary ions can be produced with a duoplasmatron, Cs ion source or a Ga ion source. The duoplasmatron commonly uses oxygen to produce either O^-, O_2^- or O_2^+ depending on the electrical polarity selected. The duoplasmatron generates many ion species, and these are filtered leaving the desired ion beam. Primary ions then pass through the primary column on the way to the sample. This column filters the beam for impurities, and controls the shape, intensity and position of the beam. The primary ions bombard the sample producing positive or negative secondary ions depending on the polarity of the sample.

Secondary ions are focused into a mass spectrometer via the use of dynamic transfer plates and lenses. These form the Cameca ion microscope which enables an image of the sample to be viewed. Once in the mass spectrometer, the ions are separated based on their energy and charge mass ratio using an electrostatic and magnetic prism. These prisms are adjusted to analyse the ions of interest, by changing their set-up to select a specific ion mass and charge. Following separation of the ions, they are then detected by either: a fluorescent screen (used to focus the beam), an electron multiplier (for quantitative analyses) or a Faraday cup (for use when the ion beam is on, but the fluorescent screen or electron multiplier aren't in use).

Data produced from the Cameca-4f ion microprobe is in counts per second (CPS). Standards of known composition are used to convert these CPS into ppm levels (element/oxide) (Figure 2.14).

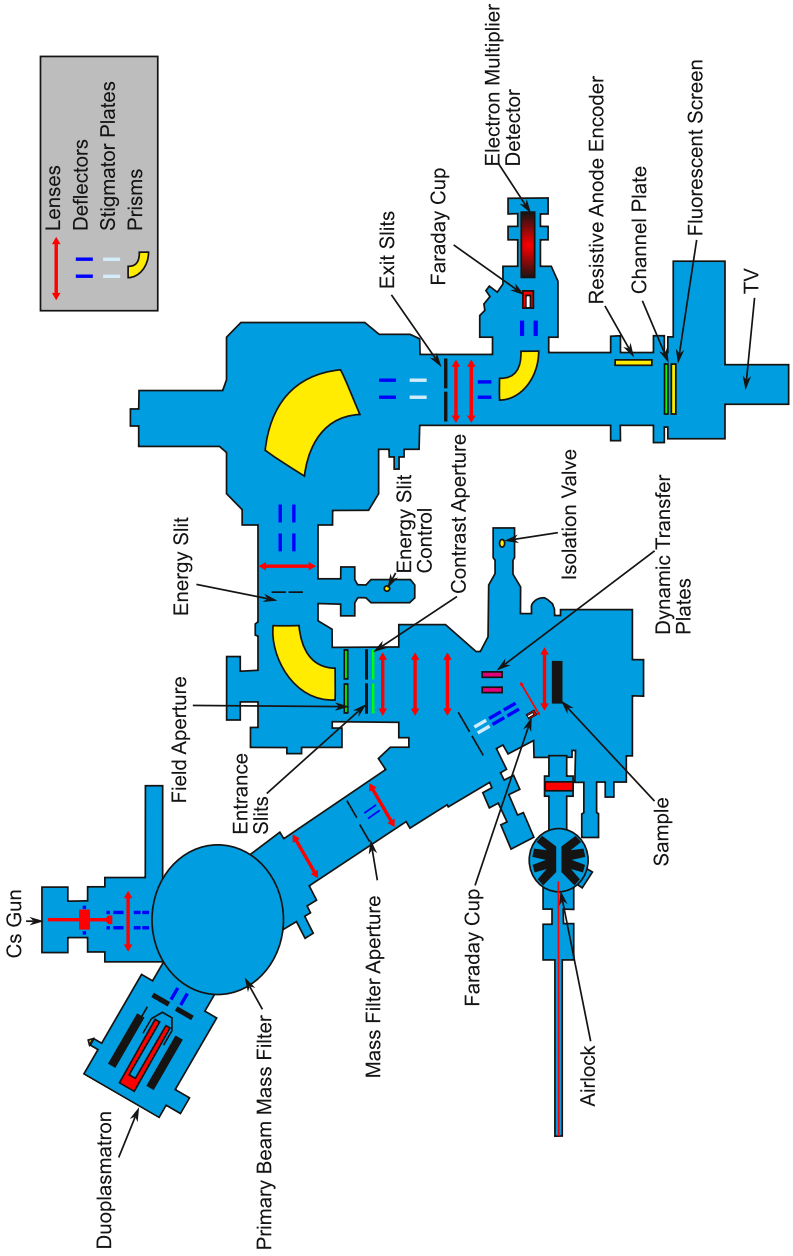

Figure 2.13: Schematic diagram of Cameca-4f Ion Microprobe, after Hiscock [2013].

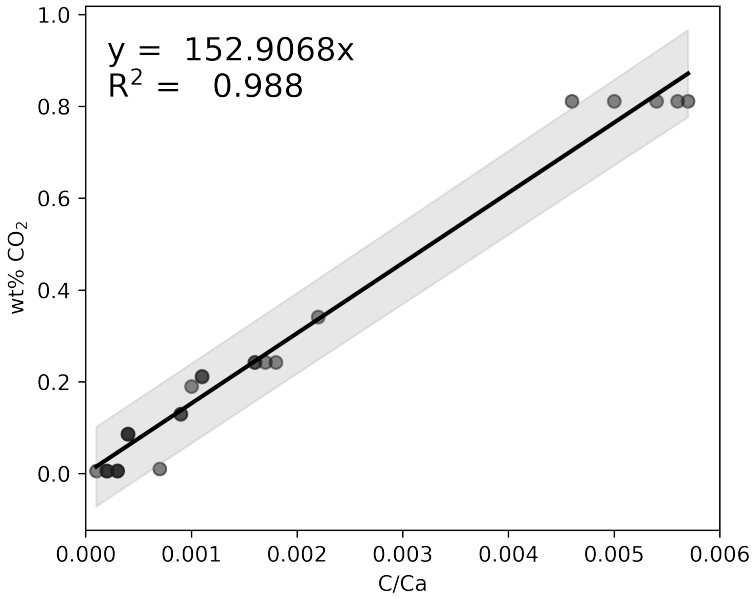

Figure 2.14: An example of a SIMS calibration curve, in this case for CO_2 in apatite. C/Ca ratios from SIMS are plotted against the known concentration of CO_2 in the apatite standards acquired using other analytical techniques. Plotted either side of the linear regression is the 95% confidence interval for the fitting.

2.5.4 Single Crystal X-ray Diffraction (SC-XRD)

Single crystal X-ray diffraction (SC-XRD) is a non-destructive technique used to determine the molecular structure and longer range ordering of a single crystal. The technique involves analysing the dimensions of a crystalline lattice, and modelling this data to determine the crystalline structure. SC-XRD data and structural refinement was carried out by collaborators in Italy using a KUMA KM4 four-circle diffractometer to test the quality of the crystals, and an Oxford Diffraction Xcalibur diffractometer to collect intensities.

Ideally, SC-XRD data is collected on a non twinned and un-cracked crystal which has been glued onto a goniometer head (sample holder) (Figure 2.15). This sample holder is then placed on the goniometer and optically aligned with the centre of the X-ray beam for all orientations of the crystal. X-rays are produced in a cathode ray X-ray tube where electrons are emitted via thermionic emission from a filament. These electrons are then fired on a target, which is usually molybdenum or copper. The deacceleration of electrons in the metal target produces one type of X-ray spectra, bremsstrahlung

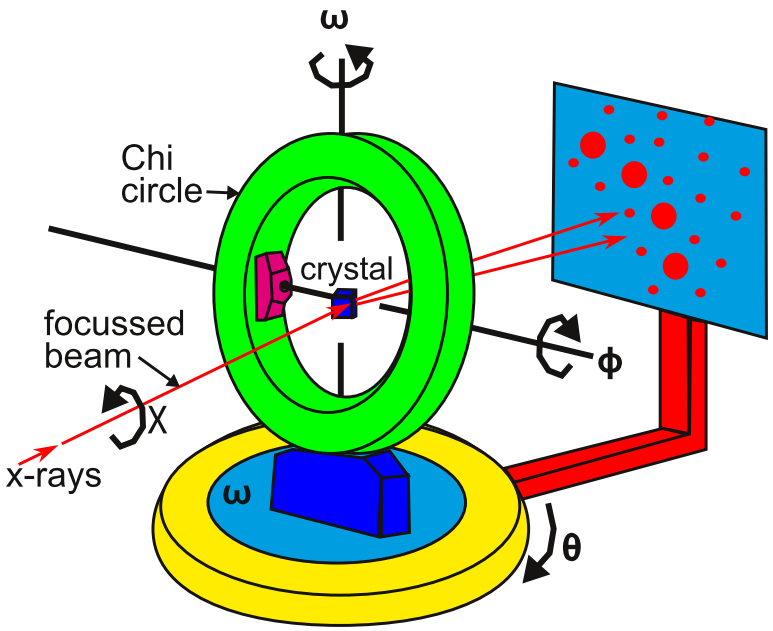

Figure 2.15: 4-circle gonoimeter (Eulerian or Kappa Geometry) [adapted from W. Craig Carter research group - MIT [2009]]. In this geometry the incident beam lies on the same plane as the detector and one of the axes the crystal rotates about.

X-rays, whereas characteristic X-rays are produced as a result of electronic transitions within the atoms of the metal. X-rays which are produced are filtered to a single wavelength, collimated, and sent toward a crystal holder where X-rays are either reflected, refracted or diffracted by the lattice of the crystal of interest.

From Figure 2.10, the difference in path length for X-rays scattered from the top plane of atoms and bottom plane is $2dsin\theta$ (Equation 2.3), if the path difference is equal to one wavelength λ then constructive interference occurs.

The spots recorded on the detector are in reciprocal space, and arise due to reflections from the crystal lattice (each spot represents a lattice plane). To determine the structure of a crystal, intensity and position for each Bragg reflection must be collected by rotating the crystal and detector to bring each reflecting plane to the measuring position so that Bragg's law is satisfied for all possible lattice planes. The crystal orientation is determined by three Eulerian angles (ϕ, χ, ω) which must be reset between measurements of different reflections [Arndt & Willis, 1966].

Whilst running a SC-XRD sample, the first requirement is to determine the unit cell

by collecting preliminary refraction data. As well as determining the primitive unit cell this also calculates the orientation matrix which relates the unit cell to the actual position of the crystal in the beam

Following the determination of the unit cell, the positions of the atoms within this cell are then measured in the main data collection run which collects accurate intensity data for all reflections. A completed run can last a couple of hours to roughly 24 hrs depending on the complexity of the crystal structure and atomic scattering factors.

After data collection, the data must go through certain processing procedures to correct for instrument and sample factors. These typically are included in the software package of the diffractometer. They include a correction for absorption, polarisation correction and extinction correction. Following data processing the phase problem has to be resolved to determine the electron density and crystal structure of the sample. For the spinel samples, existing structure solutions for spinel with similar compositions were used as a template for the initial structural determination. Following determination of the electron density, refinement can take place to attain the best fit between the observed and calculated crystal structures (F(obs) and F(calc)) using the method of least squares fitting. Among parameters that can be changed to give best fit are: site occupancy, the proportions of elements on a specific site, and correcting for anisotropy. Refinement leaves the user with a list of atoms with their relative positions in the unit cell, and the distance to their nearest atomic neighbours. Quality of the fit is evaluated by three factors, R_1, wR_2 and $GooF$ (Equations 2.4, 2.5 and 2.6 respectively):

$$R_1 = \frac{\sum ||F_{obs}| - |F_{calc}||}{\sum |F_{obs}|} \tag{2.4}$$

where F is the structure factor, which is related to the intensity of reflection it describes.

$$wR_2 = R_w(F^2) = \sqrt{\frac{\sum w(F_{obs}^2 - F_{calc}^2)^2}{\sum w(F_{obs}^2)^2}} \tag{2.5}$$

$$GooF = S = \sqrt{\frac{\sum w(F_{obs}^2 - F_{calc}^2)^2}{N_{Ref} - N_{Par}}} \tag{2.6}$$

where N_{Ref} is the number of independent reflections and N_{Par} is the number of parameters.

For a good fit R_1, wR_2 and GooF should be <5%, <12% and 0.9-1.2 respectively, and acceptable values are <7%, <20% and 0.8-1.2.

2.5.5 X-ray Absorption Spectroscopy (XAS)

X-ray absorption spectroscopy (XAS) is a technique which irradiates samples with X-rays of definite energy to investigate local geometry and structure. This technique requires the ability to scan through different energies with finely tunable X-ray beams. Currently the best facilities to produce these X-rays are at synchrotron light sources (shortened to a synchrotron, or light source), which can provide bright, finely tunable X-ray beams.

When X-rays are fired on a sample, some of the X-rays which interact are absorbed by atoms within the sample. This causes the excitation, or release, of a core electron. During an XAS experiment, absorption is quantified by measuring the intensity of the incident beam and comparing that to either the intensity of the transmitted beam, fluorescence beam or the number of Auger electrons produced, over a range of energies for the incoming incident beam.

2.5.5.1 Synchrotron facilities

Synchrotron radiation facilities are large specialist facilities where electrons are accelerated so that they travel close to the speed of light. These electrons are injected into a storage ring where very intense photon beams are produced (X-rays, infra-red and ultraviolet light) as the electron beam direction is modified. In the UK, the national synchrotron facility is the 'Diamond Light Source' (here shortened to DLS) (Figure 2.16), a third generation synchrotron at the Harwell Science and Innovation Campus in Oxfordshire.

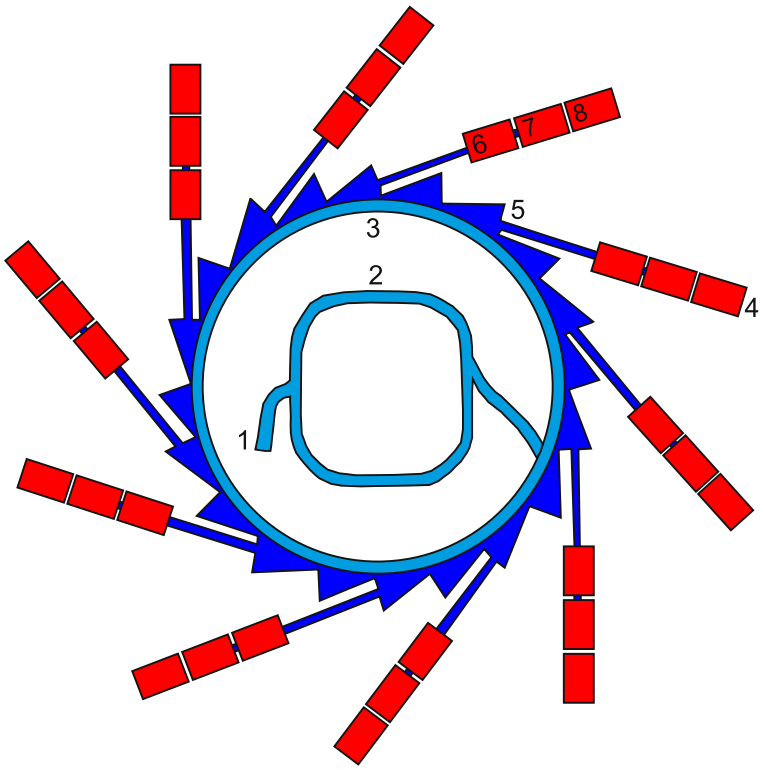

[ht]

Figure 2.16: Birds eye view diagram of the DLS synchrotron. The numbers denote the following parts of the synchrotron: 1-electron gun, 2-booster synchrotron, 3-storage ring, 4-beamline, 5-front end, 6-optics hutch, 7-experimental hutch, 8-control cabin. Adapted from Soden [2010].

Currently there are four generations of synchrotron light sources. The main differences between them are as follows:

1. First generation synchrotrons contain a storage ring and were often originally built for particle physics. As such they lack many of the required devices to 'tune' the X-rays produced from the accelerating electrons.
2. Second generation light sources were intentionally built as X-ray sources but do not have insertion devices needed to produce intense tuneable light.
3. Third generation light sources were designed to have insertion devices which provide an additional source of X-rays in the straight sections of the storage ring, and electrons travel in narrow beams due to better collimators.
4. Fourth generation light sources describe two alternate ways of generating X-rays. Free electron lasers produce extremely intense X-rays which generally damage samples, but are suitable for studying sub-picosecond time-lapses of chemical

reactions. Energy recovery linacs produce intense X-rays without the use of a storage ring.

Figure 2.16 is a bird's eye view of the third generation synchrotron at DLS. Synchrotron light is generated by producing a stream of electrons in an electron gun (1) which are passed through a linear accelerator and booster synchrotron (2) before passing into the main storage ring (3).

Whilst in the storage ring electrons travel a full circuit of the 360° orbital in approximately two millionths of a second whilst maintaining their energy. Synchrotron light is then generated by bending magnets or insertion devices in the storage ring. In these devices (bending magnets, undulators and/or wigglers) synchrotron radiation is generated from electrons spiralling around magnetic field lines at ultrarelativistic speeds (Figure 2.17). Because of the ultrarelativistic speeds, radiation emitted is in a narrow beam of light radiating in the same direction as the electron is moving (a process called beaming) [Willmott, 2011]. The type of emissions depends on the energy of the electron and the strength of the magnetic field. The field strength of bending magnets and electron energy are fixed in the storage ring, so the radiation spectrum produced is fixed. To produce high intensity broad band radiation larger than those achievable by bending magnets, wiggler magnets are used [García-Gutiérrez & Rueda, 2009]. Undulators are a type of wiggler that can produce brighter X-ray light than the bending magnet or standard wiggler [García-Gutiérrez & Rueda, 2009]. Following production of synchrotron light, it is channelled into a beam line (4) via the front end (5).

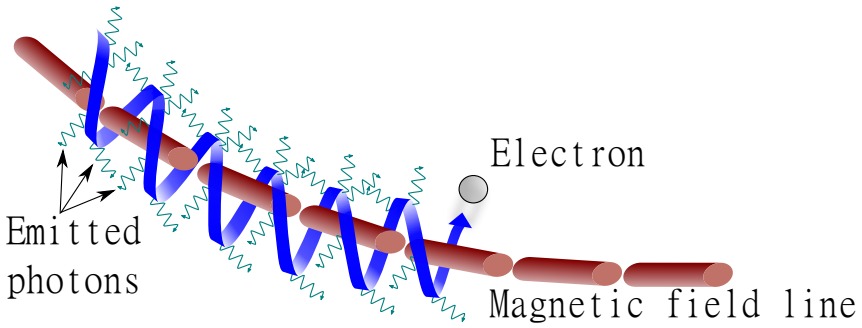

Figure 2.17: Production of synchrotron radiation by electron spiralling around a magnetic field (Adapted from https://imagine.gsfc.nasa.gov/science/toolbox/xray_generation_el.html).

The beam line consists of a series of hutches (enclosed rooms with radiation shielding). The first hutch that the X-rays enter is the optics hutch (6) which consists of mirrors and diffractors which focus the beam. Refined light from the optics hutch passes to the experimental hutch (7) where it interacts with the user's samples in a controlled environment. The experiment is controlled by the user in the final hutch of the beam line, which is known as the control cabin (8). From here they can control the alignment and position of the sample, vary the sample environment, and modify the optics for the beam line. It is from here they control the X-rays entering the beamline and experimental hutch, and acquire data whilst being shielded from the X-rays.

2.5.5.2 Beam line I18

Beam line I18 is a specialist micro focus spectroscopy beam line at DLS which uses high-brightness X-ray beams focused down to a micron spot size to study complex materials, and was used in this study. A schematic of this beam line can be found in Figure 2.18. The function of the various parts are as follows:

(a) An undulator (insertion device), which generates high-brightness synchrotron light.
(b) An aperture and slits to control the size and energy resolution of the beam.
(c) Mirrors (Toroid, HR mirrors and KB focusing mirrors) to tune the beam and remove harmonics.
(d) A monochromator to ensure that only selected X-rays of a particular energy can travel on toward a sample. Rotating the monochromator results in the ability of tuning the X-ray beam to the required energy for the K-edges of elements from P to Mo (2.14-20.00 keV), and the L_3 edges from Sr to Pu (1.94-18.06 keV).

Figure 2.19 displays the geometry of the sample stage to the incoming beam and detector(s) in the experimental hutch. In this figure X-rays from the optics hutch (beamline) enter from the right and strike a sample mounted in the sample holder on the stage in the centre of the image. The stage is recoilless, with mechanical motors inbuilt to centre and focus the sample. The stage also has the ability to rotate to alter the area in

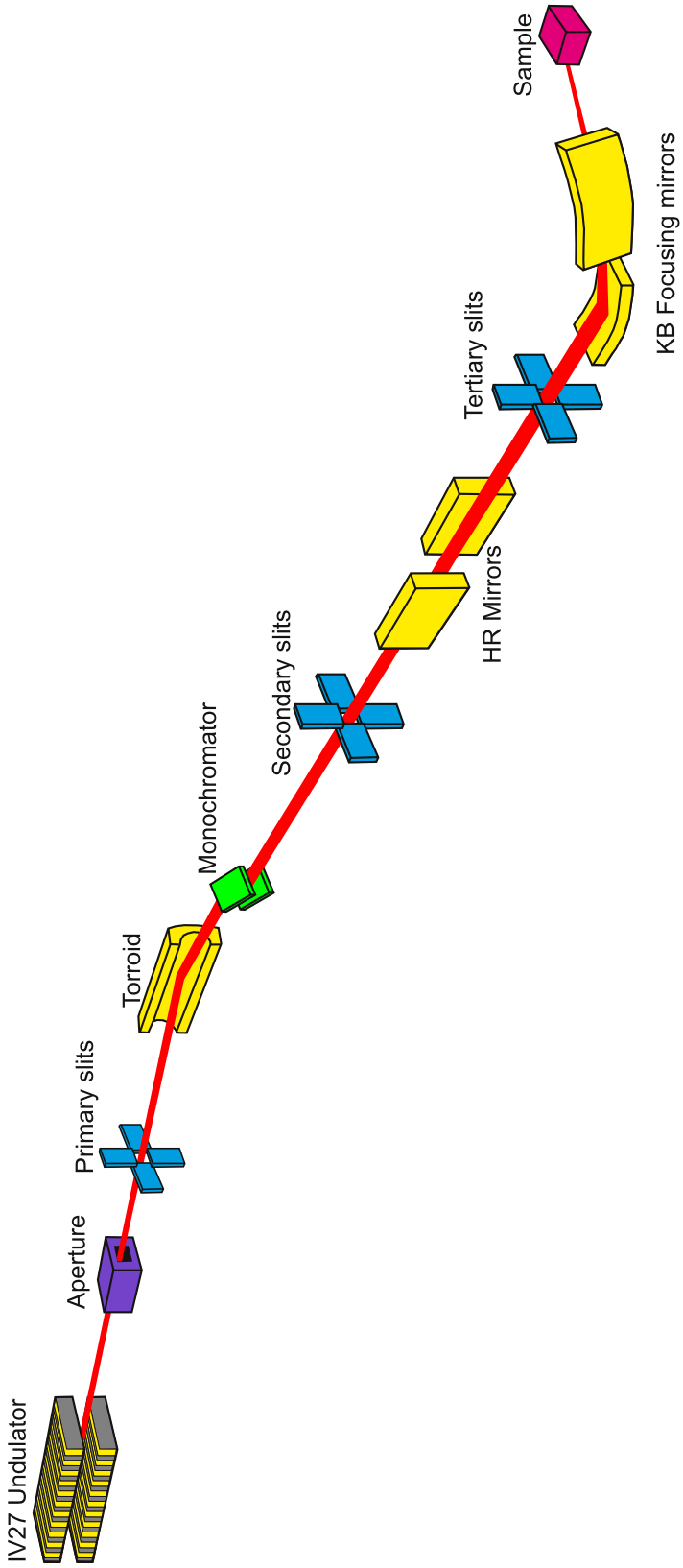

Figure 2.18: Beam line schematic of the I18 spectroscopy beam line at DLS. The beam enters the beamline from the right of the image (Adapted from http://www.diamond.ac.uk/Beamlines/Spectroscopy/I18/Specification.html).

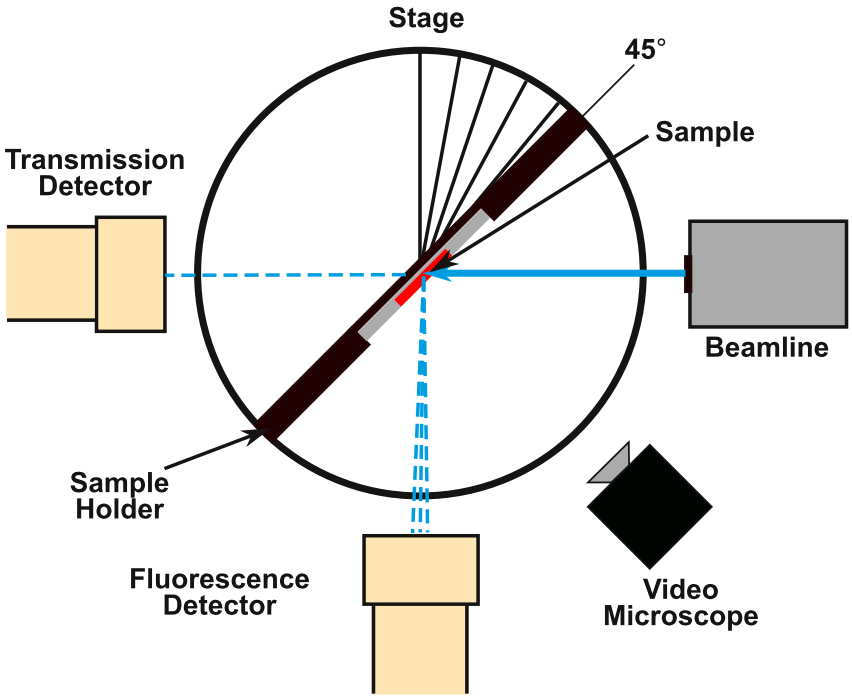

Figure 2.19: Schematic birds eye view of I18 Beam line sample-detector set-up with the stage positioned at 45° to the beam. From Hicks [2015].

which the X-rays interact with the sample. If the sample is thin (a uniform thickness of ≈ 2 absorption lengths is ideal [Calvin, 2013]), some X-rays will reach the transmission detector where the X-rays can be counted; otherwise a fluorescence detector is needed. A video microscope is also attached to the set-up so the user can view and orient the sample with respect to the beam from the control hutch whilst the X-ray beam is on.

2.5.5.3 X-ray absorption spectroscopy theory

Once the absorption of X-rays is measured (by either the fluorescence or transmission detector) over a range of energies, a spectrum is produced. A typical XAS spectrum is shown in Figure 2.21. Several typical features of a XAS spectrum are:

- Small peaks and shoulders found before the main rise in absorption (pre-edge region).
- A sharp rise in absorption called the 'edge' associated with the binding energy of a core level electron (edge).

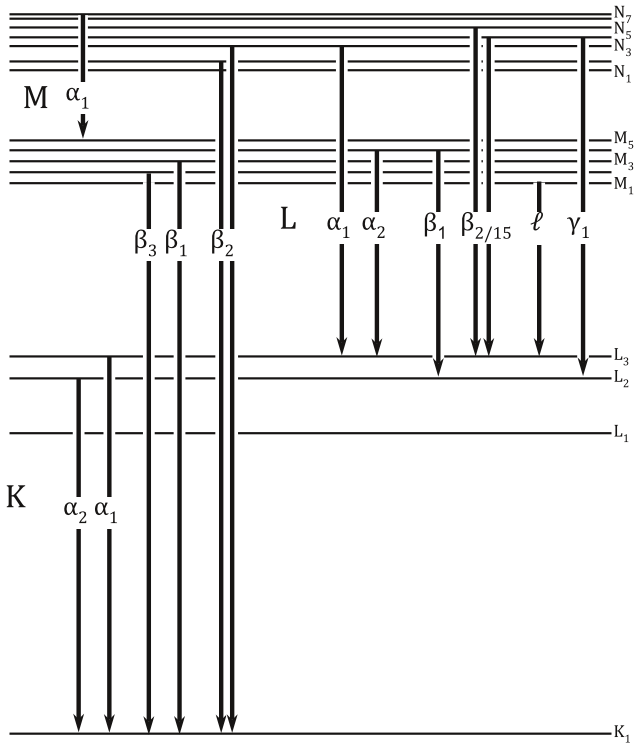

Figure 2.20: Transitions which give rise to specific emission lines.

- Small oscillations following the edge, the amplitude of which decreases with increasing energy away from the edge (post-edge region).

In general, the probability of an atom absorbing photons decreases with increasing photon energy. However a sharp rise (called an edge) is produced when the energy of the photons changes from equalling less than the binding energy of a core electron to equal or higher, this results in a sharp rise in absorption. As the energy of absorption is equal to the binding energy of a core level electron, which is unique to each element, this makes XAS an element selective technique. Excitation of electrons from the n = 1 orbital states (K shell) produce K-edges, n=2 states (L shell) L edges, and n = 3 states (M shell) M edges, etc. Figure 2.20 displays electron transitions between the N, M, L and K shells. Transitions from n=2→1 levels are called K alpha X-rays, from the n=3→1 transitions are K-beta. Transitions from n=3→2 are known as L-alpha, n=4→2 L-beta etc.

The probability that X-rays will be absorbed is given by the absorption coefficient, μ,

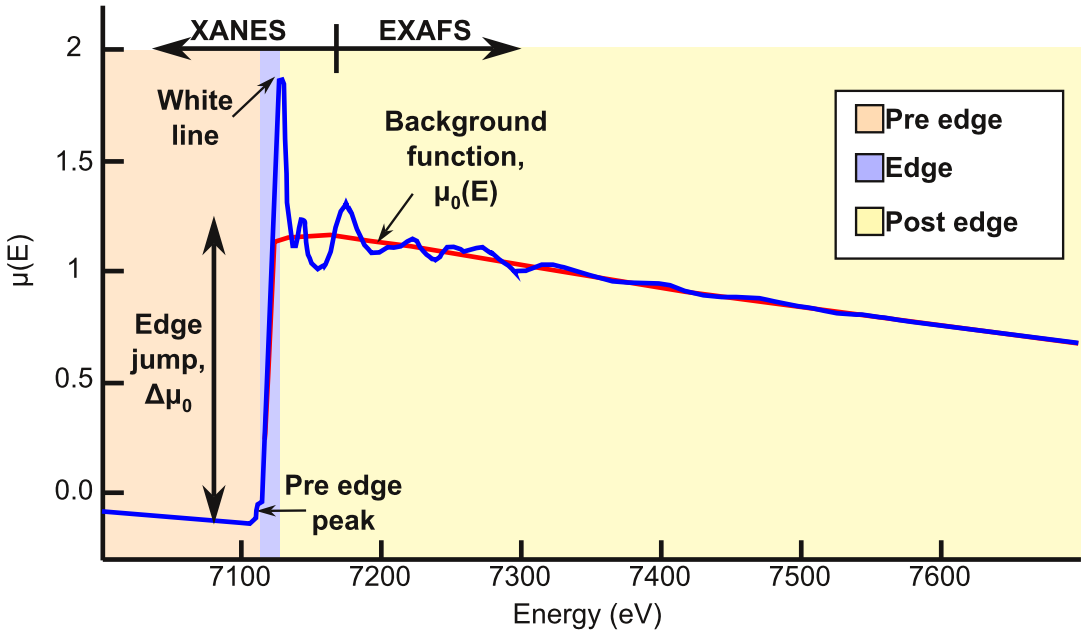

Figure 2.21: XAS spectra of FeO showing the XANES and EXAFS regions as well as the edge jump and a smooth background function which represents the absorption signal from an isolated atom (Adapted from Atominstitut - TU Wien).

which is calculated using Beer's Law:

$$I = I_0 e^{-\mu t} \tag{2.7}$$

where I_0 is the intensity of the incident beam, t the sample thickness, I is the intensity transmitted through the sample and μ is the absorption coefficient (probability X-rays will be absorbed). At most energies μ is dependent on the sample density ρ, atomic number Z, atomic mass A and the X-ray energy E:

$$\mu \approx \frac{\rho Z^4}{AE^3} \tag{2.8}$$

XAS is an element specific technique because it is simply a measure of the energy dependence of μ at and above the binding energy; because X-ray absorption requires unique quantised energies to excite core level electrons, we can select the element probed by tuning the energy of the incident X-ray beam.

The absorption coefficient as a function of energy (μE) for an isolated atom is represented by a smooth background function, with a jump in absorption ($\Delta\mu_0$) at the binding energy of a core level electron E_0 (Figure 2.21), followed by a smooth function of energy above the absorption edge. However, most materials are more complicated than isolated atoms, and due to scattering of the ejected photo electron, μE features oscillations in absorption.

The energy dependence of the absorption coefficient μE, in transmission geometry is:

$$\mu E = log(I_0/I) \tag{2.9}$$

XAS can also be quantified by measuring the intensity of a lower energy X-ray which is given off when a higher level electron drops down to fill a core level electron after absorption. When measuring the absorption coefficient as a function of energy in the fluorescence geometry, this is given by:

$$\mu E \propto I_f/I_0 \tag{2.10}$$

where I_f is the measured intensity of the fluorescence line.

An XAS spectra can be split into two regimes, the near edge structure (XANES) and the extended fine structure (EXAFS). The physics underlying these two regions are the same, although current knowledge allows more quantitative understanding of the extended spectra than is currently possible for the near edge. The XANES region (Figure 2.21) is dominated by the electronic properties and local geometry of the absorbing atom. A XANES spectrum is typically collected from $\sim$ 20 eV to $\sim$ 150 eV above the edge (Figure 2.21) [Henderson et al., 2014], with an appropriate resolution to resolve features in the XANES region, but with a larger step size for the EXAFS region. Signal in the extended region (EXAFS - Figure 2.21) is dominated by the scattering of an emitted electron with the neighbouring atoms and provides information on the local geometric structure around the absorbing atom [Henderson et al., 2014].

The XANES region is, however, sensitive to the oxidation state and molecular geometry (coordination) of the atom on the absorption site. As the oxidation state of the absorbing atom increases, the edge energy also correspondingly increases. This is because the nucleus of an atom with a higher oxidation state has less electron shielding and thus carries a higher effective charge. This requires more X-rays with greater energies to excite core electrons. The formal valence of samples has to be extracted from unknown valence samples by comparison to single valent standards in a similar coordination. A summary of how the pre-edge peaks of the Fe K-edge, and the main edge of Eu/Ce XANES spectra can be used to calculate valence can be found in section 2.5.5.4.2. XANES sensitivity to coordination manifests itself in the intensity and shape of pre-edge structures or in the intensity of transitions associated with the main edge. Pre-edge structures for the first row transition metals arise from the 1s $\rightarrow$ 3d transition, which whilst forbidden, is observed due to 3d + 4p orbital mixing and quadrapolar coupling [Penner-Hahn, 2003].

2.5.5.4 Data processing and analysis

2.5.5.4.1 Data processing

XAS data was processed and analysed in a software suite called Demeter developed by Ravel & Newville [2005]. Athena (Figure 2.22) is the data processing and XANES analysis program in Demeter. Spectra were imported into Athena by selecting the energy and FF/I0 columns from the DLS .dat file. For an ideal fluorescence scan the energy would be proportional to the ratio of I_f (FF) and I_0; however, other factors such as the thickness of the sample and detector set-up affect the proportionality constant. This is why further calibration, alignment and normalisation of the data is needed.

Following data import the first step in processing is to go through the data and deglitch any sharp deviations in measured absorption (arising from instrument effects) by simply removing the point(s) from the data or interpolating a value from the surrounding signal. However if the glitch is too wide or big, then that part of the data cannot be used. Where scans are identical and were measured on the same sample under identical

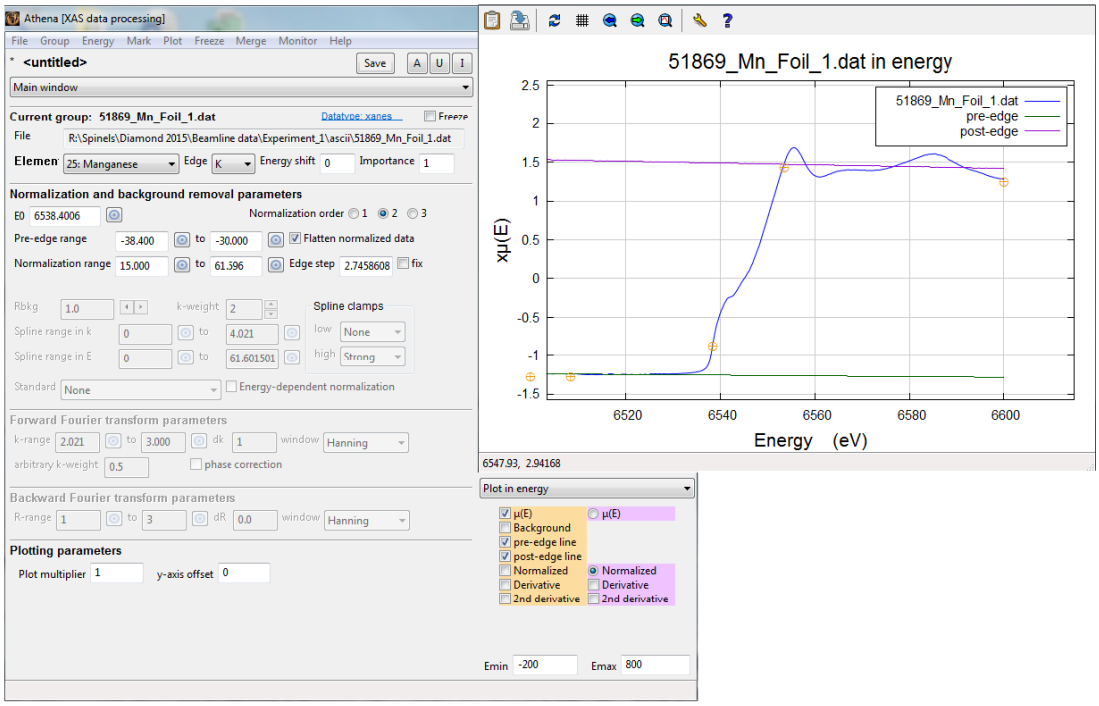

Figure 2.22: Screenshot of the Athena software.
On the left is the window where parameters are changed for normalisation and background fitting of the data, and on the right is a graphical output of the data with the pre-edge and post-edge lines shown in green and purple respectively.

conditions, they can be merged (averaged).

Following basic procedures after data import, the energy of the scans has to be calibrated and aligned to a known reference material. This is why, during the DLS beamtime, reference samples are collected on materials which have tabulated values for energy vs absorption. Mn K-edge scans were calibrated to Mn K-edge reference scans made on a Mn foil standard, and Fe K-edge scans were calibrated using the tabulated position from a Fe foil standard. The tabulated value tends to be the first peak of the first derivative, although, through time and with improved accuracy the tabulated values have changed. However, for comparative purposes, calibration should always be made to the tabulated values in Bearden & Burr [1967].

The next step is to choose the threshold energy (E_0) required to remove a photoelectron from the absorbing atom. The choice of E_0 is almost arbitrary, but some common ways in which it can be defined are:

- The first peak in the first derivative.
- The largest peak in the first derivative.
- At the top of the white line.
- Halfway up the edge.

However, if the spectra collected are noisy it is good procedure to set them all to the same E_0. In this thesis E_0 was set as the largest peak in the first derivative.

There are two more steps needed in order to compare XANES spectra: normalisation and correcting for self absorption. Normalisation is the procedure used to enable comparison of XAS spectra of different samples, whether they be of a standard and unknown, or of a sample and theoretical spectrum. The normalisation procedure basically involves determining the edge jump for a sample and performing an edge step normalisation. The edge jump is a scaling factor which includes sample effects such as the concentration of the absorbing element, effects from sample thickness, and detector effects. When comparing spectra, and for simplicity, all spectra should be scaled to an edge jump of 1. Normalisation of a spectrum is controlled by the values of E_0, the pre-edge range and the normalisation range in Athena (Figure 2.23). The edge step is determine by regressing a line in the pre-edge range and by regressing a polynomial to the normalisation range. These lines are shown as the green and magenta lines in Figure 2.23. The dotted and solid lines show two different attempts to determine the edge jump; both are plausible, and show uncertainty which needs to be carried forward through XANES analysis.

These lines are then extrapolated to E_0, and the pre-edge line E_0 crossing point is subtracted from the post-edge line crossing point to calculate the value of the edge step. Once this has been evaluated the spectrum is shifted so the pre-edge region of the data sits on the y=0 axis. The data is then divided by the edge step, completing the edge step normalisation. In Athena, the normalised data is flattened by default, which has the effect of keeping the post-edge data oscillating around the y=1 line. Flattening is achieved by determining the difference in slope between the pre- and post-edge lines and subtracting this from the data.

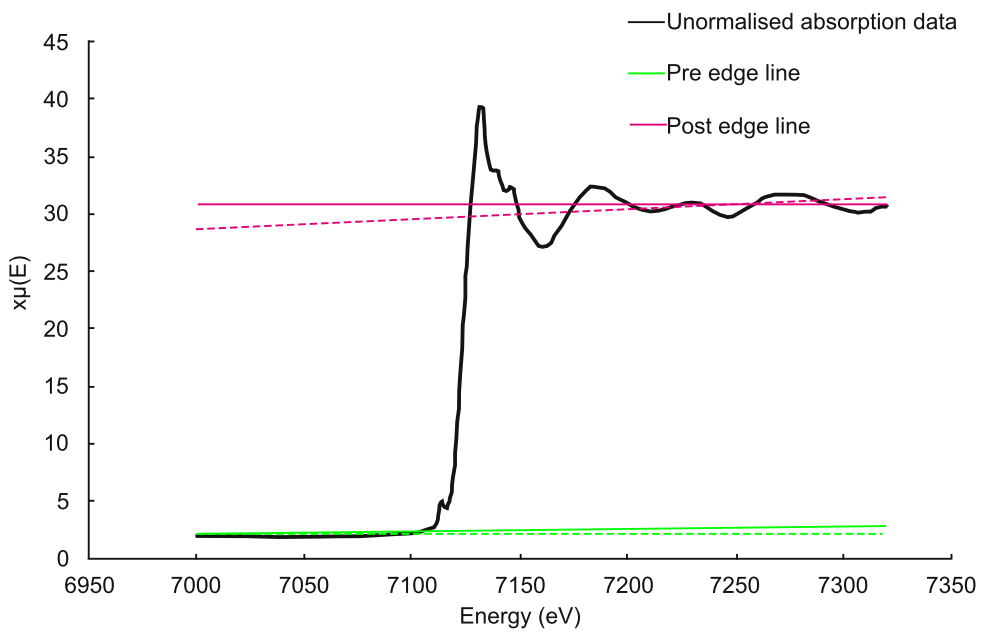

Figure 2.23: Fe K-edge un-normalised absorption spectrum which shows different plausible regression lines for the pre and post-edge regions.

The final correction needed for a XANES spectrum is correcting for a source of distortion in fluorescence measurements, self absorption. These approximate corrections require the measurement geometry to be known as well as the absorption due to other elements in the sample (need to know the sample composition). Inbuilt into the Athena program are four different algorithms to approximate the effect of self absorption. For XANES data the Fluo algorithm is applied [Haskel, 1999]. This requires the formula of the sample to be known as well as the angle of the incoming beam to the sample, the outgoing angle and scan energy.

2.5.5.4.2 Data analysis

Fingerprinting spectral features is a way of analysing XANES data by comparing the spectrum to an empirical standard. Particular features within a normalised absorption scan, or fourier transform, can be correlated to particular structural information about the sample. By identifying common features between sample spectra and empirical standards, semi-quantitative analysis can occur. Often this requires the correlation of a features' position, area or width, which is unique to a standard of known structure, with

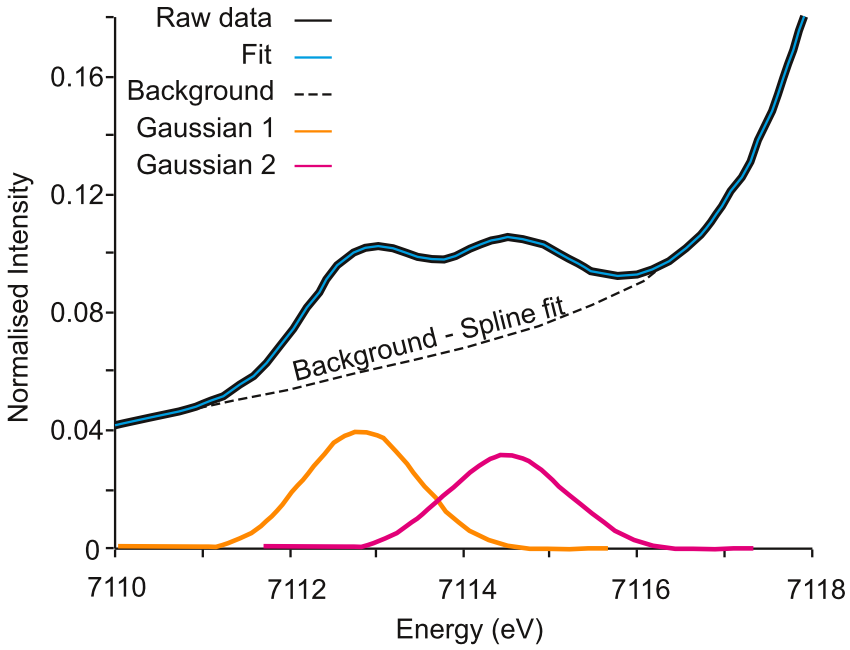

Figure 2.24: An example of fitting two Gaussian peaks to Fe K-edge data following the removal of a background function.

a sample of unknown structure. XANES analysis depends heavily on the availability of empirical standards which have a similar structure to the studied sample. Recently the ability to calculate XANES spectra from structural data has dramatically improved, and theoretical standards can now be used in conjunction with 'real' standards to fingerprint structural and electrical effects from the absorbing atom.

Pre-edge analysis

A common method of analysing the coordination and oxidation state of transitional metals is by comparing the forbidden 1s→3d transition features of the pre-edge with those of empirical standards. The amplitude and position of the pre-edge peak for Mn and Fe K-edge data were used to fingerprint the oxidation state and coordination of these two transitional metals in manganese ferrite and manganese aluminate spinel. One way to compare the standard and sample pre-edge peak data is to fit the pre-edge peak with a mathematical lineshape using Gaussian, Lorentzian, Voigt or Psuedo-Voigt functions.

Also required when fitting the pre-edge peak is the fitting of a quadratic background.

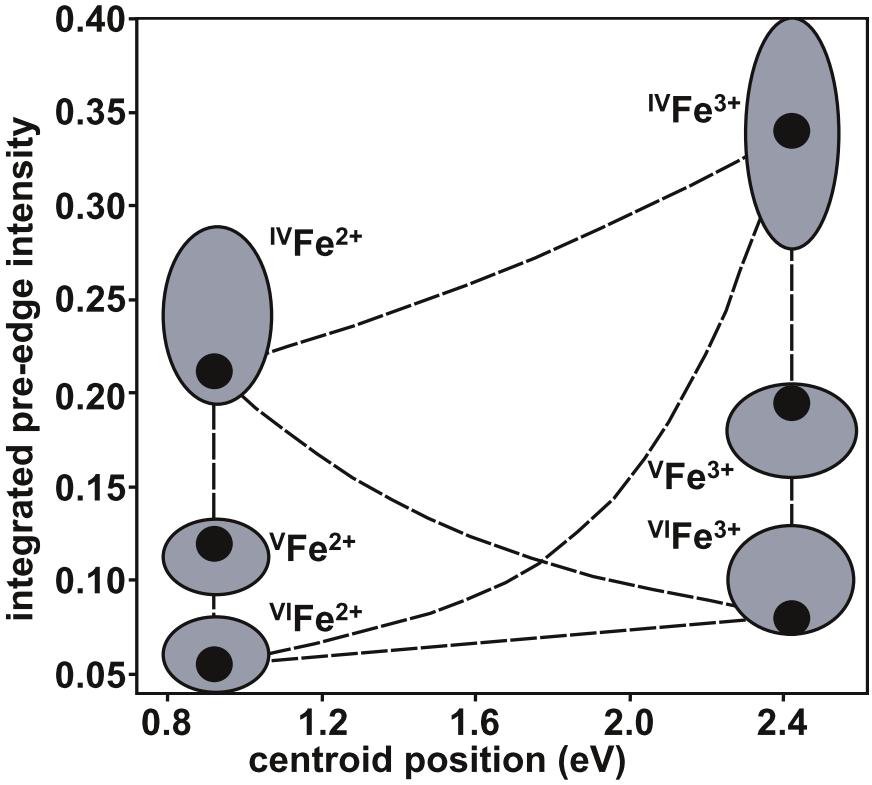

Figure 2.25: The variogram of Wilke et al. [2001] which is used to quantitatively determine the proportions of Fe^{2+} and Fe^{3+} from Fe K edge pre edge peaks in four-, five- and sixfold coordination

Comparing the weight averaged centroid position and total area of unknown samples to that of samples with known oxidation state and coordination can be used to quantitatively/semi-quantitatively determine the coordination and oxidation state of the absorbing atom.

An example of quantitatively determining the oxidation state and coordination of Fe is the variogram by Wilke et al. [2001] (Figure 2.25). This diagram displays the averaged positions of Fe^{2+} and Fe^{3+} standards in four-, five-, and sixfold coordination (Average position - Black circle, range - Grey ovals). The dotted line denotes binary mixes of staurolite, siderite, $FePO_4$ and hematite ($^{IV}Fe^{2+}$, $^{VI}Fe^{2+}$, $^{IV}Fe^{3+}$ and $^{VI}Fe^{3+}$ respectively).

L_{III} edge analysis

For Eu and Ce XANES data, quantitative data was acquired from fitting the entire

edge region. In this region white line peaks (or resonance peaks) are present due to the $2p_{3/2} \rightarrow 5d$ electronic transitions. Subtracting a background allows for the peaks associated with Eu^{2+}/Ce^{3+} and Eu^{3+}/Ce^{4+} to be fitted. It is the relative areas of these peaks which can be used to gain quantitative data about the Ce and Eu oxidation state of an unknown sample. For Ce the Ce^{3+}/Ce^{4+}ratio is equal to the peak area ratio of the resonance peaks in a normalised XANES spectra (white lines), whilst it is unclear whether the transition probabilities (the peak area) is equal for Eu^{2+} and Eu^{3+} [Takahashi et al., 2005].

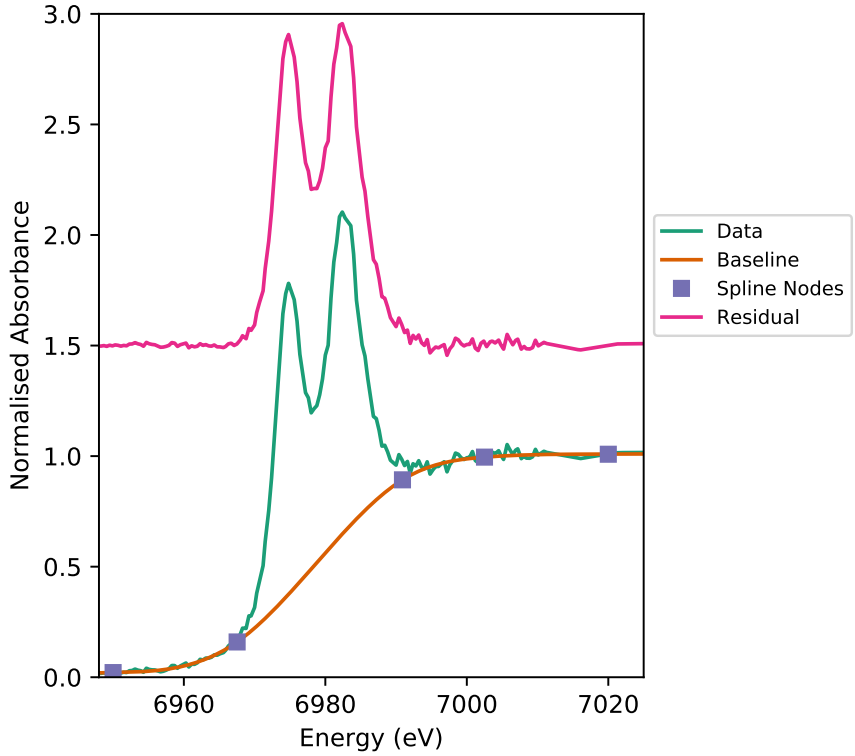

Figure 2.26: Example of a cubic spline fit (with control nodes - squares) for Eu XANES data. The background subtracted data has been y-offset for clarity.

Other techniques for analysing XANES data include principle component analysis, and linear combination fitting (LCF) (also known as linear combination analysis (LCA)).

Linear combination fitting

Linear combination fitting is a technique where XANES data can be interpreted as a mixture of standards. Therefore, for LCF to provide quantitative results, the unknown spectrum must be accurately described as a linear combination of end member stan-

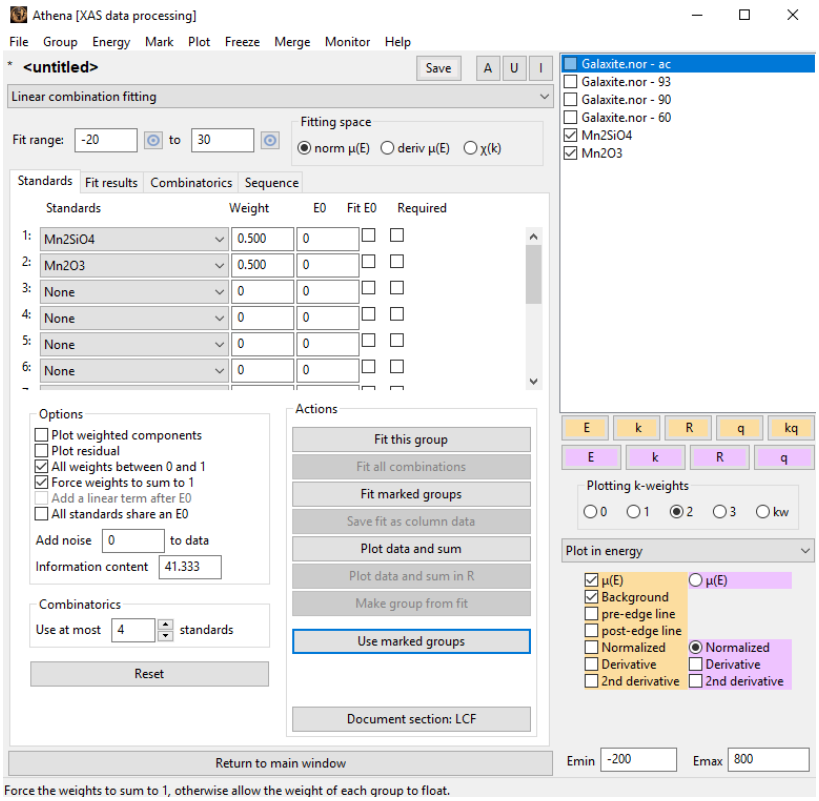

Figure 2.27: Screenshot of the linear combination fitting tool in ATHENA [Ravel & Newville, 2005]

dards. Figure 2.27 shows the linear combination fit option in the ATHENA program.

The LCF option allows one to fit an unknown sample by combining weighted standards to produce a theoretical spectrum which best matches the unknown. The procedure allows for negative loadings, and therefore, when trying to determine aspects such as oxidation state, unphysical negative loadings are often rejected in the regression. There are options of fitting normalised μ(E), derivative μ(E) or χ(k) spectra. Weights of the spectra all sum up to 100% (sum to 1), therefore, for a 3-standard fit, the first two standards have weights a, b and the third standards weight is $1 - a - b$. The weights of a and b are varied in the fitting procedure to produce a theoretical spectrum which best matches the unknown. ATHENA also provides a tool for fitting a large number of different combinations of the standards to the data (combinatorial fitting). ATHENA automatically lists the fitted combinations to the unknown spectrum by R-factor and allows the user to examine graphically and statistically each fit to choose the most appropriate combination of standards.

LCF works well when the unknown is a physical mix of the end member standards. Structural and chemical variability between the standards and unknown introduces uncertainty to the applicability and use of LCF data. Manceau et al. [2012] used LCF to fit mixed valent manganates; their study showed that with a large enough standard set, valence estimates were accurate to 0.04 valence units. The applicability of this method to other structures remains untested, although, the method has been applied to determine the average valence of Mn in Mn-bearing hercynite spinel [Bromiley et al., 2015].

3

Cation distribution and valence in synthetic Al-Mn-O and Fe-Mn-O spinel under varying oxygen fugacity conditions.

"The divisions of science are not like different lines that meet in one angle, but rather like the branches of trees that join in one trunk. ."

– Sir Francis Bacon, *The Works of Francis Bacon*

3.1 Introduction

Oxide minerals of the spinel group (from here on referred to as spinel), as well as being important constituents of the uppermost mantle, are common accessory minerals in both igneous and metamorphic rocks, and commonly occur as detrital grains in sedimentary deposits. Furthermore, spinel are found in a wide range of extra-terrestrial samples with their ubiquity suggesting a role in the formation of the solar system [Roeder, 1994]. Spinel group minerals are useful petrogenetic indicators in terrestrial magmas because they form complex solid solutions which crystallize in a wide range of magmatic compositions (e.g. chapter 1 - equation 1.7). Spinel can be found as both early and late crystallising phases during magma fractionation, and are often the first phase to form [Barnes & Roeder, 2001]. When compared to other high temperature igneous minerals such as olivine, spinel are fairly resistant to chemical and physical alteration [Cookenboo et al., 1997]. Therefore, detrital spinel found in early sedimentary deposits could record conditions (e.g. temperature, redox conditions, and pressure) prevalent in early Earth's history.

Spinel tend to have highly compatible partition coefficients for trace elements in magmatic systems. Consequently, crystallisation of a spinel phase strongly influences the budgets of trace elements. The partitioning of elements between spinel and silicate melts is strongly affected by temperature (T), oxygen fugacity (f_{O_2}) and spinel compo-

sition [Righter et al., 2006], and may also be affected by pressure (P). Spinel geochemistry can, therefore, be used as an important tool in determining fractionation trends of magmas and the trace element budget of primary basaltic magmas [Wijbrans et al., 2015], which gives insight into the source region of these melts in the mantle. The potential of spinel to determine f_{O_2} is important for further understanding magmatic differentiation, mineral assemblages and elemental partitioning [Sato, 1978]. As well as controlling the chemistry of magmas, spinel composition is sensitive to changes in the chemistry of the surrounding magma because of several substituting cations which can subtly change according to the physico-chemical conditions of the parental melt [Arai, 1992].

The complex chemistry of spinel in igneous systems is due to the extensive solid solutions and the extent of cation disorder across different crystallographic sites. Diversity in natural spinel also arises from the valence of the cations found in either the tetrahedral or octahedral sites. Divalent, trivalent, and tetravalent cations can all be accommodated into the spinel structure, and many transitional elements can be present in varying amounts of multiple valences. The general formula of spinel is typically expressed as AB_2O_4, where A and B are different cations. Common cations include Mg, Fe, Al, Zn, Mn, Cr, V, Ga, Ti, and Si. Spinel are also an important mineral group for industrial and technological applications due to their extraordinary catalytic, electrical, optical, and magnetic properties [Carta et al., 2013], which arise from their ability to incorporate many transitional elements into their structure (e.g. Fe, Mo, Zn, Ti, Cr, Mn and V).

Galaxite ($MnAl_2O_4$) and jacobsite ($MnFe_2O_4$) are two Mn spinel end members. In nature, galaxite often forms in carbonate-rich silica under-saturated metamorphosed Mn deposits [Antony et al., 1997]. Jacobsite generally forms as a primary mineral or alteration product in similar metamorphosed Mn deposits [Antony et al., 1997]. The structure of jacobsite, galaxite, and other oxide minerals with a spinel structure (spinel group minerals), consists of oxygen atoms arranged in a cubic close packed (ccp) structure, with cations filling 1/8 of the tetrahedral (T) and 1/2 of the octahedral (M) sites. An excess of metal cations will occupy normally vacant interstitial sites [Fleet,

1981; Henderson et al., 2016]. The typical space group symmetry of spines is $Fd\bar{3}m$. In an ideal '2-3 spinel' structure, divalent cations are housed on the T site, whilst trivalent cations are present on the M site. Spinel group minerals typically display variable degrees of disorder of A and B cations across the T and M sites [Redfern et al., 1999]. The amount of cation disorder can be described using the inversion parameter i, which is defined by the equation:

$$A_{1-i}B_i(A_{\frac{i}{2}}B_{1-\frac{i}{2}})_2O_4 \tag{3.1}$$

When i = 0, a '2-3' spinel is described as completely normal ($^TA^MB_2O_4$), whereas i = 1 describes an 'inverse' configuration ($^TB^M(AB)_2O_4$), and an inversion parameter of 0.67 indicates a completely disordered spinel. In a completely normal spinel, A ions fully occupy the T sites, whilst the M site is filled by B cations. Inverse spinel have half of the B and all the A cations on the M site, whilst the other B cations fully occupy the T sites. At high temperatures, i tends toward complete disorder for all compositions. '4-2' spinel are rarer than '2-3' spinel and have a tetravalent A cation, and divalent B cation [Biagioni & Pasero, 2014].

Jacobsite is a nominally 'normal' Mn^{2+}- Fe^{3+} 2-3 spinel. However, the actual assignment of cation oxidation states is difficult due to (1) the multivalent characteristic of both Mn and Fe, (2) the equilibrium $Mn^{2+} + Fe^{3+} \rightleftharpoons Mn^{3+} + Fe^{2+}$, (3) electron hopping between cation sites [Biagioni & Pasero, 2014], and (4) the similar atomic number of these elements. Fe-Mn spinel are of particular interest to industry because they provide improved performance catalysts in Fischer Tropsh synthesis [Herranz et al., 2006], are used as negative temperature coefficient (NTC) thermistors [Battault et al., 1995], act as contrasting agents in MRI imaging [Lu et al., 2009], and as hyperthermia agents in cancer treatment [Kim et al., 2009]. Galaxite is also a 'normal' spinel, although in this case assignment of Mn oxidation state is simpler due to the significant difference in atomic number between Al and Mn, as well as the single valence state of Al.

Recent work on spinel group minerals within Earth sciences has focused on the devel-

opment of calibrated thermometers, barometers, and oxygen barometers based on the partitioning of redox sensitive trace elements between spinel and melts, for use when conventional methods cannot be used [Arató & Audétat, 2017; Burger et al., 2016; Canil, 1999; Righter et al., 2006]. Manganese is a redox sensitive element which readily substitutes into both the tetrahedral and octahedral crystallographic sites in the spinel structure, and can be present either as Mn^{2+}, Mn^{3+} and/or Mn^{4+}. Mn can also be present in multiple oxidation states on the same or different sites. However, little is known about the behaviour of Mn in the spinel structure as a function of P, T and f_{O_2}, or the extent to which Mn speciation and partitioning into spinel can be used to probe f_{O_2} conditions in magmas.

Although galaxite and jacobsite spinel only occur naturally in metamorphic deposits, Mn is commonly found in major concentrations in igneous spinel. Knowledge from investigating the Mn end members galaxite and jacobsite will provide detail on 1) how Mn behaves with Al and Fe, 2) its preferred crystallographic position, 3) changes to its coordination and oxidation state with f_{O_2}. This will be useful for understanding Mn bearing spinel which have crystallised in igneous systems and could provide useful insights into the f_{O_2} of these systems.

Measuring valance states can be challenging in the simple end member spinel, and is further complicated in the solid solutions. The arrangement of cations in the spinel structure is often investigated using X-ray diffraction (XRD) and neutron diffraction (ND) data. However, this data can be ambiguous in spinel which contain cations with similar scattering properties, and is further complicated by the coupled effects of changes in valence state and ordering. Determining the oxidation state of cations on the T and M sites is also very difficult as most techniques cannot differentiate the valence state of cations. ^{57}Fe Mössbauer spectra provides important data for the valence, coordination, and ordering of Fe cations but fails to distinguish Fe^{3+} and Fe^{2+} above the Verwey transition temperature [Henderson et al., 2016]. Furthermore, Mössbauer cannot always distinguish Fe^{3+} site occupation between M and T sites [Zhang et al., 1998], and is only applicable for cations with a Mössbauer spectrum. X-ray absorption near edge structure (XANES) spectroscopy is a method which is becoming increasingly

common in determining oxidation state and coordination state in geological materials. Another technique to determine the oxidation state and coordination state in geological materials is electron energy loss spectroscopy (EELS). Unlike EELS, XANES is a non-destructive technique which can obtain spectra from samples mounted for optical and electron microscopy. As spinel is an isotropic mineral, XANES spectra can be recorded from any grain without having to account for the effects of crystallographic orientation [Berry et al., 2010].

Here, XANES K-edge data are used to provide averaged site information, which is combined with single crystal X-ray diffraction (SC-XRD) structural refinements and compositional data from electron probe microanalysis (EPMA) to provide an estimate of cation coordination and valence in synthetic jacobsite- and galaxite-like spinel (from here on, referred to as jacobsite and galaxite). This multidisciplinary approach is used to estimate the cation distribution and oxidation state for Al, Mn and Fe across the T and M sites, using previously published cation site preferences. Varying f_{O_2} conditions during synthesis are used to determine the effect of redox on either the amount, valence, or distribution of Al, Mn, and Fe in jacobsite and galaxite to determine the potential of an oxy-geobarometer based on Mn-in-spinel.

3.2 Mineral synthesis

Single crystals of jacobsite and galaxite were synthesized using a similar flux growth method to that of Andreozzi et al. [2001a]. Starting mixtures were prepared from stoichiometric proportions of analytical grade powders (MnO_2, Al_2O_3, and Fe_2O_3) and mixed with anhydrous borax ($Na_2B_4O_7$), the flux compound. The starting material was weighed and homogenized by grinding under acetone in an agate mortar before being placed in a Pt/Au(5%) crucible. This type of crucible was selected due to its low wettability and high resistance to chemical attack at high temperatures under reducing conditions. Experimental runs were performed using a platinum wound vertical tube gas-mixing furnace with Bronkhorst mass flow controllers. Oxide and flux mixes were heated to 1200 ℃ for 1 hour before cooling at 12.5 ℃/hr to the final run temperature of 900 ℃, then held for 24 hours, before being rapidly quenched. Each experiment

(except for Ga60, which was quenched by quickly raising the charge out of the hotspot) was drop quenched into water upon completion of the run. A mixture of CO_2/H_2 gas was used to control the oxygen fugacity conditions during synthesis [Deines et al., 1974], with f_{O_2} values confirmed using an Australian Oxytrol Systems solid zirconia electrolyte oxygen sensor (SIRO2 sensor). Runs JcAC and GaAC were both run with the furnace open to air (Log f_{O_2} (air) = -0.68 for all temperatures, if we assume it is behaving as an ideal gas). Runs suffixed by 93, 90, and 60 indicate the % CO_2 used in the gas mix, and equate to log f_{O_2} = -13.8, -14.2, and -15.8, respectively, at 900 ℃. Recovered experimental charges were washed in warm DI water, and filtered to dissolve the borate glass. Spinel were then mounted in epoxy, ground, and polished using standard diamond solutions for XANES and EPMA analysis. Individual crystals of each sample were selected for high-quality XRD analysis, and examined optically to ensure absence of twinning and inclusions.

3.3 Analytical methods

3.3.1 EPMA

Compositions were determined with a Cameca SX-100 electron microprobe, using an accelerating voltage of 15 keV, a 20 nA beam current with a 2μm effective beam diameter. Primary standards and analysing crystals were as follows: Al (Spinel BL8, TAP, 593.6 cps/nA), Mn (Tephroite, LLIF, 247.4 cps/nA), O (Tephroite, PCO, 46.4 cps/nA), and Fe (Fayalite, LLIF, 300.4 cps/nA). Kα lines were used for all analyses. Sample Ga60 was measured using a JEOL JXA8530F Hyperprobe, at the University of Bristol. Data for this sample was collected with an accelerating voltage of 15keV, a 10 nA beam current, and a 1μm beam diameter. Primary standards and analysing crystals were as follows: Al (B4 Spinel, TAP), Mn (Mn metal, LLIF) and Fe (Fayalite, LLIF). Transects of larger crystals indicate crystals are chemically homogeneous, and unzoned in Fe/Mn/Al/O content. However, for some samples, up to 1.2 wt % standard deviations may suggest some minor compositional variation between crystals from the same run.

3.3.2 X-ray absorption spectroscopy

Mn K-edge and Fe K-edge XANES spectra were collected on beamline I18 at the Diamond Light Source (DLS), Harwell, UK. These spectra were acquired in fluorescence geometry, with samples angled at 80° to the incident beam. A Si(111) double crystal monochromator was used to finely tune the energy of the beam, which was focused on the sample with a spot size of 6μm. Scans were measured over an energy range of 6400–6570 eV for the Mn K-edge and 7000–7320 eV for the Fe K-edge. Step size for Mn XANES scans across the pre-edge peak and main edge region was 0.25 eV. Step size for Fe XANES data was 0.25 eV over the pre-edge peak and 0.3 eV across the edge region. Following data collection, scans were imported into the ATHENA program [Ravel & Newville, 2005] where spectra were deglitched, aligned, merged, and normalized using standard in-built routines. The Fluo algorithm [Haskel, 1999] was applied to correct for self-absorption. A reference foil of Mn and Fe was used for energy calibration of the monochromator, which was applied to all spectra. The Fe K-edge calibration was set to the first inflection point of the reference foil, set at 7112 eV, and corrected to 7110.75 eV [Kraft et al., 1996]. The 7112 eV calibration value is the inbuilt default value in ATHENA [Ravel & Newville, 2005] and is generally the recommended value. Spectra were re-calibrated to 7110.75 eV as this is the most common value used in Fe K-edge pre-edge peak literature in geology, and allows for easier comparison with other work. The Mn K-edge calibration was set to the first inflection point in Mn foil, set at 6539 eV and corrected to 6537.67 eV [Kraft et al., 1996]. The AUTOBK algorithm was used to model and remove the background using a spline fit procedure. Following normalisation data was then exported to the Fityk software [Wojdyr, 2010] where a convex hull spline fit was used to subtract the background from pre-edge peaks, prior to the fitting of Gaussian peaks.

Mn single valence samples were taken to the synchrotron to collect XANES spectra. These samples included: tephroite (Mn_2SiO_4 - Mn^{2+}), rhodonite ($(Mn,Zn)SiO_3$ - Mn^{2+}), manganite ($MnO(OH)$ - Mn^{3+}), bixbyite ($(Mn,Fe)_2O_3$ - Mn^{3+}), and pyrolusite (MnO_2 - Mn^{4+}). These minerals were from the historical Cockburn museum collection

(University of Edinburgh) and following subsequent analysis it was found that many of these minerals were mislabelled/misidentified so only tephroite, bixbyite and pyrolusite were used further.

3.3.3 Single crystal XRD

Crystals of galaxite and jacobsite, observably free of defects and untwinned under a polarized transmitting-light microscope, were selected for single-crystal X-ray diffraction experiments at the Dipartimento Scienze della Terra, Università degli Studi di Milano. A preliminary test on the crystal quality was performed using a KUMA KM4 four-circle diffractometer, equipped with a point-detector and a monochromatized MoKα radiation, by the analysis of the profile of the diffraction peaks; samples with poorer observed crystallinity were discounted. Intensity data were then collected using an Oxford Diffraction Xcalibur diffractometer, equipped with a CCD detector and operating at 50 kV and 40 mA, with monochromatized MoKα radiation. A combination of ω scans, with 1° step and 10 s exposure time per frame, was chosen to maximize the redundancy and data coverage. For all the data collections, the reflection conditions agreed with the space group Fd$\bar{3}$m, as expected for galaxite and jacobsite. Intensity data were then integrated and corrected for Lorentz-polarization and absorption effects (by Gaussian integration based upon the physical description of the crystal) using the CrysAlis software package [Agilent, 2012]. Further details pertaining to the data collection protocols are given in Table 3.1.

The anisotropic structural refinements were performed using the SHELX - 97 software [Sheldrick, 1997], starting from the atomic coordinates of Lucchesi et al. [1997]. Neutral atomic scattering factors for O, Al, Mn, and Fe were taken from the International Tables for Crystallography [Wilson & Prince, 1999]. The site population was modelled with two different protocols for galaxite and jacobsite, respectively, as described below. Secondary isotropic extinction effects were corrected according to the formalism of Larson [1967], as implemented in the SHELXL-97 package [Sheldrick, 1997]. Further details pertaining to the structure refinements are given in Table 3.1.

Table 3.1: Details pertaining to the X-ray single-crystal structure refinements of the galaxite and jacobsite samples.

	GaAC	**Ga93**	**Ga90**	**Ga60**	**JcAC**	**Jc93**	**Jc90**
Crystal size (μm^3)	200 x 170 x 100	190 x 160 x 90	250 x 180 x 120	220 x 180 x 150	260 x 170 x 110	270 x 200 x 130	200 x 120 x 90
Radiation, detector type	MoKα, CCD	MoKα, CCD	MoKα, CCD	MoKα, CCD	MoKα, CCD	MoKα, CCD	MoKα, CCD
Scan type, width (°), time/frame (s)	ω, 1, 10	ω, 1, 10	ω, 1, 10	ω, 1, 10	ω, 1, 10	ω, 1, 10	ω, 1, 10
Temperature (K), Pressure (bar)	293, 1	293, 1	293, 1	293, 1	293, 1	293, 1	293, 1
Reference chemical formula, Z	$MnAl_2O_4$, 8	$MnAl_2O_4$, 8	$MnAl_2O_4$, 8	$MnAl_2O_4$, 8	$MnFe_2O_4$, 8	$MnFe_2O_4$, 8	$MnFe_2O_4$, 8
Space group	Fd$\bar{3}$m	Fd$\bar{3}$m	Fd$\bar{3}$m	Fd$\bar{3}$m	Fd$\bar{3}$m	Fd$\bar{3}$m	Fd$\bar{3}$m
a (Å)	8.3541(2)	8.3610(3)	8.3469(2)	8.2210(16)	8.4957(3)	8.4679(2)	8.5415(8)
θmax (°)	35.57	35.54	35.61	35.450	35.85	35.979	35.61
	-12 $\leq$ h $\leq$ 12	-12 $\leq$ h $\leq$ 12	-13 $\leq$ h $\leq$ 13	-11 $\leq$ h $\leq$ 11	-13 $\leq$ h $\leq$ 13	-13 $\leq$ h $\leq$ 14	-11 $\leq$ h $\leq$ 11
	-12 $\leq$ k $\leq$ 12	-13 $\leq$ k $\leq$ 13	-13 $\leq$ k $\leq$ 13	-13 $\leq$ k $\leq$ 13	-13 $\leq$ k $\leq$ 13	-11 $\leq$ k $\leq$ 10	-13 $\leq$ k $\leq$ 13
	-13 $\leq$ l $\leq$ 13	-11 $\leq$ l $\leq$ 11	-11 $\leq$ l $\leq$ 11	-11 $\leq$ l $\leq$ 11	-11 $\leq$ l $\leq$ 11	-13 $\leq$ l $\leq$ 13	-13 $\leq$ l $\leq$ 13
No. collected reflections	3652	3723	3711	3456	3852	3542	3357
No. unique reflections	85	87	85	82	90	88	79
No. unique refl. with $F_O>4\sigma(F_O)$	82	81	79	82	88	86	75
No. refined parameters	10	10	10	10	10	10	10
Extinction parameter	0.0010(6)	0.0039(6)	0.0013(5)	0.001(1)	0.014(1)	0.0030(5)	0.0075(8)
R_{int}	0.0441	0.0404	0.0288	0.0529	0.0453	0.0667	0.0799
$R_1(F)$ with $F_O>4\sigma(F_O)$	0.0183	0.0146	0.0170	0.0429	0.0144	0.0171	0.0317
wR_2 (F^2)	0.0398	0.0335	0.0331	0.0907	0.0343	0.0371	0.0366
GooF	1.774	1.523	1.550	3.583	1.749	1.719	1.595
Residual ρmax / ρmin (e-/Å^3)	+0.23/-0.28	+0.33/-0.28	+0.26/-0.26	+0.95/-0.80	+0.36/-0.28	+0.36/-0.53	+0.96/-0.59
T (8a), x =1/8							
U_{11} (Å^2)	0.0130(3)	0.0120(2)	0.0119(2)	0.0110(6)	0.0074(3)	0.0060(3)	0.0072(4)
M (16d), x =1/2							
U_{11} (Å^2)	0.0134(2)	0.0121(2)	0.0124(2)	0.0128(6)	0.0071(2)	0.0059(2)	0.0069(3)
U_{12} (Å^2)	-0.0013(1)	-0.0012(1)	-0.0011(1)	0.0001(3)	-0.00101(8)	-0.00095(9)	-0.0007(2)
O (32e)							
x (u)	0.26439(15)	0.26433(13)	0.26432(13)	0.2646(3)	0.26181(14)	0.26151(15)	0.2607(2)
U_{11} (Å^2)	0.0254(6)	0.0250(5)	0.0251(5)	0.0154(10)	0.0136(6)	0.0110(6)	0.0142(8)
U_{12} (Å^2)	-0.0030(4)	-0.0033(4)	-0.0031(4)	0.0001(7)	-0.0009(3)	0.0001(4)	-0.0001(8)
T-O (Å)	2.017(2)	2.018(2)	2.014(2)	1.987(4)	2.013(2)	2.002(2)	2.008(3)
M-O (Å)	1.9757(11)	1.9777(9)	1.9745(9)	1.943(2)	2.029(1)	2.024(1)	2.048(2)

Note: origin fixed at $\bar{3}$m; $R_{int} = \sum [F^2_O - F^2_O(\text{mean})] / \sum [F^2_{obs}]$; $R_1(F) = \sum (|F_O| - |F_C|) / \sum |F_O|$; $wR_2(F^2) = [\sum [w(F^2_O - F^2_C)^2]] / \sum [w(F^2_O)^2]]^{0.5}$; s.o.f. are given in Table 3.3, as refined atomic fraction and as electron content per site $\sum$e-. The anisotropic displacement factor exponent takes the form: $-2\pi^2[(ha^*)^2U_{11} + \ldots + 2hka^*b^*U_{12} + \ldots + 2klb^*c^*U_{23}]$.

3.4 Results

3.4.1 Galaxite

The averaged chemical compositions of the synthetic galaxite samples are summarized in Table 3.2, with Mn valence estimated based on ensuring net neutrality with O^{2-} and Al^{3+}. Samples GaAC, Ga93 and Ga90 all have similar chemical compositions, and are closer in composition to a spinel with 2:1 cations of Mn:Al, than that of end member galaxite with 2 cations of Al to 1 Mn. This means that the average oxidation state of Mn in these 3 samples must exceed 2 valence units (v.u.) to charge balance the O. In contrast, Ga60 has near equal wt. % abundance of Mn and Al and a higher wt. % O than the other samples, with a composition more similar to end member galaxite with 2:1 cations of Al:Mn.

SC-XRD refinements for the galaxite samples (i.e., "GaAC", "Ga93", "Ga90", "Ga60", Table 3.1 and 3.3) were performed using a mixed Al/Mn- scattering curve at the M and T sites. The fraction of Al and Mn at both M and T sites was simultaneously refined. For all the data sets, convergence was rapidly achieved and the variance–covariance matrix did not show any significant correlation between the refined parameters. At the end of all the refinements, the residuals in the difference-Fourier maps of the electron density were less than ± 0.3 e-/Å^3, with agreement factors $R_1(F) < 0.02$ (with $F_O > 4\sigma(F_O)$ and 10 refined parameters, Table 3.1). For the sample "Ga93", which showed a lower crystallinity as deduced based on the profile shape of the Bragg peaks, the residuals were ± 0.9 e-/Å^3, with agreement factors $R_1(F) \sim 0.04$. Atomic positions, site occupancy factors (s.o.f.), displacement parameters and bond distances are also reported in Table 3.1 and 3.3.

XANES Mn K-edge data for the galaxite samples are shown in Fig. 3.1. The spectra for GaAC, 93 and 90 are all remarkably similar with a small peak on the rising edge (6551.5 eV), followed by the white line position at approximately 6557 eV and a slight peak around 6569 eV. In comparison, the Ga60 spectrum has a more intense pre-edge peak at 6539 eV, a much more defined peak on the rising edge and a more defined peak

Table 3.2: Averaged compositions and element totals of jacobsite and galaxite samples determined by electron micrprobe[1].

	Log f_{O_2} (900°)	**Sample**	**Al**	**Mn**	**Fe**	**O**	**Total[2]**	**Formula based on 4 Oxygen**	**Est Mn valence**
	-0.68	GaAC	15.57(71)	51.86(96)	bd	32.83(38)	100.29(37)	$Mn_{1.84}Al_{1.12}O_4$	2.52
	-13.8	Ga93	15.76(37)	52.12(44)	bd	33.24(54)	100.96(38)	$Mn_{1.83}Al_{1.12}O_4$	2.54
	-14.2	Ga90	13.61(96)	54.77(127)	bd	32.01(47)	100.33(31)	$Mn_{1.99}Al_{1.01}O_4$	2.50
	-15.8	Ga60	30.95(30)	31.25(25)	bd	36.65(22)	103.21(47)	$Mn_{0.99}Al_{2.00}O_4$	2.02
Mn^{2+} Al^{3+}	$MnAl_2O_4$	Galaxite[3]	31.21	31.77	bd	37.01	-	$MnAl_2O_4$	
	-0.68	JcAC	bd	3.04(55)	66.93(56)	29.30(16)	99.27(25)	$Mn_{0.12}Fe_{2.62}O_4$	
	-13.8	Jc93	0.78(21)	19.68(84)	51.29(104)	27.07(14)	98.83(16)	$Mn_{0.85}Al_{0.07}Fe_{2.17}O_4$	
	-14.2	Jc90	0.21(8)	32.14(51)	39.20(80)	27.31(49)	98.86(93)	$Mn_{1.37}Al_{0.02}Fe_{1.64}O_4$	
Mn^{2+} Fe^{3+}	$MnFe_2O_4$	Jacobsite[3]	bd	23.82	48.43	27.75	-	$MnFe_2O_4$	

[1] Figures in parentheses are the standard deviations on the last significant figure of the average value, including element totals.
[2] Average of the element totals for all analyses.
[3] Compositions of the ideal end member.

following the main absorption crest (6569 eV). The lower peak position (6551.5 eV) may be associated with the white line peak position of Mn^{2+} whilst the main absorption peak is associated with Mn^{3+}. This suggests both the presence of Mn^{2+} and Mn^{3+} in the galaxite samples. The more intense 1s→3d transition (pre-edge peaks) found in the spectrum for Ga60 suggests a larger proportion of Mn cations on T sites [Chalmin et al., 2009]. XANES spectra for these samples lack any characteristic features in the main edge and pre-edge peak region associated with Mn^{4+}. The edge energy, white line position, and pre-edge centroid energy are all at a lower energy in the galaxite samples than their positions in standards with Mn^{4+} [Chalmin et al., 2009; Farges, 2005; Manceau et al., 2012] so it was assumed that no Mn^{4+} was present, although the presence of minor proportions of Mn^{4+} cannot be dismissed.

Peak fitting of the pre-edge peak for the galaxite samples, following background removal, shows that the 1s→3d transition peak can be modelled using up to two Gaussian peaks. The results of fitting are shown in Table 3.4. The centroid energy for all Galaxite groups are within error of each other, suggesting that the mean valence of Mn in all groups is the same so no f_{O_2} effect. However, as identified from Fig. 3.1, the pre-edge peak intensity varies between samples, suggesting that samples GaAC and Ga93 have the least amount of Mn in tetrahedral coordination and Ga60 has the most.

3.4.2 Jacobsite

The averaged EPMA data for the three jacobsite runs (JcAC, Jc93, and Jc90, Table 3.2) show a decrease in Fe and an increase in Mn under more reducing conditions. Sample JcAC is almost Mn free, and, therefore, is expected to be similar in structure to magnetite (Fe_3O_4). Samples Jc93 and Jc90 are closer in composition to ideal jacobsite, but Jc93 has excess Fe while Jc90 is deficient in Fe compared to the ideal end member.

SC-XRD refinements for the jacobsite samples (JcAC, Jc93, and Jc90) were first performed using a mixed Fe/Mn-scattering curve at the octahedral and tetrahedral sites, while the fraction of Fe and Mn at the M and T sites were simultaneously refined. However, the similar X-ray scattering factors of Fe and Mn led to a severe correlation between the refined Fe/Mn site populations. A different strategy was then adopted,

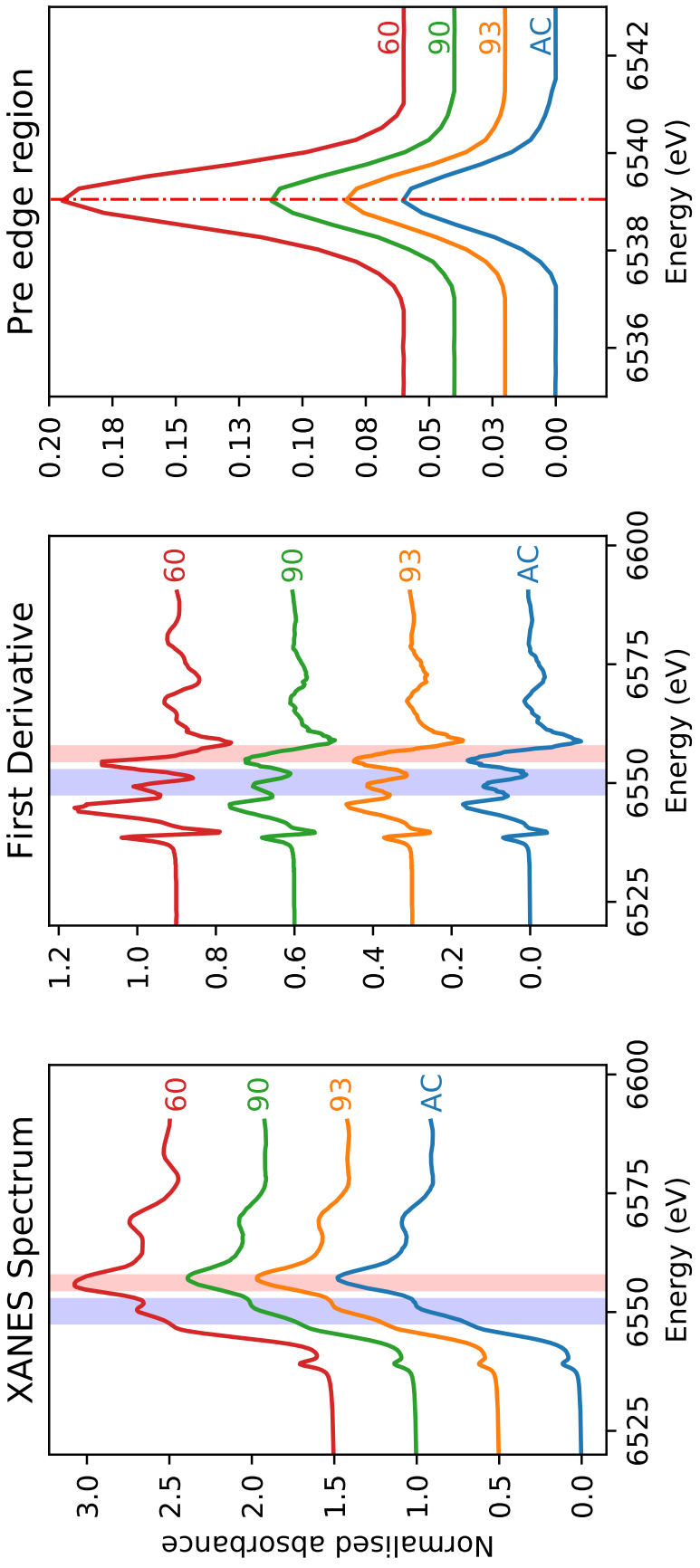

Figure 3.1: Normalized, first derivative and pre edge region Mn K-edge XANES spectra for galaxite samples AC, 93, 90 and 60 (offset vertically for clarity). The blue and red shaded regions indicate the range of white line (WL) positions for Mn^{2+} and Mn^{3+} standards respectively from Manceau et al. [2012].

where site occupancies were modelled using the scattering curve of Fe alone (i.e., the element with the highest scattering factor). The refined partial site occupancy confirms the presence of a lighter element (i.e., Mn), and the refined e- content per site represents the actual (Fe + Mn) contribution (Table 3.3). With this protocol, convergence was rapidly achieved on all the data sets, and the variance–covariance matrix did not show any significant correlation between the refined parameters. The quality of the refinements of the sample "JcAC" ($\pm$0.3 e-/Å^3, $R_1(F) \sim 0.01$) and "Jc93" ($\pm$0.5 e-/Å^3, $R_1(F) \sim 0.02$) was slightly better than that of the sample "Jc90" ($\pm$0.9 e-/Å^3, $R_1(F) \sim 0.03$; Table 3.1). Atomic positions, site occupancy factors, displacement parameters, and bond distances are also reported in Tables 3.1 and 3.3.

Stacked Fe K-edge XANES spectra for jacobsite samples are shown in Fig. 3.2. The absorption edge in Jc90 and Jc93 plots between the edge position of Fe_3O_4 and Fe_2O_3, suggesting the mean oxidation state of iron may be greater than +2.6 in these samples. The K-edge of JcAC is similar to that of Fe_2O_3, suggesting the mean valance state is close to +3, as would be expected.

The number, intensity, and centroid position of Gaussian/pseudo-Voight components which can be fitted to the 1s$\rightarrow$3d and 1s$\rightarrow$4p (quadrupolar and dipolar) electronic transitions that produce the Fe pre-edge feature can be used to extract information on the coordination and average oxidation state of Fe [Waychunas et al., 1983; Westre et al., 1997; Wilke et al., 2001]. By comparing the Fe pre-edge data to mineral standards where Fe is in a single valence, the average valence of iron can be estimated if it is assumed that there is a linear trend between centroid energy and valence state. Using tabulated values for mineral standards from [Wilke et al., 2001], Fe oxidation state has been estimated for the jacobsite samples. However, these are only approximations for the Fe redox state, as when redox state and coordination change at the same time there is a considerable non-linearity with redox and centroid position [Wilke et al., 2001].

Jc90 and Jc93 Fe K-edge pre-edge features can be fitted using two Gaussian functions. The centroid positions for these two functions were close to 7112.2 eV and 7113.2 eV. The JcAC spectrum required fitting using four Gaussian functions, with two around

Table 3.3: SC-XRD refinements for galaxite group data, and refinement which includes cation distribution based on modelling of bond lengths. $\Delta(\sum$e-$_{p.f.u.})$ % is defined as the difference of the total e- number between the structural refinement and the final refinement based on bond length modelling.

Group	Crystal formula based on the structure refinement, with site distributions	General formula based on the structure refinement	Electron distribution per site and total e- number based on the structure refinement
GaAC	$^{T}[Mn_{0.846}Al_{0.154}]^{M}[Al_{0.542}Mn_{0.458}]_2O_4$	$Mn_{1.762(36)}Al_{1.238(36)}O_4$	$\sum$e- $_{p.f.u.}$ = ^{Mn}(44.1(9) e-) + ^{Al}(16.1(4) e-) = 60.2(13) e-
Ga93	$^{T}[Mn_{0.835}Al_{0.165}]^{M}[Al_{0.545}Mn_{0.455}]_2O_4$	$Mn_{1.745(28)}Al_{1.255(28)}O_4$	$\sum$e- $_{p.f.u.}$ = ^{Mn}(43.6(6) e-) + ^{Al}(16.3(3) e-) = 59.9(9) e-
Ga90	$^{T}[Mn_{0.820}Al_{0.180}]^{M}[Al_{0.587}Mn_{0.413}]_2O_4$	$Mn_{1.646(26)}$ $Al_{1.354(26)}O_4$	$\sum$e- $_{p.f.u.}$ = ^{Mn}(41.1(7) e-) + ^{Al}(17.6(3) e-) = 58.7(10) e-
Ga60	$^{T}[Mn_{0.980}Al_{0.020}]^{M}[Al_{0.790}Mn_{0.210}]_2O_4$	$Mn_{1.340(7)}Al_{1.600(7)}O_4$	$\sum$e- $_{p.f.u.}$ = ^{Mn}(33.5(17) e-) + ^{Al}(20.8(9) e-) = 54.3(25) e-
JcAC	$^{T}[Fe_{0.936(12)}]^{M}[Fe_{0.926(11)}]_2O_4$	$^{(T+M)}Fe_{2.788(34)}O_4$	$\sum$e- $_{p.f.u.}$ = 72.5(8) e-
Jc93	$^{T}[Fe_{0.921(11)}]^{M}[Fe_{0.884(10)}]_2O_4$	$^{(T+M)}Fe_{2.689(31)}O_4$	$\sum$e- $_{p.f.u.}$ = 69.9(8) e-
Jc90	$^{T}[Fe_{0.909(11)}]^{M}[Fe_{0.937(10)}]_2O_4$	$^{(T+M)}Fe_{2.783(31)}O_4$	$\sum$e- $_{p.f.u.}$ = 72.4(7) e-

Group	Final refinement based on bond length modelling	Δ ($\sum$ e- $_{p.f.u.}$) %	Est. Average Mn valence
GaAC	$^{T}[Mn^{2+}_{0.846}Al^{3+}_{0.154}]^{M}[Al^{3+}_{0.542}Mn^{2+}_{0.075}Mn^{3+}_{0.383}]_2O_4$	0.06	2.43
Ga93	$^{T}[Mn^{2+}_{0.835}Al^{3+}_{0.165}]^{M}[Al^{3+}_{0.545}Mn^{2+}_{0.080}Mn^{3+}_{0.375}]_2O_4$	0.04	2.43
Ga90	$^{T}[Mn^{2+}_{0.820}Al^{3+}_{0.180}]^{M}[Al^{3+}_{0.587}Mn^{2+}_{0.095}Mn^{3+}_{0.318}]_2O_4$	0.05	2.39
Ga60	$^{T}[Mn^{2+}_{0.800}Mn^{3+}_{0.180}Al^{3+}_{0.020}]^{M}[Al^{3+}_{0.790}Mn^{2+}_{0.100}Mn^{3+}_{0.110}]_2O_4$	1.50	2.18

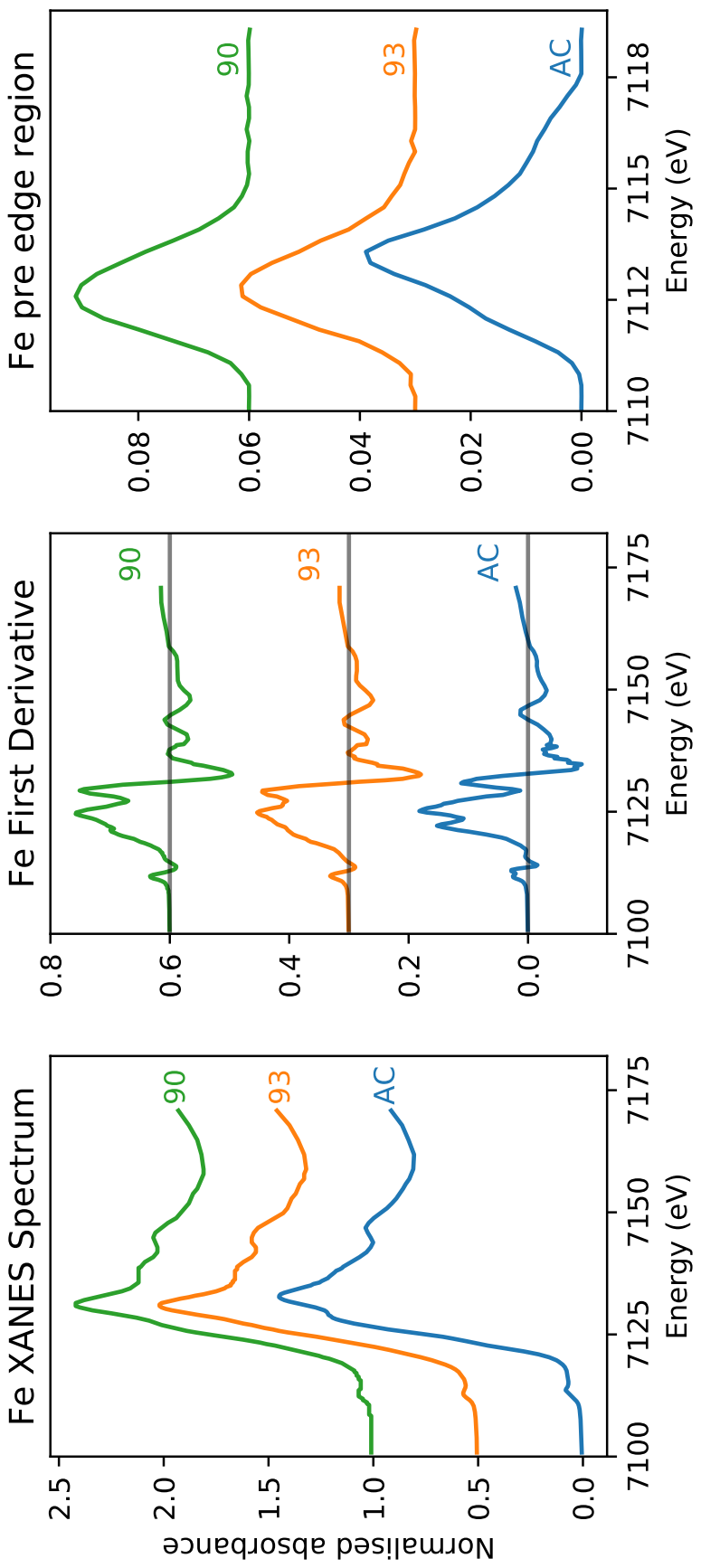

Figure 3.2: Fe K-edge XANES spectra of jacobsite spinel synthesized with: 93%, 90% CO_2 and no gas flow.

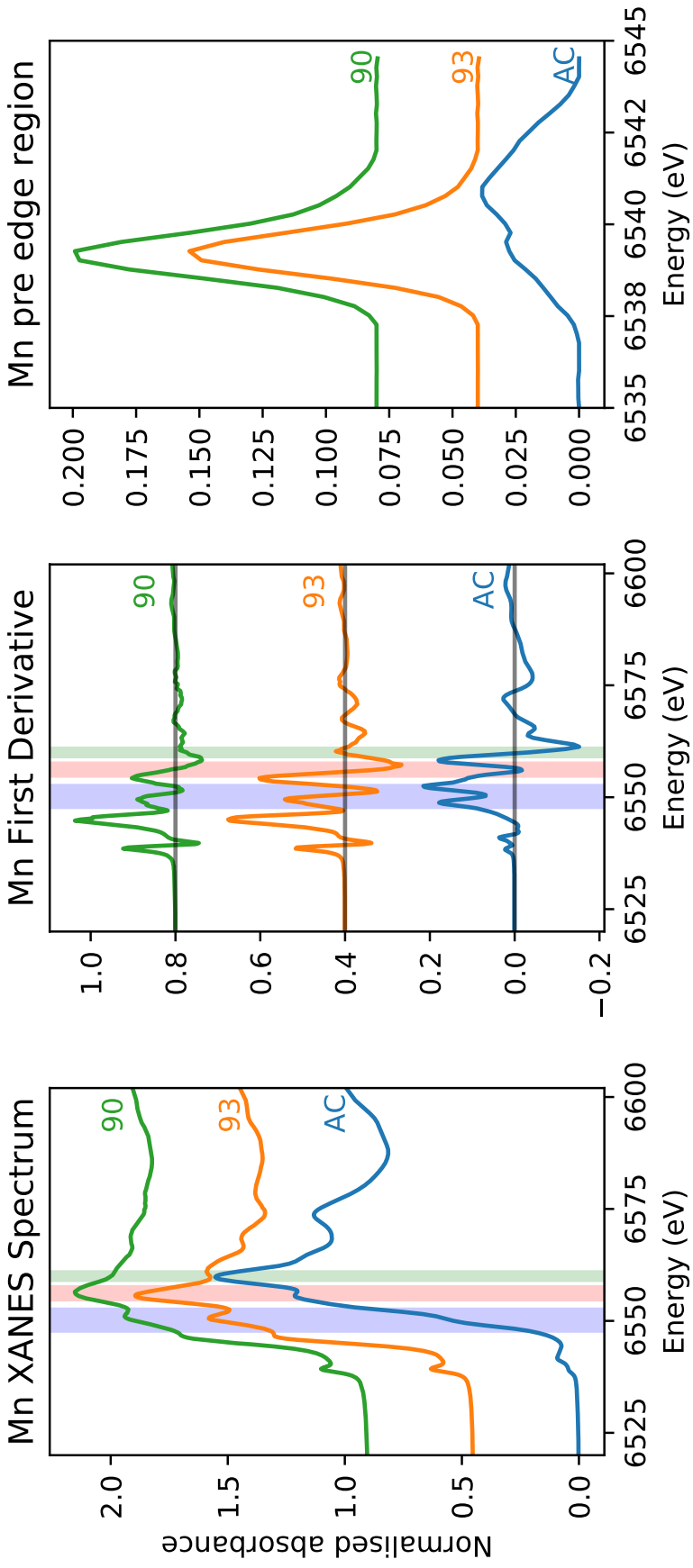

Figure 3.3: Mn K-edge XANES spectra of jacobsite spinel synthesized with: 93%, 90% CO_2 and no gas flow. The blue red, and orange shaded regions indicate the range of white line (WL) positions for Mn^{2+}, Mn^{3+} and Mn^{4+} standards respectively from Manceau et al. [2012].

7113.45 eV and two further peaks with centroid positions greater than 7115 eV, indicating either an environment around Fe which is either tetrahedral or distorted octahedral [Pinakidou et al., 2006] or long-range order around Fe involving 3d orbitals of neighbouring iron atoms [Wilke et al., 2001]. Therefore, the third and fourth peak were excluded from calculating the mean centroid position and total integrated area. The pre-edge averaged centroid position (Table 3.4) was compared to the variation of centroid position with redox ratio of mixtures found in Wilke et al. [2001]. The estimated $Fe^{3+}/\sum Fe$ values were taken for the mixtures of $^{IV}Fe^{2+}/^{VI}Fe^{3+}$which should give the maximum $\%Fe^{3+}$ for a given centroid position. JcAC plots with 98% Fe^{3+}, whilst there is approximately 74% Fe^{3+} in samples Jc93, and 70% Fe^{3+} in Jc90. The integrated pre-edge intensity suggests that sample Jc90 contains greater proportions of Fe on the M site compared to samples Jc93 and JcAC.

Table 3.4: Mn K-edge pre-peak data for galaxite and jacobsite samples, and Fe K-edge data from jacobsite spectra.

	Mn K-edge			**Fe K-edge**		
Sample	**% M**	**Centroid (eV)**	**Area**	**Centroid (eV)**	**Area**	**Est. average valence**
GaAC	52	6539.04	0.089			
Ga93	52	6539.04	0.092			
Ga90	50	6539.05	0.108			
Ga60	31	6539.02	0.216			
JcAC		6539.87	0.230	7113.14	0.090	2.98
Jc93		6539.28	0.210	7112.81	0.060	2.74
Jc90		6539.24	0.190	7112.73	0.068	2.70

The Mn K-edge spectra for the jacobsite samples are shown at the bottom of Fig. 3.3. As with Fe K-edge spectra, samples Jc90 and Jc93 have a similar shape, but different intensities, whereas the JcAC spectrum is shifted towards a higher absorption energy, which suggests Mn in this sample, on average, is in a higher redox state. For samples Jc93 and Jc90 there is a slight peak on the rising edge at approximately 6551 eV, which corresponds with the white line position of Mn^{2+} standards, and a further peak with the greatest intensity at 6557 eV, which may correspond to the white line position of Mn^{3+} standards (found over the energy range 6557-6559 eV). The JcAC samples' white line position appears to correspond to the white line position of Mn^{4+} standards. The pre-edge peak for samples Jc93 and Jc90 can be modelled using three peaks whereas

JcAC has to be modelled using more functions. A triplet is suggestive of Mn^{3+} or Mn^{4+} being present in the 93 and 90 samples [Farges, 2005]. The averaged Mn pre-edge peak centroid position is given in Table 3.4. The intensity of the 1s→3d transition suggests that Jc93 has greater amounts of T coordinated manganese than samples JcAC or Jc90. The energy position of the Mn K-edge for the jacobsite samples suggests that Jc90 and Jc93 consist of a mixture of Mn^{2+} and Mn^{3+}, and its position close to a MnO standard suggests that 2+ dominates in these samples. Whereas, the edge position of JcAC is greater than Jc93 and Jc90, and is close to the edge position of a Mn_2O_3 standard, suggestive of Mn in an oxidation state of 3+, or greater.

3.5 Discussion

The single-crystal X-ray diffraction data of the galaxite and jacobsite samples provide unit-cell constants and u parameters in agreement with those reported in the literature [e.g. Bosi et al., 2007; Essene & Peacor, 1983; Hålenius et al., 2007; Lucchesi et al., 1997]. In this class of minerals, the length of the cell edge and the polyhedral bond distances are geometrically related, which in turn reflects the degree of cation ordering among the T and M sites. The structure refinements converged with a ratio of the displacement parameters of the T, M, and oxygen sites (i.e., U_{eq}(T):U_{eq}(M):U_{eq}(O)], where U_{eq} is the equivalent isotropic atomic displacement parameter and is defined as a third of the trace of the orthogonalized matrix U_{ij}, which describes the anisotropic displacement ellipsoid) comparable to the literature data for these two spinel. Refined Al/Mn-fractions at the M and T sites in galaxite reflect the actual distribution of the two cations. In contrast, the Fe-fraction at the M and T sites in jacobsite is only "virtual" and reflects the electron content per site due to the co-presence of Fe and Mn. The calculated sums of the electron content at the T and M sites on the basis of the multi-element distribution obtained by the X-ray structure refinements and by bond length modelling/EPMA are given in Table 3.3. The parameter $\Delta(\sum e{-}_{p.f.u.})\%$ is defined as the difference of the total e- number (per formula unit) between the values obtained by the X-ray structure refinements and by bond length modelling/EPMA. This parameter provides an assessment of the consistency between the results obtained

by the different experimental methods used here.

3.5.1 Cation distribution in Galaxite

Hålenius et al. [2007] reported a stoichiometric synthetic Mn aluminate ($MnAl_2O_4$) which has a partial inverse spinel structure with an inversion parameter, i = 0.1, with Mn^{2+} strongly ordered on the T site. However, the degree of inversion for other natural and synthetic spinel is likely to be dependent on the method of preparation [Carta et al., 2008; Schreyeck et al., 2001], thermal history [Andreozzi et al., 2000; Ball et al., 2005], as well as the chemical composition of the spinel [Andreozzi et al., 2001b; Carta et al., 2009]. Thermodynamic models of cubic spinel in the Al-Mn-O system suggest that a generalized form for this system is [Chatterjee & Jung, 2014]:

$$^{T}(Mn^{2+}, Al^{3+})^{M}(Mn^{2+}, Mn^{3+}, Mn^{4+}, Al^{3+}, \square)_2O_4 \tag{3.2}$$

whereas, in the case of tetragonal Al-Mn-O spinel, Mn^{2+} and Mn^{3+} can occupy both the T and M sites. Because the galaxite samples only have one multivalent element, and by assuming that Mn^{4+} is not present in these samples, the Mn^{3+}/Mn^{2+} ratio can be calculated from the compositional average point analyses and the SC-XRD data, ensuring net electrical neutrality. Charge balance of the spinel structure can be used in the galaxite samples to determine the proportion of Mn^{2+} and Mn^{3+} cations present in each sample (i.e. the average Mn valence). The distribution of these Mn cations can then be established by ensuring the distribution between the M and T sites simultaneously satisfies the following two parameters: 1. The mean atomic number (m.a.n.) for each site, as defined by:

$$m.a.n._T = \sum\nolimits_i {}^{IV}X_iN_i \tag{3.3}$$

$$m.a.n._M = \sum\nolimits_i {}^{VI}X_iN_i \tag{3.4}$$

where X_i is the fraction of the cation species in the T and M sites, and N_i is their atomic number.

And, 2. The polyhedral bond length, calculated from a linear combination of each cation species cation-oxygen bond distances from end member spinel:

$$T - O = \sum{}_i {}^{IV}X_i {}^{IV}D_i \tag{3.5}$$

$$M - O = \sum{}_i {}^{VI}X_i {}^{VI}D_i \tag{3.6}$$

where ${}^{IV}D_i$ and ${}^{VI}D_i$ is the cation to oxygen bond distance of each cation in the T and M sites, respectively.

The X-ray structure refinement data (Table 3.3) already satisfies equations 3.3 and 3.4, so by applying equations 3.5 and 3.6, the distribution of Mn^{2+} and Mn^{3+} can be determined. The distribution of cations across the T and M sites was calculated using the cation-oxygen bond lengths listed in Table 3.5. Determining cation distribution is made simpler by first assuming that Mn^{3+} cations are found on the M sites, because of the strong preference for Mn^{2+} for the T site [Chatterjee & Jung, 2014]. However, it was found that to model Ga60, considerable amounts of Mn^{3+} were needed on the tetrahedral site (≈0.2 cations p.f.u.) to satisfy the particularly short T-O bond length.

Table 3.5: Effective cation-oxygen bond length for oxide spinels (after Lavina et al. [2002]).

	Al	**Mn^{2+}**	**Mn^{3+}**	**Mn^{4+}**	**Fe^{2+}**	**Fe^{3+}**
T-O bond length (Å)	1.774	2.040	1.880	1.770	1.996	1.891
M-O bond length (Å)	1.909	2.191	2.030	1.910	2.138	2.020

The final structural refinement with cation distribution is given in Table 3.3. When modelling mean T-O and M-O bond lengths, anything less than 0.02 Å was considered an acceptable fit [Lavina et al., 2002]. Calculated M-O bond lengths for the distribution of cations, including oxidation state, are in good agreement with the observed values from the SC-XRD data, giving Δ(M-O) $\leq$ 0.001 Å for all but the Ga60 sample, where

Δ(M-O) = 0.007 Å. However, the presence of a large residual for Δ(T-O) for GaAC, Ga93, and Ga90 T-O bond lengths ($\leq$0.025 Å), when using the 2.04 Å $^{IV}Mn^{2+}$ T-O bond length from Lavina et al. [2002] is unsatisfactory. This difference from the observed and predicted size of the T-O bond, in the galaxite samples, may suggest that a correction function is required. Hålenius et al. [2011], suggests the ^{IV}Mn-O bond length for a fully ordered end-member galaxite is 2.05 Å. Using 2.05 Å for the $^{IV}Mn^{2+}$ T-O bond length lowers the Δ(T-O) residual for GaAC, Ga93 and Ga90 to less than 0.02 Å. It is likely that the large structural relaxation is linked to cation occupancy on the M site, which not only alters the M-O bond length, but also changes the octahedral angle O-M-O, lengthening the tetrahedral distance [Bosi et al., 2011]. Distortion of the octahedral site from cubic to tetragonal symmetry, due to the Jahn-Teller effect, is expected with increasing concentration of Mn^{3+} in 6-fold coordination. However, an overall lowering of the space group from $Fd\bar{3}m$ to $I4_1/amd$ is unlikely unless concentrations of $^{VI}Mn^{3+}$ exceed 1.4 apfu [Lucchesi et al., 1997]. Additional terms have to be added to equation 3.5 to describe the effect that cation speciation on the octahedral site, has on the T-O bond lengths [Lavina et al., 2002].

$$T - O = \sum{}_i = {}^{IV}X_i{}^{IV}D_i + k_1{}^{VI}X_z \tag{3.7}$$

Where the coefficient k1 is added to account for the effect of cation Xz in the M site (where z is an element which alters the O-M-O bond angle).

The inversion parameters for samples GaAC, Ga93, and Ga90 are between 0.154 and 0.18, which is larger than the 0.1 suggested by Hålenius et al. [2007]. In contrast, the inversion parameter for sample Ga60 is closer to 0.2. Whilst both the synthetic spinel in our study and those in Hålenius et al. [2007] were flux grown in a borax flux at a final temperature of 900 ℃, our study cooled at a faster rate (12.5 ℃/hr compared to 4 ℃/hr) from peak T, did not contain a surplus of Al_2O_3 to prevent the formation of trivalent manganese, and were synthesized in more oxidized conditions (with the exception of Ga60). Additionally, whilst our samples were fast quenched in water and air, the quenching technique in Hålenius et al. [2007] only mentions runs were

completed with fast cooling to ambient temperature, hence this quenching technique may not preserve initial cation order (or disorder). These differences in experimental procedures may account for the differing inversion factor and galaxite compositions between our study and [Hålenius et al., 2007].

3.5.2 Determining the oxidation state of Fe and Mn using XANES, EPMA and SC-XRD

Cation distribution and oxidation information from the galaxite samples can be used to compare how satisfactorily existing methods of predicting average valence and coordination from XANES spectra compare. Combining EPMA, XANES, and SC-XRD data for samples where there is a sufficient difference in the scattering factors of the cations (e.g. galaxite spinel) can satisfactorily determine the structure of a spinel. Furthermore, bond length modelling in these types of samples can be used to assign cations across the T and M sites. However, for spinel where there may be significant oxygen deficiency, cation vacancies, and/or where the scattering of the cation ions are too similar, there are too many variables to correctly assign cation valence distributions across the T and M sites (e.g. manganese ferrites).

The SC-XRD data and stoichiometric calculations of the EPMA data result in slightly different crystal compositions (hence different mean oxidation state) for each galaxite sample. EPMA data suggest the mean valence of Mn in the galaxite samples is 2.51, 2.53, 2.50 and 2, respectively, for samples GaAC, Ga93, Ga90 and Ga60. In contrast, the oxidation state of Mn implied by the SC-XRD data (Table 3.3) suggests Mn in samples AC, 93 and 90 have an average valence of ≈2.41, and Ga60 has an average valence of 2.18.

XANES data can be used to determine the oxidation state of Mn and Fe. One common method of determining the average valence and coordination of atoms is by examining the pre-edge peak region of XANES spectra. The pre-edge peak is a manifestation of the 1s→3d transition in transitional metals. Fitting this pre-edge provides what is becoming the preferred technique to obtain quantitative data on cation valence and coordination information from XANES spectra. Other features in XANES spectra

which give an indication of the oxidation state of the absorbing atom are white line position and/or the position of the absorption edge. However, these features are highly sensitive to local environment and long-range ordering, and so, are not suitable to quantitatively determine mean oxidation state or coordination. Charge balance and bond length modelling of the SC-XRD data indicates the likely individual cation charges and coordination in the galaxite samples (Table 3.3). The next step is to identify how well the valence/coordination information from XRD matches that obtained from pre-edge fitting of synchrotron data.

A test of how well Mn K-edge XANES data can be used to determine oxidation state is to compare the centroid position of the pre-edge peak for the galaxite samples (Table 3.4), where mean oxidation state has been estimated by EPMA or SC-XRD, to the pre-edge peak of samples with known oxidation state. To compare this dataset to other published studies, we first assessed how the centroid position and intensity in single valence standards collected during this beamline session and a previous session ([Bromiley et al., 2015]) compared to those in Chalmin et al. [2009]. The centroid position of standards in this study and Chalmin et al. [2009] agreed within ±0.09 eV. However, when comparing the position of the pre-edge peaks for the galaxite samples (where the estimated valence is either 2.41 SC-XRD, or 2.51 EPMA) the centroid position of these samples should be ≈6539.47 eV according to Chalmin et al. [2009], compared to the measured value of 6539.04 eV (discrepancy of 0.43 eV). This questions whether we can use a small set of oxide standards to calculate average valences in oxides of differing composition. This study highlights the current inability to accurately determine the oxidation state/coordination of atoms using the 1s→3d pre-edge peak found on a Mn K-edge XANES spectrum. Part of this difficulty in determining the oxidation state of Mn using the pre-edge peak may be due to the small energy difference in centroid position between Mn^{2+}/ Mn^{3+} (0.35 eV) and Mn^{3+}/ Mn^{4+} (0.55 eV). The way XANES data is processed and fitted may also produce ambiguity in Mn valence.

Pre-edge peak fitting of the Fe K-edge has been successfully in evaluating the $Fe^{3+}/\sum Fe$ ratio in silicate glass [Berry et al., 2003; Cottrell et al., 2009a] using crystal standards. Calculating the average valence of Fe in minerals remains challenging due to the need

to accurately calibrate XANES spectra for each system investigated [Berry et al., 2010]. Factors limiting the use of XANES in determining the oxidation state of multivalent elements in minerals include: the restricted range of Fe^{2+} and Fe^{3+} found in most minerals, the effect of compositional variability and particularly the effect that crystal orientation has on the collected spectra of non isotropic minerals, and the difficulties in background fitting. In many cases, the oxidation state of redox variable elements tends to be quantified by the weak 1s→3d pre-edge, although this edge, and particular spectral backgrounds to pre-edge features, are also sensitive to changes in coordination, site symmetry and composition [Doyle et al., 2016]. Knowing the cation coordination in a sample is vital in determining the oxidation state of an unknown as shown by the variation of centroid position with redox ratio of mixtures found in Wilke et al. [2001]. A suite of well documented Fe spinel may provide the means to explore and quantify further the effects that Fe oxidation state and coordination have on the shape of a XANES spectrum due to the varying ratio of $Fe^{3+}/\sum Fe$ found in many spinel and the different degrees of inversion found in many spinel.

An alternative way to determine Mn redox states from XANES data is linear combination fitting (LCF) of single valence standards with similar structures to the mixed valent sample [Bromiley et al., 2015; Manceau et al., 2012], where the resulting fit indicates the relative proportions of each oxidation state present in the unknown sample (Chapter 2, section 2.5.5.4.1 page 65). Linear combination fitting is reliant on the unknown having the absorbing element in similar coordination to the standard. This is problematic in spinel as Fe and Mn in these samples may exist in two different coordination environments with variable distributions between both sites and these elements may also be present in multiple oxidation states in the same or different sites; therefore, it is unlikely that LCF will give accurate results. Furthermore, it is often difficult to acquire well documented standards where each oxidation state of Mn/Fe is present in all necessary coordination environments. As a first approximation, Mn average valence for the galaxite samples was determined by fitting the spectra with a linear combination fit (LCF) of MnO and Mn_2O_3 spectra in the region between 6520 and 6570 eV. LCF was carried out using the combinatorial LCF tool in the ATHENA program [Ravel &

Newville, 2005]. This tool measures all plausible standard compounds and tries fitting many different combinations of the standards to the data. Fitting was carried out to the normalised μ(E) spectra, and the weighting of the standards was fixed to be 100% of the unknown. LCF resulted in a mean Mn valence of 2.52, 2.51 and 2.55 for samples GaAC, Ga93, and Ga90, respectively, and an average oxidation state of 2.26 for Ga60. These estimated averaged oxidation states are close to those estimated from EPMA (Table 3.2), with the exception of Ga60, and generally higher than those estimated based on SD-XRD data (Table 3.3). Therefore, LCF both estimates higher average Mn valence, and indicates a change in valence in the most reduced sample (Ga60) which is not apparent from other data. LCF of jacobsite samples suggests that the oxidation state of Mn in JcAC is approximately 3+, whilst in Jc93 and Jc90 the oxidation state is 2.3 and 2.4 respectively.

Analysis of the full EXAFS spectrum may be an alternate way to determine site occupancies, although this requires ab inito calculations to produce standards by which sample spectra can be compared. Although EXAFS analysis of jacobsite has been carried out by various groups [Carta et al., 2009; Kodre et al., 2008; Yang et al., 2004] it remains uncertain as to whether this procedure could be used for more complex solid solutions.

3.5.3 Cation distribution in Mn spinel as a function of oxygen fugacity

SC-XRD refinements from individual galaxite crystals suggest a decrease in $^{T}Mn^{2+}$ and $^{M}Mn^{3+}$ with a reduction in oxygen fugacity, whilst Al^{3+} (M site and T site) and Mn^{2+} (M site) increase. These SC-XRD findings are in contrast to the EPMA data which suggest there should be a slight decrease in Al cations p.f.u. with more reduced conditions. The trend difference between these two sets of data may be due in part to EPMA data being measured on multiple crystals whereas SC-XRD data was measured on an individual crystal from a batch, selected based on size and lack of twinning.

EPMA data from jacobsite samples suggests that oxygen fugacity affects partitioning of Mn and Fe between the sodium tetraborate flux and spinel crystals, such that total Mn content in spinel increases, and Fe content decreases, with more reducing conditions.

This contrasts with the log (f_{O_2}) - T diagram from Bonsdorf et al. [1998] which suggests that Fe-rich spinel should dominate under more reduced conditions. The progressive enrichment of Mn-rich spinel with lowering f_{O_2} in this study, compared to Bonsdorf et al. [1998], may highlight an effect of different routes of synthesis. An additional effect of reduction for the jacobsite spinel is a decrease in the estimated valence of Fe from approximately 3+ to ≈2.7+ between samples AC and 93/90. Also, there is a significant lengthening of the M-O bonds between samples AC/93 and 90 which would indicate the replacement of Fe^{3+}/Mn^{3+} with Mn^{2+}/Fe^{2+}(Equation 3.4). Yamanaka & Nakahira [1973] noted that a decrease in f_{O_2} resulted in a decrease in the lattice parameter with f_{O_2}, whereas in this study, the most reduced sample has the largest lattice parameter. Differences between this study and Yamanaka & Nakahira [1973] may be because their experiments were carried out using solid state reactions whereas here mineral composition is not nominally fixed but varies as a function of the behaviour of the borax flux. Unfortunately in this work, the sodium tetraborate flux was washed away during the separation of single crystals, so the composition of the flux, and how it changes with f_{O_2} cannot be assessed. Of particular importance to this work is that in sodium borate glasses, the alkali content can strongly impact the Mn^{3+}/Mn^{2+} ratio [Paul & Lahiri, 1966], which may cause the spinel chemistry to change with melt composition.

The oxygen fugacity for runs Ga93/Jc93 and Ga90/Jc90 equates to IW +2.5 and +2.9 respectively. These values span f_{O_2} ranges which are expected for Martian rocks (e.g. nahklites and chassingnites - Wadhwa [2008], Righter et al. [2016]) as well as primitive composition basaltic rocks found on Earth [Righter et al., 2016]. The coupled variation of Fe and Mn found in the jacobsite samples run at IW +2.5 and +2.9 could have potential for helping to constrain the redox conditions of Martian and terrestrial basalts with further study.

This study suggests that there may be an observable change in the partitioning of Mn between Mn-Fe-O spinel and silicate melt. A recent study by Wijbrans et al. [2015], on the influence of composition and oxygen fugacity on spinel-melt partitioning, found that Mn is slightly incompatible in spinel (compositions ranging from pure $MnAl_2O_4$ spinel

to solid solutions with a hercynite ($FeAl_2O_4$) or Mg-chromite ($MgCr_2O_4$) component). They noted no observable effect on the partitioning of Mn with redox and change in temperature, but did observe a slight compositional effect, with higher partition coefficients for Mn in Fe^{2+}-rich spinel compared to Mg-rich spinel. This further indicates the complex interplay between partitioning behaviour, site occupancy, site distortion, and crystal chemistry in spinel group minerals. As such, although investigation of end-member compositions may provide insight into the distribution and ordering of multi-valent elements in spinel, data cannot readily be applied to modelling the effects of external influences such as f_{O_2} on valence state of Fe, and in particular, Mn.

3.6 Concluding remarks

Mn-Fe bearing spinel may have the potential to determine f_{O_2} conditions for the parental melt from which they formed, by recording the effects of f_{O_2} on element distribution (partitioning and site ordering). This may be due to lengthening of the M-O bond length in sample Jc90 which may result from a change in the cation oxidation state or species on the M site under more reducing f_{O_2}. However, decoupling the effects of temperature and oxygen fugacity on $^{T}Fe^{3+}$-$^{T}Mn^{2+}$exchange in jacobsite spinel is non-trivial. Furthermore, determining the mean oxidation state and coordination environment of Fe and Mn in spinel using XANES remains challenging if both the oxidation state and coordination of the absorbing atom changes between samples and standards. Additional insight into spinel crystal chemistry can be provided by comparing results of compositional analyses, XANES and SC-XRD refinements, although difficulties in modelling Mn XANES spectra mean that this approach is better suited to constraining the crystal chemistry of end-member compositions, rather than complex, naturally occurring spinel. In contrast to jacobsite, Mn content in galaxite spinel shows little, or no change with varying oxidation conditions of synthesis, implying that element partitioning in spinel is compositionally and structurally dependent. This indicates that variation in Mn valence in spinel is largely driven by changes in Fe valence, presumably via the exchange $Mn^{2+} + Fe^{3+} \rightleftharpoons Mn^{3+} + Fe^{2+}$.

The reason for non-stoichiometry in the samples remains unclear. Only the most re-

duced galaxite sample is close to stoichiometric, with more oxidized samples Al-deficient and Mn-rich. Unlike the findings of [Bosi et al., 2007] on Mg-Mn-Al spinel, we see no increase in trivalent Mn on the T site with more oxidized conditions based on bond length modelling (Table 3.3). XANES data indicate that valence of Mn is substantially higher than 2 in the oxidized samples. This might be explained by the observed relative partitioning of Mn^{2+} onto the T site; Mn^{3+} is more readily incorporated onto the M site, where it competes with Al^{3+}. As a consequence, more oxidized samples are more Mn-rich. In Ga60, more reducing conditions favour Mn^{2+}, and therefore, galaxite compositions are close to stoichiometric. SC-XRD data are consistent with an increase in the proportion of ^{T}Mn in Ga60, although a substantial change in average Mn valence is not observed in XANES data; in fact, it is likely that XANES data do not reveal any change in Mn valence across the galaxite samples.

Redox conditions used during synthesis imply JcAC crystals should contain only Fe^{3+} consistent with XANES data, and that Fe should be mixed valence in Jc93 and Jc90. Trends in determined Fe average valence are consistent with imposed f_{O_2} conditions. According to the exchange $Mn^{2+} + Fe^{3+} \rightleftharpoons Mn^{3+} + Fe^{2+}$, increase in proportion of Fe^{2+} should result in an increase in the proportion of Mn^{3+}. However, between samples Jc93 and Jc90 there is no obvious change in the Mn K-edge spectra suggestive of an increase in Mn valence. Decrease in f_{O_2} for jacobsite samples results in an increase in Mn contents and decrease in Fe contents. In contrast to galaxite, stoichiometric jacobsite appears to form at intermediate f_{O_2} conditions. Again, it is unclear what the driving force for this compositional change might be. However, it is logical that stoichiometric jacobsite is stable under intermediate redox conditions, as it nominally contains Mn^{2+} and Fe^{3+}. Under more reducing conditions, the average valence of Fe decreases. Partially disordered jacobsite can form a partial solid solution series with magnetite, $Fe^{2+}Fe_2^{3+}O_4$, which has an inverse spinel structure. As such, the 3+ Fe is expected to readily substitute onto the T site in jacobsite. The observed preference for Mn^{2+} to be incorporated onto the T site in spinel would, in combination with the ability for Fe to be incorporated onto either site, explain why jacobsite samples here are non-stoichiometric and Fe-rich. Under the most reduced conditions under which

jacobsite is stable (i.e. Jc90), crystals become in turn non-stoichiometric and Mn-rich. This might again relate to an increase in proportion of Mn^{2+} although this remains unsupported by XANES data.

Combining XANES and SC-XRD data can be used to create a new series of mixed valent and mixed coordination standards for further studies. Future standards could include spinel such as galaxite where there is less ambiguity in the final refined structure than jacobsite. For jacobsite, the similar scattering of Fe and Mn makes correct valence and coordination assignment much more difficult without additional data such as Mössbauer or neutron diffraction data. Additionally, the relationship between composition, site occupancy and Fe and Mn valence in spinel is complex and interdependent. As such, development of an oxy-barometer based on spinel crystal chemistry is non-trivial.

The next chapter will explore whether the mineral apatite can be used to determine f_{O_2}. Apatite is another common accessory mineral, but unlike spinel, apatite is Mn rich but Fe poor, so would circumvent many of the problems identified for the jacobsite samples. Work in this chapter has shown that Mn XANES and EPMA data can be combined to model Mn valence, and many of the techniques identified here will be carried into the apatite work.

4

The effect of melt composition and oxygen fugacity on manganese partitioning between apatite and silicate melt

"If I have seen further it is by standing on the shoulders of Giants."

– Isaac Newton, *The Correspondence Of Isaac Newton*

4.1 Introduction

Apatite [$Ca_5(PO_4)_3$(F,Cl,OH)] is an accessory mineral found in most igneous, metamorphic, and sedimentary rocks. The three primary apatite end-members (fluor-, chlor- and hydroxyapatite) relate to the three anion end members of apatite (F, Cl and OH respectively). The incorporation of these volatiles as major constituents in the apatite crystal structure make it a critical mineral for understanding melt volatile contents in terrestrial [Douce et al., 2006; Scott et al., 2015] and extra-terrestrial systems [Gross et al., 2013; McCubbin et al., 2016]. Apatite is also an important tool for exploring the trace element budgets of magmas [Nagasawa, 1970; Sha & Chappell, 1999], as its robust crystallographic structure allows for the incorporation of more than half the stable elements [Hughes, 2015]. Recent work [Konecke et al., 2017; Miles et al., 2014] has also suggested that the substitution of redox sensitive elements (e.g. Mn, S, Ce, Eu) into apatite could be used to constrain the oxygen fugacity (f_{O_2}) of the melt from which it has crystallized.

Oxygen fugacity is an important parameter within igneous systems, because, among other things, it controls mineral stabilities [Hensen, 1986; Toplis & Carroll, 1995], dictates volcanic gas composition [Moussallam et al., 2016; Wallace & Carmichael, 1992], and has implications on the metallogenesis of primary igneous ore bodies [Fleet et al., 1991]. Furthermore, estimates of f_{O_2} are used in modelling geophysical processes in the mantle [e.g. creep, electrical conductivity; Dai & Karato, 2014; Ryerson et al., 1989;

Wood & Nell, 1991] and understanding the timing of planetary scale processes, such as the oxidation of the mantle and atmosphere [Scaillet & Gaillard, 2011]. Oxygen fugacity is also an important variable when constraining the composition of the earth's core [Li & Agee, 2001] and early continental crust [Yang et al., 2014], as well as for the timing of the onset of plate tectonics [Brounce et al., 2015]. Despite the importance of f_{O_2} it remains one of the most difficult geological parameters to accurately constrain. As such, any dependence of chemical substitutions in apatite on f_{O_2} would be invaluable in constraining planetary processes.

Manganese in apatite is a minor element that can substitute for more than 1 atom per formula unit (a.p.f.u.) in the Ca2 and P sites [Deer et al., 2013; Hughes et al., 2004]. Several studies have indicated that while partitioning of Mn between apatite and silicate melt is sensitive to f_{O_2}, it is also dependent on parameters such as melt SiO_2 and total alkali content, as well as melt structure [Belousova et al., 2001; Chu et al., 2009; Miles et al., 2014; Sha & Chappell, 1999]. This work, therefore, aims to test the sensitivity of Mn partitioning between apatite and melt to f_{O_2} for a variety of silicate melt compositions, to assess its viability as an oxybarometer.

Additional work is included on the oxidation state and structural position of Fe and Mn in silicate melt as a function of f_{O_2}. The melt structure of silicate glass affects melt properties such as viscosity, density, refractive index, and mineral-melt partition coefficients. Melt structure can be controlled by the presence of various transitional elements (Fe, Ti, V, Co, etc.) which has led to renewed interest in their structural role. Fe is the dominant transitional element in nature and hence its' structural role strongly controls melt structure in natural magmas. Manganese is the third most abundant transitional metal in the the Earth's crust and accounts for 1000-2500 ppm in magmas [Mysen & Richet, 2005], yet little is known about the structural role of Mn in silicate melts. Manganese can be present in multiple oxidation states in geologic materials, although the variability of Mn^{5+}:Mn^{4+}:Mn^{3+}:Mn^{2+} in silicate magmas as a function of f_{O_2}/T conditions has not been thoroughly investigated. However, for natural silicate melt, divalent manganese is thought to dominate, even under relatively oxidising conditions [Watson, 1977]. Therefore, another objective of this study is to

conclusively determine if Mn^{3+} can be present at reduced conditions. Understanding how the valence states of Mn vary as a function of f_{O_2} is important in understanding the partitioning of Mn into apatite as a function of this parameter. An additional aim of this study is to investigate the structural position of Mn in glass and whether this also changes with the f_{O_2} of the quenched melt.

4.2 Experimental rationale

I initially set out to test the conclusion of Miles et al. [2014] that the Mn content of apatite, from a range of intermediate to silicic rocks, can be directly related to f_{O_2} via the empirical relationship:

$$log f_{O_2} = -0.0022(\pm 0.0003)\ \mathrm{Mn}(ppm) - 9.75(\pm 0.46) \tag{4.1}$$

This dependence implies that variations in f_{O_2} influences Mn apatite-melt partitioning because of a change in the relative proportions of Mn oxidation states in the melt (Mn can be found in the 2+, 3+, 4+, and 5+ oxidation states in nature, although is dominantly found as Mn^{2+} in melts [Watson, 1977]). In apatite, Mn^{2+} displays a similar ionic radius to Ca^{2+} (1.06 Å for the Ca2 site and 1.18 Å for the Ca1 site) in 7-fold (0.9 Å) and 9-fold (1 Å) coordination, whilst Mn^{3+} has a smaller ionic radius (0.72-0.67 Å; Miles et al. 2014); hence Mn^{2+} should preferentially partition into apatite from the melt compared to Mn^{3+}. To test this, an experimental calibration of changes in Mn oxidation states in apatite and silicate melt of varying compositions as a function of f_{O_2}, and how this impacts apatite-melt partitioning is required. Apatite from the three end-member compositions, in bulk compositions ranging from low to high silica covering a typical geological rock range, were chosen so that any effects of crystal chemistry and melt composition could be considered when addressing the suitability of a Mn-in-apatite oxybarometer.

Compositions PM1, Hap10 and Hap5 were based on the haplogranitic glasses from [Holtz et al., 1992]. This composition was originally chosen to grow apatite in a Fe

free system which has existing phase constraints and also has similar Si content to the zones of the Criffel Pluton. Difficulties in consistently growing large apatite in the PM1, Hap10 and Hap5 compositions led to the use of composition BMT2, a variant of the BM composition in Riker et al. [2018]. This composition has been used by Riker et al. [2018] to grow large apatite in equilibrium with silicate melt at similar temperature and pressures. The SH3 composition was chosen as a lower SiO_2 composition from Prowatke & Klemme [2006]. Again, this composition was chosen due to the advantage of existing phase equilibrium constraints, the ability to grow large apatite crystals at similar temperatures and pressures, and it allows the examination of Mn partitioning in a simplified Fe-free system.

4.3 Starting materials

Starting materials consisted of mixtures of high-purity analytical oxide (SiO_2, Al_2O_3, TiO_2, MgO, Fe_2O_3, MnO_2) and carbonate ($CaCO_3$, Na_2CO_3, and K_2CO_3) powders. Before use powders were fired and then stored in a 110 ℃ oven. The starting compositions were ground under acetone, using an agate mortar and pestle for thirty minutes, to ensure homogeneity. Powders were then loaded in a box furnace and decarbonated using a controlled heating program, which slowly ramped the temperature from 600-1000 ℃ over 6 hrs. Although this time should be adequate for full decarbonation, no check was carried out to ensure the powder was fully decarbonated. Following the decarbonation procedure, an apatite component, which consisted of tri-calcium phosphate (TCP- $Ca_3(PO_4)_2$) and either CaF_2 or $CaCl_2$ was added to the starting material, and the mixture was reground for a further thirty minutes under acetone.

At this stage, water (1.5 wt. % H_2O) was also added to the SH3 and BMT2 starting compositions in the form of gibbsite ($Al(OH)_3$) or brucite ($Mg(OH)_2$). The different piston cylinder bulk starting compositions used in this study can be found in Table 4.1. The compositions in Table 4.1 exclude the apatite component but include the water content and Al_2O_3/MgO added in the form of gibbsite and brucite respectively. Note PM1 and Hap10 were intended to be iterations of the same target starting composition, but had to be made at different times. Slight differences in the amount of weighed pow-

Table 4.1: Target bulk compositions for Mn piston cylinder runs in wt% oxide without the additional apatite component. Added to each bulk composition was a 7:3 of starting material to apatite component, consisting of 1.5 mol $Ca_3(PO_4)_2$ to either 1 mol. $CaCl_2$ (PM1/Hap10/Hap5) or 1 mol. CaF_2 (BMT2/SH3). H_2O added in the form of brucite or gibbsite. Also listed are the compositions for the gas mixing experiments (Hap2 and Hap3).

	PM1	**Hap10**	**Hap5**	**BMT2**	**SH3**	**Hap2**	**Hap3**
SiO_2	64.1	63.7	72.2	61.3	52.2	64.0	61.7
TiO_2				0.4			
Al_2O_3	17.1	17.1	13.4	18.4	17.3	17.2	16.7
FeO^T				3.1			6.8
MgO				0.2	11.5		
MnO	7.4	7.3	5.3	1.0	1.0	7.4	3.6
CaO				0.9	12.1		
Na_2O	4.7	4.7	5.4	6.1	2.7	4.5	4.7
K_2O	6.8	7.2	3.7	7.0	1.8	6.9	6.6
H_2O*				1.5	1.5		

der in Hap10 led to a higher wt% K_2O and lower wt% SiO_2 than the PM1 composition. Table 4.2 lists the final starting composition for the PC experiments with the added TCP and $CaCl_2/CaF_2$ component. Additional water (4 μL of deionised water (DI)) not listed in Table 4.2 was added to an outer Pt capsule containing an oxygen buffer and an additional 4 μL of DI water was added to an inner Pt capsule containing the starting composition in the following runs: PM1 NNO, MH 1200 Hap10, MW 1200 Hap10, Cr 1200 Hap10, NNO 1200 Hap10, Cr 1200 Hap5. Four μL of DI water was added to only the outer Pt capsules containing the buffer for experiments SH3 Cr, SH3 MH, BMT2 Cr and BMT2 MH as these experiments already had 1.1 wt% water (Table 4.2) in the starting composition in the form of brucite or gibbsite. Water is important when buffering oxygen fugacity as it is hydrogen diffusing from the outer capsule to the inner capsule, and hydrogen fugacity that controls f_{O_2} (Chapter 2, Section 2.2.1). Sample PM1 H had ≈5 wt% water added to the single Pt capsule run, whist PM1 Pt and PM1 PtC were run without additional water.

Two alloquots of Hap10 were used to make glasses at different f_{O_2} in a gas mixing furnace. These were prepared to examine the oxidation state of Mn and Mn-Fe in silicate glasses, and these two 'new' compositions were labelled Hap2 and Hap3 respectively (Table 4.1). The inclusion of a Mn-Fe bearing silicate melt (Hap3) was to identify the possibility of Mn-Fe electron exchange, by examining any difference in Mn XANES spectra obtained under the same f_{O_2} in the two different compositions.

Table 4.2: Target bulk composition for Mn piston cylinder runs including the apatite component

	PM1	Hap10	Hap5	BMT2	SH3
SiO_2	47.8	47.5	53.8	46.0	39.1
TiO_2				0.3	
Al_2O_3	12.7	12.8	10.0	13.8	13.0
FeO^T				2.3	
MgO				0.2	8.6
MnO	5.5	5.4	4.0	0.8	0.8
CaO	13.2	13.3	13.3	14.5	22.8
Na_2O	3.5	3.5	4.0	4.6	2.0
K_2O	5.1	5.4	2.8	5.3	1.4
P_2O_5	9.1	9.2	9.2	9.5	9.5
Cl	3.0	3.1	3.1		
F				1.7	1.7
H_2O				1.1	1.1

4.4 Experimental procedures

Experiments were carried out in an end-loaded piston cylinder at The University of Edinburgh. All runs were carried out using 1/2" talc-pyrex assemblies, with an internal graphite furnace, and inner crushable alumina spacers. Due to the high temperatures needed to synthesise apatite, all runs were carried out in Pt capsules 4 mm in Diameter and 5 mm in length (Chapter 2, Figure 2.1b page 37). This type of capsule has the problem that Fe will react with the Pt, with the amount/rate depending on the intrinsic f_{O_2} conditions. No steps were taken to first anneal the capsules in the starting mixture at the appropriate f_{O_2} conditions. Fe loss should only have affected runs in the BMT2 composition and would chiefly affect the most reduced run BMT2 Cr. Runs were first pressurised to $\approx$ 0.3 GPa before heating, then pressurised simultaneously with increasing temperature, which was raised at a rate of 100 ℃/min. After reaching super liquidus conditions, there was a slight over pressurisation to compensate for pressure loss during the first hour. Temperature was continuously monitored using a Pt_{100}-$Pt_{87}Rh_{13}$ thermocouple placed $\approx$ 10 ℃ from the hot spot of the assembly. All experiments were run at 1 GPa.

Runs were initially taken to super liquidus conditions (Table 4.3) to ensure the homogeneity of the starting composition. Subsequently, the temperature was cooled isobarically to the final temperature at different rates (see Table 4.3) to grow apatite of

a large enough size for subsequent analysis. These rates are based on literature data [Potts, 2016; Prowatke & Klemme, 2006] and test runs carried out in the lab. The final temperature and dwell time for each run (Table 4.3) was chosen to ensure apatite was the only phase present within the melt, allow equilibration between crystals and melt, and to also ensure apatite grains and areas of glass were a suitable size for analysis (Ostwald ripening of apatite grains). On completion of the run, samples were isobarically quenched by shutting off power to the heating circuit whilst maintaining run pressure; temperature dropped to <50 ℃ in less than 30 seconds.

Oxygen fugacity was controlled in experiments by the sample environment. Initial runs were carried out using a single Pt capsule, which is assumed to have an f_{O_2} close to the Ni – NiO (NNO) solid buffer [Bromiley, person. comm.]. Although f_{O_2} cannot be determined directly from the run products, it can be estimated by comparison with other experiments run using the same experimental procedure. In a separate series of experiments, run using the same bulk composition but doped with Eu, with the same sample preparation procedure and sample assembly, Eu XANES spectra indicate an Eu^{2+}/Eu^{3+} ratio in the melt phase close to that of the NNO buffer, as expected [Burnham et al., 2015]. A second suite of experiments were carried out using an inner graphite bucket inside a Pt capsule. As described by Médard et al. [2008], the presence of a graphite liner in the Pt capsule results in buffering of O by reaction with C, and more reducing conditions close to C - CO (CCO-1; Médard et al. 2008). Again, we cannot verify f_{O_2} conditions directly in these experiments, and it is possible that use of a Fe-free starting material here, for example, could result in slightly more reduced conditions than those described by Médard et al. [2008]. However, it is unlikely that f_{O_2} conditions in graphite-Pt capsules will be more oxidising than CCO [Médard et al., 2008], providing more reducing conditions than samples run in just Pt or with an oxidising buffer. PM1 H was a single Pt capsule experiment which contained ≈5 wt% H_2O. Oxygen fugacity in this experiment has been estimated to approach the value of the NNO buffer at the appropriate P-T conditions, imposed by the assembly material. No measurements of H were made in the melt phase due to beamsize requirements imposed by the SIMS instrument, which makes it hard to assess loss/gain of H species

during the run duration. Loss of H_2 would result in the melt becoming progressively more oxidised, whilst gain of H_2 would drive the melt to a lower f_{O_2}. Given these considerations it is unlikely that run PM1 H is anhydrous and buffering from a medium in the assembly is likely to control f_{O_2} in this run at around NNO. The oxygen fugacity of this sample is not a crucial point as it does not critically alter the conclusions on the role of f_{O_2} on mineral melt partitioning. Oxygen fugacity in subsequent experiments was controlled using the double capsule technique [e.g. Eugster, 1957; Eugster & Wones, 1962; Jakobsson, 2012]. In these runs, f_{O_2} was controlled using a series of metal-metal oxide oxygen buffers (i.e. Ni-NiO, Cr-Cr_2O_3, Fe_3O_4-Fe_2O_3, Fe_3O_4-FeO) within an outer Pt capsule that enveloped an internal Pt capsule containing the starting material. Four μL of deionized water (DI water) was micro-syringed into the bottom of all outer capsules, regardless of starting composition, prior to filing with the buffer and welding. In the $CaCl_2$ starting composition runs, 4 μL of DI water was added into the inner capsule prior to filing and welding to enable H_2 diffusion between the buffer and inner capsule to control f_{O_2}. As capsules were not weighed prior to and after the addition of water, estimates must be made to determine what wt% H_2O was added to in the inner capsule. The weight of starting material inside the inner capsules is estimated to be 0.295 $\pm$ 0.065g (based on other lab users' accounts), therefore, it is estimated that 10-15 wt% H_2O was added to runs with an inner capsule in the $CaCl_2$ starting composition. Approximated f_{O_2} values are given in Table 4.3 and were calculated based on the relevant redox buffer equations reviewed in Fegley Jr [2012]. The f_{O_2} values for experiments run with a solid state buffer could deviate from the calculated buffer values if the activity of water inside the capsule is not in unity, and in water under-saturated samples, f_{O_2} values will be lower than the coexisting hydrated buffer [Matjuschkin et al., 2015], and indicated in Table 4.3. The purpose of high-pressure experiments here, however, due to complexities in experimental design, is to synthesise apatite in equilibrium with silicate melt under a range of f_{O_2} conditions, from oxidising to reducing. Gas mixing synthesis experiments are then used to accurately constrain the influence of f_{O_2} on Mn oxidation state.

Additional experiments were carried out in a vertical tube gas mixing furnace to synthe-

sise Mn bearing glasses at controlled f_{O_2} conditions. Hap2 and Hap3 starting composition was mixed with poly-vinyl acetate (PVA) to create beads of approximately 0.5 mm diameter, and hung from a loop of thin platinum wire. Hanging samples from a thin Pt wire was chosen to minimise Fe loss from the melt because there is a continuous solid solution of Pt and Fe under reducing conditions. Multiple dry beads of the starting material mixed with PVA were hung off the end of an alumina rod at the same height, and carefully lowered into the hotspot of a vertical tube furnace to avoid thermal shock to the ceramic. Beads were lowered in at 1300 ℃ to ensure the composition was above its liquidus to avoid the formation of crystalline phases. The furnace was then made airtight and tested for gas leaks before a mixture of CO_2 and H_2 were allowed into the furnace. A carefully selected ratio of CO_2 and H_2 was selected from Deines et al. [1974] to buffer the atmosphere inside the furnace at a fixed f_{O_2} value, and was controlled by Bronkhurst mass flow controllers. Gas mixtures of 66, 76, 90.5, 98.1 and 99.5 and 100% CO_2 were used to control f_{O_2}, along with one sample run without any gas being pumped into the furnace. These approximately equate to f_{O_2} conditions of IW +1.4, IW +1.9, IW +3.0, IW +4.5, IW +5.7, IW $\sim$ +9.3 and IW $\sim$ +10.1 respectively at 1300 ℃. The beads were kept above their liquidus for 20-24 hours before the gas mixture was turned off and the sample rapidly quenched by quickly raising the samples out of the hotspot. Following sample retrieval, the beads were mounted in epoxy, ground and polished using 6, 3 and 1 μm diamond polishes.

4.5 Analytical techniques: EPMA

4.5.1 Apatite and coexisting glass

Recovered capsules were mounted in crystal bond, ground to the desired level, and polished using diamond paste. Crystal bond was later dissolved using acetone. After cleaning, samples were mounted in 1" indium mounts and carbon coated. Electron probe microanalysis data was collected using the JEOL JXA8530F Hyperprobe field emission gun electron microprobe analayser (FEG-EPMA) at the University of Bristol using the following standards and conditions for apatite and melt:

Apatite was analysed using a 10 μm beam for all conditions; the first protocol measured Na, Ca, P, F, and Cl with an accelerating voltage of 15 kV and 5 nA current. The second protocol used a 15 kV accelerating voltage and 20 nA current to measure Si, Mg, K, S, Fe, Mn, Ni, Cr, and Ti on the same spot as the first protocol. Primary standards used were albite (Na, Si), Saint John's Island olivine (Mg), sanidine (K), barite (S), NaCl (Cl), fayalite (Fe), Mn metal (Mn), Ni metal (Ni), Cr_2O_3 (Cr), TiO_2 (Ti), and Durango apatite (Ca, P, F).

The glass was analysed with the following conditions: (1) 15 kV accelerating voltage, 10 nA current for Ca, Ti, Si, Al, Na, Mg, F, K, Cl, Fe and Ni (2) 15 kV accelerating voltage, 40 nA current for Mn, Cr, and P. All analyses were collected with a 10 μm beam and both protocols analysed the same spot. Primary standards were as follows: wollastonite (Ca), Saint John's Island olivine (Mg), TiO_2 (Ti), albite (Si, Na), MgF_2 (F), sanidine (Al, K), NaCl (Cl), fayalite (Fe, Mn), Cr_2O_3 (Cr), Durango apatite (P), and Ni metal (Ni).

4.5.2 Gas mixing furnace glasses

Compositional data for the gas mixing furnace glasses were collected on the Cameca SX-100 electron microprobe analayser housed in the Grant Institute, University of Edinburgh. Glass beads from the gas mixing furnace experiments were embedded in epoxy, ground, and polished prior to analysis. Epoxy mounts were carbon coated and analysed using two different column conditions. Under condition 1, Na, Mg, Al, K, Ca and Si were measured with a 15 kV accelerating voltage and 1 nA current, whereas condition 2 was used to measure Cl, P, Fe and Mn with 15 kV accelerating voltage and 80 nA current. Counting times were 20 s on peak and 10 s on background for all elements except Fe and Mn which were measured with 40 s peak and 20 s background and 60 s peak and 30 s background respectively. The calibration standards used were Jadeite (Na), Spinel s.s. (Mg, Al), K-feldspar (K), wollastonite (Ca,Si), Durango apatite (Ca, P,), fayalite (Fe), NaCl (Cl) and PuMn (Mn metal - Mn).

4.6 Analytical techniques: SIMS

Volatile measurements in the apatite and coexisting glasses were collected by secondary ion mass spectrometry (SIMS) on a Cameca ims-4f at the NERC ion probe facility, University of Edinburgh. Prior to SIMS analysis samples were cleaned with ethanol, and then coated with 35 nm gold to provide electrical conductivity. For apatite and glass a $^{16}O^-$ primary beam with nominal current of 2.2 nA, and 10.8 keV accelerating voltage, was targeted on a sample with a 4.5 keV voltage to produce a 15 keV net impact energy. Apatite and glass measurements of the secondary ions ^{1}H, ^{11}B, ^{12}C, ^{16}O, ^{19}F, ^{26}Mg, ^{30}Si, ^{31}P, ^{35}Cl, ^{39}K, ^{42}Ca, ^{55}Mn, ^{88}Sr, ^{138}Ba, ^{139}La, ^{140}Ce and ^{151}Eu were counted on an electron multiplier for 79 seconds respectively, for each 6 cycles of the magnet. A 3-minute pre-sputter period at a raster size of 10 μm was used to pre-clean the analysis area. Secondary ions were acquired with a 25 μm image field, and the area analysed was restricted to 8-10 μm using the field aperture #2. An energy offset of 50 eV was applied (40 eV window). Additional higher resolution CO_2 measurements, in the glass and apatite phases (size permitting), were collected on additional spots. These were acquired after a 4-minute pre sputter, with a 20 μm raster, to pre clean the analysis area. Data was collected with a 60 μm image field, 50 eV offset (40 eV window), and a field aperture was used to restrict ions to 15 μm. The operated mass resolution was 900-1000, which is sufficient to separate $^{25}Mg^{2+}$ from $^{12}C^+$. The majority of CO_2 measurements reported for apatite are based on the low-resolution window measurements, using higher resolution measurements to identify the need for an Mg correction. An Mg^{2+} correction based on $^{25}Mg^{2+}$ was applied.

Only SIMS measurements for H_2O and CO_2 are given here. Other elements were measured to confirm that the analyses were not contaminated, and Eu/Ce measurements are for use in future work. Basaltic glass and apatite standards were used to quantify ion yields for ^{1}H, and CO_2 analyses based on either H/Si and C/Si (glasses) or H/Ca and C/Ca ratios (apatite). It is assumed that the absolute error is better than 10% [Hinton, person. comm.].

4.7 Analytical techniques: XANES

Mn and Fe K-edge XANES spectra were collected on experimental Pt capsules and glasses in 1" epoxy mounts at beamline I18 of the Diamond Light Source (Harwell, UK). Spectra were acquired in fluorescence mode, using a Ge detector. Beam energy was finely tuned using a Si(111) crystal monochromator. The beam size was selected by using a variety of slits and was tuned to an area of 5 μm $\times$ 5 μm. Mn K-edge scans were measured over an energy range of 6400-6750 eV with a 1 s count time per point. The pre-edge region was measured in 5 eV steps from 6400-6520 eV and from 6520-6532 eV with 1 eV steps. The edge region from 6532-6562 eV was measured with 0.2 eV steps and 6562-6580 eV with 1 eV steps. The post-edge region was collected with 3 eV steps from 6600-6750 eV. Mn K-edge energy was calibrated by defining the first inflection point in the derivative of a Mn foil standard to 6539 eV.

Fe K-edge spectra were collected from 7000-7320 eV with a 1 s count time per point. The pre-edge region was measured from 7000-7090 eV with 6.25 eV steps, and from 7090-7107 with 1 eV steps. The edge region was scanned with 0.25 eV steps from 7107-7120, 0.3 eV steps from 7120-7140 eV and 1 eV steps over 7140-7160 eV. The post edge region from 7160-7320 was measured with 3 eV steps. Fe spectra energy was calibrated to the first inflection point in the derivative of a Fe foil standard to 7112 eV.

Raw data was imported into the software Athena [Ravel & Newville, 2005], where multiple scan data were merged. Scans were also deglitched, corrected for self-absorption based on the FLUO algorithm [Haskel, 1999] and then the data was pre-edge/post-edge normalised.

Pre-edge peak fitting was carried out on the normalised data in Fityk [Wojdyr, 2010]. Pre-edge peaks were obtained from the data by fitting a convex hull spline baseline across the pre-edge region. Gaussian peaks of fixed half-width at half-maximum of 0.7 eV was fitted to the data [Chalmin et al., 2009; Wilke et al., 2001]. All data was fitted with 2 Gaussian contributions. The centroid was calculated from the area weighted centroids of the Gaussian peaks.

4.8 Experimental results

4.8.1 Piston cylinder experiments

All experiments, regardless of starting composition, contained apatite and quenched melt. In run PM1 H1 an additional pyroxene phase was found due to the lower final run temperature and/or the added water content. Apatite throughout the experiments varies in size from 2 to 500 μm, in the longest dimensions, with the largest apatite found in the least silicic melts. Modal proportions of apatite crystals are generally less than 30% and the habit of most crystals are euhedral. Synthesised apatite commonly display elongated melt inclusions trapped in their cores, running parallel to the longest axis of the crystals. Major, trace and volatile measurements for glasses from each group of starting compositions are listed below and are found in Table 4.3.

Quenched glasses for all runs are homogeneous in appearance and have low standard deviation in major and minor element analyses. Apatite reveal no evidence of chemical zonation, and low standard deviations in major and minor elements again indicate chemical homogeneity within each run (Table 4.4). This, therefore, suggests that all our experiments are in equilibrium.

4.8.1.1 Silicic compositions

Glass compositions for runs with the PM1/Hap10 starting mix resulted in a range of compositions from trachyte to phonotephroite/basaltic trachyandesite (Fig. 4.1). This range is due to varying degrees of apatite saturation, and the additional effect of crystallising an additional phase in PM1 H. This also resulted in different degrees of melt polymerisation as measured by the number of non-bridging oxygen's to tetrahedrally coordinated cations (NBO/T). PM1 H contained the most polymerised melt upon quenching (NBO/T = 0.12) and PM1 Pt the least (NBO/T = 0.43; Table 4.3), while the average NBO/T for the PM1/Hap10 quenched glasses $\approx$ 0.26. MnO contents of the glasses vary from a minimum of 4.31 wt% in PM1 H to 9.21 wt% in PM1 Pt. Melts PM1 H and PM1 Pt are so different in MnO content because PM1 H crystallised an additional Mn rich phase (identified by optical microscopy) which is likely to be a Mn

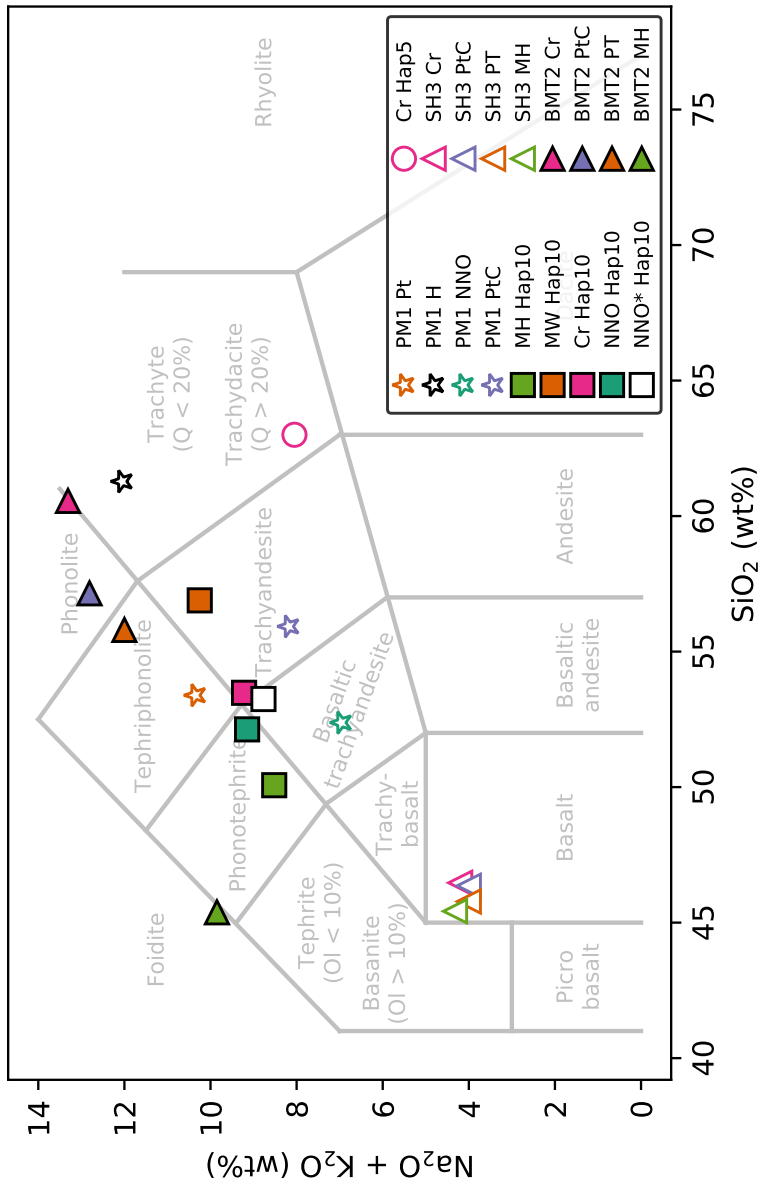

Figure 4.1: Total alkali-silica (TAS) plot for quenched melt compositions. Sample names refer to f_{O_2} buffer and starting bulk composition used in each run, see text and table 4.3 for details.

Table 4.3: Experimental parameters, and average major and trace element composition of glass for experimental runs. Errors represent 1σ. Duration relates to hours at final T, while ramp rate is degrees cooled per hour. Note: Pt = single Pt capsule, H= single Pt capsule with added H_2O, NNO = Ni-NiO buffer, MH = Fe_3O_4-Fe_2O_3 buffer, MW = Fe_3O_4-FeO buffer, Cr = Cr-Cr_2O_3 buffer, PtC = graphite capsule inside Pt. H_2O measurements were made by SIMS. NBO/T = number of non-bridging oxygen per tetrahedrally coordinated cation (see text for details).

	PM1 Pt	**PM1 H**	**PM1 NNO**	**PM1 PtC**	**MH 1200 Hap10**	**MW 1200 Hap10**
Initial T	1450	1450	1450	1450	1400	1400
Final T	1250	1100	1250	1250	1200	1200
Ramp Rate	60	60	60	60	60	60
Est. f_{O_2}	-7.0	-8.8	-7.0	-9.9	-2.9	-9.3
Duration (hrs)	23	18	20	21	19	20
Glass						
SiO_2	53.39 ± 0.64	61.86 ± 0.78	52.38 ± 0.38	56.13 ± 0.68	50.07 ± 0.58	56.89 ± 1.11
TiO_2						
Al_2O_3	14.40 ± 0.18	17.85 ± 0.27	15.51 ± 0.20	16.08 ± 0.18	14.60 ± 0.16	16.11 ± 0.17
FeO^T					1.66 ± 0.12	1.57 ± 0.09
MgO					0.10 ± 0.01	0.25 ± 0.02
MnO	9.21 ± 0.52	4.31 ± 0.34	9.06 ± 0.32	6.69 ± 0.27	7.57 ± 0.31	7.16 ± 0.53
CaO	6.10 ± 0.27	1.71 ± 0.08	4.56 ± 0.11	4.43 ± 0.13	4.05 ± 0.19	3.27 ± 0.29
K_2O	5.14 ± 0.13	6.67 ± 0.10	4.45 ± 0.07	4.85 ± 0.10	5.20 ± 0.10	6.22 ± 0.16
Na_2O	5.21 ± 0.14	5.45 ± 0.07	2.51 ± 0.09	3.38 ± 0.13	3.32 ± 0.19	4.03 ± 0.12
P_2O_5	3.46 ± 0.23	0.82 ± 0.07	2.85 ± 0.12	1.76 ± 0.11	3.62 ± 0.40	2.12 ± 0.08
Cl	2.45 ± 0.13	0.47 ± 0.03	0.29 ± 0.03	2.08 ± 0.11	0.46 ± 0.01	0.22 ± 0.01
F						
Total	99.35 ± 0.29	99.14 ± 0.99	91.6 ± 0.48	95.39 ± 0.52	90.71 ± 0.89	97.91 ± 0.45
H_2O	0.92	nm	7.79	2.78	7.97	nm
NBO/T	0.43	0.12	0.27	0.21	0.29	0.24

Table 4.3 continued

	Cr 1200 Hap10	**NNO 1200 Hap10**	**Cr 1200 Hap5**	**SH3 Cr**	**SH3 PtC**	**SH3 Pt**
Initial T	1400	1400	1400	1400	1400	1400
Final T	1200	1200	1200	1250	1250	1250
Ramp Rate	60	60	60	60	60	60
Est. f_{O_2}	-17.6	-7.6	-17.6	-16.8	-9.9	-7.0
Duration (hrs)	24	21	21	24	24	24
Glass						
SiO_2	53.48 ± 0.41	52.13 ± 0.51	63.00 ± 0.85	46.47 ± 0.43	46.36 ± 0.45	45.78 ± 0.43
TiO_2						
Al_2O_3	15.18 ± 0.15	15.41 ± 0.41	12.93 ± 0.13	15.64 ± 0.18	15.59 ± 0.18	15.47 ± 0.01
FeO^T	0.03 ± 0.01				0.04 ± 0.01	
MgO	0.07 ± 0.01	0.08 ± 0.01	0.08 ± 0.01	10.00 ± 0.07	10.18 ± 0.06	10.00 ± 0.05
MnO	7.18 ± 0.22	7.65 ± 0.33	3.88 ± 0.03	0.73 ± 0.02	0.79 ± 0.02	0.90 ± 0.01
CaO	3.32 ± 0.09	4.61 ± 0.23	2.58 ± 0.08	16.47 ± 0.20	16.46 ± 0.06	16.16 ± 0.30
K_2O	5.54 ± 0.12	5.47 ± 0.13	3.48 ± 0.08	1.58 ± 0.05	1.58 ± 0.06	1.49 ± 0.05
Na_2O	3.68 ± 0.26	3.68 ± 0.25	4.57 ± 0.13	2.62 ± 0.13	2.42 ± 0.14	2.51 ± 0.17
P_2O_5	2.70 ± 0.20	3.41 ± 0.32	2.20 ± 0.02	4.15 ± 0.12	3.99 ± 0.03	4.19 ± 0.01
Cl	0.15 ± 0.00	0.56 ± 0.05	0.08 ± 0.01			
F				1.35 ± 0.05	1.36 ± 0.05	1.37± 0.03
Total	91.39 ± 0.39	93.27 ± 0.87	92.93 ± 0.89	99.07 ± 0.48	98.78 ± 0.45	97.90 ± 0.20
H_2O	7.63	5.60	6.44	1.60	0.89	1.89
NBO/T	0.25	0.30	0.15	0.86	0.86	0.86

Table 4.3 continued

	SH3 MH	BMT2 Cr	BMT2 Pt	BMT2 MH
Initial T	1400	1500	1500	1500
Final T	1250	1350	1350	1350
Ramp Rate	60	10	10	10
Est. f_{O_2}	-2.3	-15.2	-6.0	-1.3
Duration (hrs)	24	9	9	9
Glass				
SiO_2	45.42 ± 0.50	60.56 ± 0.45	55.80 ± 0.63	45.38 ± 0.49
TiO_2		0.27 ± 0.04	0.30 ± 0.02	0.25 ± 0.01
Al_2O_3	15.33 ± 0.11	18.45 ± 0.09	17.49 ± 0.09	13.34 ± 0.21
FeO^T	1.75 ± 0.05		1.29 ± 0.05	12.08 ± 0.20
MgO	8.55 ± 0.07	0.32 ± 0.01	0.30 ± 0.01	0.28 ± 0.01
MnO	0.86 ± 0.01	0.07 ± 0.01	0.76 ± 0.01	0.58 ± 0.01
CaO	15.56 ± 0.05	3.60 ± 0.03	4.31 ± 0.12	8.11 ± 0.13
K_2O	1.66 ± 0.02	6.97 ± 0.09	6.27 ± 0.08	5.09 ± 0.08
Na_2O	2.66 ± 0.14	6.34 ± 0.17	5.73 ± 0.26	4.76 ± 0.26
P_2O_5	4.03 ± 0.02	1.35 ± 0.05	2.48 ± 0.08	5.74 ± 0.18
Cl				
F	1.28 ± 0.08	1.00 ± 0.06	1.07 ± 0.08	1.22 ± 0.07
Total	97.11 ± 0.65	99.09 ± 0.25	95.78 ± 0.37	96.88 ± 0.51
H_2O	1.89	0.48	2.07	1.90
NBO/T	0.79	0.11	0.15	0.36

rich pyroxene based on its crystal habit. Unfortunately EPMA data of the additional phase was not collected so a thorough mass balance cannot be attempted. Apatite from the PM1/Hap10 experiments have a range of Mn contents from 4.94 wt% MnO (0.74 a.p.f.u. PM1 Pt) to 7.89 wt% MnO (1.16 a.p.f.u. - PM1 NNO), with an average of 6.51 wt% MnO. Molar proportion of Cl-H_2O for these apatite display a range from more Cl rich ($X_{Cl}^{Ap} = 0.89$, PM1 Pt) in the PM1 samples to closer to pure hydroxyapatite compositions ($X_{H_2O}^{Ap} = 0.90$, Cr 1200 Hap10) in Hap10 runs. Samples run with the Cr-Cr_2O_3 buffer generally display higher $X_{H_2O}^{Ap}$ than their counterparts run in the same starting composition. Part of this may be due to the species of hydrogen present in the melt under these reduced conditions. Little/no hydrogen is expected to be present as H_2O under these conditions [Bravenec - Private communications, Holland & Powell [2003]; Pitzer & Sterner [1995]], instead, hydrogen is likely to exist dominantly as H_2 and CH_4, with the amount of CH_4 dependent on the initial C content of the melt. These hydrogen species may promote a more hydroxy-rich apatite to form. Stoichiometry of apatite suggests the majority of H in apatite is likely to be present as OH. Water in the PM1

Table 4.4: Major and trace element compositions of apatite, and associated partition coefficients for experimental runs. Errors represent 1σ. Note: Pt = single Pt capsule, H= single Pt capsule with added H_2O, NNO =Ni-NiO buffer, MH = Fe_3O_4-Fe_2O_3 buffer, MW = Fe_3O_4-FeO buffer,Cr = Cr-Cr_2O_3 buffer, PtC= graphite capsule inside Pt and nm = not measured. H_2O measurements were made by SIMS. $X_F^{Ap} = F^{Ap}/3.767$, $X_{Cl}^{Ap} = Cl^{Ap}/6.809$ and $X_{H_2O}^{Ap} = H_2O^{Ap}/1.81$. Structural formulas are calculated based on 26 anions.

	PM1 Pt	**PM1 H**	**PM1 NNO**	**PM1 PtC**
# Analyses	17	20	28	19
SiO_2	0.37 ± 0.06	0.48 ± 0.10	0.27 ± 0.05	0.45 ± 0.05
Al_2O_3	0.04 ± 0.01	0.06 ± 0.02		0.06 ± 0.03
FeO				
MgO				
MnO	4.94 ± 0.15	6.60 ± 0.25	7.89 ± 0.28	5.93 ± 0.24
CaO	48.28 ± 0.24	46.93 ± 0.37	47.51 ± 0.35	47.34 ± 0.49
K_2O	0.14 ± 0.03	0.19 ± 0.05	0.07 ± 0.03	0.13 ± 0.02
Na_2O	0.59 ± 0.04	0.60 ± 0.05	0.06 ± 0.03	0.33 ± 0.04
P_2O_5	39.89 ± 0.46	39.81 ± 0.27	40.5 ± 0.47	39.7 ± 0.63
Cl	6.03 ± 0.38	5.20 ± 0.60	0.94 ± 0.05	5.79 ± 0.91
F				
Total	100.27 ± 0.64	99.87 ± 0.62	97.28 ± 0.51	99.72 ± 0.65
H_2O	0.09	nm	1.40	0.17
CO_2	0.08	nm	0.07	0.04
Al_2O_3	0.01	0.01		0.01
FeO^T				
MgO				
MnO	0.74	0.99	1.16	0.89
CaO	9.12	8.86	8.84	8.99
K_2O	0.06	0.09	0.03	0.06
Na_2O	0.20	0.21	0.02	0.11
Sum Ca Site	10.13	10.15	10.06	10.06
P_2O_5	5.95	5.94	5.96	5.95
SiO_2	0.05	0.07	0.04	0.07
Sum P site	6.00	6.01	6.00	6.02
Cl	1.80	1.55	0.28	1.74
F				
H_2O	0.11		1.62	0.20
Sum X site	1.91		1.90	1.94
$\mathbf{X_{Cl}^{Ap}}$	0.89		0.14	0.85
$\mathbf{X_F^{Ap}}$				
$\mathbf{X_{H_2O}^{Ap}}$	0.05		0.77	0.09
$\mathbf{X^{Ap}total}$	0.94		0.91	0.94
$\mathbf{D_{Mn}^{ap/m}}$	0.54	1.53	0.87	0.89
$\mathbf{D}_{H_2O}^{ap/m}$	0.10		0.18	0.06
$\mathbf{K}_D^{Cl-H_2O}$	21.18		0.22	5.30
$\mathbf{K}_D^{F-H_2O}$				

Table 4.4 continued

	MH 1200 Hap10	**MW 1200 Hap10**	**Cr 1200 Hap10**	**NNO 1200 Hap10**
# Analyses	9	4	8	7
SiO_2	0.18 ± 0.01	0.55 ± 0.23	0.23 ± 0.02	0.27 ± 0.02
Al_2O_3				
FeO	0.14 ± 0.04	0.67 ± 0.12		
MgO		0.15 ± 0.01	0.03 ± 0.00	
MnO	5.67 ± 0.50	7.14 ± 0.49	7.30 ± 0.61	6.61 ± 0.06
CaO	49.23 ± 0.46	46.57 ± 0.66	47.76 ± 0.57	48.11 ± 0.21
K_2O	0.02 ± 0.00	0.11 ± 0.04	0.06 ± 0.02	0.05 ± 0.01
Na_2O	0.13 ± 0.03	0.28 ± 0.03	0.08 ± 0.02	0.19 ± 0.03
P_2O_5	40.83 ± 0.49	40.24 ± 0.59	40.92 ± 0.56	40.51 ± 0.50
Cl	1.15 ± 0.02	1.89 ± 0.10	0.63 ± 0.04	1.93 ± 0.03
F		0.24 ± 0.30		
Total	97.11 ± 0.39	97.86 ± 0.60	96.73 ± 0.65	97.41 ± 0.64
H_2O	1.43		1.63	1.35
CO_2	0.06		0.08	0.11
Al_2O_3				
FeO^T	0.02	0.10		
MgO		0.04	0.01	
MnO	0.83	1.06	1.07	0.97
CaO	9.12	8.71	8.85	8.98
K_2O	0.01	0.05	0.03	0.02
Na_2O	0.04	0.09	0.03	0.06
Sum Ca Site	10.03	10.05	9.98	10.04
P_2O_5	5.98	5.95	5.99	5.97
SiO_2	0.03	0.08	0.03	0.04
Sum P site	6.01	6.03	6.02	6.01
Cl	0.34	0.56	0.18	0.57
F		0.13		
H_2O	1.65		1.88	1.57
Sum X site	1.99		2.07	2.14
$\mathbf{X}_{Cl}^{\mathbf{Ap}}$	0.17		0.09	0.28
$\mathbf{X}_{F}^{\mathbf{Ap}}$				
$\mathbf{X}_{H_2O}^{\mathbf{Ap}}$	0.79		0.90	0.75
$\mathbf{X^{Ap}total}$	0.96		0.99	1.03
$\mathbf{D}_{\mathbf{Mn}}^{\mathbf{ap/m}}$	0.75	1.00	1.02	0.86
$\mathbf{D}_{H_2O}^{ap/m}$	0.18		0.21	0.24
$\mathbf{K}_{D}^{Cl-H_2O}$	0.21		0.28	0.40
$\mathbf{K}_{D}^{F-H_2O}$				

Table 4.4 continued

	Cr 1200 Hap5	**SH3 Cr**	**SH3 PtC**	**SH3 Pt**
# Analyses	6	5	6	4
SiO_2	0.27 ± 0.02	0.39 ± 0.05	0.42 ± 0.06	0.39 ± 0.10
Al_2O_3				
FeO				
MgO	0.06 ± 0.01	0.88 ± 0.01	0.86 ± 0.02	0.90 ± 0.01
MnO	6.58 ± 0.08	0.16 ± 0.01	0.19 ± 0.01	0.18 ± 0.01
CaO	48.24 ± 0.22	54.3 ± 0.18	53.96 ± 0.23	54.51 ± 0.10
K_2O	0.04 ± 0.01		0.02 ± 0.01	
Na_2O	0.18 ± 0.07			
P_2O_5	41.21 ± 0.29	41.28 ± 0.67	41.79 ± 0.48	41.39 ± 0.22
Cl	0.74 ± 0.05	0.02 ± 0.02	0.04 ± 0.01	0.03 ± 0.01
F		3.24 ± 0.19	3.34 ± 0.12	3.61 ± 0.31
Total	97.15 ± 0.27	100.33 ± 0.58	100.71 ± 0.31	101.06 ± 0.19
H_2O	1.54	0.37	0.26	0.20
CO_2	0.08	0.28	0.21	0.43
Al_2O_3				
FeO^T				
MgO	0.02	0.22	0.22	0.23
MnO	0.96	0.02	0.03	0.03
CaO	8.90	9.85	9.74	9.86
K_2O	0.02		0.01	
Na_2O	0.06			
Sum Ca Site	9.95	10.10	9.99	10.11
P_2O_5	6.01	5.92	5.96	5.91
SiO_2	0.04	0.05	0.06	0.05
Sum P site	6.04	5.97	6.02	5.97
Cl	0.22	0.01	0.01	0.01
F		1.74	1.78	1.93
H_2O	1.77	0.42	0.29	0.23
Sum X site	1.98	2.16	2.08	2.16
$\mathbf{X}^{\mathbf{Ap}}_{Cl}$	0.11		0.01	
$\mathbf{X}^{\mathbf{Ap}}_{F}$		0.86	0.89	0.96
$\mathbf{X}^{\mathbf{Ap}}_{H_2O}$	0.85	0.20	0.14	0.11
$\mathbf{X^{Ap}total}$	0.96	1.07	1.04	1.07
$\mathbf{D}^{\mathbf{ap/m}}_{\mathbf{Mn}}$	1.70	0.22	0.24	0.20
$\mathbf{D}^{ap/m}_{H_2O}$	0.24	0.23	0.30	0.11
$\mathbf{K}^{Cl-H_2O}_{D}$	0.90			
$\mathbf{K}^{F-H_2O}_{D}$		4.38	3.21	9.90

Table 4.4 continued

	SH3 MH	**BMT2 Cr**	**BMT2 Pt**	**BMT2 MH**
# Analyses	8	4	7	5
SiO_2	0.39 ± 0.10	0.32 ± 0.11	0.17 ± 0.01	0.17 ± 0.02
Al_2O_3				
FeO	0.05 ± 0.04		0.14 ± 0.02	0.61 ± 0.03
MgO	0.87 ± 0.02	0.12 ± 0.01	0.10 ± 0.01	0.07 ± 0.00
MnO	0.19 ± 0.02	0.15 ± 0.04	0.49 ± 0.06	0.27 ± 0.01
CaO	54.36 ± 0.45	54.64 ± 0.45	54.44 ± 0.15	54.40 ± 0.23
K_2O	0.02 ± 0.01	0.09 ± 0.04	0.06 ± 0.02	0.05 ± 0.01
Na_2O		0.11 ± 0.03	0.08 ± 0.02	0.09 ± 0.05
P_2O_5	41.71 ± 0.39	41.47 ± 0.36	41.52 ± 0.52	41.82 ± 0.42
Cl	0.02 ± 0.02			0.02 ± 0.02
F	3.25 ± 0.18	3.53 ± 0.21	3.26 ± 0.13	3.40 ± 0.12
Total	100.92 ± 0.44	100.5 ± 0.47	100.28 ± 0.50	100.94 ± 0.34
H_2O	0.40	0.16	0.26	0.36
CO_2	0.24	0.15	0.21	0.09
Al_2O_3				
FeO^T	0.01		0.02	0.09
MgO	0.22	0.03	0.03	0.02
MnO	0.03	0.02	0.07	0.04
CaO	9.79	9.93	9.90	9.84
K_2O	0.01	0.04	0.03	0.02
Na_2O		0.04	0.03	0.03
Sum Ca Site	10.05	10.06	10.07	10.03
P_2O_5	5.94	5.96	5.96	5.98
SiO_2	0.05	0.05	0.02	0.02
Sum P site	5.99	6.00	5.99	6.00
Cl	0.01			0.01
F	1.73	1.89	1.75	1.82
H_2O	0.45	0.18	0.29	0.41
Sum X site	2.18	2.07	2.04	2.23
$\mathbf{X}_{Cl}^{\mathbf{Ap}}$				
$\mathbf{X}_{F}^{\mathbf{Ap}}$	0.86	0.94	0.87	0.90
$\mathbf{X}_{H_2O}^{\mathbf{Ap}}$	0.22	0.09	0.14	0.20
$\mathbf{X^{Ap}total}$	1.09	1.03	1.01	1.10
$\mathbf{D}_{\mathbf{Mn}}^{\mathbf{ap/m}}$	0.22	2.14	0.65	0.47
$\mathbf{D}_{H_2O}^{ap/m}$	0.21	0.34	0.16	0.19
$\mathbf{K}_{D}^{Cl-H_2O}$				
$\mathbf{K}_{D}^{F-H_2O}$	4.43	6.50	14.39	7.94

composition range from 0.92 wt% in PM1 Pt to 7.79 wt% in PM1 NNO. PM1 Pt has so little water in its glass as the starting composition added to this run was nominally anhydrous. PM1 PtC should also have less water than PM1 H and PM1 NNO because this run was also loaded with a nominally anhydrous starting composition, however, excess water from infiltration during the run or gained during loading of the capsule is present. Glass areas in PM1 H1 were too small to collect SIMS measurements for 1H. PM1 NNO has 7.79 wt% water which is higher than the other runs due to the 4 μL of DI water added to the inner and outer capsules of this run respectively. Hap10 glasses range in water contents from 5.6-8.0 wt% with all water originating from the addition of DI water to the outer an inner Pt capsules.

Sample Cr 1200 Hap5 was run in an additional starting composition (Table 4.3). Hap 5 is similar in composition to Hap10 but contained half the amount of Mn (5 wt.%). This experiment resulted in a trachyitic glass composition. Apatite in this run contained 6.58 wt% MnO (0.96 a.p.f.u.) and the anion content is close in composition to the hydroxyl end member ($X^{Ap}_{H_2O} = 0.85$). Run Cr1200 Hap5 has similar amounts of water (6.44 wt% H_2O) in its glass to the samples in the Hap10 composition.

Experiments run in the BMT2 system, with the exception of BMT2 MH, contain glasses that range from tephriphonolite to phonolite in composition (Fig. 4.1). Sample BMT2 MH was subject to Fe contamination from the buffer, with an increase to 12.1 wt% FeO^T that changed the glass composition to a Fe-rich foidite (Fig. 4.1). The MnO content varied between 0.07 - 0.80 wt% in these quenched glasses, thought to be a result of varying apatite saturation (of apatite with different MnO content) by mass balance. Apatite from this starting composition contained variable amounts of Mn compared to SH3, with 0.02, 0.04 and 0.07 a.p.f.u. of Mn for samples BMT2 Cr, MH and Pt respectively. BMT2 Cr is closest in composition to end member FAp (F = 3.53 wt%), whilst BMT2 Pt has the least amount of F (3.26 wt%). BMT2 glasses contain 0.48 wt% (BMT2 Cr) to 2.07 wt% (BMT2 Pt) water. Runs BMT2 Pt and BMT2 MH are therefore enriched in water relative to the $\approx$ 1.1 wt% H_2O in the starting composition and BMT2 Cr depleted. Enrichment is likely to be due to the crystallisation of an apatite phase, whilst loss of water in BMT2 Cr could be due to diffusion or loss of

H_2/H_2O out of the capsule.

4.8.1.2 Basaltic compositions

The SH3 composition resulted in glasses that are basaltic in composition, ranging from 4.00-4.32 wt% total alkalis (Na_2O + K_2O) and 45.42-46.47 wt% SiO_2 (Fig. 4.1). SH3 MH shows elevated FeO levels (1.75 wt% FeO) compared to other samples in this composition presumably due to contamination from the buffer, occurring because of diffusion of Fe through the Pt into the sample. The MnO contents in these samples ranges from a minimum of 0.73 wt% MnO in SH3 Cr to a maximum of 0.90 wt% MnO in SH3 Pt. Apatite from this composition contains 0.90 wt% MgO (0.22 a.p.f.u.), and a maximum of 0.19 wt% MnO (0.03 a.p.f.u.). All apatite are close to the F end member composition with X_F^{Ap} ranging from 0.86-0.96 (Table 4.4).

Water in the SH3 glasses ranged from 0.89 wt% (SH3 PtC) to 1.89 wt% (SH3 Pt and SH3 MH). As $\approx$ 1.1 wt% water was added to the SH3 starting composition, it appears that glasses SH3 Cr, SH3 Pt and SH3 MH have become more enriched in water (likely due to the loss of an apatite component) whereas SH3 PtC has lost water, presumably by loss of H_2 diffusing through the Pt outer capsule or loss to the graphite bucket.

4.8.1.3 Carbon in apatite

Carbon measurements for apatite are listed in Table 4.4. Measurements listed are for samples which contained apatite of an appropriate size for SIMS analyses. The more silicic starting compositions resulted in apatite with lower C content than the more basaltic SH3 starting composition. For the PM1 composition the wt% CO_2 ranged from a maximum of 0.08 in PM1 Pt to a minimum of 0.04 in PM1 PtC. The Hap10/Hap5 compositions showed similar levels of carbon in apatite with a maximum of 0.11 wt% CO_2 in sample NNO 1200 Hap10 down to 0.06 wt% in MH 1200 Hap10. In BMT2, the maximum CO_2 in apatite was 0.21 wt% in BMT2 Pt down to a C content minimum in sample BMT2 MH (0.09 wt%). The SH3 composition resulted in apatite with the largest wt% CO_2 contents, ranging from a maximum of 0.43 wt% in SH3 Pt to a minimum of 0.21 wt% in SH3 PtC. Carbon present in apatite could originate from

a variety of sources. Whilst every effort was made to fully decarbonate the sample during preparation of the starting materials (heating ramp from 600-1000-600 ℃), no check was made to ensure no carbon (as carbonate) was left. Another source of carbon is carbon infiltrating into the sample from the graphite furnace. As samples run in the same starting composition range in CO_2 content, degradation of the furnace appears to be the source of some of the carbon in these experiments. Samples run in single Pt capsules commonly display elevated CO_2 levels relative to double capsule experiments or Pt-C experiments in the same composition. If we assume that all samples in the same starting composition have a similar partition coefficient/exchange coefficient for C between mineral and melt then these samples are likely to have higher C contents in the silicate melts suggesting that the excess carbon in the Pt capsules (and likely C in the double capsule samples) come from carbon infiltration from the furnace. Carbon measurements in the silicate melt have not been included because of the lack of appropriate standards for SIMS analyses.

4.8.2 Gas mixing furnace glasses

All 1300 ℃ gas mixing furnace experiments (using modified Hap10 starting composition) all quenched to glass. All glasses are trachyitic in composition with the exception of Hap3 99.5 and Hap3 98.1 which are a tephriphonolite and trachyandesite respectively (Table 4.5). The Fe-Mn bearing melts (Hap3) quenched to a black glass under all f_{O_2} conditions. Hap3 air and Hap3 100 are $\approx$ 5-10% crystalline (oxide phase, presumably magnetite) based on observations from a petrographic microscope which may affect the overall oxidation state of Fe/Mn in these runs. The Mn-only glasses (Hap2) quenched to yellow/colourless glasses under most f_{O_2} conditions, with the exception of the two most oxidised runs (Hap2 air and Hap2 100) which quenched to a dark brown/black glass. No runs in the Hap2 glasses contained any identifiable additional phases on a petrographic microscope. The colour of glasses is caused by the absorption of certain wavelengths of visible light. Usually the alkali and alkaline earth silicate matrix of glasses is colourless, with the presence of small quantities of absorbing species (in this case the transitional metal(s) Mn and/or Fe) imparting absorption of certain visible frequencies of light, resulting in a brown/black or yellow/colourless glass.

Table 4.5: Averaged compositions and oxide totals for Hap2 and Hap3 glasses determined by electron microprobe[1].

	SiO_2	Al_2O_3	FeO	Na_2O	K_2O	MnO	Total
Hap2 air	61.20 ± 1.22	19.06 ± 0.39		4.83 ± 0.08	6.68 ± 0.18	8.64 ± 0.75	100.54 ± 0.69
Hap2 100	62.40 ± 1.04	17.64 ± 0.52		4.73 ± 0.17	6.80 ± 0.18	8.70 ± 0.58	100.37 ± 0.45
Hap2 99.5	61.66 ± 0.52	17.89 ± 0.66		4.75 ± 0.10	6.81 ± 0.07	9.26 ± 0.35	100.48 ± 1.12
Hap2 98.1	62.01 ± 0.73	18.07 ± 0.29		4.64 ± 0.07	6.82 ± 0.14	9.25 ± 0.34	100.90 ± 0.32
Hap2 90.5	60.76 ± 1.27	18.61 ± 0.70		4.58 ± 0.09	6.59 ± 0.15	9.23 ± 0.42	99.88 ± 0.61
Hap2 76	62.85 ± 1.70	17.62 ± 0.91		4.14 ± 0.12	6.39 ± 0.12	9.29 ± 0.93	100.41 ± 0.53
Hap2 66	63.48 ± 0.55	17.93 ± 0.10		4.38 ± 0.74	7.10 ± 1.25	6.55 ± 0.80	99.56 ± 0.80
Hap3 air	59.67 ± 1.37	19.36 ± 0.90	4.81 ± 0.17	5.02 ± 0.11	6.96 ± 0.19	3.91 ± 0.36	99.76 ± 0.41
Hap3 100	60.62 ± 1.19	18.08 ± 0.94	5.40 ± 0.11	4.88 ± 0.13	7.02 ± 0.8	3.58 ± 0.27	99.60 ± 0.52
Hap3 99.5	57.00 ± 0.75	18.43 ± 0.13	7.61 ± 0.17	4.83 ± 0.20	6.78 ± 0.07	4.38 ± 0.11	99.07 ± 0.51
Hap3 98.1	61.28 ± 1.34	18.56 ± 0.66	8.43 ± 0.66	3.16 ± 0.12	3.88 ± 0.22	4.13 ± 0.35	99.48 ± 0.24
Hap3 90.5	60.41 ± 2.26	17.78 ± 0.60	6.65 ± 0.97	4.57 ± 0.10	6.71 ± 0.23	3.75 ± 0.58	99.90 ± 0.50
Hap3 76	61.33 ± 0.86	16.95 ± 0.26	7.05 ± 0.25	4.38 ± 0.16	6.76 ± 0.11	3.64 ± 0.12	100.14 ± 0.55
Hap3 66	61.10 ± 2.03	17.75 ± 0.52	6.06 ± 0.89	4.39 ± 0.12	7.01 ± 0.21	3.48 ± 0.53	99.80 ± 0.41

[1]The averaged analyses value for each group is given along with ± 1σ.

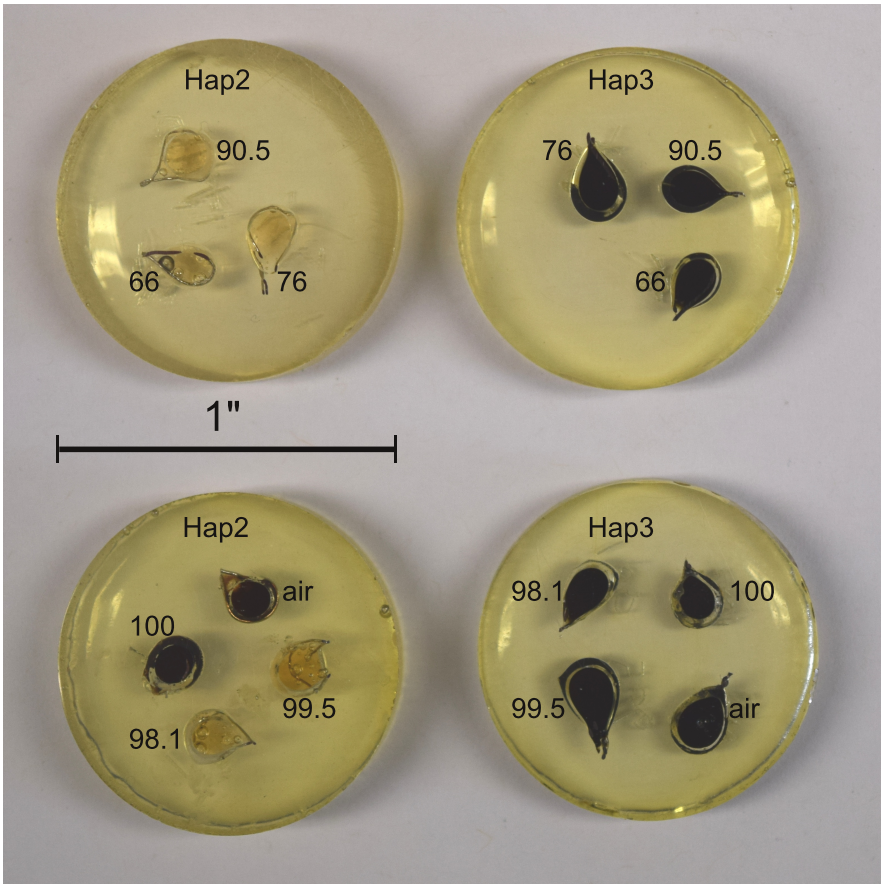

Figure 4.2: Image of glass beads from the Hap2 (Mn bearing) and Hap3 (Fe-Mn bearing) compositions mounted in a 1" epoxy block.

4.8.3 X-ray absorption near edge structure spectroscopy

4.8.3.1 Piston cylinder experiments

X-ray absorption near edge structure (XANES) spectra were collected for the PM1 composition (samples NNO, Pt, PtC) to determine if any change in the oxidation state of Mn was detectable in samples synthesised under different f_{O_2} conditions. Sample PtC should be much more reduced (NNO-2.3, where NNO ± x refers to f_{O_2} relative to the Ni-NiO buffer in log 10 units) than both the Pt and NNO samples, which are both expected to be more oxidised, around NNO+0. Spectra were obtained on both the quenched glass and apatite crystals to determine any change in Mn oxidation state in both phases.

The XANES spectra from the quenched glass (Fig. 4.3) show little variation between

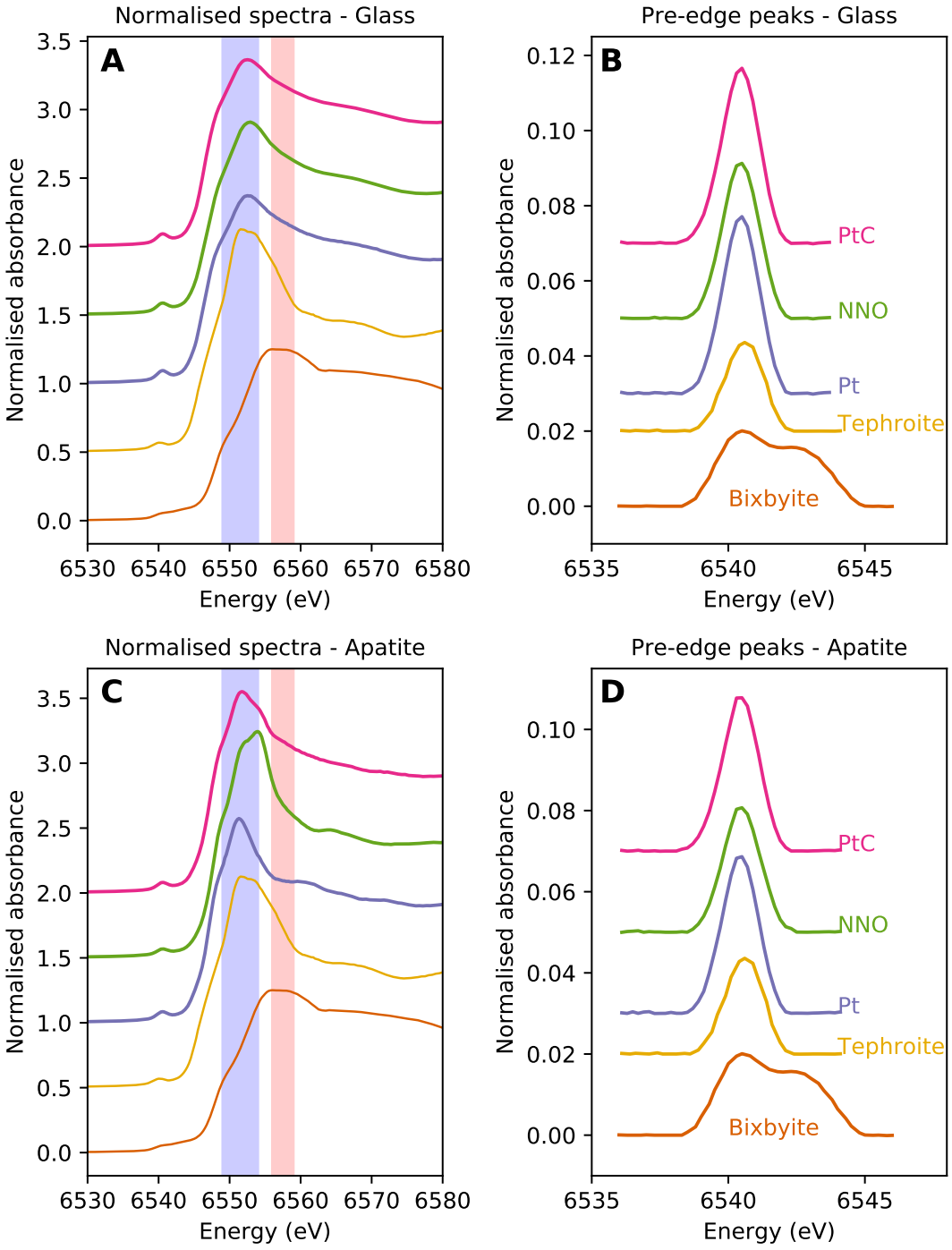

Figure 4.3: Mn K-edge XANES spectra from PC runs and standards. (A) Stacked XANES spectra for PM1-Pt glass, PtC glass and NNO glass and the standards tephroite (Mn_2SiO_4 - Mn^{2+}) and bixbyite ($(Mn,Fe)_2O_3$ - Mn^{3+}). (B) focus on the pre-edge region of A. (C) Stacked XANES spectra of PM1-Pt apatite, PtC apatite and NNO apatite , (D) focus on pre-edge peaks of C. The blue and red shaded regions on A and C indicate the range of white line (WL) positions for Mn^{2+} and Mn^{3+} standards respectively from Manceau et al. [2012].

PM1 NNO, Pt and PtC suggesting there is very little/no change in the oxidation state of Mn between these samples. When compared to tephroite (Mn_2SiO_4 – Mn^{2+}) and Mn_2O_3 (Mn^{3+}) standards, the edge position is very close to the tephroite standard suggesting Mn is in the 2+ oxidation state. There is no variation in the pre-edge peak position or intensity (Table 4.6) for these glasses. This suggests no major change in oxidation state or Mn coordination between the quenched melts, with Mn incorporated exclusively, or almost exclusively, as Mn^{2+}.

XANES spectra for the PM1 apatite grains are also displayed in Figure 4.3. There are slight differences in these 3 spectra with the position of the edge crest varying from a minimum of 6551.33 eV for PM1 Pt, 6551.75 eV for PM1 PtC and 6553.95 eV for PM1 NNO. One possibility for this shift in energy is the mean orientation of the crystals examined, rather than any change in the mean Mn oxidation state as the shape of XANES spectra is known to be affected by orientation in non isotropic minerals [Dyar et al., 2002]. A change in oxidation state is unlikely, as no significant energy shift is observed in the pre-edge region (Table 4.6.), which is less sensitive to the environment of the absorbing atom. Apatite spectra also suggests no major change in Mn oxidation state between samples, with Mn chiefly present as Mn^{2+}.

Table 4.6: Pre-edge peak fitting for PM1 Pt, PM1 PtC and PM1 NNO. Apt = apatite.

Sample	Centroid (eV)	Intensity
PM1 Pt Glass	6540.46	0.078
PM1 PtC Glass	6540.43	0.080
PM1 NNO Glass	6540.46	0.071
PM1 Pt Apt.	6540.44	0.064
PM1 PtC Apt.	6540.44	0.063
PM1 NNO Apt.	6540.49	0.054

4.8.3.2 Gas mixing furnace glasses

Mn K-edge and Fe K-edge data were also collected for the Hap2 and Hap3 glasses. Again the pre-edge peaks were fitted with Gaussian peaks to gain insight into the mean valence and coordination of Mn and Fe in these samples. Mn spectra from Hap2 glasses are shown in Figure 4.4 along with background subtracted pre-edge peaks. There appears to be no observable shift in energy between the samples suggesting that

in all spectra Mn is in a similar valence and environment. When compared to the single valence standards tephroite (Mn^{2+}) and bixbyite (Mn^{3+}) the position of the intensity averaged centroid (Table 4.7) and the location of the main edge suggests divalent Mn dominates in these glass samples. Hap2 samples have similar averaged intensity, which also suggests that Mn is in a similar coordination in all glasses.

Table 4.7: Pre-edge fitting centroid position and intensity of Hap2 and Hap3 1atm. glasses from gas mixing experiments.

		Mn		Fe	
	Log f_{O_2}	**Intensity**	**Centroid (eV)**	**Intensity**	**Centroid (eV)**
Hap2 air	-0.7	0.090	6540.50		
Hap2 100	-1.5	0.094	6940.53		
Hap2 99.5	-5.1	0.095	6540.52		
Hap2 98.1	-6.3	0.095	6540.53		
Hap2 90.5	-7.8	0.089	6540.52		
Hap2 76	-8.9	0.092	6540.53		
Hap2 66	-9.4	0.102	6540.53		
Hap3 air	-0.7	0.089	6540.48	0.165	7114.08
Hap3 100	-1.5	0.097	6540.46	0.186	7114.05
Hap3 99.5	-5.1	0.095	6540.50	0.102	7113.33
Hap3 98.1	-6.3	0.093	6540.51	0.113	7113.14
Hap3 90.5	-7.8	0.090	6540.50	0.101	7112.97
Hap3 76	-8.9	0.091	6540.50	0.100	7112.92
Hap3 66	-9.4	0.092	6540.51	0.105	7112.92
Tephroite[1] (Mn^{2+})			6540.53		
Bixbyite[1] (Mn^{3+})			6542.11		
Fayalite[2] (Fe^{2+})					7112.96
Aegirine[2] (Fe^{3+})					7114.43

[1]Standards measured during this and in previous synchrotron sessions. [2]Standards from Wilke et al. [2001] corrected for Fe calibration of 7112 eV instead of 7111.08 eV.

Mn pre-edge peak spectra for the Mn K-edge of Hap3 glass are shown in Figure 4.5. Once again, there is no observable shift in the Mn pre-edge peak energy, suggesting that in all spectra, Mn is in a similar valence and environment. The position of the intensity averaged centroid and the location of the main edge suggests Mn^{2+} dominates in these glass samples. In contrast, the Fe K-edge pre-edge peaks obtained from the same glass samples (Fig. 4.5) show a clear shift in pre-edge peak centroid to higher energy with more oxidising conditions.

The oxidation state of Fe in the Fe bearing glasses has been determined using the variogram diagram from Fiege et al. [2017] which is based on the work of Wilke et al. [2001] (Figure 4.6). Wilke et al. [2001] collected spectra for end member fourfold-, fivefold- and sixfold- coordinated ferrous and ferric standards in transmission mode

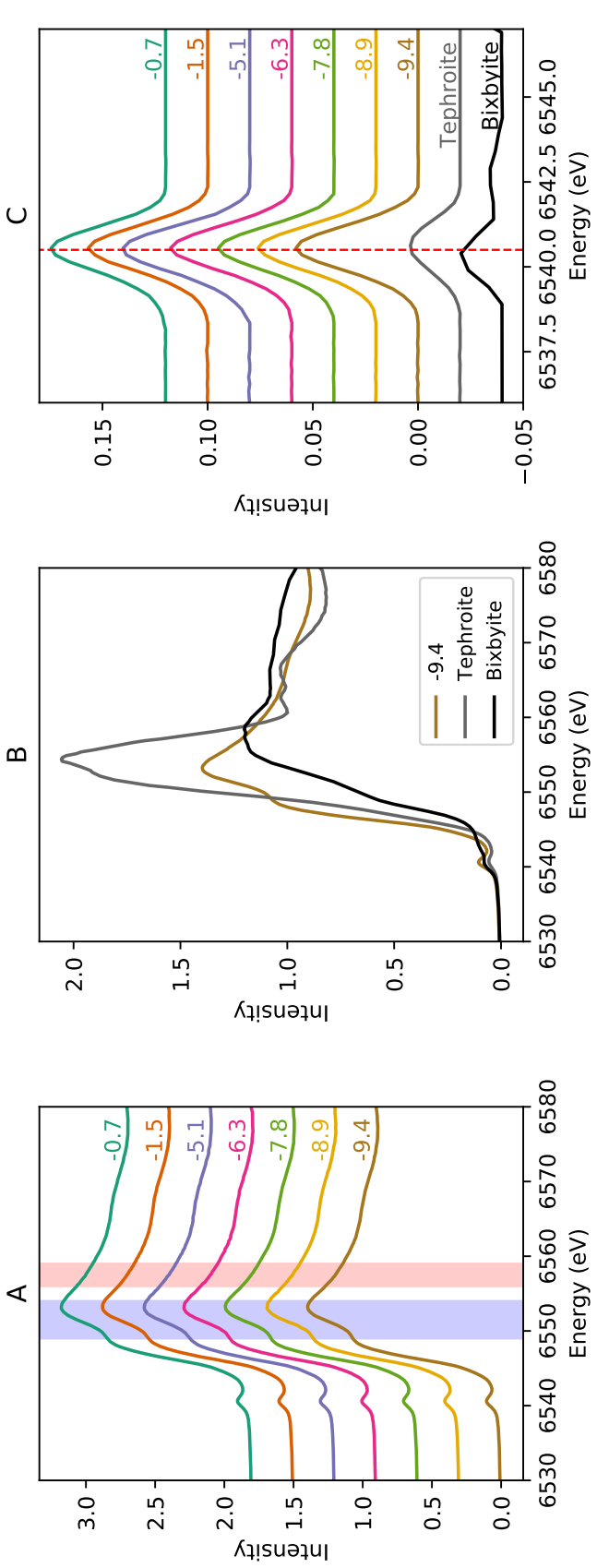

Figure 4.4: Plots of A) XANES region for Hap2 glasses, labelled in terms of absolute log f_{O_2} (air = -0.7, 100 =-1.5, 99.5=-5.1, 98.1=-6.3, 90.5=-7.8, 76=-8.9 and 66=-9.4). Each spectra have been vertically offset for clarity. The blue shaded area denotes the range in WL positions of Mn^{2+} standards and the red shaded area denotes the range in WL position for Mn^{3+} standards from Manceau et al. [2012]. B) position of the Mn^{2+} and Mn^{3+} standards (tephroite and bixybite respectively) against Hap2-66 (labelled in terms of absolute f_{O_2} as -9.4), and C) pre-edge peaks of spectra in A along with the two Mn standards, also vertically offset for clarity. The Mn^{3+}standard bixybite shows how the Mn^{3+}pre-edge peak has to be modelled with more components than the Mn^{2+} pre-edge peak.

[Wilke et al., 2001] and this has been combined with similar mineral standards collected in the fluoresecence geometry [Giuli et al., 2003] for various crystalline compounds. The grey ellipses represent the spread in intensity and centroid position for these compounds.

Samples 90.5, 76 and 66 plot in the grey ellipse representing the pre-edge intensity and centroid position for Fe^{2+} standards in five fold coordination from the work of Giuli et al. [2003]. This could suggest that all Fe in the melt is in five-fold coordination, or, Fe is in a mix of four fold, six fold coordination and potentially five-fold coordination. The centroid position for samples 98.1 and 99.5 plot closer to 1.2 eV above the Fe foil inflection point. This suggests that both samples contain Fe in a higher oxidation state than samples 90.5, 76 and 66. The samples which were synthesised under the most oxidised conditions, Hap3 air and Hap3 100, plot with a centroid position close to the pure Fe^{3+} standards, and suggest that roughly 75% of Fe is in the 3+ oxidation state. Air and 100 also plot between ^{IV}Fe and ^{VI}Fe, although, greater proportions of ^{VI}Fe may be present in these two most oxidised samples.

Over the large f_{O_2}-T space explored for the high pressure and 1 atm. glasses, I have been unable to produce any meaningful change in the oxidation state of Mn, and Mn^{2+} appears to dominate in all samples. This is unsurprising as glasses in sodium silicate and borosilicate systems synthesised in air have Mn^{3+}/Mn^{2+} ratios of 0.05-0.1 [Kohn et al., 1990], and Watson [1977] could only identify divalent Mn in silicate glasses under similar f_{O_2} conditions. The position of the Mn^{2+}/Mn^{3+}redox couple has now been added to the other data in Figure 1.5 (page 16) to create Figure 4.7, and clearly shows that trivalent Mn is only found under very oxidising conditions and is therefore unlikely to exist in substantial quantities in terrestrial magmas. The Mn data comes from the electrochemical series of redox couples in silicate melts by Schreiber [1987]. In addition to the glass, the average oxidation state of Mn in apatite also does not change as a function of f_{O_2}-T conditions over this range and is almost exclusively all Mn^{2+}.

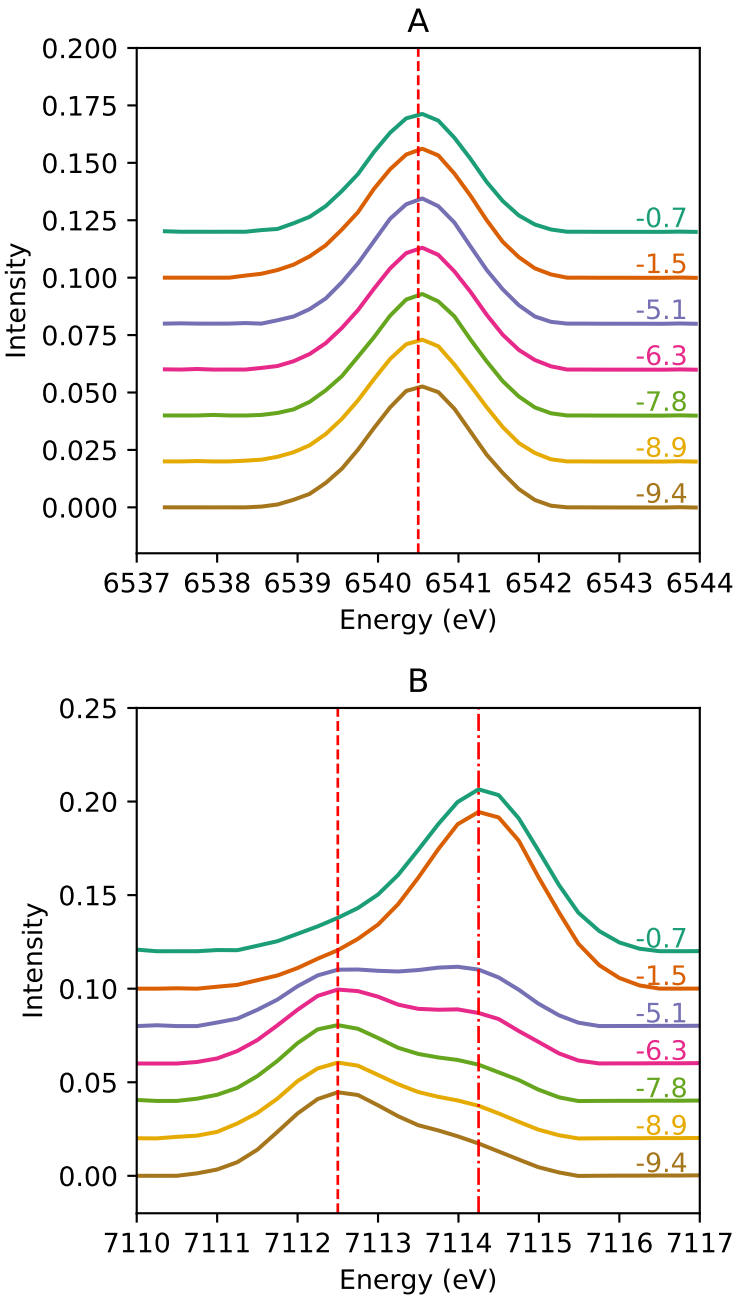

Figure 4.5: (A) Mn K-edge and (B) Fe K-edge spectra acquired on the same set of Fe-Mn doped granitic glass. Each spectra is labelled with the log f_{O_2} value at which the glass was synthesised. For reference log f_{O_2} of NNO = -6.5 at 1300 ℃.

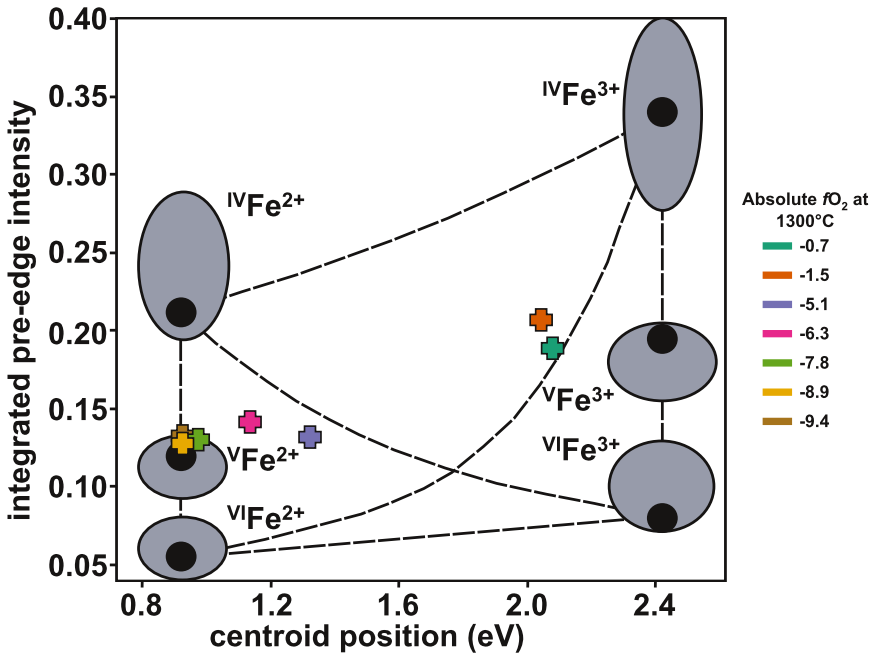

Figure 4.6: Variogram [Wilke et al., 2001] that shows the average centroid position and integrated pre-edge intensity for Fe reference crystalline compounds in single valence/single coordination (grey ellipses and black dots). Also plotted are the centroid position and intensity for the Fe-Mn doped granitic glasses from this study (crosses). For reference log f_{O_2} of NNO = -6.5 at 1300 ℃.

4.9 Discussion

4.9.1 The colour of Hap2 glasses

The optical properties of glasses is strongly influenced by their structure. The two most oxidising Hap2 glasses are dark black in colour, compared to the yellow-colourless colour of the more reduced runs. Linwood & Weyl [1942] suggests that divalent Mn when present in glass should cause a yellow-brown coloration, and trivalent Mn causes a purple colouration [Linwood & Weyl, 1942]. Linwood & Weyl [1942] suggest that the coordination of divalent Mn has little to no effect on the colour of Mn glasses. This brings into question why the more reduced runs of Hap2 are dark brown-black in colour when XANES suggests that Mn in all glasses is primarily in the 2+ oxidation state. Is the XANES technique insensitive to trivalent Mn, is the presence of nano-crystals (nanolites) affecting melt colour, or could there be an effect of Mn coordination on the colouration of divalent Mn? More work is needed to determine which hypothesis is the likely cause of the colouration.

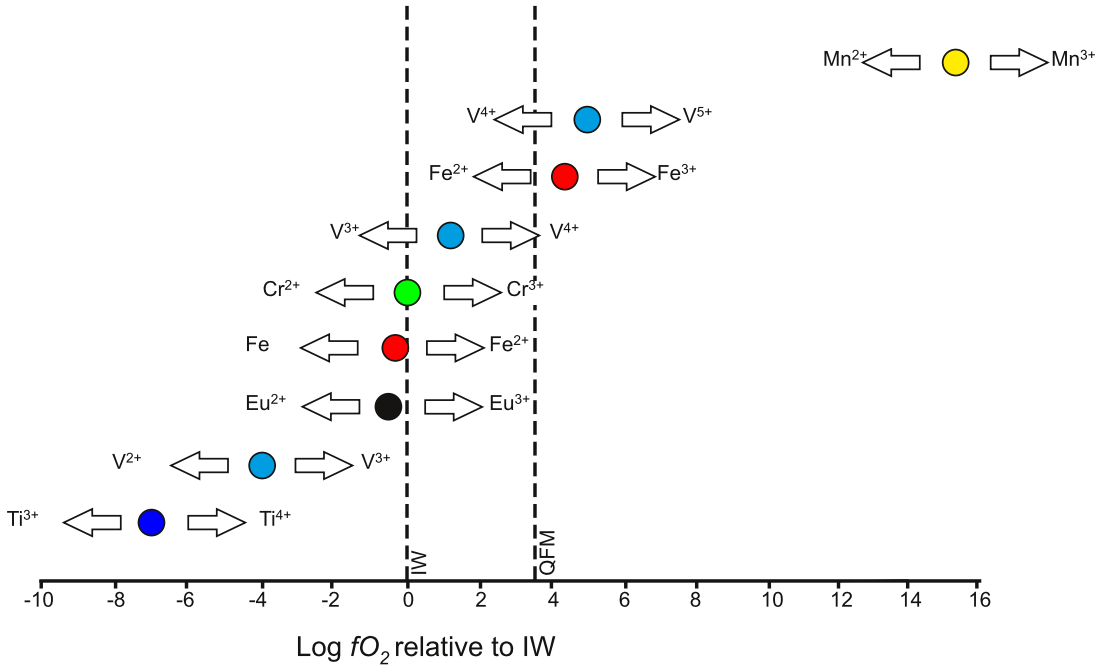

Figure 4.7: Updated version of Figure 1.5 (page 16) showing the valence state of the Mn^{2+}/Mn^{3+} redox pair. Figure adapted from Herd [2008], and Mn data is from Schreiber [1987].

4.9.2 Mn and Fe coordination in felsic glass

The coordination of Fe^{2+} in silicate glasses is still debated [Jackson et al., 2005]. This is because, according to Mössabauer, vibrational and optical absorption studies, Fe^{2+} should predominantly be in [6] coordination, whilst molecular dynamics calculations on anhydrous Fe^{2+} silicate melts suggests a continuum between [4], [5] and [6] [Jackson et al., 2005; Mysen, 2006]. More recent discussion by Alderman et al. [2017] highlights that the average Fe-O coordination number (n_{FeO}) for silicate glass is between 4.4 and 4.7 for all $Fe^{3+}/\sum Fe$ based on XRD data, which is consistent with XANES pre edge peak analysis which suggests an average n_{FeO} of 5. The XRD data would suggest that 4-fold and 5-fold Fe coordination dominates, and only a maximum of 20-35% 6-fold coordinated Fe can be present (in the case of no five-fold Fe). Bond lengths in the Fe_2SiO_{4+x} melts investigated by Alderman et al. [2017] range from 1.95-1.88 Å which is consistent with the distances associated with $Fe^{2+}O_4$ and $Fe^{3+}O_5$. Alderman et al. [2017] like the rest of the studies into the structure of Fe in silicate glass cannot conclusively determine if Fe is presence dominantly in the [4] + [5], [4] + [6] or [4] +

[5] + [6] coordination.

The anhydrous glasses synthesised in the gas mixing furnace (Figure 4.6) suggest that [6] Fe^{2+} does not dominate, as has been previously suggested, but it cannot determine if 100% Fe^{2+} is in [5] coordination or a mixture of [4], [5] and [6] coordination. Other studies using the variogram of Wilke et al. [2001] also suggest that the mean coordination of Fe^{2+} is [5] but also cannot determine the relative proportions of [4], [5] and [6].

Fe^{3+} iron is more prevalent in samples synthesised at log f_{O_2} = -0.7 and -1.5. Once again, the coordination of Fe is close to the position of [5] coordinated Fe (from extrapolation between fivefold Fe^{2+} and fivefold Fe^{3+} standard positions.). The Fe^{3+} in our samples is in an apparent higher coordination than in the variogram for felsic glasses from Fiege et al. [2017] (mostly fourfold coordinated), and acts much more like their dry basalt sample (Wi05). The Hap3 glasses may be acting more like the anhydrous glasses in Fiege et al. [2017] due to the alkali composition of the glass. Coordination of Fe in the glasses is known to be strongly related to the alkali content of melt, with [4] coordination dominating for Fe^{3+} in Na-bearing silicate rich melts and [4] and [6] dominating in Ca-bearing silicate melts [Jackson et al., 2005]. Another possibility is that there is an effect in the normalisation and self absorption correction which is affecting the intensity of the pre-edge feature.

Only a few studies have examined the structural position and oxidation state of Mn in silicate glass. Kajinami et al. [2003] looked at the structure and oxidation state of Mn in borate glass and found Mn was present in the glass as divalent ions in tetrahedral coordination. The Mn K edge pre-edge peaks from the Hap2/Hap3 compositions show no real variation in intensity or position with f_{O_2}, which suggests that Mn in the glasses are all in a similar coordination and oxidation state. Without further single and mixed coordinated Mn standards collected at the same time as the glasses in this study it is hard to determine the coordination of Mn in these samples based on XANES, as no tool, such as the variogram for Fe [Wilke et al., 2001], exists. This is probably in part due to the much smaller difference in centroid position between Mn^{2+} and

Mn^{3+} (≈0.4 eV) [Farges, 2005] compared to Fe^{2+} and Fe^{3+} (≈1.6 eV), lack of Mn standards in tetrahedral and cubic coordination, and the fact that Fe is much more important/abundant in geological systems. Based on the pre-edge peak intensity of the galaxite spinel from chapter 3, it would be expected that these samples contain a mix of fourfold and sixfold coordinated Mn, and/or may contain fivefold coordinated Mn also. Photoluminescence is a possible technique by which further information on Mn coordination in these samples could be obtained [Ehrt, 2009].

The piston cylinder samples all have Mn pre-edge peak intensities lower than the samples from the gas mixing furnace, and coordination appears to remain constant between piston cylinder runs. Lower intensities for the piston cylinder experiments would suggest a higher coordination in these samples (less tetrahedral coordination, more octahedral coordination) than the gas mixing samples. One explanation is that the piston cylinder experiments are hydrous, and that this may affect Mn coordination. Kohn et al. [1990] found that the XANES pre-edge peak intensity and Mn-O bond lengths from anhydrous glasses to hydrous silicate glasses changed, due to an increase in octahedrally coordinated Mn with water dissolution. It is also unknown whether pressure in the piston cylinder subtly alters melt structure around Mn ions, presuming that this is retained on isobaric quenching to glass.

4.9.3 The Fe oxidation state of Hap3 and comparison to the empirical expression for ferrous-ferric iron

Whilst care was taken to ensure the gas mixing furnace was gas tight, the actual f_{O_2} of these experiments was not measured in-situ with a sensor, but assumed to be close to the value for the chosen gas mix from Deines et al. [1974]. However, for the Fe-containing Hap3 glasses, the ferrous-ferric ratio of iron can be linked to oxygen fugacity at one atmosphere by the empirical relationship originally documented in Fudali [1965] and modified to account for the composition of the melt (chapter 1, section 1.3).

$$ln\left\{\frac{X_{Fe_2O_3}}{X_{FeO}}\right\} = a\ ln f_{O_2} + \frac{b}{T} + c + \sum d_i X_i \qquad (4.2)$$

Where a, b, c, and d_i are constants obtained by regression and X_i is the mole fraction of several major element oxides in the melt [Baker & Rutherford, 1996]. At the temperature and pressures in this study, f_{O_2} was calculated using the regression constants listed in Kress & Carmichael [1991] (Table 4.8).

Table 4.8: Regression coefficients listed in Kress & Carmichael [1991].

	Value	Units
a	0.196	
b	1.1492 x 10^4	K
c	-6.675	
$d_{Al_2O_3}$	-2.243	
d_{FeO^*}	-1.828	
d_{CaO}	3.201	
d_{Na_2O}	5.855	
d_{K_2O}	6.215	

Equation 4.2 can be applied to determine the ferric-ferrous ratio expected for the selected gas mixes from Deines et al. [1974]. When the temperature, composition and f_{O_2} values expected for each experiment are input into Equation 4.2 the following % Fe^{2+} for each sample are shown in Table 4.9.

Table 4.9: Comparison of % Fe^{2+} from XANES and using Equation 4.2

	Air	100	99.5	98.1	90.5	76	66
% Fe^{2+} XANES	22.8	25.4	72.9	85.1	96.4	$\sim$ 100	$\sim$ 100
$\pm$ % error XANES	0.2	0.3	0.2	0.1	0.6	UNK.	UNK.
% Fe^{2+} Eqn. 4.2	36	45	80	90.5	93.5	95	97
f_{O_2} based on % H_2	-0.7	-1.5	-5.1	-6.3	-7.8	-8.9	-9.4
f_{O_2} based on % Fe^{2+} XANES	0.7	0.4	-4.1	-5.2	-9.2	<-12	<-12

As expected, both the % Fe^{2+} values from XANES and Equation 4.2 show a decrease in the % Fe^{2+} with more oxidised conditions. However when the magnitude of the % Fe^{2+} from the two techniques is compared, the estimated values show deviation from each other, especially for the more oxidised estimates.

Variations in the two estimates may arise from shortcomings in the two techniques of calculating either Fe oxidation state from XANES or using Equation 4.2. Equation 4.2 was never tested on melts as rich in MnO as Hap3, so there might be an added compositional effect of Mn which has to be accounted for. Borisov et al. [2015] also suggested that the effect of melt composition cannot be accurately predicted using the

term $\sum d_i X_i$ due to the varying behaviour of Al_2O_3 and MgO in basaltic and silicic melts. The presence of what is presumably an oxide phase in Hap3 air/100 may also account for variation in the estimated and calculated f_{O_2}/Fe^{2+}. Finally, the actual buffered environment inside the furnace may have varied from the value predicted by Deines et al. [1974].

4.9.4 Oxygen fugacity and Mn partitioning

Although the oxidation state of Mn has been shown to be exclusively Mn^{2+} in melts, across a range of f_{O_2} conditions, we plotted up D_{Mn}^{Ap-m} (where $D = C_{Ap}/C_m$) to test the relationship defined by Miles et al. [2014] (Fig. 4.8).

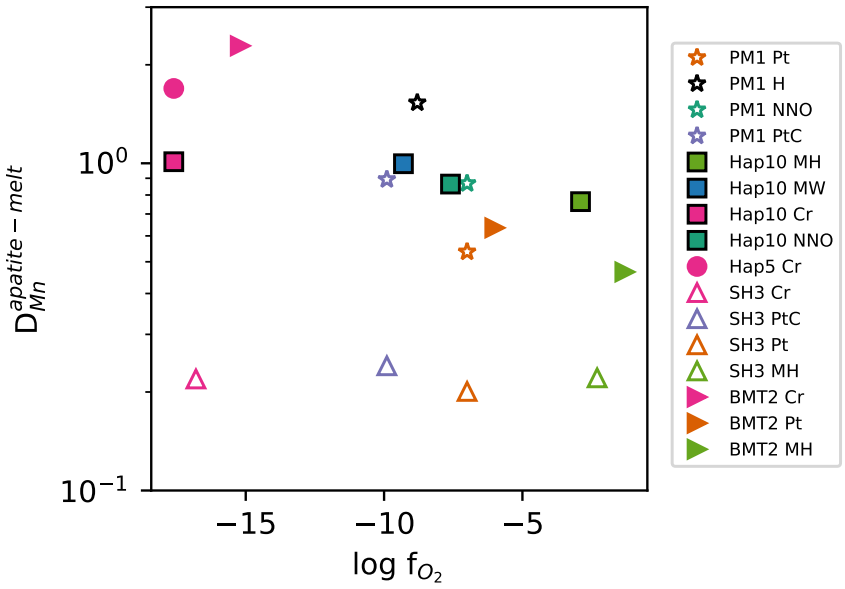

Figure 4.8: D_{Mn}^{Ap-m} plotted as a function of log f_{O_2} for apatite-melt partitioning experiments from this study.

All samples in the SH3 haplo-basaltic composition show no real variation in D_{Mn}^{Ap-m} as a function of f_{O_2}, even though there is a variation of approximately 17 log units in f_{O_2} between samples. Similarly, there is no obvious relationship between f_{O_2} and D_{Mn}^{Ap-m} for PM1 and Hap10 melt compositions. This suggests that f_{O_2} is not the main controlling parameter on Mn apatite-melt partitioning in these compositions, and that other factors have a much more significant influence on Mn partitioning. However, samples in the BMT2 composition show an increase in D_{Mn}^{Ap-m} with decreasing f_{O_2}.

This observation may indicate a link between f_{O_2} and D_{Mn}^{Ap-m}, although, this is unlikely to be due to changes in the availability of Mn^{2+} in the melt as the XANES data indicates that the Mn^{2+}/Mn^{3+} ratio does not vary over a similar range in f_{O_2} to these experiments. The f_{O_2} - D_{Mn}^{Ap-m} trend for BMT2 coincidentally corresponds to changes in melt compositions.

4.9.5 Melt polymerisation and Mn partitioning

It has long been recognised that trace element partition coefficients tend to be higher for minerals in equilibrium with more silicic melts [Blundy & Wood, 2003; Kohn & Schofield, 1994]. Although this may partly reflect disparity in the temperature and pressures of these systems, it is thought the extent of melt polymerisation is a control on element partitioning [Mahood & Stimac, 1990; Schmidt et al., 2006]. Silicic melts have a more polymerised structure which might make certain elements less compatible in the melt structure than for less polymerised (i.e. less silicic) melts. Polymerisation is a measure of the extent to which silica tetrahedra within the melt structure are linked together. As tetrahedral sites are linked together by shared oxygens (bridging oxygens), an increase in the extent of polymerisation typically means a reduction in the ability of the melt to incorporate other elements. Polymerisation of a melt can be compared in a variety of ways. In more felsic systems the aluminium saturation index (ASI: molar ratio $Al_2O_3/(Na_2O+K_2O+CaO)$) often provides an indication on melt polymerisation [Prowatke & Klemme, 2005]. However, the ratio of non-bridging oxygen's (NBO) to tetrahedrally coordinated cations (T) is becoming the standard indicator of melt polymerisation [Cottrell et al., 2009b]. NBO/T = 0 represents a fully polymerized melt, whereas 4 represents a fully depolymerised melt of isolated tetrahedral [Mysen, 1983]. Here NBO/T was calculated using the procedure originally document by Mysen et al. [1985].

Figure 4.9 displays the relationships between D_{Mn}^{Ap-m} with NBO/T and ASI for samples reported here and in equivalent literature studies. ASI data from McCubbin et al. [2015] have not been included given the lack of K_2O in their compositions. Both ASI and NBO/T parameters are intrinsically linked, but there appears to be a stronger re-

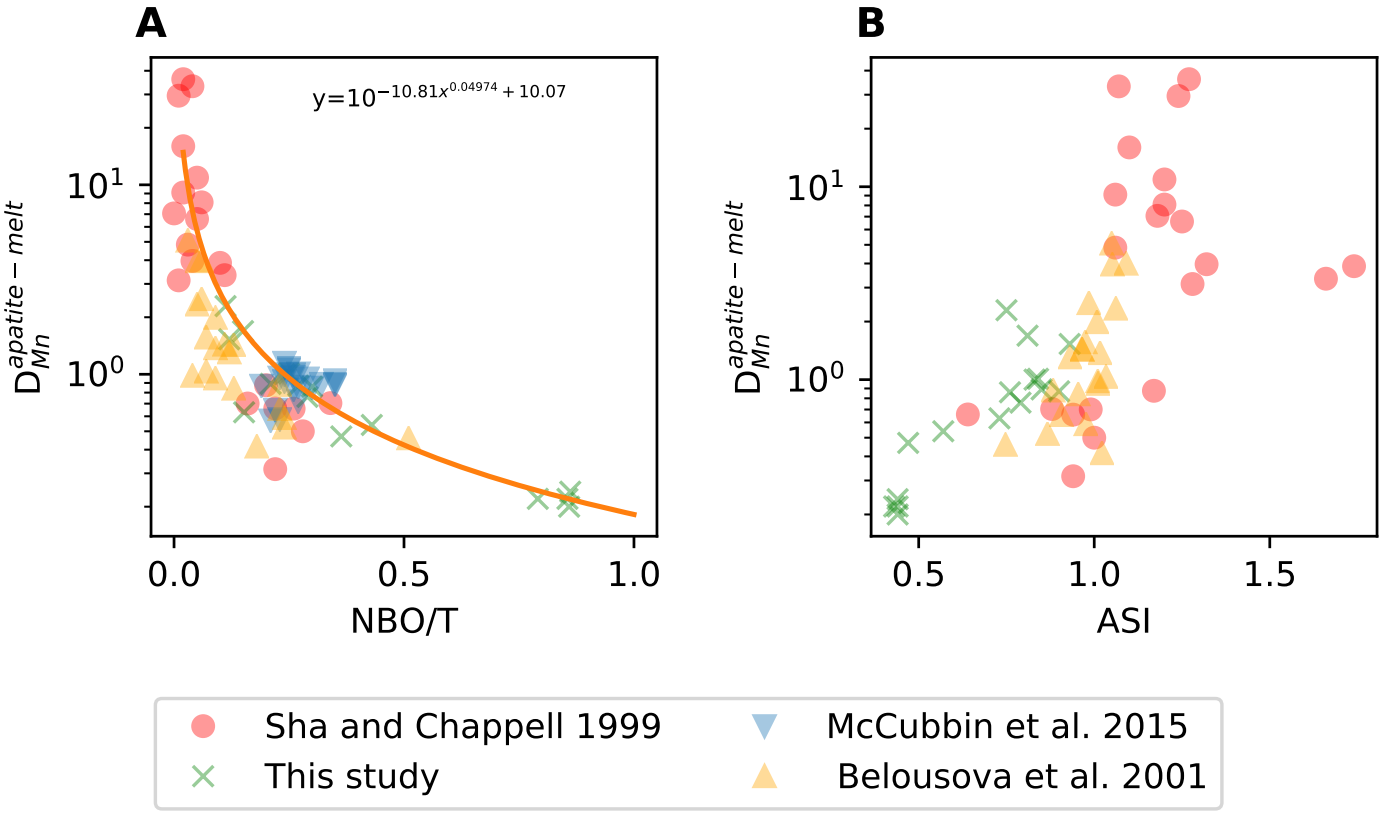

Figure 4.9: D_{Mn}^{Ap-m} plotted as a function of ASI (Aluminium saturation index) and NBO/T (number of nonbridging oxygen per tetrahedral cation) for samples in this study and those from Sha & Chappell [1999], Belousova et al. [2001], and McCubbin et al. [2015]. The power fit is fitted using data from this study, Sha & Chappell [1999], and McCubbin et al. [2015]. Belousova et al. [2001] data is not used for the power law fit because although the data shows a similar trend to other studies, there is an unexplained offset to lower NBO/T.

lationship between NBO/T and D_{Mn} than ASI, indicating melt polymerisation is more important than aluminosity in dictating Mn apatite-melt partitioning. ASI provides some detail on melt structure as Al is normally assigned as a tetrahedrally coordinated cation unless Al > Na + K + 2Ca + 2Mg. Excess Al is assigned as a non-tetrahedrally coordinated cation. ASI is also an important variable when considering the solubility of apatite in melts, with apatite solubility increasing linearly with ASI up to ASI = 1.3 [Wolf & London, 1994]. The partitioning of Mn into apatite in equilibrium with more polymerised melts appears to be considerably greater than when in equilibrium with more depolymerised melts, implying that there is a strong influence of melt structure on the partitioning of Mn between apatite and melt. This relationship may arise from the fact that Mn is most likely incorporated into melt networks onto octahedral sites. In more polymerised melts, there will be a higher fraction of bridging oxygens. As such, the availability of non-bridging oxygens is lower, and the ability of melt networks to incorporate metal cations such as Mn^{2+} will be reduced.

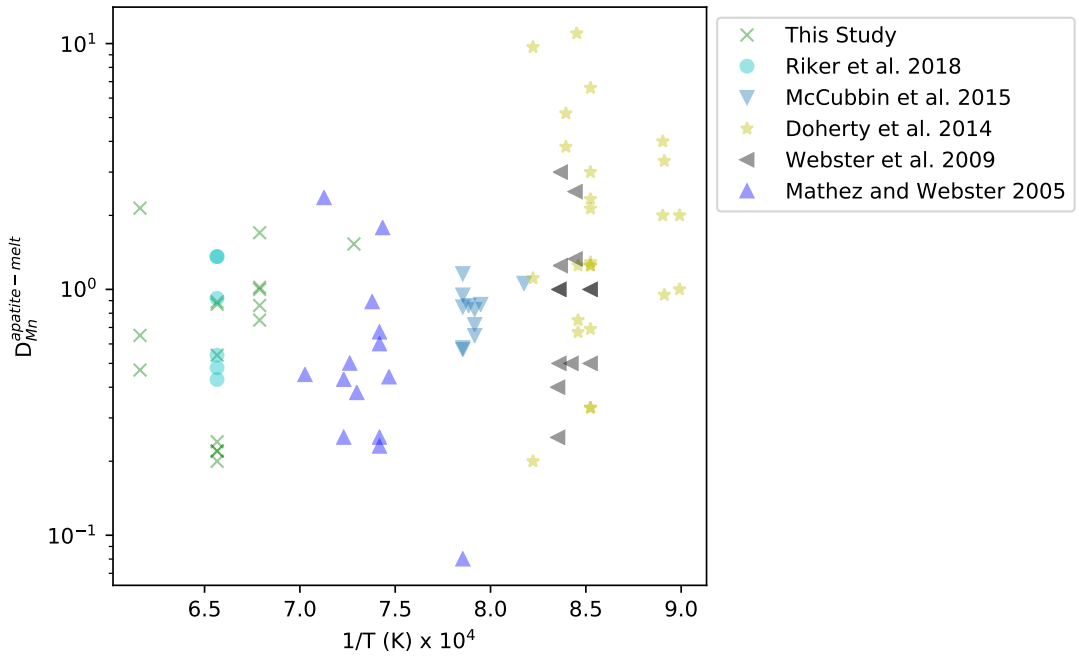

Figure 4.10: D_{Mn}^{Ap-m} plotted as a function of 1/T (K) × 10^4 for samples in this study and those from Mathez & Webster [2005], Webster et al. [2009], Doherty et al. [2014], McCubbin et al. [2015], and Riker et al. [2018].

A similar relationship was documented for D_{Mn}/D_{Zn} (olivine-melt) by Kohn & Schofield [1994], who demonstrated that melt composition has a stronger affect on mineral-melt

partitioning than temperature. Figure 4.10 shows that for the case of apatite-melt experiments, temperature is not an important control on the partitioning of Mn, and melt structure dominates. Other parameters are equally likely to be important on Mn apatite-melt partitioning (which haven't been explored here), with further work needed on the effects of crystal chemistry and crystal site size.

Mn in apatite is unlikely to behave as a simple trace element as it can occur in major element concentrations generally competing in the same crystallographic sites as Ca. This is why it is not useful to carry out a Henrian test that one might use for other traces. The availability of Ca/Mn in the melt may strongly affect the uptake of Mn into apatite. However, in this system a simple exchange coefficient cannot be applied as the Ca site can also replace Ca with various other elements, and the chemistry of this site is likely to be strongly controlled by crystal chemistry. I examined the power law relationship of Figure 4.9 for only low Mn concentrations in apatite (less than 0.1 wt% MnO in apatite), and there is still a power law relationship between D_Mn and NBO/T. The same is true when only examining samples with high Mn concentrations in apatite (<0.1 wt% MnO). This suggests that whilst not necessarily Henrian behaviour is occurring for the partition of Mn between apatite and melt, the control of melt composition still applies.

4.9.6 Mn content of apatite at Criffel pluton

Miles et al. [2014] argued that variations in Mn contents of apatite from different zones within the Criffell granitic pluton (southern Scotland) correlated with changes in melt f_{O_2}, and were relatively independent of other parameters. As the partitioning data presented here indicates there is no relationship between D_{Mn}^{Ap-m} and f_{O_2}, we used the range of compositions from our study to test other hypotheses. If we apply the NBO/T to D_{Mn}^{Ap-m} power relationship given in Figure 4.9 to the data for the Criffel pluton, we can determine apparent D_{Mn}^{Ap-m} for the relevant melt compositions. NBO/T was calculated from whole rock compositions [Miles et al., 2013b; Stephens & Halliday, 1980] for the 4 petrologically distinct zones of the pluton for which apatite Mn concentrations were available [Miles et al., 2014]. Apatite saturation temperature, and the textural

evidence that most apatite in the Criffel Pluton occurs as inclusions in other minerals [Miles et al., 2014] supports apatite being an early crystallising phase. Whilst apatite is unlikely to have crystallised in these exact whole rock compositions, they are the best estimation for the magma in which apatite crystallised, and this seems a reasonable estimation if apatite was an early crystallising phase.

Table 4.10: Whole rock geochemistry for thought to be representative of the four petrologic zones at the Criffel Pluton. [1]Values from Miles et al. [2013b]. [2]Values from Stephens & Halliday [1980].

	Zone 1 (09-17)[1]	**Zone 2 (09-18)**[1]	**Zone 3 (09-21)**[1]	**Zone 4 (274)**[2]
SiO_2	63.92	66.04	69.52	71.35
TiO_2	0.58	0.53	0.36	0.21
Al_2O_3	15.75	15.33	15.10	15.39
FeO^T	3.24	2.74	1.89	1.33
MnO	0.06	0.05	0.04	0.04
MgO	2.51	1.97	0.93	0.97
CaO	3.82	2.67	2.02	0.90
K_2O	3.35	3.86	4.20	4.70
Na_2O	4.12	3.99	3.84	3.84
P_2O_5	0.29	0.26	0.17	0.10
NBO/T	0.18	0.13	0.06	0.03

Whole rock MnO contents were combined with the modelled D_{Mn}^{Ap-m} based on NBO/T to predict apatite MnO, and then data was converted to ppm for comparison. This method can predict a reasonable fit of the predicted Mn apatite content (ppm) based on NBO/T, with measured apatite concentrations from EPMA and SIMS data (Miles et al. 2014; Fig. 4.11). The error in Figure 4.11 is large, indicating the sensitivity of apatite Mn content to the power law fit. The predicted Mn apatite content is also very sensitive to the modelled bulk rock composition and bulk rock MnO content. However, to a first approximation, it appears that the variation seen in apatite Mn concentration at Criffel can be explained solely by variations in NBO/T rather than f_{O_2}. This is, perhaps, unsurprising as XANES work indicates that over the range of f_{O_2} conditions inferred for this pluton, there is no change in the oxidation state of Mn^{2+} in silicate melt.

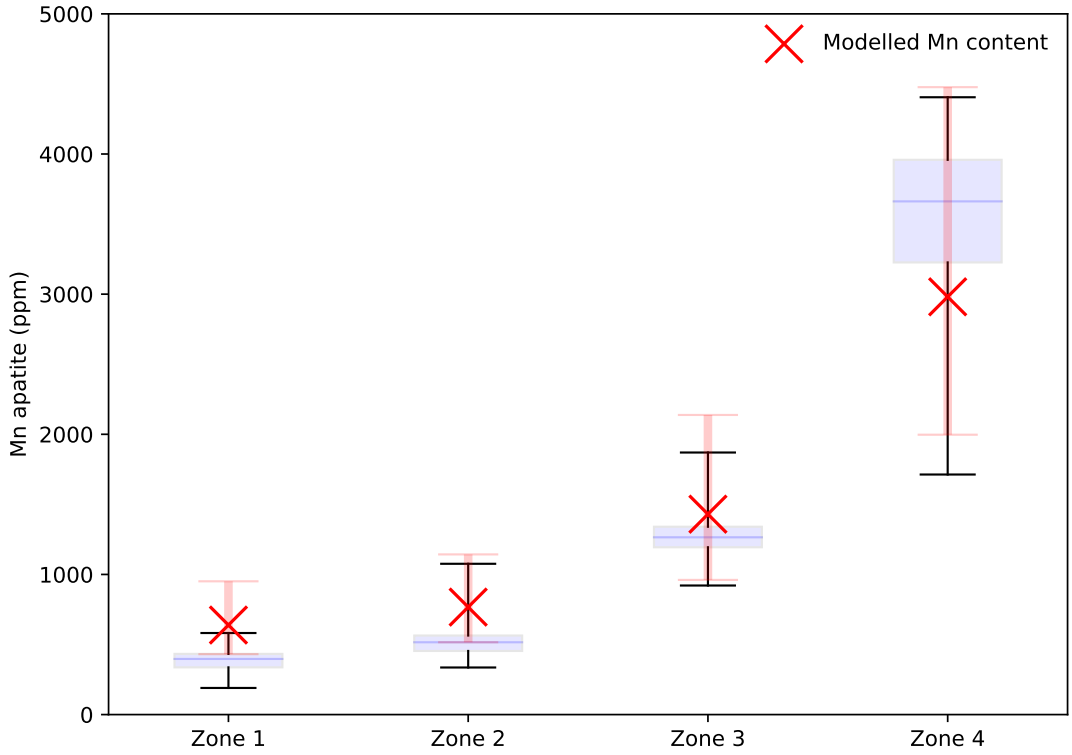

Figure 4.11: Boxplot of Mn apatite concentration (ppm) for the 4 petrologically distinct zones of the Criffel Pluton [Miles et al., 2014]. The NBO/T for the 4 zones are 0.18, 0.13, 0.06 and 0.03 for zones 1-4 respectively. The blue box highlights the interquartile range for the dataset, with the blue line indicating the median value. The black whiskers represent the range of the dataset. Overlaying this data is the apparent Mn apatite concentration (red crosses) determined from the power law relationship between NBO/T and D_{Mn}^{Ap-m} shown in Fig. 4.9, and associated error (red lines).

4.9.7 Volatile partitioning as a function of melt structure and oxygen fugacity

Manganese is unlikely to be the only element for which apatite-melt partitioning is affected by melt composition. The partitioning of anions between apatite and melt may also be affected by NBO/T. Figure 4.12 shows that D_{Cl}^{Ap-m} is also linked to melt structure for dominantly hydroxyapatite compositions ($X_{H_2O}^{Ap}$ >0.5 a.p.f.u.) where $X_{H_2O}^{Ap} \gg X_F^{Ap}$ and X_{Cl}^{Ap}. In Figure 4.12, data from this study as well as Doherty et al. [2014] and Prowatke & Klemme [2006], show a general increase in D_{Cl}^{Ap-m} with increasing polymerisation of the melt. This is similar to the trend noted for D_{Mn}^{Ap-m}, with Cl becoming more incompatible in the melt with higher degrees of polymerisation. This would suggest that as the number of non-bridging oxygens drops in the melt with increasing melt

polymerisation, so does the compatibility of Cl in the melt [Signorelli & Carroll, 2002], increasing Cl partitioning into the apatite.

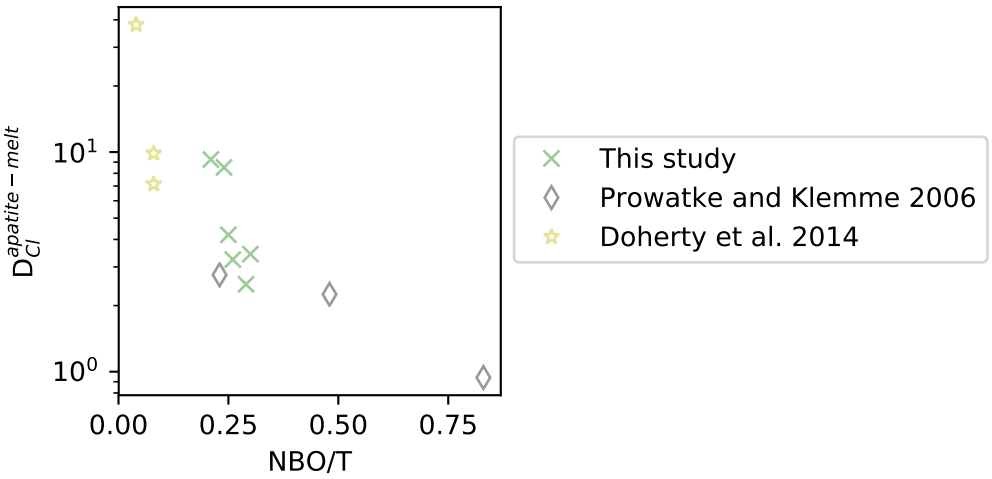

Figure 4.12: D_{Cl}^{Ap-m} against melt NBO/T for our study and literature data [Doherty et al., 2014; Mathez & Webster, 2005; Webster et al., 2009].

However, it has been argued that Nernst partition coefficients are not suitable when examining the distribution of halogens and water between apatite and melt [Boyce et al., 2014; McCubbin et al., 2015] as the combined concentration of Cl, F and OH in the apatite structure is fixed based on stoichiometry [McCubbin et al., 2015]. A more suitable measure of volatile partitioning in apatite is the exchange coefficient, K_D (Eq. 4.3). Equation 4.3 describes the exchange of OH-F between apatite and melt:

$$K_D^{OH-F} = \frac{\left(\frac{OH_{ap}}{OH_m}\right)}{\left(\frac{OH_{ap}}{OH_m}\right)} = \frac{\left(\frac{OH_{ap}}{F_{ap}}\right)}{\left(\frac{OH_m}{F_m}\right)} \tag{4.3}$$

The exchange coefficient allows the comparison of partitioning behaviour of two major elements competing for the same crystallographic site to be determined. The exchange coefficient treats F, Cl and H, as major elements, and models them in a similar fashion to the behaviour of Mg and Fe between olivine and melt [Roeder & Emslie, 1970]. Assuming ideal behaviour, K_D can be calculated using the mole fraction or wt% of each species. Therefore, instead of examining the D_{Cl}^{Ap-m} relationship with NBO/T, a more suitable parameter may be K_D^{Cl-OH}. However, K_D^{Cl-OH} data from this study is

limited, and there is no obvious relationship with NBO/T.

D_F^{Ap-m} appears to be unaffected by melt composition for runs carried out in the fluorapatite end member composition, likely reflecting that F behaves slightly differently in the melt structure to Cl, or that partitioning of F is dependent on apatite crystal chemistry and, therefore, is unaffected by melt composition.

Throughout the entire dataset, there is no obvious influence of f_{O_2} on partitioning/exchange of the anions. Therefore, it is likely that mineral-melt partitioning of these elements is controlled by additional variables, such as, element availability in the melt, temperature, and structural controls from apatite and melt.

4.10 Conclusions

Apatite-silicate melt partitioning experiments described here demonstrate that a realistic geological f_{O_2} has no discernible influence on Mn or volatile partitioning. This is consistent with the results of XANES spectroscopy, which demonstrate that over a wide range of f_{O_2} conditions, Mn is incorporated into both apatite and a range of silicate melts as Mn^{2+}. Instead, data here combined with literature data show that melt structure, and in particular the extent of melt polymerization as defined by the ratio NBO/T, controls partitioning of Mn between apatite and a range of silicate melts. The varying Mn content of apatite from the Criffel pluton can be explained by the varying degrees of melt polymerisation for samples from different zones of the pluton, rather than changes in the f_{O_2} of the parental magma, as previously suggested. More polymerised melts generally have a much higher mineral-melt partition coefficient for trace elements (e.g. Mn apatite-melt), than corresponding, less polymerised melts. Therefore, empirical relationships between variables such as f_{O_2} and the Mn content in apatite are not valid across systems where melt composition changes, and further terms in such equations are needed to constrain the influence of melt composition.

5

Europium and cerium oxidation state in, and partitioning between, apatite and silicate melt

"The observer listens to nature: the experimenter questions and forces her to reveal herself."

– Georges Cuvier

5.1 Introduction

Rare earth elements (REEs) often become concentrated in accessory minerals due to their incompatibility in most major rock forming minerals; this causes the build-up of REE. The saturation of REE in evolved magmas, and the unusual behaviour of accessory minerals promotes their concentration in these phases. Low mineral-melt distribution coefficients, and the similar, but slightly varying, geochemical behaviour of the REEs make them ideal for modelling petrogenetic processes. There is a systematic change in the ionic radius of the trivalent (3^+) REE from 1.03 Å for La^{3+} to 0.861 Å for Lu^{3+} [Hanson, 1980]. This makes the behaviour of any particular REE similar to its neighbouring REEs (i.e. REE with the atomic number one higher or lower than the element of interest), but systematically different from the atomically lighter and heavier REEs. Eu and Ce are two REEs whose behaviour, in contrast, often differs from the others as they can have a different charge of 2^+ for Eu or 4^+ for Ce.

Eu can be found in both 2+ and 3+ oxidation states for the f_{O_2} conditions prevalent in terrestrial magmatic systems (Figure 1.5, page 16). These two oxidation states have different ionic radii, meaning their mineral-melt partitioning behaviour often varies, depending on the prevalent oxidation state. In a chondorite normalised REE plot (Spider diagram e.g. Figure 5.1), Eu often is found in a position different to what is expected from extrapolating from the positions of Sm and Gd, which bound it. Eu anomalies (Eu_N/Eu^*) can either be negative or positive, depending on the mineral-

melt partition coefficient of the phase being measured, and are given by the equation:

$$Eu_N/Eu^* \; where \; Eu^* = \sqrt{(Sm_N \times Nd_N)} \tag{5.1}$$

where Eu_N, Sm_N and Nd_N are chondorite normalised values.

Ce is another REE which is found in an oxidation state other than 3+. Ce^{3+} has an ionic radius of 1.01 Å whereas, Ce^{4+}, which is also found in magmatic systems [Burnham & Berry, 2014; Smythe & Brenan, 2015], has a smaller ionic radius of 0.87 Å. Therefore, Ce^{3+} more readily substitutes into minerals with other large cation sites, for example, for Ca^{2+} which has an ionic radius of 1.00 Å (in contrast, Ce^{4+} is much more incompatible). Ce anomalies (Ce_N/Ce^*) are given by the equation:

$$Ce_N/Ce^* \; where \; Ce^* = \sqrt{(La_N \times Pr_N)} \tag{5.2}$$

where Ce_N, La_N and Pr_N are chondorite normalised values. The size of the Ce and/or Eu anomalies can be easily be changed by anomalous behaviour of La/Pr or Sm/Nd respectively. Eu and Ce anomalies in phases can also be inherited from melts if a melt arrived with a pre-existing anomaly. This may be an alternate explanation for Eu/Ce anomalies in phases, rather than the phase creating this anomaly as it crystallises.

The accessory mineral apatite ($Ca_5(PO_4)_3$(F, Cl, OH) frequently contains appreciable amounts of REE. The REE contents of apatite in bodies where REEs are particularly concentrated may even provide a viable economic source of these elements.

REEs generally substitute for Ca^{2+} from the Ca2 site in the apatite structure. Mechanisms of charge-balanced substitution of the REE into apatite could include [Pan & Fleet, 2002]:

$$REE^{3+} + M^+ = \; 2Ca^{2+} \tag{5.3}$$

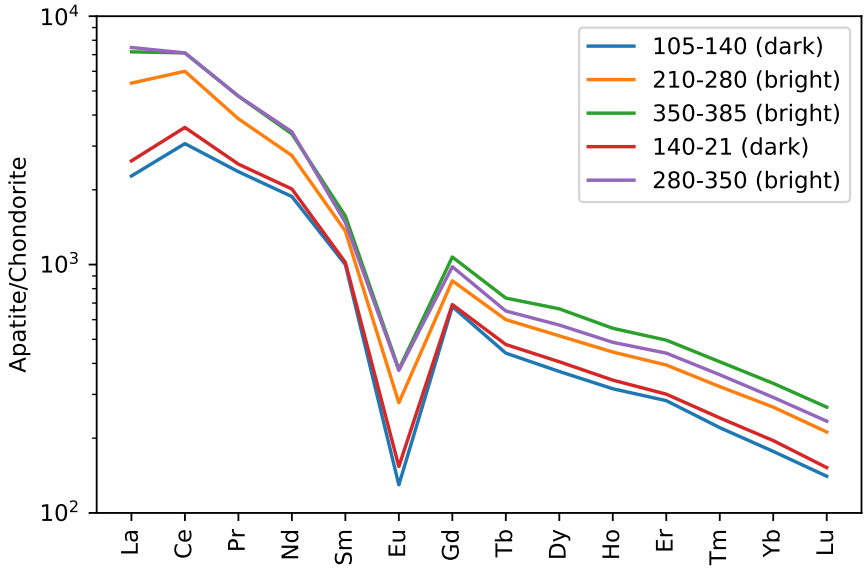

Figure 5.1: Spider diagram from Bonyadi et al. [2011] for apatite from the Se-Chahun ore deposit. The patterns show that apatite from this ore deposit have a slight positive Ce anomaly, and a negative Eu anomaly. There are a couple of options for why these apatite display a negative Ce and Eu anomaly: 1) Eu and Ce were depleted in this system prior to apatite crystallisation, 2) Eu^{2+} could be discriminated from the apatite crystal lattice under low f_{O_2} whilst other Ce accumulating phases were crystallising (or the system began low in Ce) 3) a low Eu system could produce apatite with a Ce anomaly under oxidising conditions with the discrimination of Ce^{4+} from the apatite crystal lattice. Finally a complex two stage model of high and then low oxygen fugacity (or vice versa) may have occurred [Puchelt & Emmermann, 1976].

$$REE^{3+} + SiO_4^{4-} = Ca^{2+} + PO_4^{3-} \tag{5.4}$$

$$REE^{3+} + X^{2-} = Ca^{2+} + F^{-} \tag{5.5}$$

$$2REE^{3+} + \square = 3Ca^{2+} \tag{5.6}$$

where X^{2-} is a divalent anion which substitutes into the X site, M^{+} is a monovalent cation that substitutes into the M site, and $\square$ denotes a vacancy.

Some apatites have a distinguishable negative or positive Ce and/or Eu anomaly. Eby [1975] suggested that due to the larger size of Eu^{2+} (compared to Eu^{3+}), it is preferentially excluded from incorporation into the apatite lattice. Ca^{2+} in the [7] Ca2 site has an ionic radius of 1.06 Å whereas, [9] Ca^{2+} in the Ca1 site is 1.18 Å [Shannon, 1976]. Eu^{2+} in sevenfold coordination has an ionic radius of 1.20 Å, and 1.30 Å for ninefold

coordination [Shannon, 1976]. Eu^{3+} in sevenfold coordination has an ionic radius of 1.01 Å, and 1.12 Å for ninefold coordination [Shannon, 1976], which are much closer in size to Ca^{2+} than Eu^{2+} for both Ca sites. Ce^{4+} is discriminated against in the apatite structure due to its small ionic radius [Puchelt & Emmermann, 1976]. Therefore it is expected that under f_{O_2} conditions where Eu^{2+} or Ce^{4+} dominate in a melt, less Eu or Ce will become incorporated into apatite. This raises the question whether the Ce or Eu REE anomaly in apatite can be used as a tool for determining the redox state of parental magmas when apatite is an early crystallising phase. When apatite is not an early crystallising phase, the Eu content of apatite crystallising melt may be strongly influenced by the crystallisation of feldspars (in particular plagioclase) which are known to sequester Eu, and care must be taken to address this in a future oxy-geobarometer. This study will focus specifically on how the partitioning of Ce and Eu vary into apatite from melt as a function of f_{O_2} when apatite is the only Eu bearing crystallising phase.

5.2 Starting materials

Starting material was prepared for gas mixing 'glass only' experiments and apatite bearing piston cylinder experiments. Two starting compositions were used for the piston cylinder and gas mixing experiments. These were SH3, a haplo-basaltic composition which was used (with the addition of Mn and exclusion of Eu/Ce) in the Mn apatite melt work (Chapter 4), and based on the composition by Prowatke & Klemme [2006]. The other composition L3a, was a Fe bearing composition, more felsic than SH3, and from Potts [2016]. The SH3 composition was chosen especially as 1) it has been used in the past to grow large apatite [e.g. Prowatke & Klemme, 2006; Riker et al., 2018], 2) it enables comparison to previous studies with this composition [e.g. Prowatke & Klemme, 2006; Riker et al., 2018], and 3) apart from Ce and/or Eu, there are no other multivalent elements (such as Fe) in this composition. The absence of Fe ensures there will be no Fe-Eu or Fe-Ce exchange upon quenching which might occur for the Fe-bearing L3a composition. Whilst an apatite component was added for the PC experiments, this was not added to the gas mixing starting compositions (Table 5.1). The gas mixing furnace decarbonated compositions were split into three aliquots before the addition of

either Ce oxide, Ce and Eu oxides or Eu oxide. These three different compositions were examined to determine if the presence of Ce affects the oxidation state of Eu (or vice versa) and to determine the effect of Fe on both Ce and Eu average valence. This was achieved by comparing the oxidation of Ce (or Eu) in a Ce (or Eu) only composition with Ce (or Eu) in a Ce + Eu composition. Gas mixing experiments were run at similar temperatures to the piston cylinder experiments, to allow direct comparison of glasses where f_{O_2} is more robustly controlled and monitored, compared to piston cylinder solid state buffered runs. Gas mixes were chosen to cover a large range of f_{O_2} conditions which could occur in magmatic systems on Earth (Figure 1.3, page 7).

Starting compositions were prepared from powders, ground and decarbonated from 600-1000-600 ℃ over 6 hours as described in previous chapters. An apatite component was added in the form of $Ca_3(PO_4)_2$ and CaF_2 in a 1.5:1 mole ratio. Water was added to these samples in the form of gibbsite (SH3) or brucite (L3a). A list of starting compositions can be found in Tables 5.1 and 5.2. Also listed are NBO/T values expected for quenched glasses based on: 1) no loss of alkalis on decarbonation and equilibration of the glasses at a fixed f_{O_2}, 2) no preferential loss during grinding under acetone, and 3) no element lost via alloying with the Pt wire. P_2O_5 content of the glasses has little affect on the final NBO/T. Future work is needed to accurately quantify the compositions of glass in each run using EPMA, and thoroughly constrain actual NBO/T values.

5.3 Experimental procedures

5.3.1 Piston cylinder experiments

End-loaded piston cylinder apparatus were used for high temperature, pressure experiments. Runs were conducted using 1/2" talc-pyrex assemblies with internal graphite resistance furnaces, and crushable alumina spacers. The procedure for each run (as described in chapter 2, section 2.2.1 and chapter 4, section 4.4) was to pressurise to ≈ 0.3 GPa before heating. Runs were heated during pressurisation (hot piston in technique) at a rate of 100 ℃ per minute, reaching a maximum pressure of 1 GPa for all

Table 5.1: Starting compositions for the 1 atmosphere furnace glasses and piston cylinder experiments (PC). These wt% oxide values are based on the amount of oxide/carbonate analytical powders weighed. 33 wt% apatite component was added to the piston cylinder compositions L3a-Eu and SH3-Eu in the form of 1.5:1 mol ratio of $Ca_3(PO_4)_2$ to CaF_2 respectively. NBO/T has been calculated for the 1 atm glasses and for the PC glasses without the 30 wt% apatite component.

	SH3 Ce Eu	**SH3 Ce**	**SH3 Eu**	**SH3-Eu (PC)**	**L3a Ce Eu**	**L3a Ce**	**L3a Eu**	**L3a-Eu (PC)**
SiO_2	53.03	53.35	53.26	52.64	63.76	64.10	63.97	63.33
TiO_2					2.28	2.29	2.28	2.26
Al_2O_3	17.55	17.66	17.63	17.42	8.67	8.71	8.69	8.60
FeO^T					5.46	5.49	5.47	5.43
MgO	11.65	11.72	11.70	11.61				
CaO	12.29	12.37	12.35	12.20	13.72	13.79	13.76	13.66
K_2O	1.78	1.79	1.79	1.79	1.83	1.84	1.83	1.81
Na_2O	2.77	2.78	2.78	2.75	0.73	0.74	0.74	0.72
P_2O_5					2.73	2.74	2.74	2.71
Eu_2O_3	0.54		0.50	0.07	0.49		0.51	0.06
Ce_2O_3	0.40	0.33		0.04	0.35	0.31		0.04
H_2O				1.48				1.38
NBO/T	0.66	0.66	0.66	0.79	0.45	0.45	0.45	0.56

Table 5.2: Starting composition of the piston cylinder experiments including the added apatite component (TCP, CaF_2 and $Ca_3(PO_4)_3$). These wt% oxide values are based on the amount of oxide/carbonate analytical powders weighed.

	SH3-Eu (PC)	**L3a-Eu (PC)**
SiO_2	39.42	47.43
TiO_2	0.00	1.69
Al_2O_3	13.05	6.44
FeO^T		4.07
MgO	8.70	
CaO	22.88	23.97
K_2O	1.34	1.36
Na_2O	2.06	0.54
P_2O_5	10.43	12.46
Eu_2O_3	0.05	0.04
Ce_2O_3	0.03	0.03
F	0.93	0.93
H_2O	1.11	1.03

runs, after ≈ 500 ℃. Runs were further heated to super-liquidus temperature, and were then slightly over pressurised to account for pressure loss during the first hour of the experiment. A Pt_{100}-$Pt_{87}Rh_{13}$ thermocouple was placed ≈ 10 ℃ from the hotspot of the assembly (within the capsule), and was used to monitor the temperature.

As in chapter 4, f_{O_2} was either left uncontrolled in the runs suffixed by -Pt (this indicates that only a single Pt capsule was used to house the experimental charge) or controlled by the sample assembly. In the -Pt experiments, f_{O_2} is imparted by the assembly and is estimated to be around Δ NNO. Another set of experiments were carried out inside a graphite lined Pt capsule. The f_{O_2} of the experiments run in graphite capsules can be calculated from a relationship documented in Médard et al. [2008] and is ≈ Δ IW +2. Further experiments were run in Fe capsules or with a magnetite-hematite (MH buffer: Fe_3O_4-Fe_2O_3), or Cr-Cr_2O_3 redox buffer in a double Pt capsule, similar to previous experiments where 4 μL of deionised water was added to the buffer component. Again, 4 μL of deionised water was added to the buffer component in the outer Pt capsule.

Table 5.3: Run conditions for SH3-Eu and L3a-Eu starting materials in the piston cylinder. Runs in an Fe capsule have been estimated f_{O_2}= IW buffer.

	SH3-Eu-MH	**SH3-Eu-Pt**	**SH3-Eu-PtC**	**SH3-Eu-Cr**	**SH3-Eu-Fe1250**	**L3a-Eu-MH**	**L3a-Eu-Pt-A**	**L3a-Eu-Pt-B**	**L3a-Eu-PtC**	**L3a-Eu-Fe**
Peak T	1400	1400	1400	1400	1400	1500	1500	1500	1500	1480
Final T	1250	1250	1250	1250	1250	1425	1450	1400[a]	1450	1425
Ramp Rate (℃/hr)	10	10	10	10	10	10	10	-	10	25
Duration at final T (hrs)	9	9	9	9	9	15	19	23	14	27
Buffer	MH	≈ NNO	≈ CCOH	CrCrO	≈ IW	MH	≈ NNO	≈ NNO	≈ CCOH	≈ IW
Absolute f_{O_2}	-2.32	-7.01	-9.91	-16.77	-11.35	-0.58	-5.11	-5.54	-8.23	-9.49
Relative f_{O_2} **(NNO)**	4.69	0.00	-2.91	-9.76	-4.34	4.53	0.00	0.00	-3.12	-4.38

[a]T/C failed so T based on pervious run

5.3.2 Gas mixing furnace experiments

A complimentary suite of glasses in the same two compositions as the piston cylinder experiments were synthesised in a vertical tube gas mixing furnace under a variety of f_{O_2} conditions. Starting materials were combined with poly-vinyl acetate (PVA) glue to create a bead, applied to Pt loops, and allowed to dry. For more reduced experiments, starting material was placed into molybdenum packets, made from folded Mo sheet. Multiple beads of starting material were hung from a Pt wire chandelier, which was held in the hot spot of the furnace from an alumina rod. For the more reduced experiments, multiple stamped, numbered Mo packets containing the starting material were connected by Mo wire, attached to the alumina rod, and hung in the furnace hot spot. Molybdenum packets/wire had to be used for the more reduced experiments due to repetitive failure of Pt wire experiments (which broke off the alumina rod or chandelier) under reducing conditions, presumably due to the embrittlement of the Pt wire from H_2 diffusion.

Oxygen fugacity within the furnace was controlled by the flow of mixtures of H_2 and CO_2 gas using Bronkhorst mass flow controllers. Similar total flow rates were used for all gas mixes. The mixtures of CO_2:H_2 used in this study were selected from the tables in Deines et al. [1974] to achieve the desired absolute f_{O_2} at each run temperature, and are given in Table 5.4.

Glasses were left for $\approx$ 4 hours in these preliminary experiments to minimise the loss of alkalis, and to test if the L3a and SH3 compositions would reach equilibrium. Upon completion of each run, melts were rapidly quenched by lifting the ceramic rod out of the hot spot, which lowered sample temperature to $<$ 200 ℃ in less than 30 seconds.

5.4 Analytical techniques

Prior to analyses, recovered capsules and glass chips were mounted in crystal bond or 1” epoxy blocks respectively, ground to the desired level, and polished using the 6 μm, 3 μm and 1 μm diamond polishing laps. Capsules were then dissolved from crystal bond, cleaned and placed in 1” indium mounts ready for in-situ analyses.

Table 5.4: CO_2/H_2 gas mixes, temperature of experiment and log f_{O_2} values for gas mixing experiments. Runs in air were left with no gas mixture flowing into furnace. Log $f_{O_2}$of air = -0.68 for all temperatures.

% H_2	Temperature (°C)	Log f_{O_2}
air	1325	-0.7
0.4	1350	-4.4
1.8	1325	-6.0
13.2	1325	-7.9
50	1325	-9.9
86.4	1315	-12.0
98.4	1340	-13.8
99.6	1350	-14.9

5.4.1 EPMA

Compositional data for a limited number of the PC samples were collected using the JEOL JXA8530F Hyperprobe field emission gun (FEG) electron probe microanalyser (EPMA) at the University of Bristol. 1" indium blocks containing multiple capsules from the piston cylinder were cleaned and carbon coated for analyses.

Apatite and glass were analysed using a 10 μm beam for all conditions. Apatite was measured with two separate protocols, with measurements taken on the same spot. The first measurements were: Na, Ca, P, F and Cl, with a 15 kV accelerating voltage and 5 nA current to limit volatile loss during analysis. Subsequently, measurements of Si, Mg, K, S, Fe, Cr, Ti, Ce and Eu were taken with the 15 kV accelerating voltage and 20 nA current. Primary standards were: albite (Na, Si), Saint John's Island olivine (Mg), sanidine (K), barite (S), NaCl (Cl), fayalite (Fe), Cr_2O_3 (Cr), TiO_2 (Ti), Europium glass (Eu), Cerium glass (Ce), and Durango (Ca, P, F).

Quenched glasses were analysed for Ca, Ti, Si, Al, Na, Mg, F, K, Cl, Fe and Cr with a 10 nA current and 15 kV accelerating voltage. Eu, Ce and P were measured with a 15 kV accelerating voltage and 40 nA current. Primary standards used were wollastonite (Ca), St John's Island olivine (Mg), TiO_2 (Ti), albite (Na, Si), MgF_2 (F), sanidine (Al, K), NaCl (Cl), fayalite (Fe), Cr_2O_3 (Cr), Europium glass (Eu), Cerium glass (Ce) and Durango (P).

5.4.2 SIMS

Apatite and glass Ce and Eu content, and volatile measurements by SIMS were collected on the same piston cylinder samples analysed by EPMA. Measurements were taken using a Cameca ims-4f probe at the NERC ion microprobe facility, Edinburgh. Samples had their carbon coats removed, were cleaned in ethanol and coated with ≈ 35 nm gold prior to analyses to provide good electrical conductivity. Analyses were collected on the same spots as EPMA as well as new spots to check/avoid beam damage caused by EPMA.

A primary $^{16}O^-$ beam with a 2.2 nA current and 10.8 keV accelerating voltage was focused on each sample with a 4.5 keV voltage to produce a ≈15 keV net impact energy. Secondary ions ^{1}H, ^{11}B, ^{12}C, ^{16}O, ^{19}F, ^{26}Mg, ^{30}Si, ^{31}P, ^{35}Cl, ^{39}K, ^{42}Ca, ^{55}Mn, ^{88}Sr, ^{138}Ba, ^{139}La, ^{140}Ce and ^{151}Eu were counted on an electron multiplier for 79 seconds for each, over 6 cycles of the magnet. Only SIMS measurements for H_2O, F, Cl, CO_2, Eu and Ce are given here; other elements were measured to confirm that the analyses of apatite (or glass) were not contaminated by intersecting the other phase.

Prior to analysis the beam was rastered across a 10 μm x 10 μm square for a 3 minute pre-sputter period to pre-clean the analysis area. Measurements were taken with a 50 eV energy offset (40 eV window) on a 25 μm image field. The analysis area was restricted further with a field aperture #2 down to 8-10 μm. Higher resolution CO_2 measurements for glass and apatite were collected on additional spots with a 20 μm raster, 4 minute pre-sputter and 60 eV image field, and 50 eV offset (40eV window). Field aperture # 2 was used to restrict the area ions were collected to 15 μm x 15 μm. The mass resolution of the additional CO_2 measurements (900-1000) was sufficient to separate $^{25}Mg^{2+}$ from $^{12}C^+$.

Standards used to quantify ion yields were rhyolitic, basaltic and apatite standards. Absolute error for the data is assumed to be better than 10%.

5.4.3 XANES

Ce and Eu L_3 edges were collected on beamline I18 at the Diamond Light Source, Harwell, UK. Initial measurements showed that samples (apatite and glass) were variably beam sensitive. A variety of intensity-time scans taken at the WL energies of Eu^{2+}, Eu^{3+}, Ce^{3+}, and Ce^{4+} were obtained to quantify the extent of beam damage to the samples. Following these scans it was decided to use a newly commissioned QXANES set-up to rapidly obtain lower resolution data, at much faster acquisition times. Ce and Eu QXANES scans ran for $\approx$ 3 minutes in duration, which is much quicker than the $\approx$ 17 and $\approx$ 22 minutes it takes for a normal Ce and Eu XANES scan, respectively. For samples with low concentrations of Eu and Ce, the distance between the detector and sample was varied to ensure the total detector counts were within the linear response of the detector.

Spectra were collected in fluorescence geometry with a solid-state Si detector. Most spectra were collected with the sample at an incident angle of 45° to the beam to achieve the highest X-ray counts, whilst spectra of samples with higher concentrations of the absorbing atom were collected with an incident angle of 80° to minimise overwhelming the detector. Whilst a smaller beam size would have been preferred for samples with small apatite, beam size was kept to 10 μm to reduce beam damage to the sample. Scan edge steps, counting times and energy ranges for each type of scan are shown in Table 5.5.

Table 5.5: Analysis conditions for collecting Ce and Eu XANES spectra.

	Region	Energy (eV)	Step (eV)	Counting time (s)
Eu XANES	Pre-edge	6827-6947	5	1
	Edge	6947-7011	0.2	1
	Post-edge	7011-7221	5	1
Eu QXANES	Whole spectra	6850-7150	0.4	NA
Ce XANES	Pre-edge	5615-5690	5	1
	Edge	5690-5760	0.2	1
	Post-edge	5760-5850	5	1
Ce QXANES	Whole spectra	5640-5850	0.4	NA

Eu spectra energy was calibrated using the first peak in the Eu_2O_3 spectrum, which was set at 6982.9 eV. Ce spectra were energy calibrated based on the first peak in the

CeO_2 spectrum which was set at 5731.3 eV. Spectra were imported into the software ATHENA [Ravel & Newville, 2005] where multiple scans were merged, de-glitched and sometimes smoothed prior to pre-edge/post-edge normalisation.

5.4.3.1 Beam damage

Beam induced changes in fluorescence intensity during exposure to the beam can alter the calculated peak intensities for Ce and Eu [Burnham & Berry, 2014; Burnham et al., 2015]. Certain procedures can be implemented to minimise/mitigate the effects of beam damage on a sample. One approach would be to constantly move a sample under the beam whilst collecting spectra, whilst another method would be to use an unfocused beam. However, the size limitation of apatite in these samples limited the minimum size of beam used to 5 x 5 μm, so an unfocused beam, or moving a sample relative to the beam was not an option. To reduce the intensity of the beam the maximum thickness of aluminium filter was introduced between the beam and the sample to provide adequate counts for the detector. Multiple spectra were also obtained for most samples, on different spots, to check for homogeneity in Eu/Ce oxidation state, and so spectra could be merged to reduce noise.

Photon energy normalised fluorescence yield time series scans (Figure 5.2) were collected on the Eu^{2+}, Eu^{3+}, Ce^{3+} and Ce^{4+} edge positions in apatite/melt for most samples. Spectra were collected to try to quantify the increase or decrease of these oxidation states as a function of exposure time to the beam. Whether a sample photo-oxidises or photo-reduces was expected to vary between samples due to factors such as melt/crystal composition, the presence of hydrous species in the samples, and the absorbing atoms starting oxidation state. Therefore, intensity-time scans were collected for both oxidation states of Ce and Eu on most samples. Intensity-time spectra show that the fluorescence intensity of a spectrum collected at a single energy can start changing immediately with exposure to the beam, depending on the sample being investigated.

The first step was to identify which scans, elements and oxidation states were affected by exposure to the beam. It is also important to note how long it takes each scan type

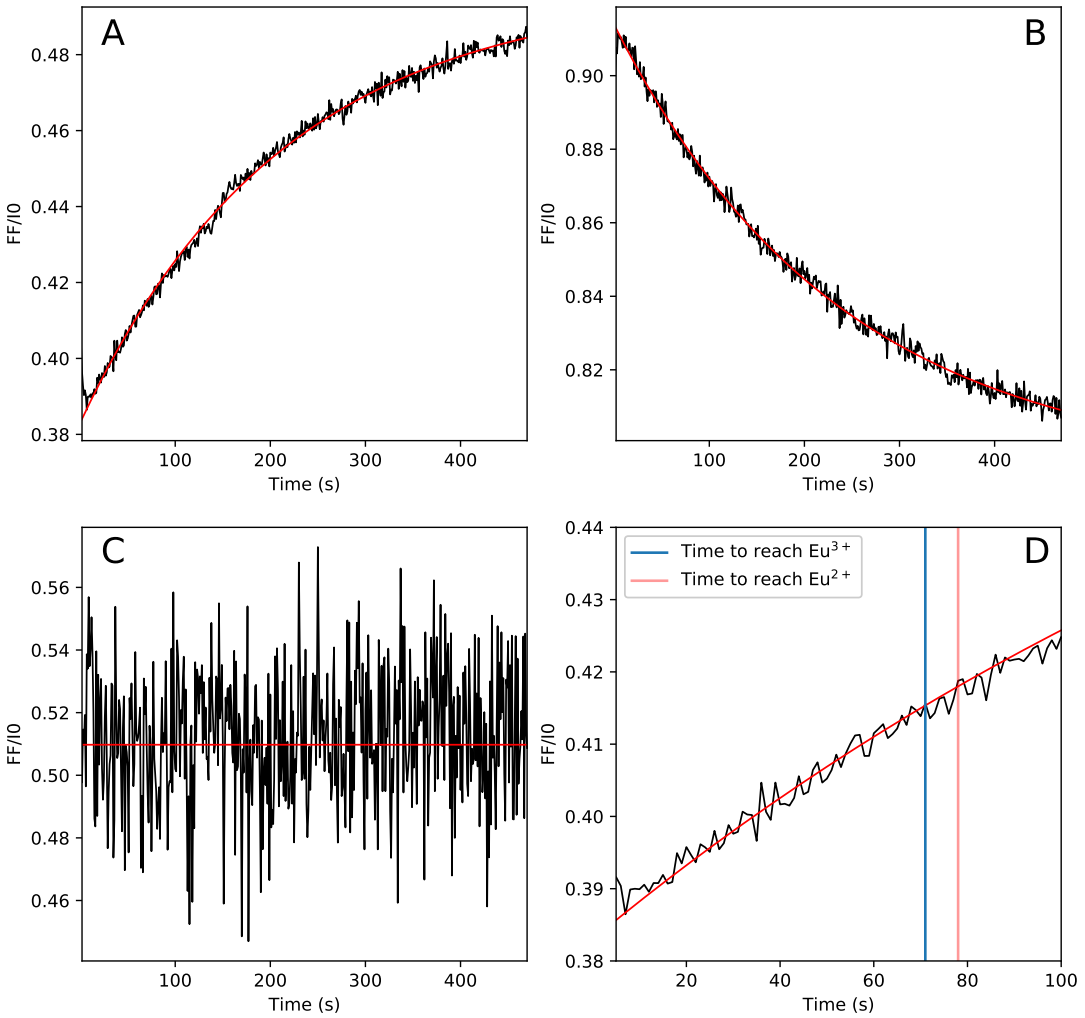

Figure 5.2: Photon energy normalised fluorescence yield vs-time test (FF test) for samples which experience (A) an increase in one oxidation state with time, (B) a decrease in an oxidation state with time, and (C) no change in oxidation state prevalence with time. (D) is a close up of (A) with an additional vertical red line showing the time it takes in a quick scan to reach the Eu^{2+} white line and the vertical blue line denotes the time it takes to reach the Eu^{3+} white line.

to reach the WL position for each oxidation state. For both the Ce and Eu slow scans it takes ≈ 9 minutes to reach the first WL and ≈ 11 minutes to reach the second. Knowing the time duration allows the application of a zero time correction for each oxidation state present, increasing or decreasing the Voigt height for each fitted oxidation state following data normalisation and fitting.

For samples where a zero time correction was required, exponentials to the FF/I0-time step spectra were fitted, and then used to back-calculate the FF/I0 of each white line position if unaffected by beam damage. Beam damaged corrected intensities of

the Voight fitted peaks were then weight averaged to determine the bulk oxidation state of the glass or mineral phase. For the QXANES scans, it was determined that no correction was necessary for any of the samples because in these scan, the time it takes to reach the first and second white line positions is much shorter (73s and 83s to reach Ce^{3+} and the second Ce^{4+} WL, and 71s and 78s to reach the Eu^{2+} and Eu^{3+} WL position.) than in the corresponding 'normal scan'. Over this much shorter timescale (3 minutes compared to 17/22 minutes) the % change in fluorescence intensity (normalised to beam current) is <7 % therefore no time-intensity correction was applied.

5.5 Results

Piston cylinder experiments produced apatite and glass (quenched melt) for the majority of runs. In run SH3-Eu-PtC an additional unidentified phase was noted. This phase appears to contain negligible amounts of Eu and, therefore, should not affect Eu partitioning. Apatite crystal size ranges from <1 by <1 μm to 100 by 800 μm in size, and often contain melt inclusions that run parallel to the c-axis of the crystal (Figure 5.3).

SH3 glasses in Table 5.6 range from the basanite field of the total alkali silica (TAS) diagram to trachy-basaltic in composition. The NBO/T for these samples range from a minimum of 0.64 for sample SH3-Eu-PtC to a maximum of 0.91 for sample SH3-Eu-Pt. Ce_2O_3 contents of the glass were below the detection limit (DL) of EPMA (99% confidence DL = 0.04 wt% Ce_2O_3), hence the values from SIMS have been used. Ce_2O_3 values from SIMS range from 0.05-0.06 wt %. Eu_2O_3 contents of the glass range from 0.10-0.12 wt% (EPMA) and are within error of the SIMS measurements (Table 5.6). H_2O measurements indicate that SH3-Eu-PtC has lost about half its initial water compared to the amount added to the starting composition. The buffering by C is expected to mitigate the effect of water loss in relation to the f_{O_2} of the run. No CO_2 measurements are available for the melt as insufficient standard measurements were taken.

Compositions for apatite in equilibrium with glasses in Table 5.6 are given in Table 5.7.

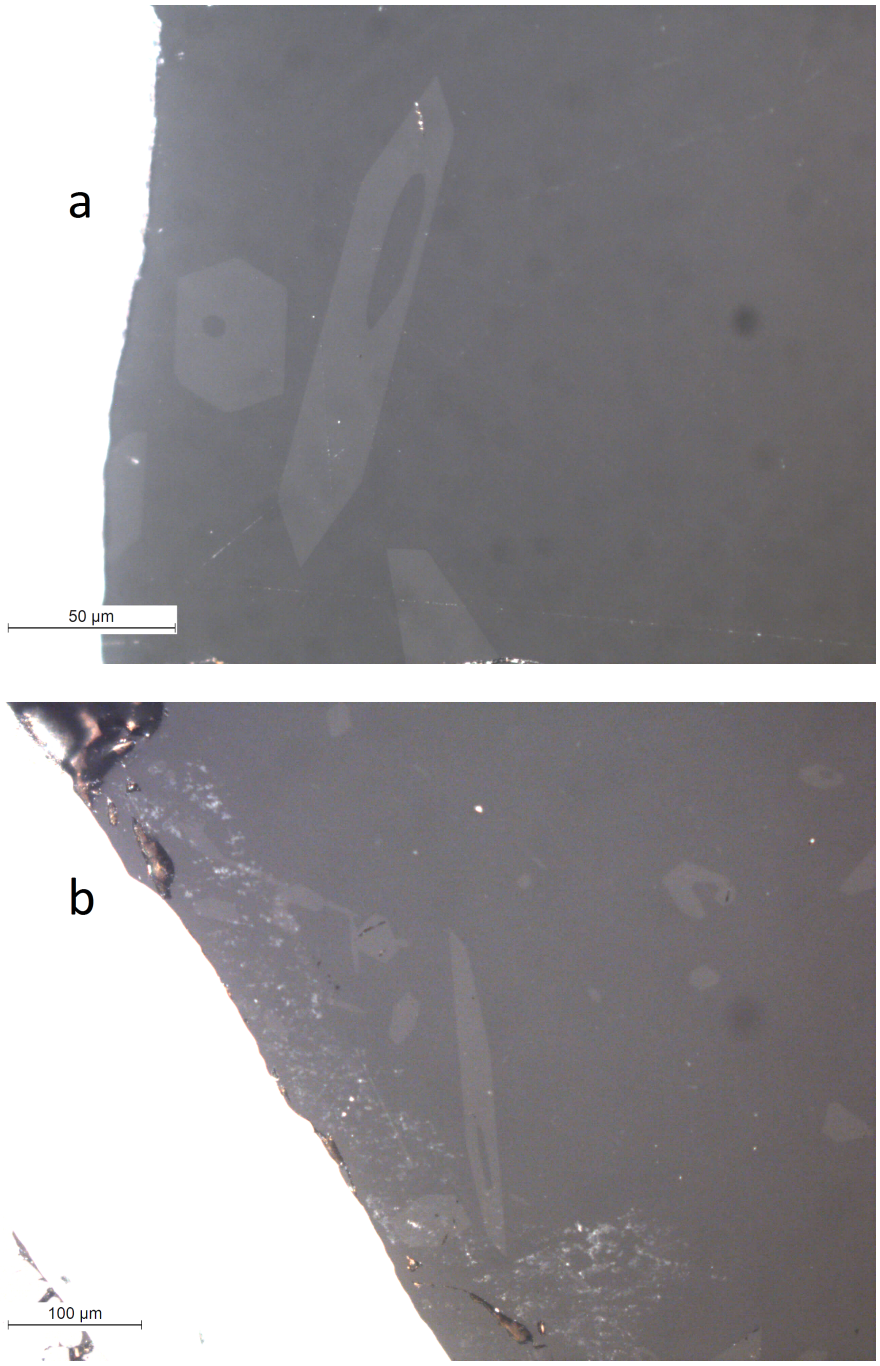

Figure 5.3: Pictures of piston cylinder runs with glass and apatite with melt inclusions. A) example(s) of an apatite with a melt inclusion from SH3-Eu-Pt. B) Example of an apatite with a melt inclusion from SH3-Eu-MH.

Table 5.6: EPMA composition of glass from the SH3 composition (missing SH3-Eu-Fe1250) PC runs. Values in parentheses represent 1 standard deviation of the averaged measurement. Measurements denoted with a * are from SIMS.

	SH3-Eu-MH	**SH3-Eu-Pt**	**SH3-Eu-PtC**	**SH3-Eu-Cr**
SiO_2	45.93 (0.62)	44.74 (0.35)	49.25 (0.49)	47.31 (0.38)
Al_2O_3	14.86 (0.13)	15.34 (0.12)	18.15 (0.22)	15.75 (0.09)
FeO	3.13 (0.08)			
MgO	8.34 (0.05)	9.97 (0.06)	8.93 (0.13)	9.37 (0.10)
Cr_2O_3				0.42 (0.05)
CaO	15.65 (0.08)	18.10 (0.12)	14.35 (0.34)	16.32 (0.05)
Na_2O	2.45 (0.12)	2.26 (0.14)	2.97 (0.12)	2.52 (0.16)
K_2O	1.53 (0.03)	1.48 (0.05)	1.99 (0.10)	1.56 (0.05)
P_2O_5	4.11 (0.04)	3.87 (0.07)	3.16 (0.06)	4.08 (0.07)
Eu_2O_3	0.10 (0.01)	0.10 (0.01)	0.12 (0.02)	0.11 (0.02)
Cl	0.03 (0.00)	0.02 (0.00)	0.02 (0.00)	0.01 (0.00)
F	1.19 (0.08)	3.00 (0.12)	1.08 (0.08)	1.08 (0.05)
Total	97.31	98.89	100.04	98.54
H_2O*	2.47	1.44	0.63	1.62
NBO/T	0.84	0.91	0.64	0.80
Ce_2O_3*	0.07	0.05	0.05	0.06
Eu_2O_3*	0.14	0.12	0.13	0.14

Apatite belong to the F-OH join and range from nearly 100% F component (SH3-Eu-Pt) to 80% F component (SH3-Eu-MH). The wt% Eu_2O_3 in apatite is a maximum of 0.47 in SH3-Eu-Cr and minimum (0.35 wt%) in SH3-Eu-Pt. Ce contents range from 0.16 wt% Ce_2O_3 (SH3-Eu-MH and -Pt) to 0.21 wt% Ce_2O_3 (SH3-Eu-PtC). Apatite shows significant CO_2 content (0.22-0.31 wt%). There are two possible sources of CO_2 in the melt for these runs 1) infiltration into the capsule from the graphite furnace, or 2) CO_2 was present at the start of the run due to incomplete decarbonation. All starting mixes were decarbonated from from 600-1000-600 ℃ over 6 hours which should be sufficient to fully decompose the carbonate powders, therefore the likely source in these runs is infiltration into the capsule from degradation of the furnace.

Gas mixing furnace melts all quenched to glass. The glass beads are generally colourless in the SH3 composition and blacky-brown in the L3a composition due to the presence of Fe, with little change in colour with f_{O_2}. These beads often have crystallites, but it is assumed that these do not affect the Eu oxidation state of the glass beads and were avoided as much as possible during analysis (Figure 5.4).

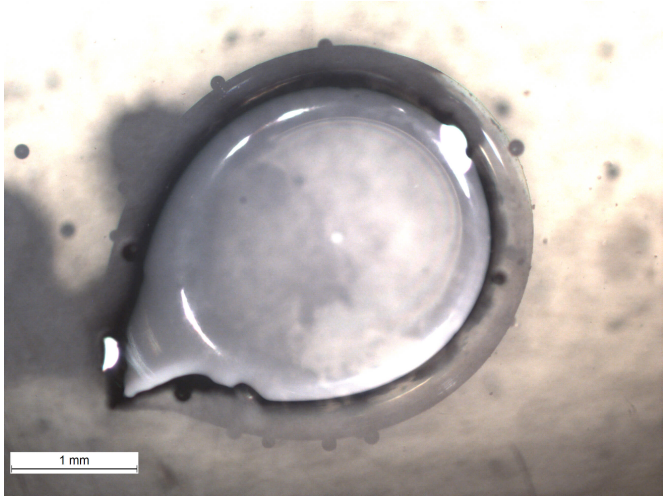

(a) Example bead from the SH3 composition.

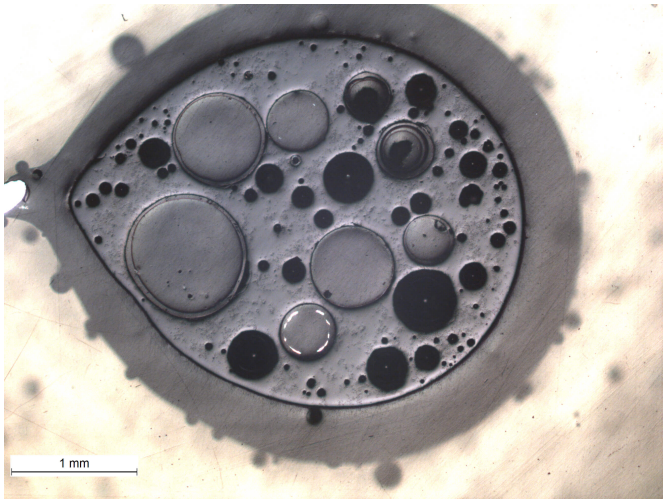

(b) Example bead from L3a composition.

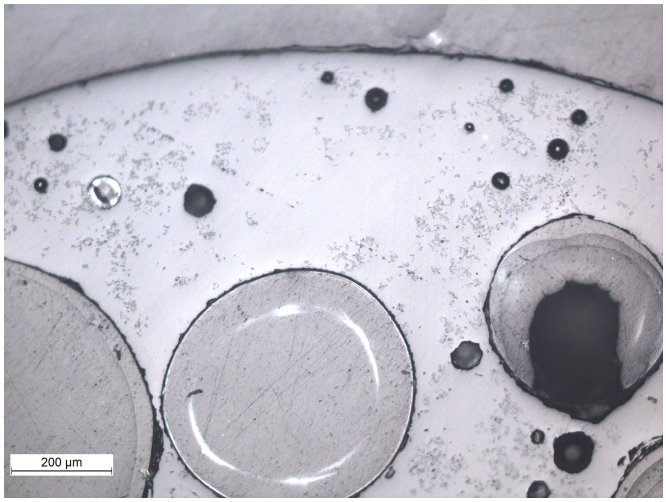

(c) Close up of bead in (b) to show size of cryptocrysts, and areas of 'clean' glass.

Figure 5.4: Representative reflected light images of beads synthesised in the gas mixing furnace in the SH3 and L3a compositions.

Table 5.7: EPMA composition of apatite from the SH3 composition and their associated stoichiometery based on EPMA measurements and approach 1 from [Ketcham, 2015]. Values in parentheses represent 1 standard deviation of the averaged measurement. Values denoted by a * indicate SIMS measurements, and the error on these values is approximately 10%.

	SH3-Eu-MH	**SH3-Eu-Pt**	**SH3-Eu-PtC**	**SH3-Eu-Cr**
SiO_2	0.47 (0.05)	0.41 (0.02)	0.42 (0.05)	0.49 (0.04)
FeO	0.10 (0.03)			
MgO	0.86 (0.02)	0.78 (0.02)	0.89 (0.01)	0.84 (0.01)
CaO	53.96 (0.23)	54.36 (0.22)	54.07 (0.24)	53.87 (0.17)
Na_2O	0.05 (0.03)			
K_2O	0.01 (0.01)		0.01 (0.01)	
P_2O_5	41.73 (0.25)	41.90 (0.44)	41.67 (0.35)	41.53 (0.48)
Eu_2O_3	0.42 (0.04)	0.35 (0.02)	0.38 (0.03)	0.47 (0.02)
Ce_2O_3	0.16 (0.01)	0.16 (0.01)	0.21 (0.00)	0.19 (0.01)
Cl	0.04 (0.01)	0.02 (0.01)	0.06 (0.01)	0.03 (0.01)
F	3.08 (0.12)	3.66 (0.06)	3.23 (0.20)	3.21 (0.21)
Total	100.94	101.68	100.98	100.69
Ce_2O_3*	0.15	0.19	0.22	0.19
H_2O*	0.46	0.18	0.25	0.41
F*	3.17	3.68	3.76	3.20
Cl*	0.05	0.02	0.06	0.03
CO_2*	0.31	0.22	0.25	0.22
Ca	9.71	9.76	9.75	9.74
Na	0.02	0.00	0.00	0.00
Ce	0.01	0.01	0.01	0.01
Eu	0.02	0.02	0.02	0.03
Fe	0.01	0.00	0.00	0.00
K	0.00	0.00	0.00	0.00
Mg	0.22	0.19	0.22	0.21
$\sum$Ca site	10.00	9.99	10.01	9.99
P	5.94	5.94	5.93	5.93
Si	0.08	0.07	0.07	0.08
$\sum PO_4$ site	6.01	6.01	6.01	6.01
F	1.64	1.94	1.72	1.71
Cl	0.01	0.01	0.02	0.01
OH	0.35	0.05	0.26	0.28

Following transects of multiple beads, taking XANES spectra from rim to core, it was found that the oxidation state of the glass beads were variable. For both the SH3 and L3a compositions, the outer edge of the beads were found to be more oxidised than spectra taken 20-40 μm into the bead, where the most reduced spectra was produced. In the L3a composition, spectra also became more oxidised again towards the centre of the beads. This suggests that the L3a composition did not fully reach equilibrium during the runtime of the experiments, probably due to the slow diffusion of O^{2-}.

An oxidised edge of the beads in both compositions may suggest that cooling on the outside of the beads has caused a change in the proportion of Eu^{2+}/Eu^{3+} compared to the thermally insulated insides of the beads. However, the temperature difference to cause the large change in $Eu^{3+}/\sum Eu$ would have to be large, and hence is thought unlikely. The largest range in $Eu^{3+}/\sum Eu$ was found in sample L3a Ce Eu 99.6 and ranged from 0.14-0.53, this equates to an f_{O_2} error of Δ 2.3 log f_{O_2}. The difference in $Eu^{3+}/\sum Eu$ and $Ce^{3+}/\sum Ce$ in transects from most other samples is much smaller with no difference in oxidation between spots noticed in samples synthesised below 86.4 % H_2. Composition SH3 appears to be less affected by varying oxidation state compared to the L3a composition. Degassing of Na, K and P from the surface of the bead may provide one method by which the outer shell of the bead becomes more oxidised. An alternate hypothesis would be that the edge partially re-equalised upon quenching and so record different f_{O_2} conditions. Following the results of the transect, XANES spectra were collected away from the edge of the beads to avoid the partial f_{O_2} reaction of the rim but were also close enough to the edge to gain equilibrium with the furnace atmosphere. The change in the oxidation state of the glass beads is unlikely to be due to self absorption, as testing the self-absorption algorithm in ATHENA (FLUO) [Haskel, 1999; Ravel & Newville, 2005] for fluorescence samples shows that the intensities of the peaks associated with each oxidation state are both equally affected by self absorption and so remain relative to one another with self absorption.

5.5.1 Eu oxidation state - SH3 compositions

Eu XANES spectra from the SH3-Ce-Eu suite of 1 atm glasses synthesised in 50% H_2 is shown in Figure 5.5 to 5.7. Figure 5.5 shows significant amounts of the two white line peaks present in most spectra. These white line (WL) peaks are assigned to the $2p_{3/2} \rightarrow$ 5d transitions associated with Eu^{2+} and Eu^{3+}. The energy difference between these peaks is large ($\sim$ 8 eV) which means the peaks are well resolved and the contributions from each oxidation state can be determined. The relative heights of these peaks vary systematically as a function of f_{O_2}. Quantitative data on the relative oxidation states of Eu and other REE L_3 edge XANES data can be found by deconvoluting spectra to obtain the peaks associated with the $2p_{3/2} \rightarrow$ 5d transitions for Eu^{2+} and Eu^{3+}. Eu

mean valence can either be obtained from the relative peak heights, or areas of the fitted arctangents, depending on the fitting procedure.

5.5.1.1 Fitting

There are various ways that quantitative information can be extracted from the L_3 edge of transitional metals, actinides and lanthanides. Traditionally, data is extracted by fitting an arctangent and Lorentzian peaks to each $2p_{3/2} \rightarrow 5d$ transition present (based on first principles) [Röhler, 1985]. Therefore, for a sample which contains Eu^{2+} and Eu^{3+} two arctangents and two Lorentzians are necessary to fit each XANES spectrum. In this study we have fixed the centre of each arctangent to the centre of the corresponding Lorentzian peak, and the amplitude of both arctangents is fixed, so that their intensity is relative to the relative average areas of the two Lorentzian peaks (Figure 5.5). The width of the arctangents are also fixed at 3.91 eV, which represents the core-hole lifetime [Krause & Oliver, 1979]. For this fitting technique, the relative areas of the Lorentzian peaks are used to obtain valence estimates.

Alternative methods for fitting the Eu L_3 edge data have also been tested. These include:

1. Fitting one arctangent to the data, along with two Lorentzians (Figure 5.6) [e.g. Rakovan et al., 2001], where the width and position of the arctangent are allowed to vary. The areas of the two Lorentzians represent the relative proportions of Eu^{2+} and Eu^{3+}.

2. Fitting an error function step, (a suitable approximation to the continuum step [Outka & Stöhr, 1988]), with two Voigt peaks of the same width (Figure 5.7). Voigt peaks were chosen as they account for instrumental broadening (Gaussian component) as well as a transition to bound states (Lorentzian component) [Pedersen & Jørgensen, 1996]. The relative heights of the Voigt peaks are used to obtain valence estimates.

3. Manually fitting a cubic spline by interpolating the data several eVs before and after the 2p-5d transitions, before fitting two Voigt peaks (not shown). The

relative heights of the Voigt peaks are used to obtain valence estimates.

The differences in the $Eu^{2+}/\sum Eu$ values for various fitting techniques for samples in the SH3 Ce Eu glass series are shown in Figure 5.8. Fitting using two arctangent steps and 2 Lorentzian peaks, or an error function and 2 Voigt peaks, results in sample SH3-Ce-Eu-1.8 (log $f_{O_2} \approx$ -6) having more calculated Eu^{3+} than the sample run at 0.4% H_2 (log $f_{O_2} \approx$ -4.4). This either reflects a failing of these two fitting methods, or that the oxidation state in the sample never reached equilibrium, and hence has a higher Eu^{3+}.

In this study we have assumed that the transition probabilities of Eu^{2+} and Eu^{3+} species are equal, and therefore, the area ratio of the Lorentz peaks (or height of Voigt peaks) is equal to the peak area ratio of the Eu^{2+} and Eu^{3+} species. However, the sum of the area of both the Eu^{2+} contribution and Eu^{3+} contribution decreases with a decrease in the f_{O_2}. This may suggest that a correction is needed either for 1) differing transition probabilities or 2) for the self absorption effect. However, this cannot be evaluated until a full suite of compositional data is available and/or a XANES spectrum is acquired for an Eu^{2+} standard, that is currently not available. Ideally a full series of mixed valence standards of known oxidation state and coordination are also required.

The results for the subsequent spectra fitting will only be reported based on fits which comprised of 2 arctangent functions and 2 Lorentzian peaks, because this method is least subjective, most widely used, and has many constraints (The width of the arctan-

Table 5.8: % $Eu^{3+}/\sum Eu$ for glass beads synthesised under controlled f_{O_2} conditions in a vertical tube gas mixing furnace. Calculated based on the fitting of two arctangents and two Lorentzian functions to each spectra. The first column indicates the % of H_2 to CO_2 with the exception of 'air' where no gas was pumped into the furnace. SH3* and L3a* are the estimated % $Eu^{3+}/\sum Eu$ based on Equation 5.7 below, which is from Burnham et al. [2015].

	SH3 Ce Eu	**SH3 Eu**	**L3a Ce Eu**	**L3a Eu**	**Log f_{O_2}**	**SH3***	**L3a***
air	99		100	100	-0.7	99	98
0.4	90	91	100		-4.4	90	85
1.8	91				-6.0	81	72
13.2	85	89	100	94	-7.9	59	46
50	56				-9.9	31	21
86.4	52	44		21	-12.0	13	8
98.4	38	34	18	9	-13.8	4	3
99.6	22	19	27	11	-14.9	2	1

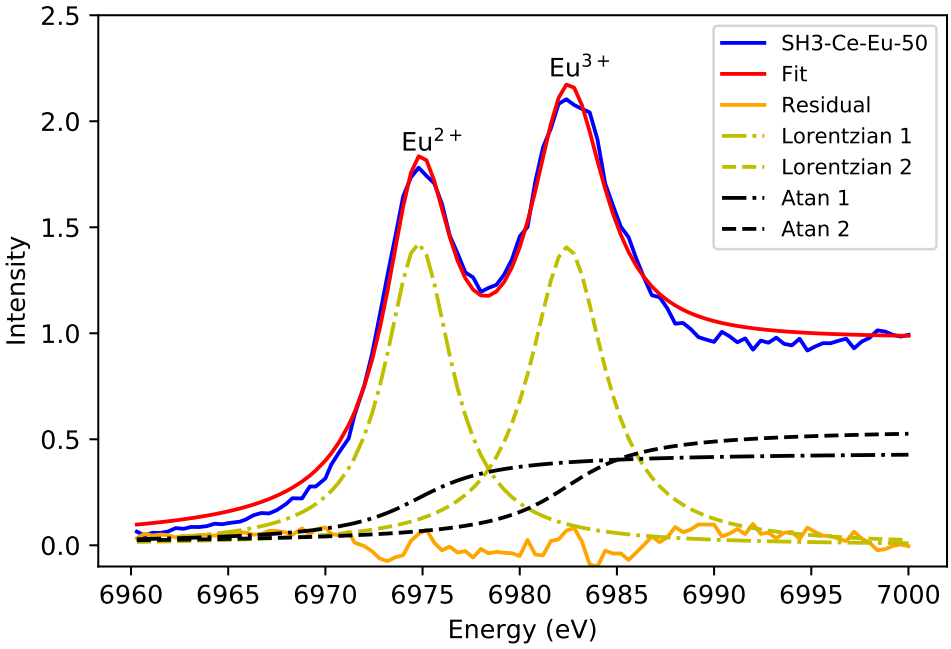

Figure 5.5: Example fit of two arctangent steps and two Lorentzian peaks to a merged Eu QXANES spectrum of SH3-Ce-Eu-50 (gas mixing run with 50% H_2 see Tables 5.4 and 5.8).

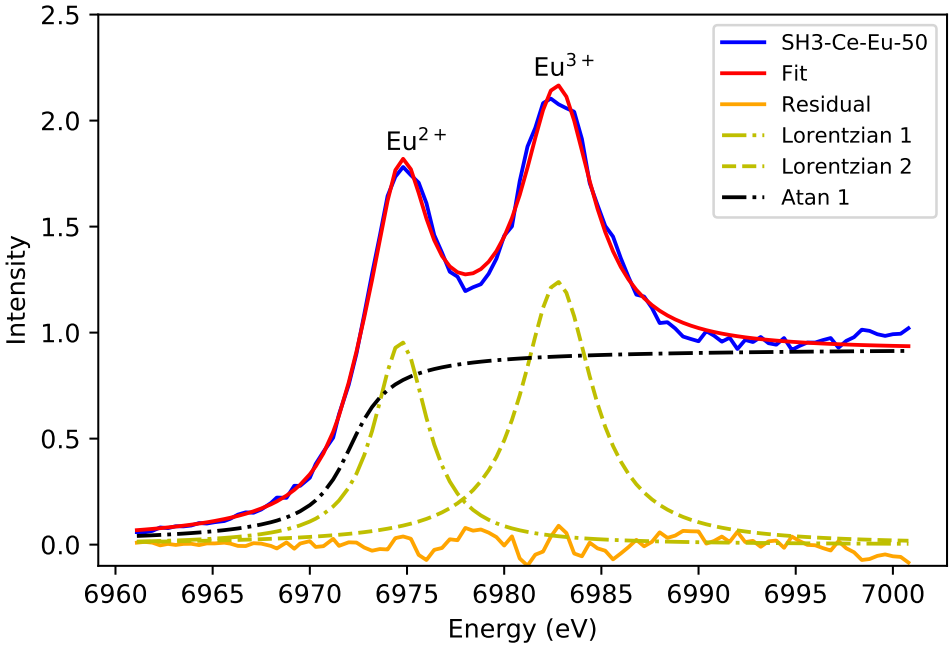

Figure 5.6: Example fit of one arctangent step and two Lorentzian peaks to a merged Eu QXANES spectrum of SH3-Ce-Eu-50.

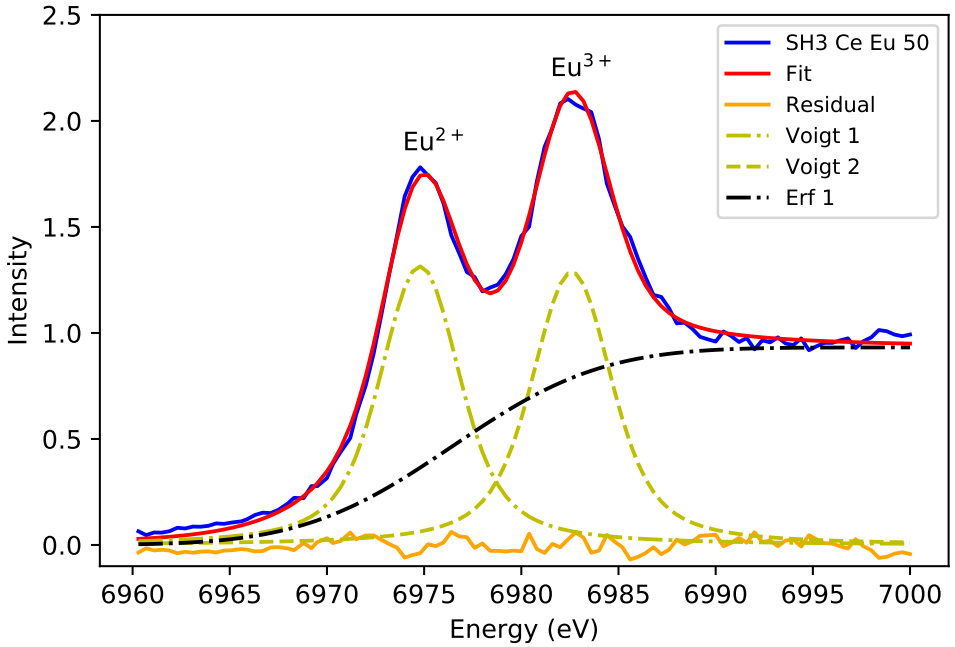

Figure 5.7: Example fit of one error function step and two Voigt peaks to a merged Eu QXANES spectrum of SH3-Ce-Eu-50.

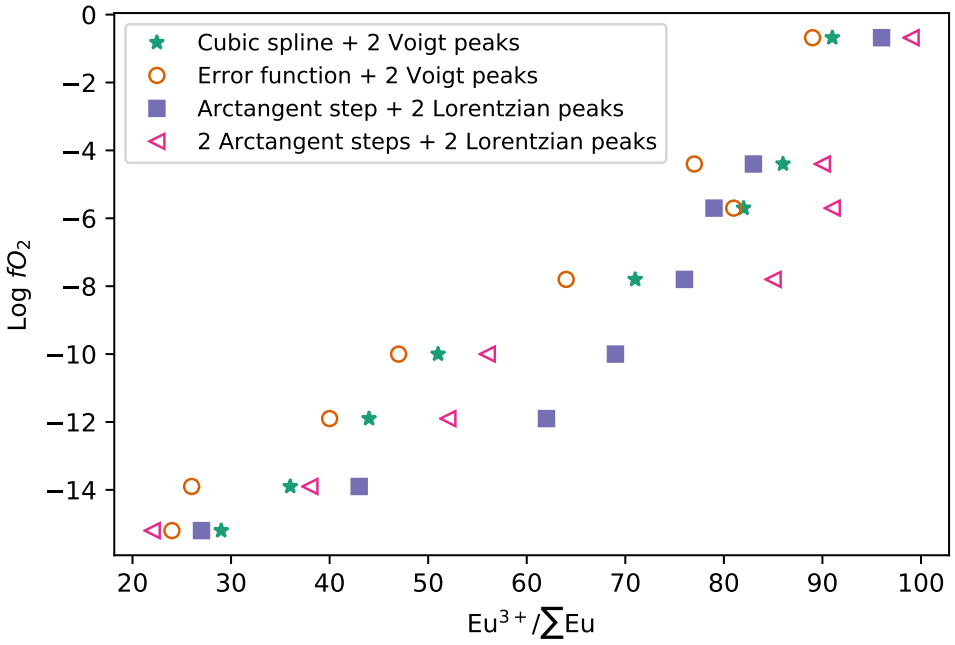

Figure 5.8: Difference in % $Eu^{3+}/\sum Eu$ for the four different fitting approaches. QXANES spectra for the SH3-Ce-Eu series of glasses have been fitted with a) cubic spline and 2 Voigt peaks, b) an error function and 2 Voigt peaks, c) an arctangent step and 2 Lorentzian peaks and d) 2 arctangent steps and 2 Lorentzian peaks. An example fit for SH3-Ce-Eu-50 from b, c and d can be found in figures 5.7, 5.6, and 5.5 respectively.

gents are fixed to the core-hole lifetime, heights and centres of the arctangent functions fixed to the positions and relative heights of the Lorentzian peaks). The shape of this fitting also approaches the sigmoidal shape of the relationship between $Eu^{3+}/\sum Eu$ and f_{O_2} suggesting this fitting approach is the best. Whilst there may be an error in absolute $Eu^{2+}/\sum Eu$ with this fitting procedure, the error in Δ $Eu^{2+}/\sum Eu$ between samples should be small.

5.5.1.2 Data

The corresponding spectra for coexisting apatite-glass in the SH3 composition are shown in Figure 5.9. Initial visual inspection implies that the oxidation state of Eu in apatite is unaffected by f_{O_2}, whereas the oxidation state of the corresponding glasses display an increase in Eu^{3+} with f_{O_2}, except for SH3-Eu-Fe1250.

The proportions of Eu^{2+} and Eu^{3+} in the SH3 composition piston cylinder apatite-melt experiments can be found in Table 5.9, along with the initial estimate of f_{O_2}. As determined visually, the oxidation state of Eu in apatite are within error of each other, and therefore, do not change with f_{O_2}. This implies, as expected, that Eu^{3+} is preferentially incorporated into apatite, although $\approx$ 5% of Eu is present in the Eu^{2+} oxidation state.

Table 5.9: % $Eu^{3+}/\sum Eu$ obtained by fitting two arctangents and two Lorentzian functions for apatite and quenched melt from piston cylinder compositions SH3-Eu and L3a-Eu.

	Glass	**Apatite**	**Log f_{O_2}**
SH3-Eu-MH	100	95	-2.32
SH3-Eu-Pt	92	94	-7.01
SH3-Eu-PtC	84	94	-9.91
SH3-Eu-Fe1250	89	NA	-11.35
L3a-Eu-MH	98	93	-0.58
L3a-Eu-Pt-A	95	95	-5.11
L3a-Eu-Pt-B	96	95	-5.54
L3a-Eu-PtC	58	74	-8.23
L3a-Eu-Fe	37	NA	-9.49

$Eu^{3+}/\sum Eu$ in the glass phase changes from 100% Eu^{3+} to 84% Eu^{3+} with decreasing f_{O_2}, again, as would be expected. An exception to this is sample SH3-Eu-Fe1250 which should have a lower $Eu^{3+}/\sum Eu$ than SH3-Eu-PtC glass, but doesn't.

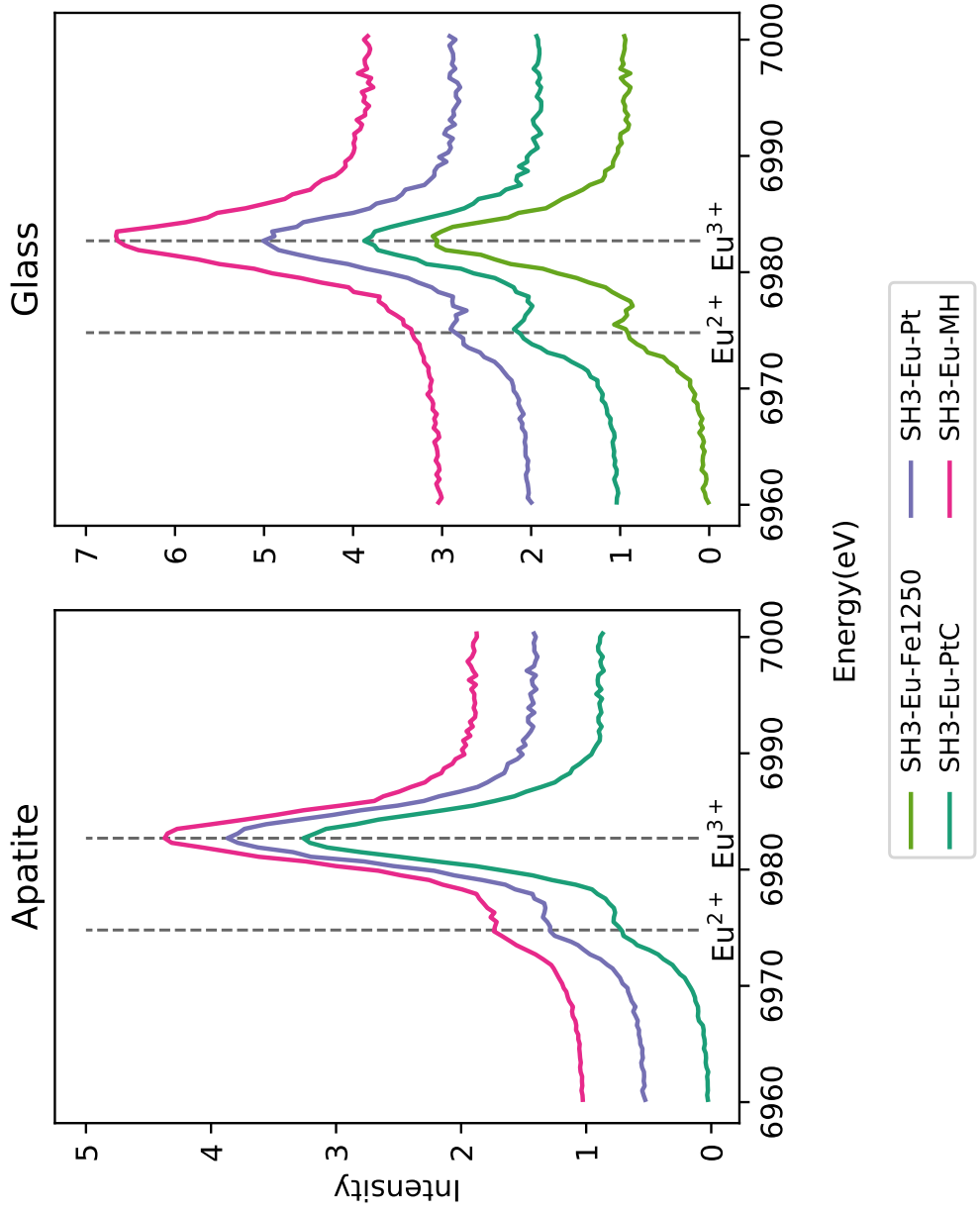

Figure 5.9: Eu L_3 edge spectra obtained on apatite and glasses synthesised in the piston cylinder in the SH3 composition.

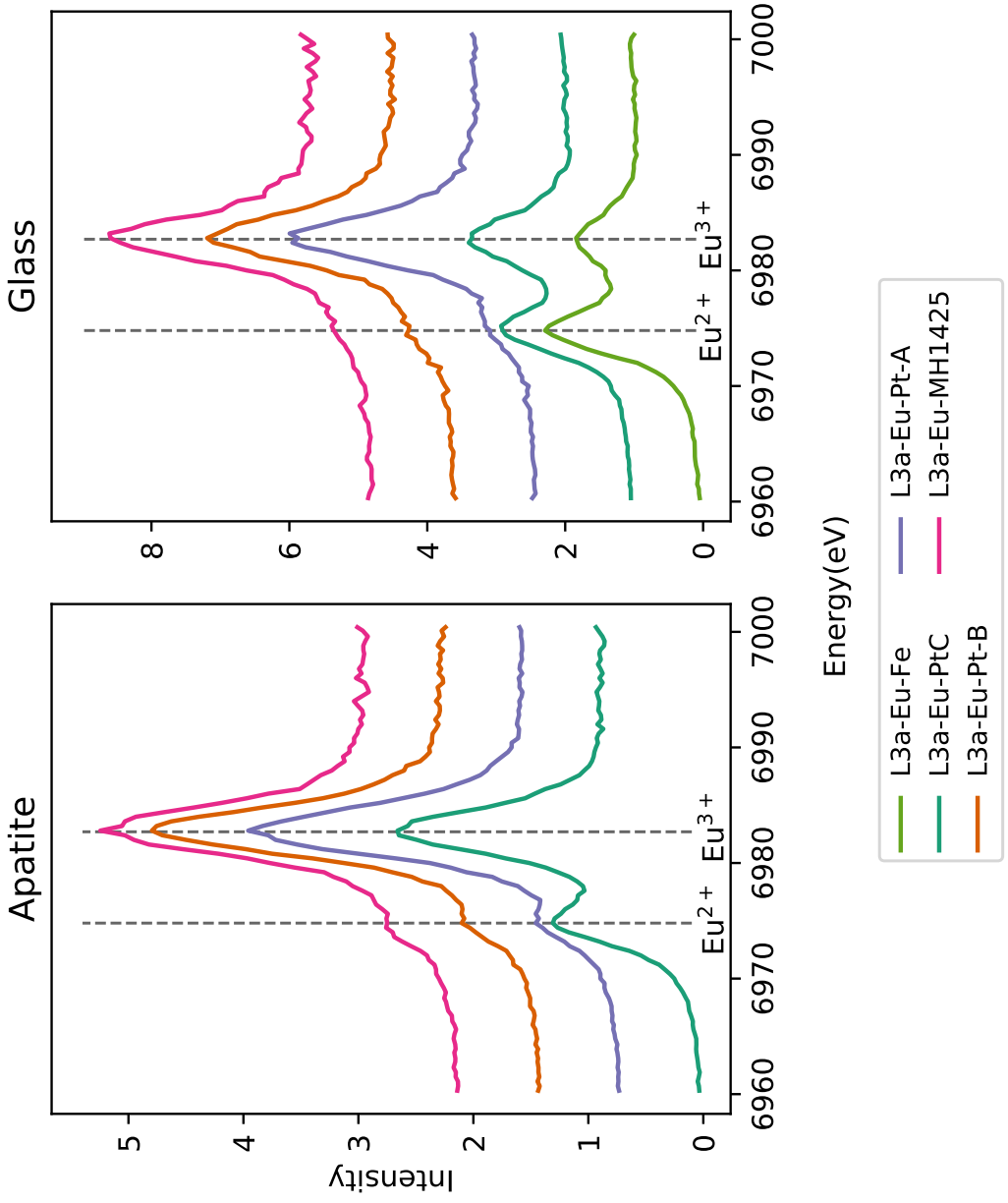

Figure 5.10: Eu L_3 edge spectra of apatite and coexisting glass for piston cylinder runs in the L3a composition.

5.5.2 Eu oxidation state - L3a compositions

The L3a-Ce-Eu suite shows no change in $Eu^{3+}/\sum Eu$ for the three most oxidised samples for which spectra was obtained (L3a-Ce-Eu-air, -0.4 and -13.2, Table 5.8), which are all 100% Eu^{3+}. This could result from samples not being in the furnace long enough for the redox state to become in equilibrium with the furnace atmosphere, due to the slower diffusion of O^{2-} in more viscous melts [Cicconi et al., 2009]. Spectra for apatite and coexisting glass from piston cylinder experiments are shown in Figure 5.10, and the $Eu^{3+}/\sum Eu$ for the L3a piston cylinder experiments are listed in Table 5.9. Apart from L3a-Eu-PtC the ratio of Eu^{2+} to Eu^{3+} in apatite appears not to change with f_{O_2}. Apatite from L3a-Eu-PtC appear to have a larger Eu^{2+} peak suggesting a higher proportion of this oxidation state. Glass spectra from the L3a-Eu piston cylinder experiments show a much greater decrease in the % $Eu^{3+}/\sum Eu^{2+}$ for L3a-Eu-PtC and -Fe relative to the more oxidising runs. Both the L3a piston cylinder and tube furnace glasses display lower % of Eu^{3+} under the most reducing conditions when compared to their SH3 counterparts but higher proportions of Eu^{3+} under more oxidising conditions. Whilst the difference in % Eu^{3+} for the piston cylinder experiments can be explained by the possible curvature of the Eu^{3+}/Eu^{2+} equilibria with temperature, this cannot be the case for the furnace glasses. There are a couple of possibilities for the differences between SH3 and L3a furnace glasses. The first may be that there exists a redox couple between Fe and Eu which would be very important in geological systems where they tend to exist together in silicate melts. Burnham et al. [2015] observed a change in the $Eu^{3+}/\sum Eu$ during the quench of Eu-Fe bearing melts. This makes it difficult to link the final oxidation state of quenched glasses containing Fe to the % Eu^{3+} during cooling; however, it is unlikely that Fe-Eu exchange could be used to explain both the greater proportions of Eu^{3+} at high f_{O_2} and lower proportions under the most reducing conditions. Another possibility is that it is harder to quantify either Eu^{2+} at high f_{O_2} or Eu^{3+} under lower f_{O_2} in the L3a compositions using XANES than it was for the SH3 composition. However, no obvious difference was noticed whilst fitting the L3a spectra compared to the SH3 composition. Finally, the L3a composition is much more felsic than SH3, and so the effect of melt composition/melt structure may also explain

the differences in $Eu^{3+}/\sum Eu$.

5.5.3 Ce oxidation state

Ce L_3 edge XANES spectra for the gas mixing furnace glasses are much noisier than the corresponding Eu L_3 edge data due to lower concentrations of Ce than Eu. Spectra with the most noise had to be smoothed with a 2 kernel size boxcar average before being processed. Following smoothing, Ce spectra were fitted with a different procedure than the Eu L_3 edge. Fitting Ce L_3 edge data is much harder because: 1) $Ce^{4+}/\sum Ce$ in natural melts is low for the range of f_{O_2} conditions associated with magmatic processes on Earth [Burnham & Berry, 2014; Smythe & Brenan, 2015], 2) Ce^{4+} manifests itself as two peaks associated with the $2p_{3/2} \rightarrow (4f\text{Ł})5d$ and $2p_{3/2} \rightarrow (4f^0)5d$ transitions (Figure 5.11) (where Ł denotes an electron in a 2p orbital of oxygen transferred to a 4f orbital of Ce) and, 3) the difference between the Ce^{4+} peak at 5730 eV and the Ce^{3+} peak (5726 eV) is small, making it hard to resolve subtle changes in spectra.

Ce L_3 edge data was fitted with a single arctangent step function and up to 3 Lorentzian peaks (Figure 5.12, 1 associated with Ce^{3+} and two associated with Ce^{4+}. The intensity of the Ce^{4+} peak at $\approx$ 5730 eV was set to 1.09 $\times$ Lorentzian height of the peak at $\approx$ 5740 eV (Figure 5.11) which is the difference in the two Lorentzian heights for the CeO_2 standard. The fit results of the glass bead data are presented in Table 5.10. It appears that there is no Ce^{4+} in the L3a composition, most likely due to the charge-coupled reaction $Ce^{4+} + Fe^{2+} = Ce^{3+} + Fe^{3+}$ upon quenching [Burnham & Berry, 2014]. This is important as it suggests that in natural glass samples, Ce oxidation state will never be preserved, and mineral-melt partition data may be the only way to determine initial f_{O_2} (i.e Ce oxidation state). The SH3 suite of glasses (Ce-Eu and Ce) both show a decrease in $Ce^{4+}/\sum Ce$ to 0 with increasing f_{O_2}. These estimates of Ce valency are likely to reflect the maximum valence as two (or more) arctangent functions are needed to represent the transition to the continuum for the 3+ and 4+ oxidation states of Ce [Bianconi et al., 1987].

Glass Ce L_3 XANES spectra from the piston cylinder runs in the L3a composition are too noisy to obtain estimates of the Ce redox state, but visual inspections suggest that

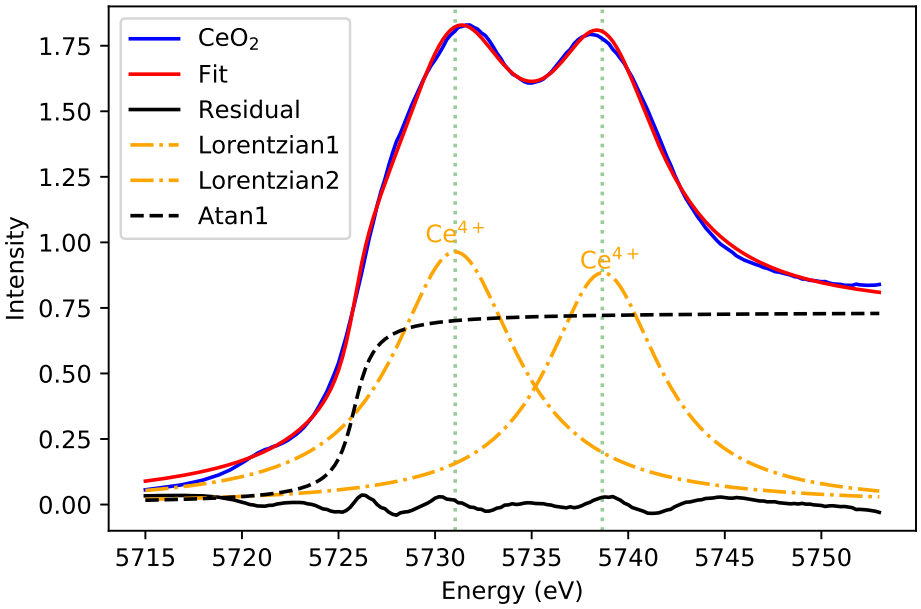

Figure 5.11: Ce L_3 edge CeO_2 spectrum (Ce^{4+}).

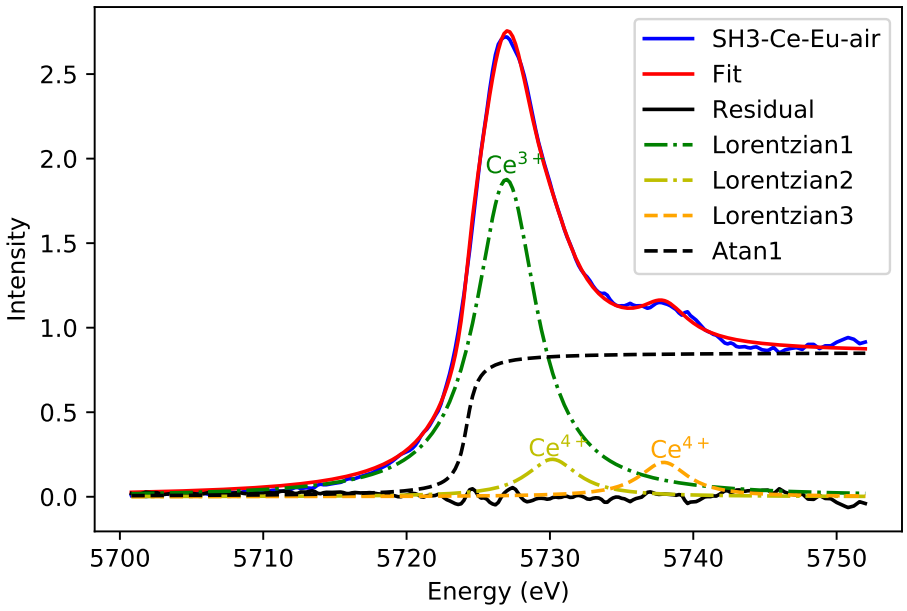

Figure 5.12: Example fitting of a Ce L_3 edge XANES spectrum.

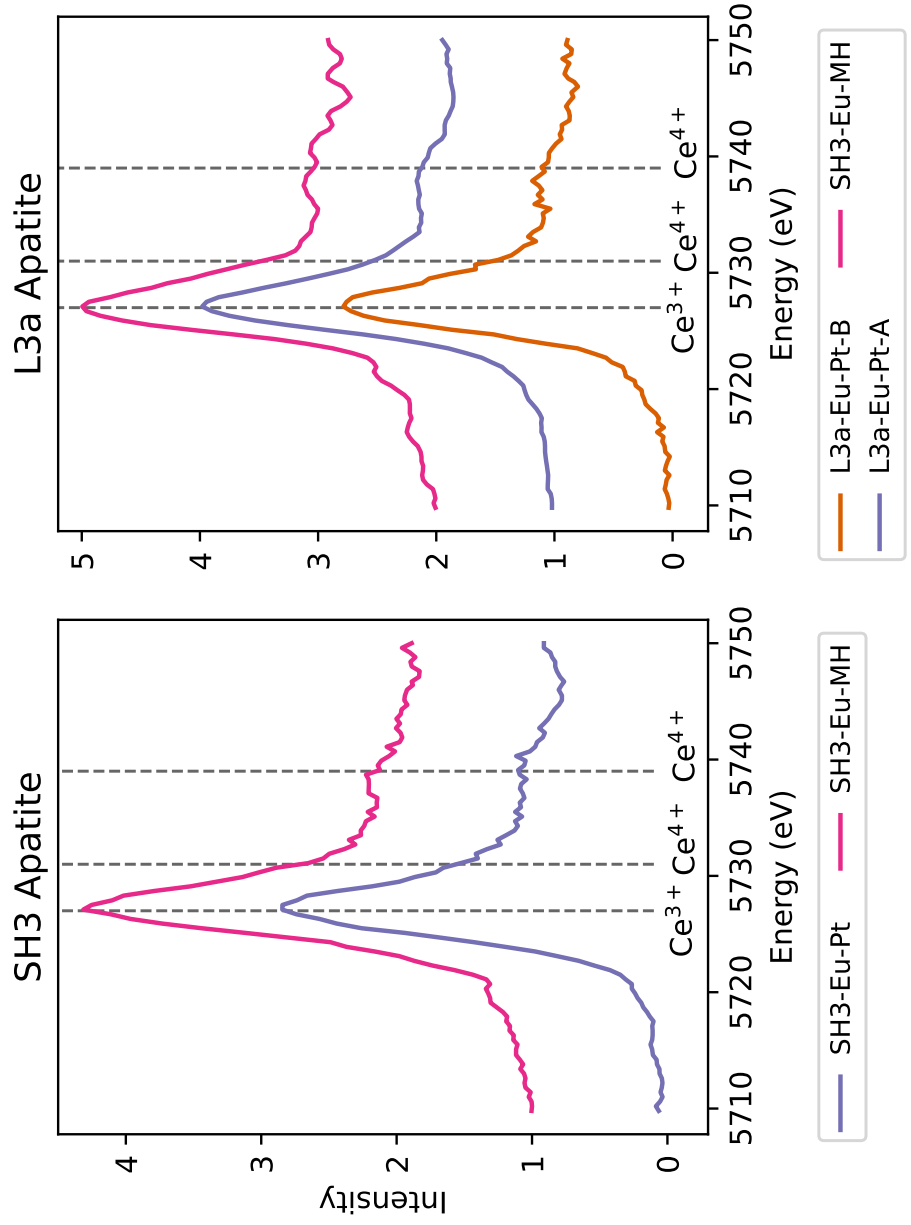

Figure 5.13: XANES Ce L_3 edge spectra from apatite from the SH3 and L3a compositions synthesised in the piston cylinder. Marked on each plot is a dotted line indicating the centroid position of the main peaks associated with Ce^{3+} and Ce^{4+}.

Table 5.10: % $Ce^{4+}/\sum Ce$ for glass beads synthesised under controlled f_{O_2} conditions in a vertical tube gas mixing furnace. Calculated based on the fitting of a single arctangent and up to 3 Lorentzian functions for each spectrum. The first column indicates the % of H_2 to CO_2 with the exception of 'air' where no gas was pumped into the furnace.

	SH3 Ce Eu	**SH3 Ce**	**L3a Ce Eu**	**L3a Ce**	**Log f_{O_2}**
air	12		0	0	-0.68
0.4	10	9	0	0	-4.4
1.8	9				-6.0
13.2	6	6	0	0	-7.9
50	0			0	-9.9
98.4		7	0	0	-13.8
99.6	0	0	0	0	-14.9

Table 5.11: Peak fitting results using a single arctangent and up to 3 Lorentzian functions for Ce L_3 edge spectra from apatite synthesised in the piston cylinder in the SH3 and L3a compositions. Also provided are the estimated log f_{O_2} for each run.

	SH3-Eu-MH	**SH3-Eu-Pt**	**L3a-Eu-MH1425**	**L3a-Eu-Pt-A**	**L3a-Eu-Pt-B**
$Ce^{4+}/\sum Ce$	9	12	13	12	12
Log f_{O_2}	-2.32	-7.01	-0.58	-5.11	-5.54

Ce^{3+} dominates. The higher concentration of Ce in the apatite phase makes it much easier to obtain a clean spectrum, and Figure 5.13 shows spectra for each run, produced by merging multiple separate spectra. There is a visible peak at ≈ 5740 eV associated with Ce^{4+}, but Ce^{3+} (5726 eV) again dominates. Fit results from the apatite spectra are shown in Table 5.11. The fit results show that apatite is dominated by a Ce^{3+} component, with up to ≈ 10% Ce in the 4+ oxidation state. However, there is no systematic change in the proportion of $Ce^{4+}/\sum Ce$ with f_{O_2} observed in these apatite.

5.6 Discussion

5.6.1 Oxygen fugacity and the oxidation states of Eu and Ce in glass

5.6.1.1 Oxidation state of Eu in silicate glasses.

There is a clear decrease in the proportion of $Eu^{3+}/\sum Eu$ with decreasing f_{O_2} for both melt compositions. The SH3 Ce Eu and SH3 Eu $Eu^{3+}/\sum Eu$ values are within error of the fitting procedure. This would suggest that no redox couple exists between Ce and Eu in this melt composition. There is still the question of how well glasses in the L3a

composition have equilibrated; runs in the air-13.2% H_2 gas mixes consisting of nearly all Eu^{3+}. Differences between redox state in the 2 compositions could indicate an effect of melt structure and chemistry, in particular, the presence of Fe. The mean Eu oxidation state in L3a Eu 86.4, 98.4 and 99.6 runs, and L3a Ce Eu 98.4 are all 10-20% less Eu^{3+} than their SH3 counterparts. This might indicate that melts with lower NBO/T display lower $Eu^{3+}/\sum Eu$ at the same temperature and f_{O_2} than experiments ran in more depolymerised melts. A relationship between melt composition and $Eu^{3+}/\sum Eu$ has already been documented for Eu by Burnham et al. [2015].

Burnham et al. [2015] developed an empirical relationship between the f_{O_2}, NBO/T and $Eu^{3+}/\sum Eu$ (Equation 5.7) for silicate melt/glasses based on in-situ XANES data:

$$Eu^{3+}/\sum Eu = \frac{1}{1+10^{-0.25 log fO_2 - \frac{6410}{T} - 1.1 NBO/T + 2.6}} \tag{5.7}$$

This relationship can be used to estimate the $Eu^{3+}/\sum Eu$ for samples in the SH3 series and L3a series gas mixing furnace experiments, if the f_{O_2}, temperature and melt NBO/T are known. For these series, NBO/T has been estimated based on the nominal starting compositions (Table 5.1). Plotted on Figure 5.14 are the fit results (2 arctangents and 2 Voigts) for the SH3 series glasses along with the calculated values based on Equation 5.7.

The values for fitting glass in this study with two Lorentzian and two arctangent functions are up to $\approx$ 40% higher than the modelled values. This could suggest that a correction is needed for the area of Eu^{2+} relative to Eu^{3+} in our samples. Overestimating the proportion of Eu^{3+} may be due to assuming the areas of the Eu^{2+} WL transition is equal to the Eu^{3+} transition, when in fact they may not be [Rakovan et al., 2001]. Additionally, the NBO/T calculated here is based on the starting material before decarbonation; so loss of volatiles and changes in oxide proportions may also play a role in the divergence in values. Finally, if the log f_{O_2} values for each run was off by 2 log units, this could also explain the discrepancy. Alternatively, the empirical relationship in Burnham et al. [2015] was never tested for alkali bearing compositions due to their

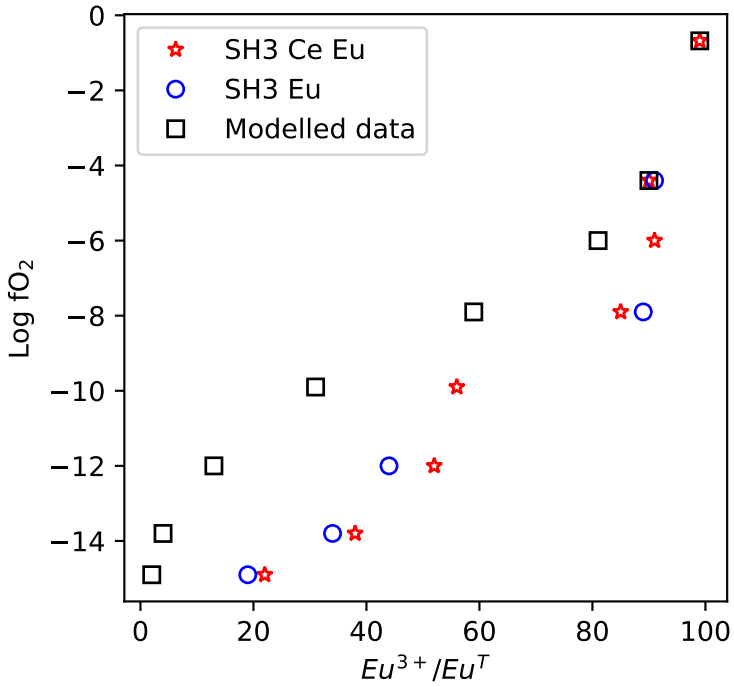

Figure 5.14: % $Eu^{3+}/\sum Eu$ for samples from the SH3 Ce and Ce Eu 1 atm. compositions. Also plotted are the values modelled on the empirical relationship in Burnham et al. [2015] (Equation 5.7).

expected volatility and loss during in-situ experiments. If the glasses in this study retain a significant alkali component, this may affect the applicability of Equation 5.7. Further work is needed to fully evaluate the compositions of these glasses (EPMA), calibrating the absolute f_{O_2} values for various gas mixes at these temperatures, and examining the effect of alkalis on Equation 5.7.

Piston cylinder glasses from the SH3 composition see a 16% drop in Eu^{3+} across a log f_{O_2} range of $\approx$ 7.6. It would be expected that the change in $Eu^{3+}/\sum Eu$ should be much larger across this range of f_{O_2} if this melt composition conforms to equation 5.7 and the melt f_{O_2} was continuously being buffered. Apatite preferentially incorporates Eu^{3+}, so the growth of apatite should force the melt to more Eu^{2+} rich if f_{O_2} was not being continuously buffered. However, the 16% drop in Eu^{3+} should represent a large enough Δ log f_{O_2} to identify if there is any change in the mineral-melt partition of Eu between SH3-Eu-MH and SH3-Eu-PtC.

The $Eu^{3+}/\sum Eu$ range for piston cylinder glasses from the L3a composition is much

larger than the SH3 piston cylinder glasses. Glasses in this composition should be much more polymerised than their SH3 counterparts, and hence it would be expected that for similar f_{O_2} values they would display a higher proportion of Eu^{2+}. L3a piston cylinder runs generally ran under hotter conditions than SH3 (100-150 ℃). Whilst this would mean that the absolute f_{O_2} is lower, relative to an oxygen buffer (e.g. MH, NNO, C-CO), relative f_{O_2} should remain constant. Therefore, for samples run in the same composition and with the same buffer, but at different temperature, the $Eu^{3+}/\sum Eu$ should be identical (assuming the temperature dependence of the $Eu^{2+} \rightleftharpoons Eu^{3+}$ buffer is parallel to Ni-NiO buffer). This was confirmed with runs L3a-Eu-Pt-A and L3a-Eu-Pt-B where both runs should have log f_{O_2} values equal to the NNO buffer, but the absolute log f_{O_2} value differs, due to the differing final T. The $Eu^{3+}/\sum Eu$ for these runs are equal (within error).

5.6.1.2 Oxidation state of Ce in silicate glass

The oxidation state of Ce in silicate melts which contain Fe is not retained upon quenching due to the exchange of $Ce^{4+} + Fe^{2+} = Ce^{3+} + Fe^{3+}$ with all Ce^{4+} reducing to Ce^{3+} upon quenching [Burnham & Berry, 2014]. Therefore, for nearly all geological systems Ce oxidation state of melts is not an indicator of f_{O_2}. Whilst there is no evidence of a redox couple between Eu and Ce, it is unclear whether Ce is also preserved in Fe free melts where another redox sensitive element is present. The SH3 composition glass beads are Fe-free, hence the effect of f_{O_2} can be evaluated for this composition. Ce^{4+} is present down to log f_{O_2} = -7.9 in these glass beads, which is below the FMQ buffer (-7.2) at these temperatures. Figure 5.15 shows the position at which 50/50 Ce^{3+} and Ce^{4+} exist in basaltic melts [Schreiber, 1987]. Its' position is towards the top extreme of f_{O_2} conditions recorded in rocks from the Earth.

Therefore, Ce mineral-melt partitioning has the potential to be used to determine f_{O_2} up to conditions approaching FMQ. From this study, the effect of melt composition (Fe-free melts) cannot be determined, in contrast to the Eu bearing melts. This would have to be refined in the future, as recent work by Smythe & Brenan [2015] has contradicted the findings of Burnham & Berry [2014], and found that increasing melt polymerisation

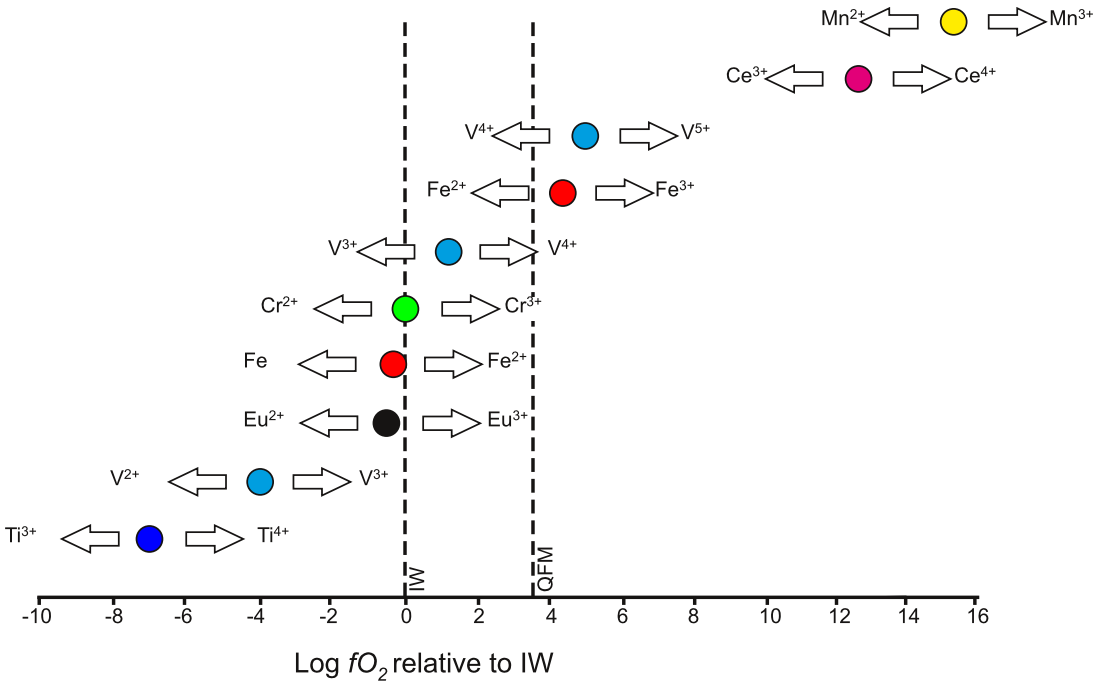

Figure 5.15: New iteration of Figure 1.5 (page 16) including the positions of the Ce^{3+}/Ce^{4+} and Mn^{2+}/Mn^{3+} redox pairs. Adapted from Herd [2008], and including Ce and Mn information from [Schreiber, 1987].

(NBO/T) resulted in a increased abundance of Ce^{4+} relative to Ce^{3+}.

5.6.2 Ce and Eu oxidation state in apatite and apatite composition as a function of oxygen fugacity

The oxidation state of Eu and Ce in apatite for the SH3 and L3a compositions are given in Tables 5.9, and 5.11. Table 5.9 shows no change in the oxidation state of Eu in apatite under different redox conditions (From 100% $Eu^{3+}/\sum Eu$ to 84%), and are in agreement with the majority of L3a piston cylinder samples. However, L3a-Eu-PtC suggests a higher proportion of Eu^{2+} than the other L3a piston cylinder examples. As apatite in the L3a-Eu-PtC runs were generally much smaller (10 x 30 μm) than apatite from other runs in this composition, the higher proportion of Eu^{2+} may be explained by contamination of XANES spectra with the melt component. However, multiple apatite XANES spectra (4) from the L3a-Eu-PtC composition display a much higher Eu^{2+} component which may suggest that this is a 'real' feature and not due to contamination. Without compositional data on this set of piston cylinder experiments, it is hard to speculate on the incorporation of Eu^{2+} in the apatite structure, and any

possible coupled substitution mechanisms.

5.6.3 Apatite-melt partitioning

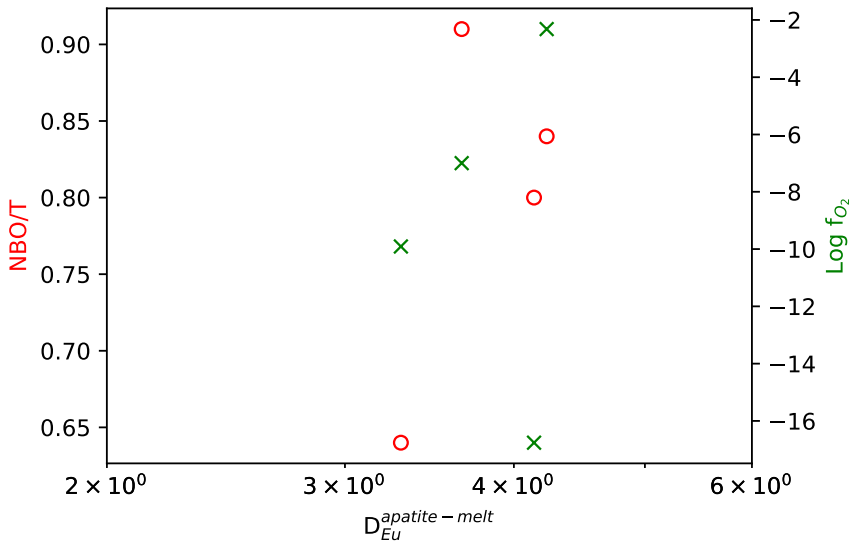

Figure 5.16: $D_{Eu}^{Ap-melt}$ vs NBO/T (red circles) or f_{O_2} (green crosses) for SH3-Eu-MH, -Pt, -PtC and -Cr.

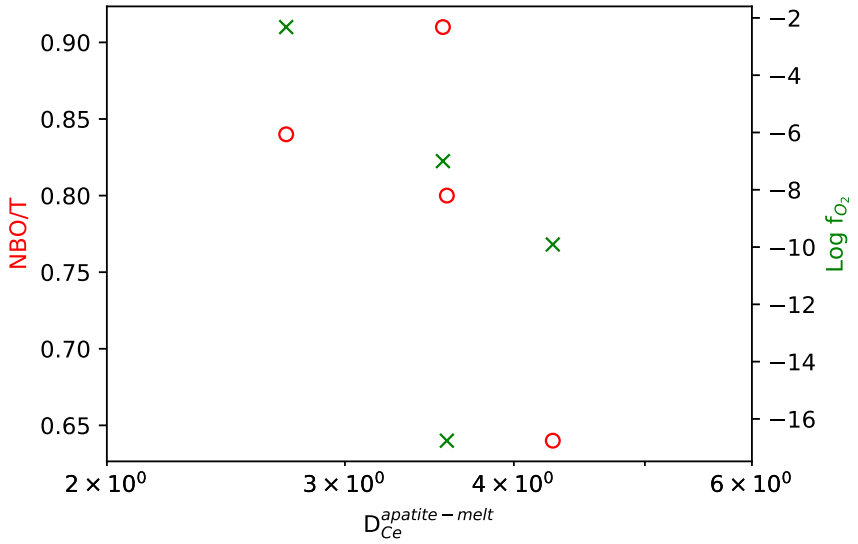

Figure 5.17: $D_{Ce}^{Ap-melt}$ vs NBO/T (red circles) or f_{O_2} (green crosses) for SH3-Eu-MH, -Pt, -PtC and -Cr.

Apatite-melt partition data is currently only available for the SH3 Eu piston cylinder data. This data (Figure 5.16) shows a tentative decrease in $D_{Eu}^{Ap-melt}$ with decreasing f_{O_2} for samples SH3-Eu-MH, -Pt and -PtC, but not for sample -Cr. Sample SH3-Eu-Cr

was run with a Cr buffer, and Cr diffusion through the inner Pt capsule has led to 0.42 wt% Cr_2O_3 in the glass phase. Due to the overlap of the Cr K edge (5989 eV) and L_3 edge of Ce (5723 eV) XANES data wasn't collected on this sample. This makes it difficult to assess whether the Cr-Cr_2O_3 buffer successful buffered f_{O_2} and therefore, the sample may provide anomalous data. Another hypothesis is that Cr in the melt has changed melt composition, which has led to a possible change in melt structure which is affecting mineral-melt partitioning. It would be expected that as the availability of Eu^{2+} increases in silicic melts (i.e. the proportion of Eu^{3+} decreases), the Eu content of apatite should correspondingly decrease (i.e. there is a decrease in the $D_{Eu}^{Ap-melt}$). Tentative results from this study support this but further work is needed to determine the effect of melt composition, temperature, and f_{O_2} on $D_{Eu}^{Ap-melt}$. There is no clear relationship between $D_{Eu}^{Ap-melt}$ and melt structure (NBO/T), with samples SH3-Eu-Pt, -PtC and -Cr suggesting a decrease in $D_{Eu}^{Ap-melt}$ with increasing polymerisation. This is contrary to the findings of Watson & Green [1981], who suggested there should be increasing $D_{Eu}^{Ap-melt}$ with more silicic melts.

If $D_{Ce}^{Ap-melt}$ was sensitive to f_{O_2} then $D_{Ce}^{Ap-melt}$ should decrease with increasing f_{O_2}, as the prevalence of Ce^{4+} increases in the melt. Figure 5.17 documents the effect of a) f_{O_2} and b) NBO/T on $D_{Ce}^{Ap-melt}$ for samples from the SH3-Eu composition. There appears to be an effect of f_{O_2} on $D_{Ce}^{Ap-melt}$ if one again discounts the SH3-Eu-Cr sample. Once more, there is no clear relationship with melt polymerisation. Further work is needed to obtain more data to deconvolve the effects of composition, temperature, f_{O_2} and melt structure on $D_{Ce}^{Ap-melt}$ and $D_{Eu}^{Ap-melt}$.

5.6.4 XANES fitting of the L3 edge

The L_3 edge of Eu has been fitted in numerous ways in this study. Figure 5.8 shows that fitting the same XANES spectrum with various background functions and peak functions results in a 20% difference in $Eu^{3+}/\sum Eu$ depending on the shapes/functions chosen. Ideally, if the glasses had their $Eu^{3+}/\sum Eu$ independently verified via another technique, then these beads could be used as standards, and would indicate which fitting procedure was optimal for the Eu L_3 edge. The difference in $Eu^{3+}/\sum Eu$ depending on

the fit procedure also indicates why comparison to literature data is difficult unless the same procedure was used on both sets of data.

Further work is also needed to find the optimised procedure to fit the Ce L_3 edge. Currently the edge has been fitted with one arctangent for all electron transitions, and should probably be fitted with at least 3 (or more) arctangents to represent the 2 transitions associated with CeO_2 and the transition associated with Ce in the 3+ oxidation state. Also ignored, is the slight pre-edge peak at 5720 eV associated with CeO_2.

5.7 Eu and Ce oxy-geobarometers and applicability to other terrestrial bodies

The oxidation state of Ce and Eu in terrestrial silicate melts seems to vary much more than Mn. Whilst Ce is predominantly in the 3+ oxidation state up to relatively oxidised conditions, little Ce^{4+} is needed to make a Ce anomaly. Only 0.05-0.1% of Ce is thought to be in the 4+ oxidation state in terrestrial silicate melts [Burnham & Berry, 2012], and yet Ce anomalies can still be observed in minerals such as zircon where the partition of Ce^{4+} relative to REE^{3+} is strong and/or the melt in which zircon crystallises has become enriched in Ce^{4+}. The redox conditions on Earth are considered to be more oxidised than the other rocky bodies (Mercury, Venus, the Moon and Mars) in our solar system (Figure 1.3, page 7). Therefore, the use of a Ce based oxy-geobarometer would likely be unviable in these bodies if the f_{O_2} was much lower.

Eu, on the other hand, is predominantly found as Eu^{3+} under terrestrial conditions, and 40-80% Eu as Eu^{2+} is expected for f_{O_2} conditions associated with lunar melts [Schreiber, 1977]. Therefore, an Eu based oxy-geobarometer would be useful for determining a wide range of planetary redox conditions, and not just Earth. However, the intensity of lunar anomalies cannot be directly related to f_{O_2} as almost all lunar mare basalts have negative Eu anomalies and anorthositic lunar highland samples have a positive Eu anomaly [Jones, 2016]. The difference in the sign and magnitude between these two lunar samples is not due to f_{O_2}, but to the concentration of Eu in plagioclase

under reducing conditions and the separation of plagioclase leaving a depleted liquid (lunar mare basalt) [Jones, 2016]. Therefore, a future oxy-geobarometer should be calibrated based on Eu mineral-melt partitioning, rather than the magnitude and sign of an anomaly. This also highlights that care has to be taken in understanding the f_{O_2} of extraterrestrial bodies, as like the Earth, these bodies may not be equilibrated with redox state [Jones, 2004] and so conclusions about planetary f_{O_2} based on the small selection of meteorites is limited.

A variety of silicate melt compositions have been used to grow apatite during this work, but as of yet have not been compared to natural silicate melts found on the Earth, Moon, Mars etc. The L3a composition was originally designed to replicate silicate melts similar in composition to lunar melts which crystallise apatite [Potts, 2016] (Table 5.1, page 156) and any findings, therefore, should be directly applicable to these compositions. The other starting composition in the Eu study, SH3, is a haplobasaltic composition (Table 5.1, page 156). Whilst this composition has similar SiO_2 contents to Lunar (lunar mare) and Martian (Shergotty meteorite) basalts, SH3 is lacking Fe which could be a problem when using as analogue for these magmas as they generally contain ≈ 20 wt% FeO. The SH3 composition is also much richer in Al_2O_3, P_2O_5, and the alkalis when compared to extraterrestrial basalts, and hence, future work in developing an extraterrestrial oxy-geobarometer should focus on a different basaltic composition.

5.8 Conclusions

Preliminary results from this study suggests that the partitioning of $D_{Eu}^{Ap-melt}$ and $D_{Ce}^{Ap-melt}$ may indeed record magmatic f_{O_2}. Apatite shows a strong preference for Eu^{3+} and cannot incorporate appreciable amounts of Eu^{2+}. However, silicate glasses can incorporate Eu in both the 2+ and 3+ oxidation states. A progressive change in the Eu^{3+}/Eu^{2+} ratio in magmatic systems, over a large range in f_{O_2} is expected to change the Eu content of apatite. Conversely, for Ce, Ce^{3+} is much more compatible in apatite than Ce^{4+}, whilst both oxidation states are incorporated into silicate glass. Therefore a decrease in the Ce^{4+}/Ce^{3+} ratio of silicate glasses is expected to result in higher Ce contents of apatite than a higher Ce^{4+}/Ce^{3+} ratio. Eu^{3+}/Ce^{3+} cannot

substitute directly for Ca^{2+} in the apatite structure without coupled substitution or the introduction of vacancies for charge balance (e.g. Equations 5.3-5.6). Table 5.7 suggests that one substitution mechanism likely to be present in these samples is coupled substitution with Na. There is no obvious need for Ce/Eu to substitute on the P site, as this site appears full based on stoichiometric calculations.

Further work is needed to examine the relationship between f_{O_2} and $D_{Ce}^{Ap-melt}/D_{Eu}^{Ap-melt}$, and explain the discrepancy in the $Eu^{3+}/\sum Eu$ value for L3a-Eu-PtC (the current hypothesis is spectra for the oxidation state of Eu in apatite in this sample has been contaminated by the glass phase due to the small crystal size relative to the beam). In geological systems, the crystallisation of minerals such as plagioclase, which concentrate a specific oxidation state of Eu, makes developing an oxy-gebarometer much more complicated. If apatite can be proven to be an early crystallising phase (liquidus phase), this bypasses the problem of feldspar crystallisation; otherwise the crystallisation of other Eu phases has to be taken into account in any future oxy-barometer. Also, Eu concentrations of natural apatite are usually much lower than Ce which could also hinder a Eu based oxy-barometer compared to Ce. Ce contents of most apatite are generally high enough to measure using EPMA, but Eu contents of most apatite would generally be below the EPMA detection limit, and would have to be measured by a technique with a lower detection limit like SIMS. Further work needs to fully assess the controls of temperature, pressure and melt composition on $D_{Eu}^{Ap-melt}$ and $D_{Ce}^{Ap-melt}$.

6

Conclusions and Future work

"In nature's infinite book of secrecy a little I can read."

– William Shakespeare *Antony and Cleopatra 1.2.10-11*

6.1 Introduction

The object of this thesis was to investigate how the crystal chemistry of accessory minerals, in particular apatite, responded to the f_{O_2} of their parental melt. The raison d'être for this work was the study by Miles et al. [2014] who suggested a strong correlation between the Mn concentration in apatite from calc-alkaline felsic rocks and the f_{O_2} of the parental melt. Initial work focused on spinel which can often be found as a Mn-rich phase, and can be synthesised in a gas mixing furnace to grow large crystals suitable for XANES work. The simpler structure of spinel compared to apatite, allowed the testing of various fitting and fingerprinting techniques to determine the Mn valence state from XANES spectra and to determine how the Mn valence state and crystal chemistry of Mn rich spinel respond to a change in f_{O_2}.

Following work on spinel, shift focused to the sensitivity of apatite crystal chemistry to redox state. To fully determine the effect of f_{O_2} on the Mn concentration in apatite, experiments were needed to determine (a) the change in Mn oxidation state in silicate melts as a function of f_{O_2}, (b) what oxidation state of Mn, if any, is preferentially incorporated into apatite, (c) how Mn apatite-melt partitioning is affected by f_{O_2}, and (d) other parameters which affect Mn apatite-melt partitioning. Finally, preliminary work was carried out in determining how Ce and Eu in apatite is also affected by f_{O_2}.

6.2 Summary of results

6.2.1 Spinel

Spinel are a very common accessory mineral which can incorporate a considerable amount of Mn into their crystal structure. Spinel are much easier to synthesise under controlled f_{O_2} conditions in a gas mixing furnace than apatite, as volatile components (e.g. OH, F, Cl, P_2O_5) are not key constituents in their mineral formula. The simple cubic crystallographic structure of spinel makes it much easier to predict the distribution of cations over the tetrahedral and octahedral crystallographic sites, and understanding how this may vary for a range in f_{O_2} conditions. The isotropic nature of spinel limits the appearance of crystallographic effects in Mn XANES spectra, which makes it easier to assign any shape change to change in the oxidation state or coordination of the absorbing atom.

The crystal chemistry of Al-Mn-O spinel are shown to be essentially unaffected by f_{O_2}. Mn content, oxidation state, and coordination are controlled chiefly by crystal chemistry and cation site geometry. In contrast, Mn-Fe-O spinel may have the potential to record f_{O_2} conditions, with Mn concentration, and cation species/valence on the octahedral site all effected by f_{O_2}. This work showed the difficulty of determining the valence state of Mn via XANES when coordination and valence simultaneously change, and issues in controlling Mn redox in Fe-Mn bearing phases due to electron transfer. In synthesised spinel, Mn was distributed across both the M and T crystallographic sites and was also present in multiple oxidation states in each site.

6.2.2 Apatite

Apatite is a largely Fe-free mineral, and previous work suggests a preferential partitioning of Mn onto the Ca2 site, thus mitigating some of the concerns raised by the spinel work. An experimental study into apatite-silicate melt partition of Ce, Eu and Mn are all presented in this thesis. Samples have been analysed with SIMS, EPMA and XANES analysis to indicate composition, and valence of Ce, Eu and Mn in the apatite and glass (quenched melt) phases.

XANES work on glasses synthesised in a gas mixing furnace under a variety of f_{O_2} conditions representative of those on Earth are presented here. The XANES data suggest that the oxidation state of Mn in silicate melt is dominantly, if not wholly, 2+ over a range of f_{O_2} conditions ($\approx$ 9 log units). These results suggests Mn^{3+} is not present in substantial amounts in magmatic systems. It is unlikely this is due to preferential exclusion of the Mn^{3+} cation in the melt structure due to its size. Mn^{3+} is similar in size to Fe^{3+} in both tetrahedral and octahedral coordination, casting doubt on this simple explanation. As such, it cannot be completely excluded that the methods of XANES analysis used here fails to distinguish Mn^{3+} from the rest of the Mn K-edge spectrum. Apatite XANES data also suggests that under a wide variety of f_{O_2} conditions, Mn remains in the same oxidation state (2+). This is due to the the cation size of Mn^{2+} in seven-fold coordination (0.90 Å), which is more similar in size to the Ca^{2+} in the Ca2 site (1.06 Å) than Mn^{3+} (0.67-0.72 Å) [Miles et al., 2014]. Therefore, it is unlikely that Mn oxidation state, or mineral-melt partitioning, could be used to determine the f_{O_2} of parental magmas over a wide range of f_{O_2} conditions.

$D_{Mn}^{Ap-melt}$ partition coefficients show no systematic change with f_{O_2}. This supports the hypothesis, based on XANES data, that Mn is (nearly) wholly in the 2+ oxidation state in silicate glasses over the range of terrestrial f_{O_2} conditions. Instead, $D_{Mn}^{Ap-melt}$ is strongly influenced by the ratio of bridging oxygens (NBO) to tetrahedra (T) (NBO/T) in the melt phase. This work finds that the trends between Mn concentration in apatite from felsic melts and f_{O_2} documented in Miles et al. [2014] can instead be explained in progressive change in melt composition and melt polymerisation, with more polymerised melts having a much greater $D_{Mn}^{Ap-melt}$ than their less polymerised counterparts. This is probably driven by the reduced availability of non bridging oxygens in more polymerised melts; this means that the melt structure cannot incorporate as many metal cations, such as Mn^{2+}. Melt structure is often not considered during trace element modelling. The Miles et al. [2014] data shows that even subtle variations in melt structure/chemistry likely to occur during prolonged geological processes can have a strong influence on mineral-melt partitioning.

The lack of an affect of f_{O_2} on the partitioning of Mn between apatite and melt has led

to an examination of other redox sensitive trace elements that partition into apatite. Ce and Eu in apatite are another two redox sensitive elements which can substitute into the apatite structure. A preliminary study was carried out to determine how f_{O_2} of magmas affects the partitioning of these two REEs in two separate compositions, SH3 - a haplo-basaltic composition and L3a - a more felsic (dacitic) composition. Results show that glasses containing Fe do not preserve Ce^{4+} upon quenching, and the $Eu^{3+}/\sum Eu$ is somewhat affected. This has important consequences when trying to determine the Ce/Eu oxidation state of natural melts which often contain Fe. The haplobasaltic SH3 composition, due to the lack of Fe, preserved Ce^{4+} upon quenching, and showed that Ce^{4+} is present in small, but appreciable amounts, down to f_{O_2} conditions associated with the FMQ buffer. Eu on the other-hand, contains significant proportions (22% $Eu^{3+}/\sum Eu$) of Eu^{3+} down to f_{O_2} conditions associated with IW - 4.7, and has up to 10% $Eu^{3+}/\sum Eu$ at IW +5.8. Therefore, an Eu based oxy-geobarometer would be suitable for use on a wide variety of planetary material (Fig. 1.3, page 7), including material from the early Earth, Moon, and Mars.

Ce and Eu valence in apatite is dominantly in the 3+ oxidation state across a wide range of conditions. This shows that the oxidation state of these elements in apatite is tightly controlled by the crystallographic structure of apatite. The cation sizes of Ce^{3+} (1.07 Å sevenfold coordination) and Eu^{3+} (1.01 Å sevenfold coordination) are much more similar in size to Ca^{2+} (1.06 Å sevenfold coordination) than Ce^{4+} (probably less than 0.97 Å in sevenfold coordination) and Eu^{2+} (1.20 Å sevenfold coordination) [Shannon, 1976]. In contrast, the structure of a silicate melt is much more flexible, and hence both Ce^{3+}/Ce^{4+} and Eu^{2+}/Eu^{3+}can be present in the melt, with their proportions mainly effected by f_{O_2} and melt composition. As such, both Ce and Eu partitioning between apatite and SH3 melt should vary as a function of f_{O_2}. Therefore, there is potential for an Ce or Eu oxy-geobarometer, although more work is needed into examining other controls on these partitioning coefficients, in particular melt composition and extent of melt polymerisation.

6.3 X-ray absorption near edge structure, and estimates of Ce, Eu and Mn valency

Much of this work has examined how different features in the X-ray absorption near edge structure (XANES) of materials can be used to determine the oxidation state of Mn, Ce and Eu. The Mn K-edge has been used in this thesis to obtain information on the formal valence and coordination of Mn in spinel, apatite and quenched melt (glass). It is often difficult to use the Mn K-edge to determine coordination/valence due to the large differences in spectra of single coordination, single valence standards, where spectra obtained on two different chemical composition (but same valence and coordination) compounds vary in their edge position by up to 4.5 eV. Therefore, this work focused on examining the pre-edge peak which results from the 1s $\rightarrow$ 3d transition. Valence/coordination estimates from this feature are supposed to be less sensitive to scattering from neighbouring atoms surrounding the central absorbing Mn atom. Spinel work highlighted that the Mn pre-edge is also sensitive to neighbouring atoms. Spinel work also indicated that determining quantitative information on average Mn valence in complex minerals is currently un-achievable (based on the current set of standards and methods recorded in the literature) using the Mn pre-edge. There are other ways of determining the valence of Mn from the Mn K-edge, one is linear combination fitting of the unknown with single valence standards in a similar coordination as the unknown. Often it is hard to acquire such standards, and this approach only works well for substances which can be described as a linear mixture of the two standards. Further work is needed to accurately determine the valence and coordination of Mn using XANES, and could include work on other electronic edges such as the M_3 edge.

Eu and Ce spectra were collected for the L_3 edge. The composition of the Eu apatite and glasses had to be Mn free, as collecting conventional scans of the Eu L_3 edge is not possible for samples which contain high concentrations of Mn [Rakovan et al., 2001] due to interference from the K-M_3 and K-M_2 transitions. Therefore a wavelength dispersive spectrometer would be needed to determine the valence state of Eu [Rakovan et al., 2001] in natural samples containing significant Mn. Fitting procedures used in

this work highlight the importance of fitting both single valence single coordinated samples and unknown spectra with the same number and types of background and peak functions. This work has assumed that there is no effect of coordination on the predicted % $Eu^{3+}/\sum$Eu and % $Ce^{4+}/\sum$Ce, which may need to be further investigated. The L_3 edge is not the only electron transition for which XANES data of Eu and Ce can be collected to determine average valency. The $M_{4,5}$ edge can also be used to determine Ce valence, is more sensitive to Ce^{4+} content, and due to the lower energy of the $M_{4,5}$ edge relative to the L_3 edge, is less sensitive to beam damage [Smythe & Brenan, 2015]. It would be interesting to compare the results of the two edges in determining Ce and/or Eu valence.

6.4 Future work

Following the research outcomes described in this work, this section will describe the possible lines for further development:

- Much more work is needed to develop the potential of an Eu/Ce based apatite oxy-geobarometer. Currently, whilst it appears that the partition coefficient of Eu or Ce is affected by f_{O_2} more work is needed to explore this across a larger range of f_{O_2} conditions. Currently little is known about the role of apatite mineral chemistry and partitioning of $D_{Eu}^{apt-melt}$ or $D_{Ce}^{apt-melt}$. Work needs to go into fully assessing the substitution of these elements into the apatite structure and whether either of them are affected by the cation or anion compositions (e.g. Eu - Al relationship in pyroxene [McKay et al., 1994]). Additional work is needed to examine the effects of pressure, temperature, melt composition and other variables on $D_{Eu}^{apt-melt}$ or $D_{Ce}^{apt-melt}$, and how sensitive these partition coefficients are to sub solidus annealing.

- Currently there is no one definitive way of accurately determining the absolute oxidation state of Mn, Eu and Ce using XANES in complex geological samples. Further work with simple and more complex standards is needed to determine a viable method of calculating redox state in a variety of samples where both

coordination and oxidation state of the absorbing atom varies. This would require calibrants where the oxidation state and coordination of the absorbing atom would have to be determined by other methods such as Mössabuer, EELS or wet chemistry. Also useful would be to determine the oxidation state of silicate melts in situ [Burnham & Berry, 2014; Burnham et al., 2015] as this would avoid any quenching effects with Fe. Furthermore, the complexity of scattering from the nearest neighbours needs to be accounted for to fathom how sample composition changes the shape of a XANES spectrum.

- This work highlights the dominant influence of melt structure on Mn mineral-melt partitioning. More insight is needed to fully understand the role trace elements play in the structure of silicate melts, and how this varies under different melt compositions. Work is needed to evaluate the role melt structure has on existing, and future tools which use the mineral-melt partition coefficients of trace elements. In particular, a dominant influence of the proportion of NBO on metal cation partitioning, at least for Mn, suggests that the availability of cation sites in the melt is a key driver in mineral-melt partitioning. This appears to be true for minerals like apatite, where preferential element incorporation onto a single, or small number of sites can be considered in simple terms such as cation radius. A similar influence of melt structure/composition might be expected for other multi-valent elements, including Eu and Ce, partitioning between mineral and melt phases. As such, a predictive framework for modelling the effect of composition on melt structure, and for quantifying the ratio of NBO/T would be considerable practical use in geochemistry.

- The ratio of NBO/T used in this work has only been calculated very crudely, and needs to be tested for the effect of other parameters such as different melt compositions, Fe contents, volatile contents, and changing $Fe^{3+}/\sum Fe$ content. In this work Fe has all been assigned as a network modifier, but whilst ferrous iron is generally a network modifier, Fe^{3+} can act as both, with Fe^{3+} acting as a network former when charge balanced with sufficient metal cations [Mysen, 1983]. Therefore, it is also likely that f_{O_2} will have an affect on the NBO/T ratio,

changing the availability of Fe^{3+}, and potentially having other subtle effects on melt structure, which are yet to be identified. We need further experimental studies and modelling work to accurately determine NBO/T ratios for a wide range of magmatic compositions easily.

Future experimental partitioning studies, as shown here, need to be designed to explore the effects of subtle variations in melt chemistry on element partitioning. Apatite data documented in chapter 4 provides a perfect example of how small compositional variations within a small body like the Criffel pluton results in considerable changes in mineral chemistry. This dominant influence of melt chemistry must, therefore, be considered carefully in future work.

References

Agilent (2012). Xcalibur CCD system, Crysalis software system.

Alderman, O., Lazareva, L., Wilding, M., Benmore, C., Heald, S., Johnson, C., Johnson, J., Hah, H.-Y., Sendelbach, S., Tamalonis, A., Skinner, L., Parise, J., & Weber, J. (2017). Local structural variation with oxygen fugacity in fe2sio4+x fayalitic iron silicate melts. *Geochimica et Cosmochimica Acta*, 203, 15 – 36.

Andreozzi, G. B., Bosi, F., & Garramone, F. (2001a). Synthetic spinels in the $(Mg,Fe^{2+},Zn)(Al,Fe^{3+})_2O_4$ system. II. Preliminary chemical and structural data of hercynite and magnesioferrite samples. *Periodico di Mineralogia*, 70(2), 193–204.

Andreozzi, G. B., Lucchesi, S., Skogby, H., & Della Giusta, A. (2001b). Compositional dependence of cation distribution in some synthetic $(Mg,Zn)(Al,Fe^{3+})_2O_4$ spinels. *European Journal of Mineralogy*, 13(2), 391 LP – 402.

Andreozzi, G. B., Princivalle, F., Skogby, H., & Della Giusta, A. (2000). Cation ordering and structural variations with temperature in $MgAl_2O_4$ spinel: An X-ray single-crystal study. *American Mineralogist*, 85(9), 1164–1171.

Antony, J. W., Bideaux, R. A., Bladh, K. W., & Nicols, M. C. (1997). *Handbook of Mineralogy Volume III: Halides, Hydroxides, Oxides*. Chantilly: Mineralogical Society of America.

Arai, S. (1992). Chemistry of chromian spinel in volcanic rocks as a potential guide to magma chemistry. *Mineralogical Magazine*, 56(383), 173–184.

Arató, R. & Audétat, A. (2017). Experimental calibration of a new oxybarometer for silicic magmas based on vanadium partitioning between magnetite and silicate melt. *Contributions to Mineralogy and Petrology*, 172(7), 52.

Arculus, R. J. (1985). Oxidation status of the mantle: past and present. *Annual Review of Earth and Planetary Sciences*, 13(1), 75–95.

Arndt, U. W. & Willis, B. T. M. (1966). *Single Crystal Diffractometry*. Cambridge Monographs on Physics. Cambridge University Press.

Bacon, C. R. & Hirschmann, M. M. (1988). Mg/Mn partitioning as a test for equilibrium between coexisting Fe-Ti oxides. *American Mineralogist*, 73(1-2), 57–61.

Baker, L. L. & Rutherford, M. J. (1996). The effect of dissolved water on the oxidation state of silicic melts. *Geochimica et Cosmochimica Acta*, 60(12), 2179–2187.

Ball, J. A., Pirzada, M., Grimes, R., Zacate, M. O., Price, D. W., & Uberuaga, B. P. (2005). Predicting lattice parameter as a function of cation disorder in $MgAl_2O_4$ spinel. *Journal of Physics: Condensed Matter*, 17(48), 7621–7631.

Barnes, S. J. & Roeder, P. L. (2001). The Range of Spinel Compositions in Terrestrial Mafic and Ultramafic Rocks. *Journal of Petrology*, 42(12), 2279.

Battault, T., Legros, R., & Rousset, A. (1995). Structural and electrical properties of iron manganite spinels in relation with cationic distribution. *Journal of the European Ceramic Society*, 15(11), 1141–1147.

Bearden, J. A. & Burr, A. F. (1967). Reevaluation of X-Ray Atomic Energy Levels. *Reviews of Modern Physics*, 39(1), 125–142.

Belousova, E. A., Walters, S., Griffin, W. L., & O'Reilly, S. Y. (2001). Trace-element signatures of apatites in granitoids from the Mt Isa Inlier, northwestern Queensland. *Australian Journal of Earth Sciences*, 48(4), 603–619.

Berry, A. J., O'Neill, H. S., Jayasuriya, K. D., Campbell, S. J., & Foran, G. J. (2003). XANES calibrations for the oxidation state of iron in a silicate glass. *American Mineralogist*, 88(7), 967–977.

Berry, A. J., Yaxley, G. M., Woodland, A. B., & Foran, G. J. (2010). A XANES calibration for determining the oxidation state of iron in mantle garnet. *Chemical Geology*, 278(1–2), 31–37.

Biagioni, C. & Pasero, M. (2014). The systematics of the spinel-type minerals: An overview. *American Mineralogist*, 99(7), 1254–1264.

Bianconi, A., Marcelli, A., Dexpert, H., Karnatak, R., Kotani, A., Jo, T., & Petiau, J. (1987). Specific intermediate-valence state of insulating $4f$ compounds detected by L_3 x-ray absorption. *Physical Review B*, 35(2), 806–812.

Blundy, J. & Wood, B. (2003). Partitioning of trace elements between crystals and melts. *Earth and Planetary Science Letters*, 210(3–4), 383–397.

Bonsdorf, G., Schäfer, K., Teske, K., Langbein, H., & Ullmann, H. (1998). Stability region and oxygen stoichiometry of manganese ferrite. *Solid State Ionics*, 110(1), 73–82.

Bonyadi, Z., Davidson, G. J., Mehrabi, B., Meffre, S., & Ghazban, F. (2011). Significance of apatite REE depletion and monazite inclusions in the brecciated Se-Chahun iron oxide-apatite deposit, Bafq district, Iran: Insights from paragenesis and geochemistry. *Chemical Geology*, 281(3-4), 253–269.

Borisov, A., Behrens, H., & Holtz, F. (2015). Effects of melt composition on Fe^{3+}/Fe^{2+} in silicate melts: a step to model ferric/ferrous ratio in multicomponent systems. *Contributions to Mineralogy and Petrology*, 169(2), 24.

Borisov, A. A. (2013). Mutual interaction of redox pairs in silicate melts: $V^{5+}/V^{4+}/V^{3+}/V^{2+}$ tetrad and other equilibria. *Petrology*, 21(4), 305–315.

Bosi, F., Andreozzi, G. B., Hålenius, U., & Skogby, H. (2011). Zn-O tetrahedral bond length variations in normal spinel oxides. *American Mineralogist*, 96(4), 594–598.

Bosi, F., Hålenius, U., Andreozzi, G. B., Skogby, H., & Lucchesi, S. (2007). Structural refinement and crystal chemistry of Mn-doped spinel: A case for tetrahedrally coordinated Mn^{3+} in an oxygen-based structure. *American Mineralogist*, 92(1), 27–33.

Botcharnikov, R. E., Koepke, J., Holtz, F., McCammon, C., & Wilke, M. (2005). The effect of water activity on the oxidation and structural state of Fe in a ferro-basaltic melt. *Geochimica et Cosmochimica Acta*, 69(21), 5071–5085.

Boyce, J. W., Liu, Y., Rossman, G. R., Guan, Y., Eiler, J. M., Stolper, E. M., & Taylor, L. A. (2010). Lunar apatite with terrestrial volatile abundances. *Nature*, 466, 466.

Boyce, J. W., Tomlinson, S. M., McCubbin, F. M., Greenwood, J. P., & Treiman, A. H. (2014). The lunar apatite paradox. *Science*, 344(6182), 400–402.

Bromiley, G. D., Gatta, G. D., & Stokes, T. (2015). Manganese incorporation in synthetic hercynite. *Mineralogical Magazine*, 79(3).

Brounce, M., Kelley, K. A., Cottrell, E., & Reagan, M. K. (2015). Temporal evolution of mantle wedge oxygen fugacity during subduction initiation. *Geology*, 43(9), 775–778.

Buddington, A. F., Fahey, J. J., & Vlisidis, A. C. (1955). Thermometric and petrogenetic significance of titaniferous magnetite. *American Journal of Science*, 253(9), 497–532.

Buddington, A. F. & Lindsley, D. H. (1964). Iron-Titanium Oxide Minerals and Synthetic Equivalents. *Journal of Petrology*, 5(2), 310.

Burger, P., Shearer, C., Papike, J., Bell, A., & Muttik, N. (2016). Igneous Spinel Chemistry as a Function of Temperature and Oxygen Fugacity in Martian Melts. In *Lunar and Planetary Science Conference*, volume 47 of *Lunar and Planetary Inst.˜Technical Report* (pp. 1769).

Burnham, A. D. & Berry, A. J. (2012). An experimental study of trace element partitioning between zircon and melt as a function of oxygen fugacity. *Geochimica et Cosmochimica Acta*, 95, 196–212.

Burnham, A. D. & Berry, A. J. (2014). The effect of oxygen fugacity, melt composition, temperature and pressure on the oxidation state of cerium in silicate melts. *Chemical Geology*, 366, 52–60.

Burnham, A. D., Berry, A. J., Halse, H. R., Schofield, P. F., Cibin, G., & Mosselmans, J. F. W. (2015). The oxidation state of europium in silicate melts as a function of oxygen fugacity, composition and temperature. *Chemical Geology*, 411, 248–259.

Calvin, S. (2013). *XAFS for Everyone*. Taylor & Francis.

Cameca (2013). SX 100 Electron Probe Micro Analyzer [image]'. Avaliable at: `https://eps.utk.edu/research/images/CAMECA.jpg` [accessed 13 Sep. 2016].

Canil, D. (1997). Vanadium partitioning and the oxidation state of Archaean komatiite magmas. *Nature*, 389, 842–845.

Canil, D. (1999). Vanadium partitioning between orthopyroxene, spinel and silicate melt and the redox states of mantle source regions for primary magmas. *Geochimica et Cosmochimica Acta*, 63(3–4), 557–572.

Carl Zeiss Microscopy GmbH (2017). The Technology Behind ZEISS Crossbeam.

Carmichael, I. S. E. & Ghiorso, M. S. (1990). The effect of oxygen fugacity on the redox state of natural liquids and their crystallizing phases. *Reviews in Mineralogy and Geochemistry*, 24(1), 191–212.

Carmichael, I. S. E. & Nicholls, J. (1967). Iron-titanium oxides and oxygen fugacities in volcanic rocks. *Journal of Geophysical Research*, 72(18), 4665–4687.

Carta, D., Casula, M. F., Falqui, A., Loche, D., Mountjoy, G., Sangregorio, C., & Corrias, A. (2009). A Structural and Magnetic Investigation of the Inversion Degree in Ferrite Nanocrystals MFe_2O_4 (M = Mn, Co, Ni). *The Journal of Physical Chemistry C*, 113(20), 8606–8615.

Carta, D., Casula, M. F., Mountjoy, G., & Corrias, A. (2008). Formation and cation distribution in supported manganese ferrite nanoparticles: an X-ray absorption study. *Physical Chemistry Chemical Physics*, 10(21), 3108–3117.

Carta, D., Marras, C., Loche, D., Mountjoy, G., Ahmed, S. I., & Corrias, A. (2013). An X-ray absorption spectroscopy study of the inversion degree in zinc ferrite nanocrystals dispersed on a highly porous silica aerogel matrix. *The Journal of Chemical Physics*, 138(5), 54702.

Chalmin, E., Farges, F., & Brown, G. E. (2009). A pre-edge analysis of Mn K-edge XANES spectra to help determine the speciation of manganese in minerals and glasses. *Contributions to Mineralogy and Petrology*, 157(1), 111–126.

Chatterjee, S. & Jung, I.-H. (2014). Critical evaluation and thermodynamic modeling of the Al–Mn–O (Al_2O_3–MnO–Mn_2O_3) system. *Journal of the European Ceramic Society*, 34(6), 1611–1621.

Cherniak, D. J. (2010). Diffusion in Accessory Minerals: Zircon, Titanite, Apatite, Monazite and Xenotime. *Reviews in Mineralogy and Geochemistry*, 72(1), 827–869.

Christie, D. M., Carmichael, I. S. E., & Langmuir, C. H. (1986). Oxidation states of mid-ocean ridge basalt glasses. *Earth and Planetary Science Letters*, 79(3), 397–411.

Chu, M.-F., Wang, K.-L., Griffin, W. L., Chung, S.-L., O'Reilly, S. Y., Pearson, N. J., & Iizuka, Y. (2009). Apatite Composition: Tracing Petrogenetic Processes in Transhimalayan Granitoids. *Journal of Petrology*, 50(10), 1829.

Cicconi, M. R., Giuli, G., Paris, E., Ertel-Ingrisch, W., & Dingwell, B. (2009). Europium structural role in silicate glasses: Reduction kinetics at low oxygen fugacity. *Journal of Physics: Conference Series*, 190, 9–13.

Cookenboo, H. O., Bustin, R. M., & Wilks, K. R. (1997). Detrital chromian spinel compositions used to reconstruct the tectonic setting of provenance; implications for orogeny in the Canadian Cordillera. *Journal of Sedimentary Research*, 67(1), 116–123.

Cottrell, E. & Kelley, K. A. (2011). The oxidation state of Fe in MORB glasses and the oxygen fugacity of the upper mantle. *Earth and Planetary Science Letters*, 305(3–4), 270–282.

Cottrell, E., Kelley, K. A., Lanzirotti, A., & Fischer, R. A. (2009a). High-precision determination of iron oxidation state in silicate glasses using XANES. *Chemical Geology*, 268(3–4), 167–179.

Cottrell, E., Walter, M. J., & Walker, D. (2009b). Metal-silicate partitioning of tungsten at high pressure and temperature: Implications for equilibrium core formation in Earth. *Earth and Planetary Science Letters*, 281(3-4), 275–287.

Dai, L. & Karato, S.-i. (2014). Influence of oxygen fugacity on the electrical conductivity of hydrous olivine: Implications for the mechanism of conduction. *Physics of the Earth and Planetary Interiors*, 232, 57–60.

Deer, W. A., Howie, R. A., & Zussman, J. (2013). *An Introduction to the Rock-Forming Minerals*. Mineralogical Society of Great Britain and Ireland.

Deines, P., Earth, P. S. U., & Station, M. S. E. (1974). *Temperature-oxygen fugacity tables for selected gas mixtures in the system C-H-O at one atmosphere total pressure*. University Park : College of Earth and Mineral Sciences, Pennsylvania State University.

Dickenson, M. P. & Hess, P. C. (1981). Redox equilibria and the structural role of iron in alumino-silicate melts. *Contributions to Mineralogy and Petrology*, 78(3), 352–357.

Dickenson, M. P. & Hess, P. C. (1986). The structural role and homogeneous redox equilibria of iron in peraluminous, metaluminous and peralkaline silicate melts. *Contributions to Mineralogy and Petrology*, 92(2), 207–217.

Doherty, A. L., Webster, J. D., Goldoff, B. A., & Piccoli, P. M. (2014). Partitioning behavior of chlorine and fluorine in felsic melt-fluid(s)-apatite systems at 50MPa and 850-950 ℃. *Chemical Geology*, 384, 94–109.

Douce, A. E. P., Roden, M., Patiño Douce, A. E., & Roden, M. (2006). Apatite as a probe of halogen and water fugacities in the terrestrial planets. *Geochimica et Cosmochimica Acta*, 70(12), 3173–3196.

Doyle, P. M., Berry, A. J., Schofield, P. F., & Mosselmans, J. F. W. (2016). The effect of site geometry, Ti content and Ti oxidation state on the Ti K-edge XANES spectrum of synthetic hibonite. *Geochimica et Cosmochimica Acta*, 187, 294–310.

Duba, A., Boland, J. N., & Ringwood, A. E. (1973). The Electrical Conductivity of Pyroxene. *The Journal of Geology*, 81(6), 727–735.

Dyar, M. D., Gunter, M. E., Delaney, J. S., Lanzarotti, A., & Sutton, S. R. (2002). Systematics in the structure and XANES spectra of pyroxenes, amphiboles, and micas as derived from oriented single crystals. *The Canadian Mineralogist*, 40(5), 1375–1393.

Eby, G. N. (1975). Abundance and distribution of the rare-earth elements and yttrium in the rocks and minerals of the Oka carbonatite complex, Quebec. *Geochimica et Cosmochimica Acta*, 39(5), 597–620.

Ehrt, D. (2009). Photoluminescence in glasses and glass ceramics. *IOP Conference Series: Materials Science and Engineering*, 2(1), 012001.

Eschenfelder, A. H. (1958). Ionic Valences in Manganese - Iron Spinels. *Journal of Applied Physics*, 29(3), 378–380.

Essene, E. J. & Peacor, D. R. (1983). Crystal chemistry and petrology of coexisting galaxite and jacobsite and other spinel solutions and solvi. *American Mineralogist*, 68(3-4), 449–455.

Eugster, H. P. (1957). Heterogeneous Reactions Involving Oxidation and Reduction at High Pressures and Temperatures. *The Journal of Chemical Physics*, 26(6), 1760–1761.

Eugster, H. P. & Wones, D. R. (1962). Stability Relations of the Ferruginous Biotite, Annite. *Journal of Petrology*, 3(1), 82–125.

Evans, K., Elburg, M., & Kamenetsky, V. (2012). Oxidation state of subarc mantle. *Geology*, 40(9), 783.

Ewa, S., Monika, K.-M., Hans-Jürgen, F., Richard, W., Dieter, R., Anja, S., & Ulrich, S. (2016). Determination of volatile concentrations in fluorapatite of Martian shergottite NWA 2975 by combining synchrotron FTIR, Raman spectroscopy, EMPA, and TEM, and inferences on the volatile budget of the apatite host-magma. *Meteoritics & Planetary Science*, 51(2), 390–406.

Farges, F. (2005). Ab initio and experimental pre-edge investigations of the Mn K -edge XANES in oxide-type materials. *Pysical Review B*, 71(15), 155109.

Fegley Jr, B. (2012). *Practical chemical thermodynamics for geoscientists*. Academic Press.

Fiege, A., Ruprecht, P., Simon, A. C., Bell, A. S., Göttlicher, J., Newville, M., Lanzirotti, T., & Moore, G. (2017). Calibration of Fe XANES for high-precision determination of Fe oxidation state in glasses: Comparison of new and existing results obtained at different synchrotron radiation sources. *American Mineralogist*, 102(2), 369–380.

Fitzgerald, P. G., Sorkhabi, R. B., Redfield, T. F., & Stump, E. (1995). Uplift and denudation of the central Alaska Range: A case study in the use of apatite fission track thermochronology to determine absolute uplift parameters. *Journal of Geophysical Research: Solid Earth*, 100(B10), 20175–20191.

Fleet, M. E. (1981). The structure of magnetite. *Acta Crystallographica Section B*, 37(4), 917–920.

Fleet, M. E., Stone, W. E., & Crocket, J. H. (1991). Partitioning of palladium, iridium, and platinum between sulfide liquid and basalt melt: Effects of melt composition, concentration, and oxygen fugacity. *Geochimica et Cosmochimica Acta*, 55(9), 2545–2554.

France, L., Ildefonse, B., Koepke, J., & Bech, F. (2010). A new method to estimate the oxidation state of basaltic series from microprobe analyses. *Journal of Volcanology and Geothermal Research*, 189(3–4), 340–346.

Frost, B. R. (1991). Introduction to oxygen fugacity and its petrologic importance. *Reviews in Mineralogy and Geochemistry*, 25(1), 1–9.

Frost, D. J. & McCammon, C. A. (2008). The Redox State of Earth's Mantle. *Annual Review of Earth and Planetary Sciences*, 36(1), 389–420.

Fudali, R. F. (1965). Oxygen fugacities of basaltic and andesitic magmas. *Geochimica et Cosmochimica Acta*, 29(9), 1063–1075.

Gaillard, F., Scaillet, B., & Arndt, N. T. (2011). Atmospheric oxygenation caused by a change in volcanic degassing pressure. *Nature*, 478(7368), 229–232.

Gaillard, F., Scaillet, B., Pichavant, M., & Bény, J.-M. (2001). The effect of water and f_{O_2} on the ferric–ferrous ratio of silicic melts. *Chemical Geology*, 174(1–3), 255–273.

Gaillard, F., Schmidt, B., Mackwell, S., & McCammon, C. (2003). Rate of hydrogen–iron redox exchange in silicate melts and glasses. *Geochimica et Cosmochimica Acta*, 67(13), 2427–2441.

García-Gutiérrez, M. C. & Rueda, D. R. (2009). Bases of synchrotron radiation, light sources, and features of x-ray scattering beamlines. In *Applications of synchrotron light to scattering and diffraction in materials and life sciences* (pp. 1–22). Springer.

Gerlach, T. M. (1993). Oxygen buffering of Kilauea volcanic gases and the oxygen fugacity of Kilauea basalt. *Geochimica et Cosmochimica Acta*, 57(4), 795–814.

Gerlach, T. M. & Nordlie, B. E. (1975). The C-O-H-S gaseous system; Part III, Magmatic gases compatible with oxides and sulfides in basaltic magmas. *American Journal of Science*, 275(4), 395–410.

Ghiorso, M. S. (1997). Thermodynamic Models of Igneous Processes. *Annual Review of Earth and Planetary Sciences*, 25(1), 221–241.

Ghiorso, M. S. & Sack, O. (1991). Fe-Ti oxide geothermometry: thermodynamic formulation and the estimation of intensive variables in silicic magmas. *Contributions to Mineralogy and Petrology*, 108(4), 485–510.

Giuli, G., Paris, E., Pratesi, G., Koeberl, C., & Cipriani, C. (2003). Iron oxidation state in the Fe-rich layer and silica matrix of Libyan Desert Glass: A high-resolution XANES study. *Meteoritics & Planetary Science*, 38(8), 1181–1186.

Griffin, B. J. & Michael, J. R. (2006). Where is SEM Resolution Reality in 2006: How do we Measure it and What are the Limits? *Microscopy and Microanalysis*, 12(S02), 1452–1453.

Gross, J., Filiberto, J., & Bell, A. S. (2013). Water in the martian interior: Evidence for terrestrial MORB mantle-like volatile contents from hydroxyl-rich apatite in olivine–phyric shergottite NWA 6234. *Earth and Planetary Science Letters*, 369-370, 120–128.

Grossman, L., Fedkin, A. V., & Simon, S. B. (2012). Formation of the first oxidized iron in the solar system. *Meteoritics & Planetary Science*, 47(12), 2160–2169.

Groves, A. W. & Mourant, A. E. (1929). Inclusions in the apatites of some igneous rocks. *Mineralogical Magazine*, 22(125), 92–9.

Hagen, A. & Öestby, J. (2006). Oxidation States of Mn, Cr, and Co in Mixed Spinels Studied by XANES. In *7th European Solid Oxide Fuel Cell Forum, 2006*: Lucerne Fuel Cell Forum 2006, Lucerne (Switzerland), 3 Jul 2006 - 7 Jul 2006 Proceedings (cd-rom), 2006.

Haggerty, S. E. (1979). The aeromagnetic mineralogy of igneous rocks. *Canadian Journal of Earth Sciences*, 16(6), 1281–1293.

Haggerty, S. E. (1990). Redox State of the Continental Lithosphere. In M. Menzies (Ed.), *Continental Mantle* (pp. 87–105). Oxford: Claredon Press.

Haggerty, S. E. (2016). Spinel in planetary systems. *American Mineralogist*, 101(1), 5–6.

Hålenius, U., Bosi, F., & Skogby, H. (2007). Galaxite, $MnAl_2O_4$, a spectroscopic standard for tetrahedrally coordinated Mn^{2+} in oxygen-based mineral structures. *American Mineralogist*, 92(7), 1225–1231.

Hålenius, U., Bosi, F., & Skogby, H. (2011). A first record of strong structural relaxation of TO_4 tetrahedra in a spinel solid solution. *American Mineralogist*, 96(4), 617–622.

Hanson, G. N. (1980). Rare Earth Elements in Petrogenetic Studies of Igneous Systems. *Annual Review of Earth and Planetary Sciences*, 8, 371–406.

Haskel, D. (1999). FLUO: Correcting XANES for self-absorption in fluorescence measurements.

Heier, K. & Buddington, A. F. (1956). Thermometric and petrogenetic significance of titaniferous magnetite; discussion and reply. *American Journal of Science*, 254(8), 506–515.

Henderson, C. M. B., Pearce, C. I., Charnock, J. M., Harrison, R. J., & Rosso, K. M. (2016). An X-ray magnetic circular dichroism (XMCD) study of Fe ordering in a synthetic $MgAl_2O_4$-Fe_3O_4 (spinel-magnetite) solid-solution series: Implications for magnetic properties and cation site ordering. *American Mineralogist*, 101(6), 1373–1388.

Henderson, G. S., de Groot, F. M. F., & Moulton, B. J. A. (2014). X-ray Absorption Near-Edge Structure (XANES) Spectroscopy. *Reviews in Mineralogy and Geochemistry*, 78(1), 75–138.

Hensen, B. J. (1986). Theoretical phase relations involving cordierite and garnet revisited: the influence of oxygen fugacity on the stability of sapphirine and spinel in the system Mg-Fe-Al-Si-O. *Contributions to Mineralogy and Petrology*, 92(3), 362–367.

Herd, C. D. K. (2008). Basalts as Probes of Planetary Interior Redox State. *Reviews in Mineralogy and Geochemistry*, 68(1), 527–553.

Herranz, T., Rojas, S., Ojeda, M., Pérez-Alonso, F. J., Terreros, P., Pirota, K., & Fierro, J. L. G. (2006). Synthesis, Structural Features, and Reactivity of Fe-Mn Mixed Oxides Prepared by Microemulsion. *Chemistry of Materials*, 18(9), 2364–2375.

Hicks, L. J. (2015). *X-ray spectroscopy and electron microscopy of planetary materials*. PhD thesis, University of Leicester.

Hiscock, M. (2013). *The Importance of Grain Boundary Diffusion: An Experimental Study*. Thesis for the degree of doctor of philosophy, The University of Edinburgh.

Holland, H. D. (2002). Volcanic gases, black smokers, and the great oxidation event. *Geochimica et Cosmochimica Acta*, 66(21), 3811–3826.

Holland, T. & Powell, R. (2003). Activity–composition relations for phases in petrological calculations: an asymmetric multicomponent formulation. *Contributions to Mineralogy and Petrology*, 145(4), 492–501.

Holtz, F., Behrens, H., Dingwell, D. B., & Taylor, R. P. (1992). Water solubility in aluminosilicate melts of haplogranite composition at 2 kbar. *Chemical Geology*, 96(3), 289–302.

Hu, S., Lin, Y., Zhang, J., Hao, J., Feng, L., Xu, L., Yang, W., & Yang, J. (2014). NanoSIMS analyses of apatite and melt inclusions in the GRV 020090 Martian meteorite: Hydrogen isotope evidence for recent past underground hydrothermal activity on Mars. *Geochimica et Cosmochimica Acta*, 140, 321–333.

Huebner, J. S. & Sato, M. (1970). The Oxygen Fugacity - Temperature Relationships of Manganese Oxide and Nickel Oxide Buffers. *American Mineralogist*, 55, 934–952.

Hughes, J. M. (2015). The many facets of apatite. *American Mineralogist*, 100(5-6), 1033–1039.

Hughes, J. M., Cameron, M., & Crowley, K. D. (1989). Structural variations in natural F, OH, and Cl apatites. *American Mineralogist*, 74(7-8), 870–876.

Hughes, J. M., Ertl, A., Bernhardt, H.-J., Rossman, G. R., & Rakovan, J. (2004). Mn-rich fluorapatite from Austria: Crystal structure, chemical analysis, and spectroscopic investigations. *American Mineralogist*, 89(4), 629–632.

Hughes, J. M. & Rakovan, J. F. (2015). Structurally Robust, Chemically Diverse: Apatite and Apatite Supergroup Minerals. *Elements*, 11(3), 165–170.

Ihinger, P. D. & Stolper, E. (1986). The color of meteoritic hibonite: an indicator of oxygen fugacity. *Earth and Planetary Science Letters*, 78(1), 67–79.

Jackson, W. E., Farges, F., Yeager, M., Mabrouk, P. A., Rossano, S., Waychunas, G. A., Solomon, E. I., & Brown, G. E. (2005). Multi-spectroscopic study of Fe(II) in silicate glasses: Implications for the coordination environment of Fe(II) in silicate melts. *Geochimica et Cosmochimica Acta*, 69(17), 4315 – 4332.

Jakobsson, S. (2012). Oxygen fugacity control in piston-cylinder experiments. *Contributions to Mineralogy and Petrology*, 164(3), 397–406.

Jakobsson, S., Blundy, J., & Moore, G. (2014). Oxygen fugacity control in piston-cylinder experiments: a re-evaluation. *Contributions to Mineralogy and Petrology*, 167(6), 1007.

Jones, J. H. (2004). Redox Conditions Among the Terrestrial Planets. In S. Mackwell & E. Stansbery (Eds.), *Lunar and Planetary Science Conference*, volume 35 of *Lunar and Planetary Science Conference*.

Jones, J. H. (2016). Section 2. trace element partitoning in the 1970's. *Geochemical Perspectives*, 5(2), 153.

Kajinami, A., Kotake, T., Deki, S., & Kohara, S. (2003). The structural analysis of manganese borate glass by high-energy X-ray diffraction measurement. *Nuclear Instruments and Methods in Physics Research Section B: Beam Interactions with Materials and Atoms*, 199, 34–37.

Kennedy, G. C. (1948). Equilibrium between volatiles and iron oxides in igneous rocks. *American Journal of Science*, 246(9), 529–548.

Ketcham, R. A. (2015). Technical Note: Calculation of stoichiometry from EMP data for apatite and other phases with mixing on monovalent anion sites. *American Mineralogist*, 100(7), 1620–1623.

Kim, D.-H., Zeng, H., Ng, T. C., & Brazel, C. S. (2009). T_1 and T_2 relaxivities of succimer-coated $MFe_2^{3+}O_4$ (M=Mn^{2+}, Fe^{2+} and Co^{2+}) inverse spinel ferrites for potential use as phase-contrast agents in medical MRI. *Journal of Magnetism and Magnetic Materials*, 321(23), 3899–3904.

Kodre, A., Arčon, I., Padežnik Gomilšek, J., & Makovec, D. (2008). An Expanded EXAFS Model of Man, Zn, and Fe Spinel Nanoparticles. *Acta Chimica Slovenica*, 55(1), 125–131.

Kohn, S. C., Charnock, J. M., Henderson, C. M. B., & Greaves, G. N. (1990). The structural environments of trace elements in dry and hydrous silicate glasses; a manganese and strontium K-edge X-ray absorption spectroscopic study. *Contributions to Mineralogy and Petrology*, 105(3), 359–368.

Kohn, S. C. & Schofield, P. F. (1994). The importance of melt composition in controlling trace-element behaviour: an experimental study of Mn and Zn partitioning between forsterite and silicate melts. *Chemical Geology*, 117(1), 73–87.

Konecke, B. A., Fiege, A., Simon, A. C., Parat, F., & Stechern, A. (2017). Co-variability of S^{6+}, S^{4+}, and S^{2-} in apatite as a function of oxidation state : Implications for a new oxybarometer. *American Mineralogist*, 102(3), 548–557.

Kraft, S., Stümpel, J., Becker, P., & Kuetgens, U. (1996). High resolution x-ray absorption spectroscopy with absolute energy calibration for the determination of absorption edge energies. *Review of Scientific Instruments*, 67(3), 681–687.

Krause, M. O. & Oliver, J. H. (1979). Natural Widths of Atomic K and L Levels, Kα X-Ray Lines and Several KLL Auger Lines. *Journal of Chemical and Physical Reference Data*, 8(2), 329–337.

Kress, V. C. & Carmichael, I. S. E. (1991). The compressibility of silicate liquids containing Fe_2O_3 and the effect of composition, temperature, oxygen fugacity and pressure on their redox states. *Contributions to Mineralogy and Petrology*, 108(1), 82–92.

la Tourrette, T. & Wasserburg, G. J. (1997). Self diffusion of europium, neodymium, thorium, and uranium in haplobasaltic melt: The effect of oxygen fugacity and the relationship to melt structure. *Geochimica et Cosmochimica Acta*, 61(4), 755–764.

Larson, A. C. (1967). Inclusion of secondary extinction in least-squares calculations. *Acta Crystallographica*, 23(4), 664–665.

Lavina, B., Salviulo, G., & Giusta, A. D. (2002). Cation distribution and structure modelling of spinel solid solutions. *Physics and Chemistry of Minerals*, 29(1), 10–18.

Lee, C.-T. A., Luffi, P., Le Roux, V., Dasgupta, R., Albaréde, F., & Leeman, W. P. (2010). The redox state of arc mantle using Zn/Fe systematics. *Nature*, 468(7324), 681–685.

Lenaz, D. & Skogby, H. (2013). Structural changes in the $FeAl_2O_4$-$FeCr_2O_4$ solid solution series and their consequences on natural Cr-bearing spinels. *Physics and Chemistry of Minerals*, 40(7), 587–595.

Li, J. & Agee, C. B. (2001). The effect of pressure, temperature, oxygen fugacity and composition on partitioning of nickel and cobalt between liquid Fe-Ni-S alloy and liquid silicate: Implications for the Earth's core formation. *Geochimica et Cosmochimica Acta*, 65(11), 1821–1832.

Lindsley, D. H. (1976). The crystal chemistry and structure of oxide minerals as exemplified by the Fe-Ti oxides. *Reviews in Mineralogy*, 3, L1–L60.

Linwood, S. H. & Weyl, W. A. (1942). The Fluorescence of Manganese in Glasses and Crystals. *Journal of the Optical Society of America*, 32(8), 443–453.

Lu, J., Ma, S., Sun, J., Xia, C., Liu, C., Wang, Z., Zhao, X., Gao, F., Gong, Q., Song, B., Shuai, X., Ai, H., & Gu, Z. (2009). Manganese ferrite nanoparticle micellar nanocomposites as MRI contrast agent for liver imaging. *Biomaterials*, 30(15), 2919–2928.

Lucchesi, S., Russo, U., & Della Giusta, A. (1997). Crystal chemistry and cation distribution in some Mn-rich natural and synthetic spinels. *European Journal of Mineralogy*, 9(1), 31–42.

Mahood, G. A. & Stimac, J. A. (1990). Trace-element partitioning in pantellerites and trachytes. *Geochimica et Cosmochimica Acta*, 54(8), 2257–2276.

Manceau, A., Marcus, M. A., & Grangeon, S. (2012). Determination of Mn valence states in mixed-valent manganates by XANES spectroscopy. *American Mineralogist*, 97(5-6), 816–827.

Mao, M., Rukhlov, A. S., Rowins, S. M., Spence, J., & Coogan, L. A. (2016). Apatite Trace Element Compositions: A Robust New Tool for Mineral Exploration*. *Economic Geology*, 111(5), 1187–1222.

Marks, M. A. W., Scharrer, M., Ladenburger, S., & Markl, G. (2016). Comment on "Apatite: A new redox proxy for silicic magmas?" [Geochimica et Cosmochimica Acta 132 (2014) 101–119]. *Geochimica et Cosmochimica Acta*, 183, 267–270.

Mathez, E. A. & Webster, J. D. (2005). Partitioning behavior of chlorine and fluorine in the system apatite-silicate melt-fluid. *Geochimica et Cosmochimica Acta*, 69(5), 1275–1286.

Matjuschkin, V., Brooker, R. A., Tattitch, B., Blundy, J. D., & Stamper, C. C. (2015). Control and monitoring of oxygen fugacity in piston cylinder experiments. *Contributions to Mineralogy and Petrology*, 169(1), 9.

Mattioli, G. S., Baker, M. B., Rutter, M. J., & Stolper, E. M. (1989). Upper Mantle Oxygen Fugacity and Its Relationship to Metasomatism. *The Journal of Geology*, 97(5), 521–536.

McCanta, M. (2005). Potential Effects of Melt Composition on Redox Ratio: Implications for Oxygen Fugacity Measurements. In S. Mackwell & E. Stansbery (Eds.), *36th Annual Lunar and Planetary Science Conference*, volume 36 of *Lunar and Planetary Inst.˜Technical Report*.

McCubbin, F. M., Boyce, J. W., Srinivasan, P., Santos, A. R., Elardo, S. M., Filiberto, J., Steele, A., & Shearer, C. K. (2016). Heterogeneous distribution of H_2O in the Martian interior: Implications for the abundance of H_2O in depleted and enriched mantle sources. *Meteoritics and Planetary Science*, 51(11), 2036–2060.

McCubbin, F. M., Jolliff, B. L., Nekvasil, H., Carpenter, P. K., Zeigler, R. A., Steele, A., Elardo, S. M., & Lindsley, D. H. (2011). Fluorine and chlorine abundances in lunar apatite: Implications for heterogeneous distributions of magmatic volatiles in the lunar interior. *Geochimica et Cosmochimica Acta*, 75(17), 5073–5093.

McCubbin, F. M., Steele, A., Hauri, E. H., Nekvasil, H., Yamashita, S., & Hemley, R. J. (2010). Nominally hydrous magmatism on the Moon. *Proceedings of the National Academy of Sciences*, 107(25), 11223 LP – 11228.

McCubbin, F. M., Vander Kaaden, K. E., Tartèse, R., Boyce, J. W., Mikhail, S., Whitson, E. S., Bell, A. S., Anand, M., Franchi, I. A., Wang, J., & Hauri, E. H. (2015). Experimental investigation of F, Cl, and OH partitioning between apatite and Fe-rich basaltic melt at 1.0-1.2 GPa and 950-1000 ℃. *American Mineralogist*, 100(8-9), 1790–1802.

McKay, G., Le, L., Wagstaff, J., & Crozaz, G. (1994). Experimental partitioning of rare earth elements and strontium: Constraints on petrogenesis and redox conditions during crystallization of antarctic angrite lewis cliff 86010. *Geochimica et Cosmochimica Acta*, 58(13), 2911 – 2919.

Médard, E., McCammon, C. A., Barr, J. A., & Grove, T. L. (2008). Oxygen fugacity, temperature reproducibility, and H_2O contents of nominally anhydrous piston-cylinder experiments using graphite capsules. *American Mineralogist*, 93(11-12), 1838–1844.

Miles, A., Graham, C., Hawkesworth, C., Gillespie, M., Dhuime, B., & Hinton, R. (2013a). Using Zircon Isotope Compositions to Constrain Crustal Structure and Pluton Evolution: the Iapetus Suture Zone Granites in Northern Britain. *Journal of Petrology*, 55(1), 181.

Miles, A. J., Graham, C. M., Hawkesworth, C. J., Gillespie, M. R., & Hinton, R. W. (2013b). Evidence for distinct stages of magma history recorded by the compositions of accessory apatite and zircon. *Contributions to Mineralogy and Petrology*, 166(1), 1–19.

Miles, A. J., Graham, C. M., Hawkesworth, C. J., Gillespie, M. R., Hinton, R. W., & Bromiley, G. D. (2014). Apatite: A new redox proxy for silicic magmas? *Geochimica et Cosmochimica Acta*, 132, 101–119.

Morton, A. & Yaxley, G. (2007). Detrital apatite geochemistry and its application in provenance studies. In J. Arribas, M. J. Johnsson, & S. Critelli (Eds.), *Sedimentary Provenance and Petrogenesis: Perspectives from Petrography and Geochemistry*. Geological Society of America.

Moussallam, Y., Edmonds, M., Scaillet, B., Peters, N., Gennaro, E., Sides, I., & Oppenheimer, C. (2016). The impact of degassing on the oxidation state of basaltic magmas: A case study of Kīlauea volcano. *Earth and Planetary Science Letters*, 450, 317–325.

Mysen, B. & Richet, P. (2005). Chapter 17 - natural melts. In B. Mysen & P. Richet (Eds.), *Silicate Glasses and Melts*, volume 10 of *Developments in Geochemistry* (pp. 503 – 524). Elsevier.

Mysen, B. O. (1983). The structure of silicate melts. *Annual Review of Earth and Planetary Sciences*, 11(1), 75–97.

Mysen, B. O. (2006). The structural behavior of ferric and ferrous iron in aluminosilicate glass near meta-aluminosilicate joins. *Geochimica et Cosmochimica Acta*, 70(9), 2337 – 2353.

Mysen, B. O. & Virgo, D. (1980). Trace element partitioning and melt structure: An experimental study at 1 atm pressure. *Geochimica et Cosmochimica Acta*, 44(12), 1917 – 1930.

Mysen, B. O., Virgo, D., Harrison, W. J., & Scarfe, C. M. (1980). Solubility mechanisms of H_2O in silicate melts at high pressures and temperatures; a Raman spectroscopic study. *American Mineralogist*, 65(9-10), 900–914.

Mysen, B. O., Virgo, D., & Seifert, F. A. (1985). Relationships between properties and structure of aluminosilicate melts. *American Mineralogist*, 70, 88–105.

Nagasawa, H. (1970). Rare earth concentrations in zircons and apatites and their host dacites and granites. *Earth and Planetary Science Letters*, 9(4), 359–364.

Nitsan, U. (1974). Stability field of olivine with respect to oxidation and reduction. *Journal of Geophysical Research*, 79(5), 706–711.

O'Neill, H. & Wall, V. J. (1987). The Olivine—Orthopyroxene—Spinel Oxygen Geobarometer, the Nickel Precipitation Curve, and the Oxygen Fugacity of the Earth's Upper Mantle. *Journal of Petrology*, 28(6), 1169.

Outka, D. A. & Stöhr, J. (1988). Curve fitting analysis of near-edge core excitation spectra of free, adsorbed, and polymeric molecules. *The Journal of Chemical Physics*, 88(6), 3539–3554.

Oxford Instruments Analytical (2002). *Wavelength Dispersive X-ray Microanalysis Explained*. Technical report, Oxford Instruments Analytical and Oxford Instruments Analytical Limited.

Pan, Y. & Fleet, M. E. (2002). Compositions of the Apatite-Group Minerals: Substitution Mechanisms and Controlling Factors. *Reviews in Mineralogy and Geochemistry*, 48(1), 13–49.

Papike, J. J., Karner, J. M., & Shearer, C. K. (2005). Comparative planetary mineralogy: Valence state partitioning of Cr, Fe, Ti, and V among crystallographic sites in olivine, pyroxene, and spinel from planetary basalts. *American Mineralogist*, 90(2-3), 277–290.

Pasero, M., Kampf, A. R., Ferraris, C., Pekov, I. V., Rakovan, J., & White, T. J. (2010). Nomenclature of the apatite supergroup minerals. *European Journal of Mineralogy*, 22(2), 163–179.

Pasteris, J. D., Wopenka, B., & Valsami-Jones, E. (2008). Bone and Tooth Mineralization: Why Apatite? *Elements*, 4(2), 97–104.

Paul, A. & Lahiri, D. (1966). Manganous-manganic equilibrium in alkali borate glasses. *Journal of the American Ceramic Society*, 49(10), 565–568.

Pawley, A. R., Holloway, J. R., & McMillan, P. F. (1992). The effect of oxygen fugacity on the solubility of carbon-oxygen fluids in basaltic melt. *Earth and Planetary Science Letters*, 110(1), 213–225.

Peacock, S. A. (1990). Fluid Processes in Subduction Zones. *Science*, 248(4953), 329 LP – 337.

Pedersen, K. R. & Jørgensen, J.-E. (1996). XANES study of rare-earth valency and 4f hybridization in $Pb_2Sr_2Ln_{1-x}Ca_xCu_3O_8$ for Ln = Ce, Pr and Tb. *Physica C: Superconductivity*, 264(3), 185–190.

Penner-Hahn, J. (2003). 2.13 - x-ray absorption spectroscopy. In J. A. McCleverty & T. J. Meyer (Eds.), *Comprehensive Coordination Chemistry II* (pp. 159 – 186). Oxford: Pergamon.

Petry, C., Chakraborty, S., & Palme, H. (2004). Experimental determination of Ni diffusion coefficients in olivine and their dependence on temperature, composition, oxygen fugacity, and crystallographic orientation. *Geochimica et Cosmochimica Acta*, 68(20), 4179–4188.

Pinakidou, F., Katsikini, M., Paloura, E. C., Kavouras, P., Kalogirou, O., Komninou, P., Karakostas, T., & Erko, A. (2006). On the coordination environment of Fe- and Pb-rich solidified industrial waste: An X-ray absorption and Mössbauer study. *Journal of Non-Crystalline Solids*, 352(28–29), 2933–2942.

Pitzer, K. S. & Sterner, S. M. (1995). Equations of state valid continuously from zero to extreme pressures with h2o and co2 as examples. *International Journal of Thermophysics*, 16(2), 511–518.

Potts, N. J. (2016). *Using Lunar Apatite to Assess the Volatile Inventory of the Lunar Interior*. PhD thesis, The Open University.

Prowatke, S. & Klemme, S. (2005). Effect of melt composition on the partitioning of trace elements between titanite and silicate melt. *Geochimica et Cosmochimica Acta*, 69(3), 695–709.

Prowatke, S. & Klemme, S. (2006). Trace element partitioning between apatite and silicate melts. *Geochimica et Cosmochimica Acta*, 70(17), 4513–4527.

Puchelt, H. & Emmermann, R. (1976). Bearing of rare earth patterns of apatites from igneous and metamorphic rocks. *Earth and Planetary Science Letters*, 31(2), 279–286.

Rakovan, J., Newville, M., & Sutton, S. (2001). Evidence of heterovalent europium in zoned llallgua apatite using wavelength dispersive XANES. *American Mineralogist*, 86(5-6), 697–700.

Ravel, B. & Newville, M. (2005). ATHENA, ARTEMIS, HEPHAESTUS: data analysis for X-ray absorption spectroscopy using IFEFFIT. *Journal of Synchrotron Radiation*, 12(4), 537–541.

Redfern, S. A. T., Harrison, R. J., O'Neill, H. S. C., & Wood, D. R. R. (1999). Thermodynamics and kinetics of cation ordering in $MgAl_2O_4$ spinel up to 1600 ℃ from in situ neutron diffraction. *American Mineralogist*, 84(3), 299–310.

Reiche, I., Vignaud, C., Champagnon, B., Panczer, G., Brouder, C., Morin, G., Solé, V. A., Charlet, L., & Menu, M. (2001). From mastodon ivory to gemstone: The origin of turquoise color in odontolite. *American Mineralogist*, 86(11-12), 1519–1524.

Righter, K., Sutton, S. R., Danielson, L., Pando, K., & Newville, M. (2016). Redox variations in the inner solar system with new constraints from vanadium XANES in spinels. *American Mineralogist*, 101(9), 1928–1942.

Righter, K., Sutton, S. R., Newville, M., Le, L., Schwandt, C. S., Uchida, H., Lavina, B., & Downs, R. T. (2006). An experimental study of the oxidation state of vanadium in spinel and basaltic melt with implications for the origin of planetary basalt. *American Mineralogist*, 91(10), 1643–1656.

Riker, J., Humphreys, M. C. S., Brooker, R. A., & De Hoog, J. C. M. (2018). First measurements of OH-C exchange and temperature-dependent partitioning of OH and halogens in the system apatite–silicate melt. *American Mineralogist*, 103(2), 260–270.

Roeder, P. L. (1994). Chromite; from the fiery rain of chondrules to the Kilauea Iki lava lake. *The Canadian Mineralogist*, 32(4), 729–746.

Roeder, P. L. & Emslie, R. F. (1970). Olivine-liquid equilibrium. *Contributions to Mineralogy and Petrology*, 29(4), 275–289.

Röhler, J. (1985). L_{III}-absorption on valence fluctuating materials. *Journal of Magnetism and Magnetic Materials*, 47-48(C), 175–180.

Rubatto, D. & Hermann, J. (2007). Experimental zircon/melt and zircon/garnet trace element partitioning and implications for the geochronology of crustal rocks. *Chemical Geology*, 241(1), 38 – 61. Crustal Dynamics; links between geochronology and petrology.

Rubie, D. C., Frost, D. J., Mann, U., Asahara, Y., Nimmo, F., Tsuno, K., Kegler, P., Holzheid, A., & Palme, H. (2011). Heterogeneous accretion, composition and

core–mantle differentiation of the Earth. *Earth and Planetary Science Letters*, 301(1), 31–42.

Ryerson, F. J., Durham, W. B., Cherniak, D. J., & Lanford, W. A. (1989). Oxygen diffusion in olivine: Effect of oxygen fugacity and implications for creep. *Journal of Geophysical Research: Solid Earth*, 94(B4), 4105–4118.

Sato, M. (1978). Oxygen fugacity of basaltic magmas and the role of gas-forming elements. *Geophysical Research Letters*, 5(6), 447–449.

Scaillet, B. & Gaillard, F. (2011). Redox state of early magmas. *Nature*, 480(7375), 48–49.

Schmidt, M. W., Connolly, J. A. D., Günther, D., & Bogaerts, M. (2006). Element partitioning: The role of melt structure and composition. *Science*, 312(5780), 1646–1650.

Schreiber, H. D. (1977). Redox states of Ti, Zr, Hf, Cr, and Eu in basaltic magmas-an experimental study. In *Lunar and Planetary Science Conference Proceedings*, volume 8 (pp. 1785–1807).

Schreiber, H. D. (1987). An electrochemical series of redox couples in silicate melts: A review and applications to geochemistry. *Journal of Geophysical Research: Solid Earth*, 92(B9), 9225–9232.

Schreiber, H. D., Merkel, R. C., Schreiber, V. L., & Balazs, G. B. (1987). Mutual interactions of redox couples via electron exchange in silicate melts: Models for geochemical melt systems. *Journal of Geophysical Research: Solid Earth*, 92(B9), 9233–9245.

Schreyeck, L., Wlosik, A., & Fuzellier, H. (2001). Influence of the synthesis route on $MgAl_2O_4$ spinel properties. *J. Mater. Chem.*, 11(2), 483–486.

Scott, J. A. J., Humphreys, M. C. S., Mather, T. A., Pyle, D. M., & Stock, M. J. (2015). Insights into the behaviour of S, F, and Cl at Santiaguito Volcano, Guatemala, from apatite and glass. *Lithos*, 232, 375–394.

Seghedi, I., Ntaflos, T., & Pécskay, Z. (2008). The Gataia Pleistocene lamproite: a new occurrence at the southeastern edge of the Pannonian Basin, Romania. *Geological Society, London, Special Publications*, 293(1), 83–100.

Sha, L.-K. & Chappell, B. W. (1999). Apatite chemical composition, determined by electron microprobe and laser-ablation inductively coupled plasma mass spectrometry, as a probe into granite petrogenesis. *Geochimica et Cosmochimica Acta*, 63(22), 3861–3881.

Shannon, R. D. (1976). Revised effective ionic radii and systematic studies of interatomic distances in halides and chalcogenides. *Acta Crystallographica Section A*, 32(5), 751–767.

Sheldrick, G. (1997). Shelx-97-a program for crystal structure refinement.

Sickafus, K. E., Wills, J. M., & Grimes, N. W. (1999). Structure of Spinel. *Journal of the American Ceramic Society*, 82(12), 3279–3292.

Signorelli, S. & Carroll, M. R. (2002). Experimental study of Cl solubility in hydrous alkaline melts: Constraints on the theoretical maximum amount of Cl in trachytic and phonolitic melts. *Contributions to Mineralogy and Petrology*, 143(2), 209–218.

Smythe, D. J. & Brenan, J. M. (2015). Cerium oxidation state in silicate melts: Combined f_{O_2}, temperature and compositional effects. *Geochimica et Cosmochimica Acta*, 170, 173–187.

Soden, R. (2010). Inside the Large Hadron Collider at CERN.

Stephens, W. E. & Halliday, A. N. (1980). Discontinuities in the composition surface of a zoned pluton, Criffell, Scotland. *GSA Bulletin*, 91(3), 165–170.

Stormer, J. C. & Carmichael, I. S. E. (1971). Fluorine-hydroxyl exchange in apatite and biotite: A potential igneous geothermometer. *Contributions to Mineralogy and Petrology*, 31(2), 121–131.

Sutton, S. R., Karner, J., Papike, J., Delaney, J. S., Shearer, C., Newville, M., Eng, P., Rivers, M., & Dyar, M. D. (2005). Vanadium K edge XANES of synthetic and natural basaltic glasses and application to microscale oxygen barometry. *Geochimica et Cosmochimica Acta*, 69(9), 2333–2348.

Tait, K., Ball, N. A., & Hawthorne, F. C. (2015). Pieczkaite, ideally $Mn_5(PO_4)_3Cl$, a new apatite-supergroup mineral from Cross Lake, Manitoba, Canada: Description and crystal structure. *American Mineralogist*, 100(5-6), 1047–1052.

Takahashi, Y., Kolonin, G. R., Shironosova, G. P., Kupriyanova, I. I., Uruga, T., & Shimzu, H. (2005). Determination of the Eu(II)/Eu(III) ratios in minerals by X-ray absorption near-edge structure (XANES) and its application to hydrothermal deposits. *Mineralogical Magazine*, 69(2), 179–190.

Taura, H., Yurimoto, H., Kurita, K., & Sueno, S. (1998). Pressure dependence on partition coefficients for trace elements between olivine and the coexisting melts. *Physics and Chemistry of Minerals*, 25(7), 469–484.

Tepper, J. H. & Kuehner, S. M. (1999). Complex zoning in apatite from the Idaho Batholith; a record of magma mixing and intracrystalline trace element diffusion. *American Mineralogist*, 84(4), 581–595.

Terada, K. & Sano, Y. (2012). In-Situ U–Pb Dating of Apatite by Hiroshima-SHRIMP: Contributions to Earth and Planetary Science. *Mass Spectrometry*, 1(2), A0011.

Toplis, M. J. & Carroll, M. R. (1995). An Experimental Study of the Influence of Oxygen Fugacity on Fe-Ti Oxide Stability, Phase Relations, and Mineral—Melt Equilibria in Ferro-Basaltic Systems. *Journal of Petrology*, 36(5), 1137.

Trail, D., Watson, E. B., & Tailby, N. D. (2011). The oxidation state of Hadean magmas and implications for early Earth's atmosphere. *Nature*, 480(7375), 79–82.

Vaughn, J. S., Lindsley, D. H., Nekvasil, H., Hughes, J. M., & Phillips, B. L. (2018). Complex f,cl apatite solid solution investigated using multinuclear solid-state nmr methods. *The Journal of Physical Chemistry C*, 122(1), 530–539.

Venezky, D. Y. & Rutherford, M. J. (1999). Petrology and Fe–Ti oxide reequilibration of the 1991 Mount Unzen mixed magma. *Journal of Volcanology and Geothermal Research*, 89(1–4), 213–230.

Verhoogen, J. (1962). Oxidation of Iron-Titanium Oxides in Igneous Rocks. *The Journal of Geology*, 70(2), 168–181.

W. Craig Carter research group - MIT (2009). X-ray Diffraction.

Wadhwa, M. (2008). Redox Conditions on Small Bodies, the Moon and Mars. *Reviews in Mineralogy and Geochemistry*, 68(1), 493–510.

Wallace, P. & Carmichael, I. S. E. (1992). Sulfur in basaltic magmas. *Geochimica et Cosmochimica Acta*, 56(5), 1863–1874.

Warner, S., Martin, R. F., Abdel-Rahman, A.-F. M., & Doig, R. (1998). Apatite as a monitor of fractionation, degassing, and metamorphism in the Sudbury igneous complex, Ontario. *The Canadian Mineralogist*, 36, 981–999.

Watson, E. B. (1977). Partitioning of manganese between forsterite and silicate liquid. *Geochimica et Cosmochimica Acta*, 41(9), 1363–1374.

Watson, E. B. & Green, T. H. (1981). Apatite/liquid partition coefficients for the rare earth elements and strontium. *Earth and Planetary Science Letters*, 56, 405–421.

Waychunas, G. A., Apted, M. J., & Brown, G. E. (1983). X-ray K-edge absorption spectra of Fe minerals and model compounds: Near-edge structure. *Physics and Chemistry of Minerals*, 10(1), 1–9.

Webster, J. D., Tappen, C. M., & Mandeville, C. W. (2009). Partitioning behavior of chlorine and fluorine in the system apatite–melt–fluid. II: Felsic silicate systems at 200 MPa. *Geochimica et Cosmochimica Acta*, 73(3), 559–581.

Westre, T. E., Kennepohl, P., DeWitt, J. G., Hedman, B., Hodgson, K. O., & Solomon, E. I. (1997). A Multiplet Analysis of Fe K-Edge 1s $\rightarrow$ 3d Pre-Edge Features of Iron Complexes. *Journal of the American Chemical Society*, 119(27), 6297–6314.

White, T., Ferraris, C., Kim, J., & Madhavi, S. (2005). Apatite - An Adaptive Framework Structure. *Reviews in Mineralogy and Geochemistry*, 57(1), 307–401.

Wijbrans, C. H., Klemme, S., Berndt, J., & Vollmer, C. (2015). Experimental determination of trace element partition coefficients between spinel and silicate melt: the influence of chemical composition and oxygen fugacity. *Contributions to Mineralogy and Petrology*, 169(4), 45.

Wilde, S., Valley, J., Peck, W., & Graham, C. (2001). Evidence from detrital zircons for the existence of continental crust and oceans on the Earth 4.4Gyr ago. *Nature*, 409, 175–178.

Wilke, M., Farges, F., Petit, P.-E., Brown, G. E., & Martin, F. (2001). Oxidation state and coordination of Fe in minerals: An Fe K-XANES spectroscopic study. *American Mineralogist*, 86(5-6), 714–730.

Willmott, P. (2011). *An introduction to synchrotron radiation: Techniques and applications*. Wiley Blackwell.

Wilson, A. J. C. & Prince, E. (1999). International Tables for Crystallography Vol. C, Mathematical, Physical and Chemical Tables. *Dordrecht, Holland*, 1.

Wojdyr, M. (2010). Fityk: a general-purpose peak fitting program. *Journal of Applied Crystallography*, 43(5 Part 1), 1126–1128.

Wolf, M. B. & London, D. (1994). Apatite dissolution into peraluminous haplogranitic melts: An experimental study of solubilities and mechanisms. *Geochimica et Cosmochimica Acta*, 58(19), 4127–4145.

Wood, B. J. (1991). Oxygen barometry of spinel peridotites. *Reviews in Mineralogy and Geochemistry*, 25(1), 417–432.

Wood, B. J. & Nell, J. (1991). High-temperature electrical conductivity of the lower-mantle phase (Mg, Fe)O. *Nature*, 351, 309.

Wood, B. J., Walter, M. J., & Wade, J. (2006). Accretion of the Earth and segregation of its core. *Nature*, 441(7095), 825–833.

Wyllie, P. J., Cox, K. G., & Biggar, G. M. (1962). The Habit of Apatite in Synthetic Systems and Igneous Rocks. *Journal of Petrology*, 3(2), 238.

Yamanaka, T. & Nakahira, M. (1973). Dependence of the cation distribution in Manganese ferrite, $MnFe_2O_4$, on temperature and oxidation. *Mineralogical Journal*, 7(2), 202–220.

Yang, A., Harris, V. G., Calvin, S., Zuo, X., & Vittoria, C. (2004). Extended X-ray absorption fine structure analysis of cation distribution in $MnFe_2O_4$ single crystal films and artificial ferrite structures. *IEEE Transactions on Magnetics*, 40(4), 2802–2804.

Yang, X., Gaillard, F., & Scaillet, B. (2014). A relatively reduced Hadean continental crust and implications for the early atmosphere and crustal rheology. *Earth and Planetary Science Letters*, 393, 210–219.

Zhang, Z. J., Wang, Z. L., Chakoumakos, B. C., & Yin, J. S. (1998). Temperature Dependence of Cation Distribution and Oxidation State in Magnetic Mn-Fe Ferrite Nanocrystals. *Journal of the American Chemical Society*, 120(8), 1800–1804.

Appendices

APPENDIX A

Single crystal Al-Mn-O and Fe-Mn-O spinel compositions

Edinburgh EPMA measurements (wt% element).

Analysis name	Al	Mn	Fe	O	Total
GaAC 1 / 1	15.01	52.62		32.62	100.25
GaAC 2 / 1	15.57	51.93	0.05	33.05	100.61
GaAC 3 / 1	14.68	53.32		32.68	100.70
GaAC 4 / 1	14.36	53.39		32.06	99.82
GaAC 5 / 1	15.79	51.49		32.61	99.93
GaAC 6 / 1	16.13	50.84		32.87	99.86
GaAC 7 / 1	15.08	52.34		32.72	100.16
GaAC 8 / 1	16.57	51.02		33.44	101.05
GaAC 9 / 1	16.31	50.61		33.38	100.33
GaAC 10 / 1	16.19	51.14		32.94	100.30
Ga93 1 / 1	17.74	48.31	0.09	35.01	101.14
Ga93 2 / 1	15.83	52.65		32.33	100.82
Ga93 3 / 1	15.74	52.11		32.88	100.77
Ga93 4 / 1	15.60	52.13		32.59	100.34
Ga93 5 / 1	11.44	57.35	0.06	31.63	100.47
Ga93 6 / 1	15.41	52.39		33.31	101.14
Ga93 7 / 1	16.06	51.84		33.54	101.46
Ga93 8 / 1	15.21	52.41		33.34	100.96
Ga93 9 / 1	13.43	55.04		32.40	100.90
Ga93 10 / 1	16.30	51.31		34.05	101.69
Ga90 1 / 1	12.45	56.14		31.88	100.51
Ga90 2 / 1	15.01	52.67		32.55	100.23
Ga90 3 / 1	12.83	55.71		31.50	100.05
Ga90 4 / 1	17.65	48.63		33.62	99.90
Ga90 5 / 1	12.53	56.23		31.76	100.51
Ga90 6 / 1	13.27	55.38		31.90	100.58
Ga90 7 / 1	14.10	54.08		32.27	100.47
Ga90 8 / 1	14.99	53.14		32.83	100.98
Ga90 9 / 1	13.74	54.81		31.37	99.92
Ga90 10 / 1	11.89	57.03		31.35	100.28

Edinburgh EPMA measurements (wt% element) **(continued)**

Analysis name	Al	Mn	Fe	O	Total
JcAC 1 / 1	0.05	4.51	65.58	29.34	99.48
JcAC 2 / 1	0.04	3.37	66.84	29.29	99.55
JcAC 3 / 1		3.12	66.93	29.39	99.45
JcAC 4 / 1		1.56	68.57	29.52	99.66
JcAC 5 / 1		1.96	67.89	29.61	99.46
JcAC 1 / 2		3.81	66.20	29.41	99.41
JcAC 2 / 2		4.00	66.06	29.66	99.74
JcAC 3 / 2		2.85	67.17	29.23	99.26
JcAC 4 / 2		3.44	66.58	29.44	99.47
JcAC 5 / 2		2.65	67.44	29.59	99.69
JcAC 6 / 2		2.12	67.79	29.30	99.22
JcAC 7 / 2		1.63	68.22	29.03	98.89
JcAC 8 / 2		3.44	66.20	29.01	98.66
JcAC 9 / 2		2.75	66.96	29.41	99.12
JcAC 10 / 2		3.05	66.85	29.16	99.06
JcAC 11 / 2		2.02	67.97	29.31	99.30
JcAC 12 / 2		1.55	68.38	29.36	99.28
JcAC 13 / 2		3.70	66.19	29.43	99.33
JcAC 14 / 2		3.86	66.21	29.23	99.29
JcAC 15 / 2		2.86	67.23	29.31	99.41
JcAC 16 / 2		2.55	67.40	28.96	98.92
Jc93 1 / 1	0.41	18.97	52.50	26.90	98.79
Jc93 2 / 1		10.85	61.27	26.96	99.09
Jc93 3 / 1	0.03	11.47	60.41	26.40	98.31
Jc93 4 / 1	0.63	18.28	52.88	27.04	98.83
Jc93 5 / 1	0.69	20.05	51.16	27.19	99.09
Jc93 6 / 1	1.07	20.55	49.95	27.09	98.66
Jc93 7 / 1	0.76	20.60	50.10	27.33	98.80
Jc93 8 / 1	1.67	20.26	49.81	27.04	98.77
Jc93 9 / 1	1.00	19.09	51.65	26.89	98.62
Jc93 10 / 1	0.93	20.28	50.78	27.07	99.06
Jc90 1 / 1	0.14	5.63	59.99	25.05	90.81
Jc90 2 / 1	0.18	32.70	38.89	27.59	99.36
Jc90 4 / 1	0.34	31.48	39.92	27.34	99.07
Jc90 5 / 1	0.20	32.73	37.67	26.26	96.86
Jc90 6 / 1	0.13	25.52	43.75	28.82	98.21
Jc90 8 / 1	0.17	31.66	40.11	27.81	99.75
Jc90 9 / 1	0.22	6.88	58.75	25.29	91.15
Jc90 1 / 2	0.70	29.12	37.44	22.82	90.08
Jc90 2 / 2	0.38	35.24	35.98	27.66	99.26
Jc90 3 / 2	0.10	32.48	39.15	27.49	99.21
Jc90 4 / 2	0.28	31.79	39.48	27.35	98.91

Bristol EPMA measurements (wt% element).

Analysis name	**Al**	**Mn**	**Fe**	**O**	**Total**
Ga60-1	31.31	31.35		36.96	99.60
Ga60-2	31.33	31.18		36.93	99.47
Ga60-3	28.97	33.10		35.44	97.60
Ga60-4	30.84	31.65		36.67	99.24
Ga60-5	30.90	31.44		36.67	99.11
Ga60-6	30.79	31.14		36.48	98.51
Ga60-7	30.40	31.48		36.28	98.31
Ga60-8	31.01	31.14		36.64	98.84
Ga60-9	31.18	30.86		36.74	98.92
Ga60-10	30.79	31.01		36.45	98.34

APPENDIX B

Manganese bearing apatite and melt compositions

B.1 Apatite EPMA measurements

Apatite EPMA measurements (wt% element

Analysis name	SiO_2	Al_2O_3	FeO	MgO	MnO	CaO	K_2O	Na_2O	P_2O_5	Cl	F	Total
PM1 Pt 1	0.31	0.03			4.89	48.47	0.10	0.56	40.11	6.34		100.82
PM1 Pt 2	0.36				4.77	48.46	0.11	0.54	39.94	6.11		100.32
PM1 Pt 4	0.38	0.04			5.13	48.09	0.14	0.63	39.72	6.54		100.68
PM1 Pt 5	0.39	0.06			5.05	48.30	0.15	0.61	39.76	5.98		100.31
PM1 Pt 6	0.29	0.05			4.94	48.31	0.12	0.50	39.89	5.84		99.94
PM1 Pt 7	0.36				5.10	47.93	0.15	0.54	40.18	6.35		100.63
PM1 Pt 9	0.53	0.04			5.13	48.22	0.22	0.56	40.18	5.85		100.73
PM1 Pt 11	0.41	0.03			5.07	48.13	0.15	0.58	39.33	6.20		99.91
PM1 Pt 13	0.33	0.03			5.01	48.17	0.14	0.59	40.12	6.31		100.71
PM1 Pt 14	0.35				4.93	48.14	0.14	0.65	40.13	6.12		100.49
PM1 Pt 15	0.32	0.04			4.68	47.79	0.13	0.56	38.82	6.79		99.13
PM1 Pt 17	0.48				4.80	48.45	0.22	0.65	39.82	5.89		100.34
PM1 Pt 18	0.36	0.04			5.06	48.31	0.13	0.63	39.54	5.59		99.66
PM1 Pt 19	0.40				4.89	48.23	0.10	0.60	40.49	5.87		100.61
PM1 Pt 20	0.32	0.04			4.83	48.36	0.14	0.54	40.21	5.46		99.92
PM1 Pt 21	0.30				4.69	48.53	0.11	0.62	39.31	5.36		98.93
PM1 Pt 25	0.34	0.03			5.01	48.80	0.14	0.62	40.66	5.89		101.49
PM1 H 1	0.37	0.04			6.53	46.93	0.16	0.59	40.09	4.93		99.64
PM1 H 3	0.34	0.04			6.72	46.81	0.12	0.54	39.87	6.02		100.46
PM1 H 4	0.58	0.08			7.25	46.17	0.24	0.55	39.73	5.40		99.99
PM1 H 8	0.37				6.44	47.01	0.14	0.63	39.85	5.89		100.36
PM1 H 10	0.39	0.05			6.54	47.37	0.12	0.55	39.72	5.89		100.62
PM1 H 11	0.51	0.07			6.61	46.91	0.19	0.59	39.96	4.28		99.11
PM1 H 12	0.48				6.23	47.33	0.19	0.58	40.36	4.38		99.58
PM1 H 13	0.52	0.08			6.31	47.26	0.22	0.61	40.00	4.22		99.22
PM1 H 14	0.44	0.04			6.67	47.25	0.16	0.64	39.58	5.72		100.50

Apatite EPMA measurements (wt% element) **(continued)**

Analysis name	**SiO_2**	**Al_2O_3**	**FeO**	**MgO**	**MnO**	**CaO**	**K_2O**	**Na_2O**	**P_2O_5**	**Cl**	**F**	**Total**
PM1 H 16	0.43				6.43	47.21	0.17	0.60	40.15	5.40		100.42
PM1 H 18	0.56	0.06			6.77	46.34	0.24	0.57	39.61	4.44		98.59
PM1 H 19	0.58	0.09			6.89	46.48	0.21	0.63	39.82	4.65		99.35
PM1 H 20	0.70	0.10			6.60	46.99	0.26	0.58	39.27	5.43		99.91
PM1 H 21	0.43	0.04			6.56	47.33	0.19	0.60	39.47	5.51		100.14
PM1 H 22	0.47	0.06			6.30	46.96	0.16	0.64	40.03	5.46		100.09
PM1 H 25	0.47	0.04			6.25	47.05	0.20	0.58	39.73	4.33		98.65
PM1 H 26	0.48	0.08			6.88	46.58	0.22	0.52	39.91	5.59		100.26
PM1 H 27	0.59	0.10			6.77	46.31	0.25	0.71	39.36	5.51		99.61
PM1 H 28	0.58	0.05			6.58	47.15	0.23	0.62	39.66	5.42		100.29
PM1 H 29	0.35	0.04			6.65	47.22	0.10	0.65	39.97	5.59		100.58
PM1 NNO 2	0.25				7.64	47.71	0.03	0.10	40.80	1.04		97.56
PM1 NNO 3	0.27	0.07			8.05	47.24	0.07	0.03	40.47	0.93		97.11
PM1 NNO 4	0.25	0.04			8.08	46.93	0.10	0.06	40.66	0.90		97.02
PM1 NNO 5	0.29	0.05			7.57	47.70	0.05	0.04	40.63	1.02		97.35
PM1 NNO 6	0.23	0.05			7.55	48.28	0.05	0.02	41.42	0.93		98.52
PM1 NNO 7	0.24				7.35	48.16	0.05	0.05	40.22	0.98		97.04
PM1 NNO 8	0.22				7.69	47.92	0.08	0.08	40.44	0.97		97.42
PM1 NNO 9	0.28	0.06			8.12	47.26	0.14	0.10	41.19	0.93		98.08
PM1 NNO 10	0.35	0.05			8.18	47.35	0.12	0.05	40.39	0.89		97.38
PM1 NNO 11	0.34	0.04			8.05	46.93	0.14	0.11	39.95	0.86		96.42
PM1 NNO 12	0.36	0.04			8.18	47.14	0.11	0.03	39.81	0.91		96.59
PM1 NNO 14	0.22				7.60	47.56	0.06	0.03	40.45	0.95		96.87
PM1 NNO 15	0.25				7.90	47.76	0.07	0.04	40.35	0.93		97.29
PM1 NNO 16	0.34	0.06			8.09	47.46	0.11	0.06	40.28	0.92		97.31
PM1 NNO 20	0.25	0.03			8.07	47.46	0.07	0.08	40.83	0.94		97.74

Apatite EPMA measurements (wt% element) **(continued)**

Analysis name	**SiO_2**	**Al_2O_3**	**FeO**	**MgO**	**MnO**	**CaO**	**K_2O**	**Na_2O**	**P_2O_5**	**Cl**	**F**	**Total**
PM1 NNO 21	0.36	0.04			8.18	47.10	0.09	0.06	40.87	1.00		97.71
PM1 NNO 22	0.26				8.07	47.35	0.05	0.03	41.07	0.99		97.84
PM1 NNO 23	0.33				8.15	47.25	0.11	0.05	41.04	0.96		97.91
PM1 NNO 25	0.31				8.09	47.33	0.10	0.03	40.02	0.92		96.83
PM1 NNO 26	0.19				7.87	47.59	0.06	0.09	39.96	0.89		96.68
PM1 NNO 27	0.24				7.94	47.47	0.06	0.07	39.95	0.84		96.57
PM1 NNO 28	0.21				7.12	48.21	0.02	0.04	40.65	0.95		97.22
PM1 NNO 31	0.22				7.74	47.62	0.09	0.07	41.36	0.88		97.99
PM1 NNO 33	0.36				8.23	47.25	0.06	0.06	39.61	0.99		96.57
PM1 NNO 34	0.25				7.84	47.62	0.05	0.06	40.39	0.94		97.16
PM1 NNO 35	0.28				7.81	47.87	0.04	0.12	40.20	0.91		97.25
PM1 NNO 36	0.24				8.01	47.51	0.03	0.05	40.22	0.95		97.03
PM1 NNO 37	0.24				7.85	47.31	0.09	0.06	40.81	0.93		97.30
PM1 C 1	0.50	0.04			5.97	47.81	0.12	0.34	39.91	4.45		99.13
PM1 C 2	0.48	0.05			5.80	48.24	0.11	0.30	40.44	4.21		99.61
PM1 C 3	0.42	0.04			5.74	47.97	0.12	0.33	39.90	4.75		99.26
PM1 C 5	0.40				6.05	46.95	0.10	0.29	38.87	6.53		99.21
PM1 C 6	0.40	0.04			6.15	47.21	0.12	0.35	40.47	4.60		99.34
PM1 C 10	0.46	0.07			6.18	47.06	0.11	0.32	39.32	6.59		100.11
PM1 C 11	0.40	0.08			5.83	47.03	0.13	0.37	39.95	5.03		98.81
PM1 C 13	0.47	0.11			5.84	47.28	0.16	0.39	40.26	5.40		99.91
PM1 C 14	0.39	0.04			6.38	46.84	0.11	0.30	39.78	6.41		100.24
PM1 C 15	0.39				5.72	48.08	0.10	0.29	40.60	4.64		99.84
PM1 C 16	0.44				6.39	47.12	0.12	0.31	39.69	6.99		101.08
PM1 C 17	0.58	0.07			6.04	46.92	0.18	0.42	38.99	6.17		99.37
PM1 C 19	0.51	0.05			6.24	46.18	0.15	0.35	39.47	5.97		98.91

Apatite EPMA measurements (wt% element) **(continued)**

Analysis name	**SiO_2**	**Al_2O_3**	**FeO**	**MgO**	**MnO**	**CaO**	**K_2O**	**Na_2O**	**P_2O_5**	**Cl**	**F**	**Total**
PM1 C 24	0.44	0.07			5.72	47.42	0.12	0.35	39.50	6.48		100.10
PM1 C 26	0.46	0.04			5.88	47.20	0.15	0.31	38.49	6.49		99.02
PM1 C 27	0.47	0.06			5.80	47.33	0.14	0.32	38.62	6.93		99.68
PM1 C 28	0.47	0.04			5.74	47.61	0.13	0.36	40.55	6.05		100.95
PM1 C 29	0.42	0.08			5.76	47.61	0.14	0.32	39.59	6.57		100.49
PM1 C 30	0.47	0.12			5.53	47.51	0.14	0.33	39.83	5.67		99.60
MH 1200 Hap10 1	0.17		0.13		5.60	49.09	0.02	0.12	40.93	1.13		96.97
MH 1200 Hap10 3	0.19				5.12	49.58		0.10	40.95	1.13		96.85
MH 1200 Hap10 4	0.19		0.10		4.90	50.06		0.14	41.41	1.18		97.80
MH 1200 Hap10 5	0.18		0.13		5.67	49.08	0.03	0.10	41.31	1.14		97.41
MH 1200 Hap10 7	0.19		0.15		5.32	49.01	0.03	0.11	41.30	1.18		96.96
MH 1200 Hap10 9	0.18		0.18		6.11	49.13	0.02	0.12	40.79	1.14		97.56
MH 1200 Hap10 1b	0.19		0.09		5.69	49.51	0.02	0.16	40.08	1.16		96.72
MH 1200 Hap10 3b	0.17		0.13		6.21	49.23	0.02	0.16	40.14	1.18		97.00
MH 1200 Hap10 5b	0.16		0.20		6.38	48.40	0.02	0.18	40.53	1.13		96.71
MW 1200 Hap10 1	0.64		0.59	0.17	7.41	45.65	0.15	0.28	39.66	2.00	0.63	97.14
MW 1200 Hap10 4	0.84		0.70	0.13	7.61	46.55	0.14	0.32	39.84	1.89		98.18
MW 1200 Hap10 5	0.40		0.82	0.15	6.50	47.16	0.09	0.25	40.93	1.89	0.32	98.49
MW 1200 Hap10 7	0.34		0.58	0.15	7.05	46.92	0.07	0.29	40.54	1.76		97.62
Cr 1200 Hap10 1	0.25				6.28	48.59	0.04	0.08	41.03	0.58		96.68
Cr 1200 Hap10 3	0.23			0.03	7.48	47.53	0.06	0.07	41.73	0.62		97.47
Cr 1200 Hap10 4	0.22				7.01	47.81	0.06	0.07	40.18	0.62		95.79
Cr 1200 Hap10 5	0.20				7.01	48.24	0.06	0.06	41.12	0.64		97.12
Cr 1200 Hap10 6	0.23			0.04	7.78	47.41	0.06	0.05	41.37	0.69		97.40

Apatite EPMA measurements (wt% element) **(continued)**

Analysis name	**SiO_2**	**Al_2O_3**	**FeO**	**MgO**	**MnO**	**CaO**	**K_2O**	**Na_2O**	**P_2O_5**	**Cl**	**F**	**Total**
Cr 1200 Hap10 7	0.26			0.04	8.04	46.92	0.09	0.10	40.11	0.65		95.82
Cr 1200 Hap10 8	0.19			0.03	7.93	47.32	0.06	0.11	41.08	0.66		96.97
Cr 1200 Hap10 9	0.22				6.84	48.31	0.04		40.77	0.60		96.55
NNO 1200 Hap10 1	0.27				6.57	48.26	0.05	0.22	41.35	1.98		98.34
NNO 1200 Hap10 3	0.28				6.62	47.99	0.05	0.12	39.78	1.91		96.44
NNO 1200 Hap10 4	0.28				6.52	48.16	0.04	0.18	40.51	1.96		97.48
NNO 1200 Hap10 5	0.28				6.60	47.83	0.07	0.19	40.50	1.88		96.92
NNO 1200 Hap10 6	0.24				6.63	47.90	0.04	0.20	40.65	1.93		97.35
NNO 1200 Hap10 7	0.25				6.60	48.38	0.07	0.20	40.08	1.92		97.28
NNO 1200 Hap10 8	0.29				6.72	48.27	0.07	0.18	40.71	1.94		98.07
Cr 1200 Hap5 2	0.48			0.06	6.65	48.06	0.04	0.12	41.77	0.78		97.59
Cr 1200 Hap5 4	0.17			0.06	6.44	48.26	0.03	0.19	41.23	0.78		97.19
Cr 1200 Hap5 5	0.19			0.06	6.53	48.06	0.04	0.24	41.08	0.78		96.76
Cr 1200 Hap5 6	0.19			0.06	6.64	48.57	0.04	0.24	40.99	0.73		97.21
Cr 1200 Hap5 7	0.19			0.05	6.64	48.43	0.02	0.08	41.14	0.66		97.04
Cr 1200 Hap5 8	0.53			0.05	6.60	48.06	0.07	0.22	41.04	0.69		97.07
SH3 Cr 1	0.40			0.89	0.16	54.39			41.67	0.03	3.18	100.76
SH3 Cr 2	0.45			0.89	0.18	54.41			40.26	0.03	3.33	99.62
SH3 Cr 4	0.32			0.86	0.16	54.29			40.95		3.44	100.14
SH3 Cr 5	0.38			0.88	0.16	54.00			41.64	0.04	2.93	100.08
SH3 Cr 8	0.38			0.87	0.15	54.43			41.89		3.31	101.06
SH3 PtC 9	0.50			0.88	0.19	54.18	0.02		40.98	0.04	3.32	100.15
SH3 PtC 10	0.67			0.87	0.18	54.02	0.03		41.77	0.04	3.24	100.79

Apatite EPMA measurements (wt% element) **(continued)**

Analysis name	**SiO_2**	**Al_2O_3**	**FeO**	**MgO**	**MnO**	**CaO**	**K_2O**	**Na_2O**	**P_2O_5**	**Cl**	**F**	**Total**
SH3 PtC 11	0.54			0.84	0.19	53.59			42.34	0.03	3.18	100.78
SH3 PtC 12	0.48			0.85	0.20	53.75	0.03		41.90	0.04	3.42	100.64
SH3 PtC 13	0.45			0.85	0.19	54.09	0.02		41.58	0.05	3.50	100.78
SH3 PtC 14	0.38			0.84	0.17	54.10			42.14	0.02	3.40	101.10
SH3 Pt 3	0.42			0.91	0.19	54.53			41.22	0.04	3.81	101.14
SH3 Pt 4	0.36			0.89	0.18	54.43			41.63		3.29	100.78
SH3 Pt 6	0.50			0.90	0.17	54.45			41.17	0.03	3.93	101.18
SH3 Pt 7	0.40			0.89	0.19	54.65			41.52	0.03	3.41	101.15
SH3 MH 1	0.34		0.08	0.87	0.20	54.43	0.03		41.21	0.02	3.24	100.48
SH3 MH 2	0.28		0.09	0.89	0.17	54.57	0.02		42.01		3.17	101.27
SH3 MH 3	0.31		0.06	0.92	0.21	54.64	0.03		41.60	0.05	3.49	101.35
SH3 MH 5	0.49			0.88	0.19	54.20			41.73	0.04	2.98	100.58
SH3 MH 6	0.57		0.07	0.86	0.19	54.21			42.14		3.12	101.23
SH3 MH 7	0.33		0.06	0.89	0.21	54.00	0.02		42.11		3.41	101.06
SH3 MH 8	0.37		0.08	0.86	0.20	54.75	0.02		41.73		3.19	101.22
SH3 MH 9	0.42			0.84	0.17	54.11			41.12	0.03	3.43	100.20
BMT2 Cr 1	0.28			0.12	0.11	54.81	0.05	0.06	41.49		3.70	100.64
BMT2 Cr 4	0.40			0.12	0.13	54.36	0.13	0.13	41.95		3.61	100.89
BMT2 Cr 5	0.30			0.12	0.21	54.20	0.07	0.14	41.10		3.59	99.83
BMT2 Cr 9	0.31			0.13	0.15	55.18	0.12	0.11	41.33		3.23	100.65
BMT2 Pt 1	0.15		0.14	0.08	0.37	54.48	0.02	0.08	42.35		3.19	100.86
BMT2 Pt 2	0.16		0.14	0.09	0.47	54.16	0.05	0.06	41.35		3.45	99.95
BMT2 Pt 3	0.17		0.18	0.11	0.54	54.48	0.07	0.07	40.75		3.29	99.65

Apatite EPMA measurements (wt% element) **(continued)**

Analysis name	**SiO_2**	**Al_2O_3**	**FeO**	**MgO**	**MnO**	**CaO**	**K_2O**	**Na_2O**	**P_2O_5**	**Cl**	**F**	**Total**
BMT2 Pt 4	0.17		0.12	0.12	0.46	54.45	0.06	0.12	41.14		3.13	99.78
BMT2 Pt 6	0.18		0.15	0.11	0.53	54.46	0.09	0.08	41.57		3.14	100.33
BMT2 Pt 7	0.17		0.14	0.10	0.50	54.67	0.05	0.08	41.92		3.20	100.89
BMT2 Pt 8	0.16		0.14	0.11	0.53	54.42	0.06	0.10	41.58		3.39	100.52
BMT2 MH 1	0.15		0.60	0.07	0.27	54.23	0.04		41.90		3.41	100.77
BMT2 MH 2	0.20		0.66	0.08	0.28	54.16	0.05	0.09	41.59	0.02	3.30	100.49
BMT2 MH 4	0.15		0.60	0.07	0.27	54.43	0.05	0.13	41.81	0.03	3.49	101.06
BMT2 MH 6	0.18		0.60	0.07	0.27	54.76	0.05	0.13	41.33		3.55	100.98
BMT2 MH 7	0.15		0.60	0.07	0.26	54.40	0.04	0.08	42.45	0.02	3.26	101.41

B.2 Glass EPMA measurements

Glass EPMA measurements (wt% element, - below detection limit).

Analysis name	SiO_2	TiO_2	Al_2O_3	FeO	MgO	MnO	CaO	K_2O	Na_2O	P_2O_5	Cl	F	Total
PM1 Pt 1	54.06		14.21			9.58	6.05	5.21	5.10	2.95	2.27		99.43
PM1 Pt 2	53.85		14.59			8.79	5.91	5.13	5.30	3.43	2.35		99.35
PM1 Pt 3	53.43		14.40			9.10	6.16	5.42	5.41	3.45	2.44		99.81
PM1 Pt 4	53.25		14.30			9.17	6.21	5.18	5.12	3.46	2.59		99.27
PM1 Pt 5	53.18		14.15			9.79	6.28	5.09	5.21	3.37	2.59		99.66
PM1 Pt 6	53.18		14.40			9.74	6.24	5.03	5.12	3.37	2.56		99.63
PM1 Pt 7	53.28		14.22			9.45	6.18	5.08	5.54	3.33	2.34		99.42
PM1 Pt 8	53.09		14.35			9.54	6.35	5.06	5.10	3.46	2.53		99.48
PM1 Pt 9	52.73		14.14			9.89	6.28	4.96	5.43	3.34	2.61		99.39
PM1 Pt 10	53.29		14.15			9.64	6.11	5.08	5.16	3.39	2.50		99.32
PM1 Pt 11	54.58		14.54			8.55	5.68	5.39	5.19	3.11	2.38		99.41
PM1 Pt 12	54.35		14.66			8.33	5.62	5.19	5.21	3.33	2.23		98.94
PM1 Pt 13	54.34		14.54			8.32	5.52	5.27	5.07	3.72	2.25		99.03
PM1 Pt 14	53.69		14.42			8.91	5.95	5.14	5.04	3.67	2.48		99.30
PM1 Pt 15	52.94		14.66			8.53	6.08	5.13	5.26	3.88	2.44		98.92
PM1 Pt 16	52.42		14.53			9.55	6.33	5.13	5.28	3.60	2.52		99.36
PM1 Pt 17	52.39		14.49			9.30	6.30	5.01	5.12	3.55	2.59		98.75
PM1 Pt 18	52.89		14.53			9.67	6.47	4.94	5.11	3.84	2.36		99.81
PM1 H 1	61.65		17.95			4.09	1.65	6.82	5.53	0.89	0.44		99.03
PM1 H 2	61.70		17.94			3.78	1.61	6.69	5.41	0.68	0.48		98.28
PM1 H 3	61.32		17.90			4.11	1.73	6.79	5.47	0.79	0.45		98.58
PM1 H 4	61.99		17.79			4.04	1.67	6.70	5.51	0.76	0.43		98.89
PM1 H 5	61.43		17.57			4.34	1.83	6.72	5.39	0.85	0.43		98.57
PM1 H 9	60.24		17.18			4.84	1.88	6.55	5.49	0.94	0.49		97.62
PM1 H 10	61.69		17.84			4.23	1.67	6.78	5.38	0.84	0.51		98.94
PM1 H 11	61.46		17.41			4.37	1.62	6.66	5.41	0.80	0.47		98.20

Glass EPMA measurements (wt% element) **(continued)**

Analysis name	**SiO_2**	**TiO_2**	**Al_2O_3**	**FeO**	**MgO**	**MnO**	**CaO**	**K_2O**	**Na_2O**	**P_2O_5**	**Cl**	**F**	**Total**
PM1 H 12	62.56		17.82			4.32	1.63	6.72	5.49	0.79	0.54		99.88
PM1 H 13	62.65		18.16			4.57	1.68	6.47	5.47	0.80	0.50		100.28
PM1 H 14	62.80		18.14			4.77	1.79	6.57	5.53	0.76	0.46		100.83
PM1 H 15	63.13		17.94			4.78	1.77	6.61	5.38	0.82	0.52		100.94
PM1 H 16	60.78		18.07			4.40	1.74	6.61	5.30	0.95	0.45		98.30
PM1 H 17	62.27		18.09			4.28	1.72	6.60	5.53	0.86	0.43		99.79
PM1 H 18	62.28		17.89			3.71	1.72	6.71	5.49	0.76	0.47		99.01
PM1 NNO 1	52.69		15.48			9.25	4.61	4.56	2.67	3.04	0.25		92.55
PM1 NNO 2	52.46		15.40			8.72	4.70	4.45	2.49	3.00	0.34		91.57
PM1 NNO 3	52.06		15.40			8.79	4.47	4.42	2.45	2.76	0.28		90.61
PM1 NNO 4	52.69		15.69			9.11	4.58	4.49	2.41	2.75	0.24		91.97
PM1 NNO 5	52.20		15.87			9.12	4.70	4.43	2.54	2.90	0.29		92.03
PM1 NNO 6	52.42		15.61			8.92	4.63	4.28	2.48	2.75	0.30		91.40
PM1 NNO 7	52.52		15.56			9.30	4.58	4.38	2.56	2.64	0.28		91.81
PM1 NNO 8	52.52		15.63			9.27	4.52	4.44	2.60	2.71	0.28		91.97
PM1 NNO 9	52.32		15.47			8.98	4.57	4.47	2.59	2.78	0.35		91.52
PM1 NNO 10	52.12		15.30			9.27	4.46	4.50	2.48	2.82	0.30		91.24
PM1 NNO 11	52.31		15.41			8.90	4.62	4.44	2.58	2.84	0.29		91.39
PM1 NNO 12	51.93		15.33			9.36	4.47	4.46	2.52	2.80	0.25		91.14
PM1 NNO 13	52.32		15.50			9.32	4.48	4.54	2.45	2.87	0.33		91.81
PM1 NNO 14	52.52		15.77			9.30	4.40	4.45	2.47	2.98	0.26		92.16
PM1 NNO 15	52.04		15.40			9.17	4.65	4.40	2.56	3.09	0.30		91.61
PM1 NNO 16	52.21		15.75			9.21	4.55	4.48	2.58	2.83	0.31		91.91
PM1 NNO 17	51.94		15.66			9.04	4.71	4.37	2.30	2.90	0.31		91.23
PM1 NNO 18	53.57		15.03			8.01	4.34	4.57	2.35	2.75	0.29		90.91

Glass EPMA measurements (wt% element) **(continued)**

Analysis name	**SiO_2**	**TiO_2**	**Al_2O_3**	**FeO**	**MgO**	**MnO**	**CaO**	**K_2O**	**Na_2O**	**P_2O_5**	**Cl**	**F**	**Total**
PM1 PtC 1	55.89		15.80			6.54	4.50	4.82	3.40	1.79	2.28		95.03
PM1 PtC 2	55.47		15.95			6.71	4.55	4.86	3.58	1.66	2.25		95.03
PM1 PtC 3	55.97		16.17			6.54	4.44	4.83	3.38	1.68	2.18		95.18
PM1 PtC 4	55.74		16.36			6.88	4.65	4.82	3.39	1.84	2.22		95.89
PM1 PtC 5	55.82		16.21			7.00	4.48	4.87	3.56	1.73	2.06		95.73
PM1 PtC 6	55.57		15.84			7.16	4.36	4.92	3.14	1.60	1.98		94.56
PM1 PtC 7	56.51		16.14			6.45	4.35	4.94	3.41	1.74	2.03		95.58
PM1 PtC 8	55.84		15.91			6.73	4.45	4.83	3.42	1.79	2.06		95.04
PM1 PtC 9	55.89		15.81			6.52	4.45	4.90	3.45	1.61	2.04		94.67
PM1 PtC 10	57.11		16.15			6.28	4.40	4.90	3.18	1.80	1.96		95.79
PM1 PtC 11	56.45		16.36			6.78	4.31	4.82	3.39	1.72	2.00		95.83
PM1 PtC 12	57.31		16.24			6.67	4.16	4.67	3.15	1.98	1.95		96.13
PM1 PtC 13	54.69		15.99			7.22	4.67	4.67	3.31	1.95	2.16		94.66
PM1 PtC 15	56.15		16.01			6.61	4.42	4.79	3.46	1.74	2.08		95.26
PM1 PtC 17	56.79		16.09			6.32	4.37	5.05	3.32	1.79	1.98		95.71
PM1 PtC 18	56.88		16.19			6.60	4.28	4.95	3.51	1.68	1.99		96.08
MH 1200 Hap10 1	49.98		14.55	1.66	0.10	7.84	3.99	5.17	3.38	3.74	0.46		90.87
MH 1200 Hap10 2	50.14		14.77	1.73	0.12	8.02	4.28	5.07	3.43	4.09	0.47		92.15
MH 1200 Hap10 3	49.22		14.52	1.68	0.11	7.67	4.17	5.17	3.29	4.03	0.46		90.36
MH 1200 Hap10 4	50.38		14.72	1.67	0.11	7.41	3.98	5.16	3.50	3.83	0.46		91.31
MH 1200 Hap10 5	50.79		14.36	1.73	0.08	7.69	4.17	5.18	3.51	3.70	0.47		91.75
MH 1200 Hap10 B1	49.79		14.71	1.70	0.09	7.62	3.94	5.17	3.10	3.65	0.47		90.36
MH 1200 Hap10 B2	50.96		14.67	1.45	0.09	7.15	3.80	5.35	2.93	2.97	0.44		89.86
MH 1200 Hap10 B4	49.98		14.72	1.47	0.09	7.06	3.83	5.38	3.39	3.00	0.44		89.43
MH 1200 Hap10 B5	49.40		14.37	1.81	0.09	7.66	4.33	5.17	3.35	3.60	0.47		90.32

Glass EPMA measurements (wt% element) **(continued)**

Analysis name	**SiO_2**	**TiO_2**	**Al_2O_3**	**FeO**	**MgO**	**MnO**	**CaO**	**K_2O**	**Na_2O**	**P_2O_5**	**Cl**	**F**	**Total**
MW 1200 Hap10 3	57.83		16.00	1.60	0.23	6.56	2.97	6.36	3.91	2.03	0.22		97.78
MW 1200 Hap10 4	55.66		16.03	1.64	0.26	7.52	3.55	6.25	4.16	2.17	0.23		97.55
MW 1200 Hap10 5	57.18		16.30	1.47	0.27	7.41	3.30	6.04	4.03	2.16	0.22		98.42
Cr 1200 Hap10 1	54.03		14.98	0.01	0.06	7.01	3.24	5.67	3.66	2.50	0.15		91.33
Cr 1200 Hap10 2	53.70		15.25	0.03	0.08	6.88	3.27	5.66	3.36	2.47	0.15		90.91
Cr 1200 Hap10 3	53.52		15.23	0.04	0.08	7.26	3.36	5.46	3.96	2.83	0.15		91.92
Cr 1200 Hap10 4	53.01		15.37	0.04	0.07	7.37	3.29	5.43	3.92	2.84	0.15		91.59
Cr 1200 Hap10 5	53.15		15.09	0.02	0.07	7.35	3.46	5.48	3.53	2.85	0.15		91.18
NNO 1200 Hap10 1	52.22		15.78		0.08	7.33	4.49	5.46	3.89	3.13	0.52		93.06
NNO 1200 Hap10 3	52.66		15.55		0.08	7.87	4.47	5.56	3.89	3.53	0.58		94.71
NNO 1200 Hap10 4	51.65		14.99		0.06	7.92	4.88	5.30	3.46	3.76	0.62		93.39
Cr 1200 Hap5 1	62.08		13.05		0.09	3.92	2.57	3.59	4.40	2.21	0.09		92.10
Cr 1200 Hap5 2	62.31		12.99		0.08	3.87	2.55	3.44	4.56	2.21	0.08		92.22
Cr 1200 Hap5 3	63.85		13.01		0.07	3.86	2.67	3.53	4.70	2.17	0.09		94.09
Cr 1200 Hap5 4	63.91		12.89		0.08	3.89	2.46	3.42	4.50	2.22	0.09		93.66
Cr 1200 Hap5 5	62.87		12.72		0.07	3.84	2.64	3.41	4.68	2.20	0.08		92.60
SH3 Cr 1	46.42		15.42		9.99	0.75	16.22	1.58	2.44	4.19		1.34	98.40
SH3 Cr 2	46.24		15.69		10.01	0.71	16.65	1.60	2.73	4.14		1.29	99.10
SH3 Cr 3	47.19		15.58		9.91	0.73	16.29	1.50	2.55	3.95		1.43	99.19
SH3 Cr 4	46.04		15.62		9.99	0.74	16.62	1.62	2.74	4.23		1.33	98.93
SH3 Cr 5	46.44		15.90		10.12	0.72	16.58	1.62	2.67	4.25		1.37	99.73
SH3 PtC 1	46.64		15.74	0.03	10.19	0.78	16.50	1.65	2.60	4.00		1.32	99.44

Glass EPMA measurements (wt% element) **(continued)**

Analysis name	**SiO_2**	**TiO_2**	**Al_2O_3**	**FeO**	**MgO**	**MnO**	**CaO**	**K_2O**	**Na_2O**	**P_2O_5**	**Cl**	**F**	**Total**
SH3 PtC 2	46.48		15.56	0.03	10.25	0.78	16.38	1.58	2.26	4.02		1.37	98.73
SH3 PtC 3	46.88		15.30	0.04	10.11	0.79	16.42	1.51	2.51	3.97		1.33	98.93
SH3 PtC 4	45.84		15.74	0.05	10.23	0.80	16.53	1.62	2.36	4.00		1.36	98.55
SH3 PtC 5	45.95		15.58	0.03	10.11	0.82	16.46	1.51	2.36	3.94		1.43	98.25
SH3 Pt 9	46.28		15.46		9.94	0.89	15.83	1.43	2.31	4.19		1.34	97.70
SH3 Pt 9b	45.58		15.48		10.04	0.90	16.24	1.51	2.56	4.19		1.40	97.88
SH3 Pt 10	45.50		15.48		10.03	0.89	16.41	1.53	2.65	4.18		1.37	98.11
SH3 MH 1	45.97		15.40	1.75	8.55	0.86	15.58	1.66	2.84	4.00		1.16	97.78
SH3 MH 2	45.95		15.41	1.78	8.62	0.87	15.60	1.65	2.57	4.05		1.36	97.84
SH3 MH 3	44.95		15.24	1.73	8.60	0.85	15.59	1.64	2.68	4.02		1.33	96.68
SH3 MH 4	45.21		15.40	1.81	8.55	0.84	15.50	1.69	2.47	4.06		1.25	96.78
SH3 MH 5	45.04		15.18	1.67	8.45	0.87	15.51	1.67	2.71	4.05		1.30	96.46
BMT2 Cr 1	60.60	0.22	18.36		0.31	0.08	3.59	7.04	6.40	1.29		1.08	99.05
BMT2 Cr 2	59.99	0.28	18.47		0.30	0.08	3.62	7.06	6.32	1.39		1.02	98.74
BMT2 Cr 3	60.46	0.33	18.54		0.32	0.07	3.56	6.99	6.42	1.40		1.03	99.36
BMT2 Cr 4	61.24	0.30	18.36		0.33	0.07	3.64	6.86	6.06	1.38		0.92	99.29
BMT2 Cr 5	60.49	0.24	18.52		0.31	0.05	3.60	6.90	6.50	1.30		0.94	99.00
BMT2 Pt 2	56.48	0.33	17.58	1.37	0.29	0.74	4.15	6.20	5.36	2.36		1.10	95.99
BMT2 Pt 3	56.02	0.27	17.42	1.25	0.28	0.76	4.31	6.33	5.90	2.51		1.03	96.06
BMT2 Pt 4	55.74	0.29	17.54	1.27	0.31	0.75	4.35	6.36	5.74	2.50		0.98	95.81
BMT2 Pt 5	54.97	0.29	17.40	1.29	0.30	0.77	4.43	6.20	5.91	2.53		1.16	95.25
BMT2 MH 1	44.73	0.24	13.03	12.30	0.29	0.59	8.32	4.98	4.42	5.96		1.13	95.99

Glass EPMA measurements (wt% element) **(continued)**

Analysis name	**SiO_2**	**TiO_2**	**Al_2O_3**	**FeO**	**MgO**	**MnO**	**CaO**	**K_2O**	**Na_2O**	**P_2O_5**	**Cl**	**F**	**Total**
BMT2 MH 2	45.18	0.26	13.31	12.27	0.28	0.58	8.12	5.15	5.05	5.89		1.17	97.27
BMT2 MH 3	45.26	0.24	13.58	12.09	0.29	0.59	7.98	5.04	4.77	5.70		1.30	96.90
BMT2 MH 4	45.97	0.26	13.49	11.86	0.29	0.57	8.10	5.15	4.61	5.51		1.23	97.07
BMT2 MH 5	45.75	0.23	13.30	11.90	0.27	0.58	8.04	5.15	4.98	5.66		1.28	97.15